

Copyright
by
Moslem Taghavifar
2014

The Dissertation Committee for Moslem Taghavifar Certifies that this is the approved version of the following dissertation:

**Enhanced Heavy Oil Recovery
By Hybrid Thermal-Chemical Processes**

Committee:

Gary A. Pope, Supervisor

Kamy Sepehrnoori, Co-Supervisor

Mojdeh Delshad

Kishore Mohanty

Roger T. Bonnecaze

**Enhanced Heavy Oil Recovery
By Hybrid Thermal-Chemical Processes**

by

Moslem Taghavifar, B.E.; M.S.

Dissertation

Presented to the Faculty of the Graduate School of

The University of Texas at Austin

in Partial Fulfillment

of the Requirements

for the Degree of

Doctor of Philosophy

The University of Texas at Austin

May 2014

Dedication

To my family.

Acknowledgements

I would like to express my deepest gratitude to my advisors, Dr. Gary Pope and Dr. Kamy Sepehrnoori, for their continuous guidance, support, and encouragement. I have greatly benefited from their vast experience. I also appreciate the valuable comments and feedback of my committee members, Dr. Kishore Mohanty, Dr. Mojdeh Delshad, and Dr. Roger Bonnecaze. Special thanks go to Dr. Eric de Rouffignac and Dr. Robert McNeil for their contribution to my research. I am also thankful to the industrial sponsors of the Chemical EOR industrial affiliates program in the Center for Petroleum and Geosystems Engineering for funding this research.

I wish to thank my friends and colleagues, Corinne Stokes, Behdad Aminzadeh, Reza Ganjdanesh, Hamed Darabi, Mohammad Evazi, Gayani Kennedy, and Robert Fortenberry, who I learned from one way or another. Thanks as well to Frankie Hart, Roger Terzian, Joanna Castillo, and Esther Barrientes for administrative support.

Finally, many thanks go to my family for their love and support throughout my PhD work.

Enhanced Heavy Oil Recovery

By Hybrid Thermal-Chemical Processes

Moslem Taghavifar, Ph.D.

The University of Texas at Austin, 2014

Supervisor: Gary A. Pope, Kamy Sepehrnoori

Developing hybrid processes for heavy oil recovery is a major area of interest in recent years. The need for such processes originates from the challenges of heavy oil recovery relating to fluid injectivity, reservoir heating, and oil displacement and production. These challenges are particularly profound in shaley thin oil deposits where steam injection is not feasible and other recovery methods should be employed. In this work, we aim to develop and optimize a hybrid process that involves moderate reservoir heating and chemical enhanced oil recovery (EOR).

This process, in its basic form, is a three-stage scheme. The first stage is a short electrical heating, in which the reservoir temperature is raised just enough to create fluid injectivity. After electrical heating has created sufficient fluid injectivity, high-rate high-pressure hot water injection accelerates the raise in temperature of the reservoir and assists oil production. At the end of hot waterflooding the oil viscosities are low enough for an Alkali-Co-solvent-Polymer (ACP) chemical flood to be performed where oil can efficiently be mobilized and displaced at low pressure gradients.

A key aspect of ultra-low IFT chemical flood, such as ACP, is the rheology of the microemulsions that form in the reservoir. Undesirable rheology impedes the displacement of the chemical slug in the reservoir and results in poor process performance or even failure. The viscosity of microemulsions can be altered by the addition of co-solvents and branched or twin-tailed co-surfactants and by an increase in temperature. To reveal the underlying mechanisms, a consistent theoretical framework was developed. Employing the membrane theory and electrostatics, the significance of charge and/or composition heterogeneity in the interface membrane and the relevance of each to the above-mentioned alteration methods was demonstrated. It was observed that branched co-surfactants (in mixed surfactant formulations) and temperature only modify the saddle-splay modulus (\bar{k}) and bending modulus (k) respectively, whereas co-solvent changes both moduli. The observed rheological behavior agrees with our findings.

To describe the behavior of microemulsions in flow simulations, a rheological model was developed. A key feature of this model is the treatment of the microemulsion as a bi-network. This provides accuracy and consistency in the calculation of the zero-shear viscosity of a microemulsion regardless of its type and microstructure. Once model parameters are set, the model can be used at any concentration and shear rate. A link between the microemulsion rheological behavior and its microstructure was demonstrated. The bending modulus determines the magnitude of the viscous dissipations and the steady-shear behavior. The new model, additionally, includes components describing the effects of rheology alteration methods.

Experimental viscosity data were used to validate the new microemulsion viscosity model. Several ACP corefloods showing the large impact of microemulsion viscosity on process performance were matched using the UTCHEM simulator with the new microemulsion rheology model added to the code.

Finally, numerical simulations based on Peace River field data were performed to investigate the performance of the proposed hybrid thermal-chemical process. Key design parameters were identified to be the method of heating, duration of the heating, ACP slug size and composition, polymer drive size, and polymer concentration in the polymer drive. An optimization study was done to demonstrate the economic feasibility of the process. The optimization revealed that short electrical heating and high-rate high-pressure waterflooding are necessary to minimize the energy use and operational expenses. The optimum slug and polymer drive sizes were found to be ~ 0.25 PV and ~ 1 PV, respectively. It was shown that the well costs dominate the expenditure and the overall cost of the optimized process is in the range of 20-30 $\$/bbl$ of incremental oil production.

Table of Contents

List of Tables.....	xii
List of Figures	xiii
Chapter 1: Introduction	1
Chapter 2: Background.....	5
2.1 Introduction	5
2.2 Oil/water/surfactant Phase Behavior	6
2.3 Theories to Describe the Phase Transitions.....	10
2.3.1 Winsor R Ratio.....	10
2.3.2 Hydrophilic-Lipophilic Balance (HLB)	11
2.3.3 Phase Inversion Temperature	11
2.3.4 Packing Parameter.....	12
2.3.5 Equivalent Alkane Carbon Number (EACN).....	14
2.3.6 Hydrophilic-Lipophilic Deviation (HLD).....	15
2.3.7 Membrane Theory.....	16
2.4 Microstructure	18
2.4.1 Dilute Microemulsions.....	18
2.4.2 Concentrated Microemulsions.....	20
2.4.3 Bicontinuous Microemulsion	23
Chapter 3: Microemulsion Rheology Alteration Mechanisms.....	32
3.1 Background.....	32
3.2 Experimental Observations.....	34
3.3 Theory.....	36
3.3.1 Effect of Branched Co-surfactant.....	38
3.3.2 Effect of Co-solvent	44
3.3.3 Effect of Temperature	54

Chapter 4: Microemulsion Rheology Model.....	57
4.1 Literature Review	57
4.2 Model Formulation	59
4.2.1 Zero-shear Viscosity	60
4.2.2 Effect of Shear Rate	69
4.2.3 Effects of Co-solvent, Branched Co-surfactant, and Temperature ...	72
4.3 Results	74
Chapter 5: Microemulsion Rheology in the Presence of Polymer	82
5.1 Surfactant/Polymer Interactions in Aqueous Solution	82
5.2 Size of Polymer Coil.....	86
5.3 Polymer Partitioning in Microemulsion Systems	88
5.4 Inclusion of Polymer in the Rheology Model	92
5.5 Results	96
Chapter 6: UTCHEM Thermal Module Modification and Verification	109
6.1 Variable Temperature Input.....	109
6.2 Thermal Conductivity.....	109
6.3 Microemulsion Heat Capacity	110
6.4 Comparison With CMG-STARS.....	111
6.5 Chemical Flooding Example	112
Chapter 7: HTCP Development and Optimization.....	116
7.1 Literature Review	116
7.2 Recovery Scheme and Wellbore/Electrode Configurations	118
7.3 Rock and Fluid Properties	120
7.3.1 Thermal Properties	121
7.3.2 Electrical Conductivity.....	122
7.3.3 Oil Viscosity.....	124

7.4 Simulation Model	125
7.4.1 Electrical Heating	126
7.4.2 Chemical Flooding	128
7.4.3 Effects of Heterogeneities	129
7.5 Optimization	139
7.5.1 Field-scale Sensitivity Analysis	141
7.5.2 Results	143
Chapter 8: Summary, Conclusions and Recommendations.....	148
8.1 Summary and Conclusions	148
8.2 Recommendations	150
Appendix A	154
Appendix B.....	166
Bibliography.....	202

List of Tables

Table 3.1: Characteristics of the microemulsion samples	35
Table 3.2: Comparison of the Gouy-Chapman length and Coulomb coupling for microemulsion samples “A” and “B”	47
Table 3.3: The Gouy-Chapman length and Coulomb coupling parameter the microemulsion sample “D”.	55
Table 4.1: Differences of the microemulsion samples.....	76
Table 4.2: Softened synthetic reservoir brine used in Walker (2011) samples	76
Table 4.3: Model parameters	76
Table 5.1: Polyacrylamide gyration radius data	87
Table 5.2: Chemical formulation for Upamali (2014) microemulsion samples	96
Table 5.3: Corefloods’ specifications	102
Table 5.4: Rheology model parameters	102
Table 5.5: Comparison of corefloods’ performances and simulation results (numbers in parentheses)	103
Table 5.6: Summary of coreflood input parameters	103
Table 6.1: Simulation model parameters for the single-phase hot water injection.....	112
Table 6.2: The ACP flood model parameters	113
Table 7.1: Analogy of electrical and fluid injection operating conditions	135
Table 7.2: Design parameters for optimization.....	140
Table 7.3: Unit prices for cost calculations	140

List of Figures

<p>Figure 2.1: Phase behavior of surfactant/oil/water. (a) Experimental phase diagram of the ternary system $C_{10}E_5$-water-octane from (Strey 1993; Daicic et al. 1995). (b) Fish diagram of the ternary system $C_{12}E_5$-water-decane at equal volume fractions of water and oil. The diagram shows the number of phases as the surfactant volume fraction and temperature change. Symbol “L” denotes microemulsion and “L_α” lamellar liquid crystal phase. Note the transition as surfactant concentration is increased, denoted by “$L + L_\alpha$” (Wennerström and Olsson 2009). (c) Solubilization ratios vs. salinity (Levitt et al. 2006).</p>	9
<p>Figure 2.2: Surfactant packing shape and associated schematic aggregate structures at different “packing parameter” or “shape factor”, v/a_0l_c (Israelachvili 1994, 2011).</p>	14
<p>Figure 2.3: Variation of average droplet radius (or characteristic length for Type III microemulsion) with phase transition from <i>Type I</i> \rightarrow <i>III</i> \rightarrow <i>II</i>; (a) drop radius vs. salinity for an anionic surfactant (Huh 1983). (b) drop radius vs. temperature for nonionic surfactant (Strey 1994).</p>	19
<p>Figure 2.4: Fast- and slow-mode diffusion (a) O/W microemulsion containing SDS, octanol, octane, and brine (Peter et al. 2001). The dashed line represents the diffusion constant extracted from the Stokes-Einstein relation. (b) O/W microemulsion composed of brine, paraffin oil, AOT, and $C_{12}(EO)_4$ (Hattori et al. 2007).</p>	21
<p>Figure 2.5: electrical conductivities of W/O microemulsion vs. droplet volume fraction. The left curve corresponds to more attractive droplets than the right curve (Langevin 1988).</p>	22
<p>Figure 2.6: Voronoi polyhedrons of the Talmon-Prager model (Langevin 1988).</p>	29
<p>Figure 2.7: Phase diagram of a microemulsion with no spontaneous curvature ($\rho_0 \rightarrow \infty$). The volume fraction $\tilde{\phi}_s = \phi_s/\phi_m$, where ϕ_s, is the volume fraction of surfactant, and $\phi_m = \exp(4\pi k/\alpha k_B T)$. The water volume fraction is ϕ_w and $\phi = \phi_w + \phi_s/2$. The numbers indicate the number of coexisting phases and the tie lines in the two-phase region are shown. (a) $f_w^* = f_o^*$ Inset: The details of the tie lines at small volume fractions. (b) $f_o^* = f_w^*/2$ (Safran et al. 1986).</p>	29

Figure 2.8: FFEM images (10 000×instrument magnification) of freeze fractured microemulsions of the ternary system H ₂ O– <i>n</i> -octane–C12E5 at different WOR. a) $\phi_w = 0.6$ b) $\phi_w = 0.5$ c) $\phi_w = 0.4$ The arrow in c indicates a saddle point (Burauer et al. 2003).	31
Figure 2.9: Periodic embedded minimal surfaces of non-positive Gaussian curvature: (a, b) unit cell is gyroid (Gózdź and Hołyst 1996).	31
Figure 3.1: Rheology of microemulsion samples with $\phi_o \sim 0.4$ (Dustin Walker 2011). Microemulsion “A” is created by only using surfactant at 55 °C. Samples “B” and “C” are created by addition of 1wt% co-solvent to “A”. The composition of microemulsion “D” is similar to that of “A” but temperature is raised by 30 °C. Additionally, samples “B”, “C”, and “D” contain branched IOS as co-surfactant. Lines are for eye-guidance.	35
Figure 3.2: (a) Schematic representation of the arrangement of co-surfactant molecules. (b) Schematic representation of the arrangement of co-solvent molecules. In both cases the micelles core is filled with oil.	37
Figure 3.3: Component self-diffusion coefficients (at 20 °C) in microemulsions composed of sodium dodecyl sulfate (SDS) (1.99% by weight), butanol (3.96%), toluene (46.25%), and brine (46.8%) (Guering and Lindman 1985). While the self-diffusion coefficient of brine decreases with microemulsion phase evolution from Type <i>I</i> → <i>III</i> → <i>II</i> , that of oil increases. Surfactant (i.e. SDS) retains a comparatively low self-diffusion coefficient in all phase types whereas the co-solvent (i.e. butanol) self-diffusion coefficient remains close to that of the continuous phase. Lines are for eye-guidance.	38
Figure 3.4: Schematic diagram demonstrating that the mixing of twin-tailed and single-chain surfactant results in the formation of saddle-splay structures at salinities between the optimum salinities of the two surfactants. Differences in the affinities of the two surfactants result in concentration heterogeneity at concave and convex parts of the resulting hyperboloid (a)2D, (b)3D.....	43
Figure 3.5: Snapshots of Monte-Carlo simulations demonstrating the distributions of counterions at different coupling parameters: $\Xi = 0.1$ or weak-coupling limit where Poisson-Boltzmann theory is accurate and $\Xi = 100$ or strong-coupling regime (Moreira and Netz 2000). (b) Reduced counterion distribution $\Lambda \equiv \rho_+(z)(2\pi l_B b^2)$ for weak Coulomb limit ($\Lambda = \frac{1}{(1+z/b)^2}$) compared to strong coupling limit ($\Lambda = \exp(-z/b)$). At $z = b$, the cumulated counterions (shadowed region) half-compensate the charge of the surface (Messina 2009).....	48

Figure 3.6: Schematic diagram demonstrating the curvature induced by non-uniform distribution of the co-solvent; (a) without (b) with co-solvent – the dark ring is covered by co-solvent.	51
Figure 3.7.b: The data shows the rheology of CPCI/hexanol/brine with $\phi_{solvent} = 0.85$ at $T = 24$ °C (Mahjoub et al. 1996). The ratio of co-solvent (hexanol) to surfactant (CPCL) is 1.075 for the L_{α} phase and 1.15 for the L_3 phase.....	53
Figure 3.8: Effect of temperature on the rheology of a microemulsion composed of AOT/decane/brine with $\phi_o = 0.15$ and $\phi_s \sim 0.3$. The lamellar-like sample is at $T = 21.1$ °C and the disordered at $T = 18.4$ °C (Kotlarchyk et al. 1992).	55
Figure 4.1: Normalized long-time self-diffusivity of hard-spheres (Ottewill and Williams 1987) and uncharged (Evilevitch et al. 2001) and negatively-charged (Peter et al. 2001) oil-in-water (O/W) droplet microemulsions. The behavior of uncharged microemulsion is hard-sphere-like while because of the long-range electrostatic potential of charged microemulsion, D_s^L (hence D_s^S) remains finite. This phenomenon makes the viscosity singularity less severe.....	63
Figure 4.2: Relative zero-shear viscosity of droplet microemulsions. (a) Dilute O/W (Leaver and Olsson 1994) and W/O (Berg et al. 1987) microemulsions. For the sake of comparison, the theory prediction ($\eta_{or} = 1 + 2.5\phi + 6.2\phi^2$) for hard-spheres (Batchelor 1977) is included. (b) Concentrated O/W (Leaver and Olsson 1994) and W/O (Peyrelasse et al. 1988; Sheu et al. 1989) microemulsions. At high concentrations the O/W viscosities deviate from the model prediction. Emulsification failure occurs at $\phi_m = 0.581$ (Leaver and Olsson 1994) which was used in the generalized Krieger and Dougherty (Equation (4.2)) and included in the graph for comparison.	66
Figure 4.3: Comparison of normalized experimental steady shear viscosity of dispersions and microemulsions (ME) as a function of Péclet number. Dispersion data are characterized as Brownian with $\phi = 0.47$ (Cheng et al. 2011), charge stabilized with $\phi = 0.47$ (Foss and Brady 2000; Van der Werff and De Kruif 1989), and stabilized by polymer brush with $\phi = 0.5$ (Wagner and Brady 2009). Microemulsion data are adapted from (Dustin Walker 2011). Despite their lower concentration, microemulsions behave similar to hard-spheres. All lines are for eye-guidance.....	71
Figure 4.4: Increase of onset of shear-thinning behavior by the addition of co-solvent and/or branched co-surfactant. In the presence of enough good co-solvent the sample losses its rheology dependency to shear rate (i.e. $\alpha = 0$) and behaves Newtonian.....	73

Figure 4.5: Comparison of calculated and measured apparent viscosity. The experimental data are adapted from (Dustin Walker 2011). (a) Apparent viscosity versus oil volume fraction in microemulsion at $\gamma = 100 \text{ s}^{-1}$. (b) Steady-shear rheology of microemulsion samples with $\phi_o \sim 0.4$. Note that each sample represents a different subset here. Within each subset, salinity is the only variable to create the phase shift. Sample “A” is created by only using surfactant at $55 \text{ }^\circ\text{C}$, while samples “B” and “C” contain 1 wt% co-solvent. Sample “D” contains no co-solvent but the temperature was raised to $85 \text{ }^\circ\text{C}$	77
Figure 4.6: Comparison of calculated and measured apparent viscosities for data from (Lu et al. 2013). (a) Apparent viscosity versus oil volume fraction in microemulsion at $\gamma = 10 \text{ s}^{-1}$. (b) Steady-shear rheology of microemulsion samples with different oil volume fractions. Since the phase shift is caused by only varying the salinity, only one set of model parameters are adequate to describe the behavior of all the samples.....	78
Figure 4.7: Example 3D microemulsion rheology versus shear rate and ϕ based on Walker et al. (2012; Dustin Walker 2011) data.....	80
Figure 4.8: Variation of maximum zero-shear viscosity, η_{0m} , as a function of the intrinsic interface property, ν . η_{0m} values are experimental data and ν is the relevant model parameter. Note that ν closely resembles the interface bending modulus, k , and it varies between $0.3 \leq \nu \leq 2.5$	81
Figure 5.1: Associative (left) and segregative (right) surfactant/polymer phase separation at salinities higher than aqueous solubility limit, adapted from Holmberg (2003).	83
Figure 5.2: Formation of branched micelles in a cloudy solution (Holmberg 2003).	84
Figure 5.3: Lamellar (left) and cubic (right) phase microstructures (Holmberg 2003). ...	84
Figure 5.4: Onset salinity of phase separation is shifted to the left in the presence of polymer (Pope et al. 1982).	85
Figure 5.5: Schematic graph of water surface tension in the presence of polymer (Holmberg 2003).	85
Figure 5.6: radius of gyration of a polymer coil.	86
Figure 5.7: Polyacrylamide gyration radius in brine versus its molecular weight. The data are adapted from (Ball and Pitts 1984; Jia et al. 2009; Mihcakan and C.W. 1986; Omari et al. 1989).	88

Figure 5.8: Polymer partitioning for a balanced C ₁₂ E ₅ -water-decane-dextran microemulsion (Kabalnov et al. 1996).	90
Figure 5.9: Microemulsion viscosity for octane-brine-TRS1080-XANFLOOD system as phase type changes from <i>Type I</i> → <i>III</i> → <i>II</i> (Pope et al. 1982).	90
Figure 5.10: Schematic depiction of polymer-microemulsion microstructure and polymer partitioning as the microemulsion type evolves. Typical polymers used in chemical EOR are only water-soluble and therefore Type I microemulsion contains the entire polymer that is present. In Type III and II systems, polymer partitions between the microemulsion phase and the excess brine. The partitioning is mainly governed by the size exclusion mechanism which implies low partitioning if polymer has a large gyration radius compared to micro-emulsion characteristic domain size.....	91
Figure 5.11: (a) Schematic demonstration of salinity effect on the polymer gyration radius and oil-in-water (O/W) micelle size in the Type I salinity window. As salinity increases the polymer coil shrinks while the micelle size grows. (b) Schematic illustration of the effect of polymer on the zero-shear viscosity of a Type I microemulsion. Without the polymer, the viscosity of the microemulsion increases with increasing salinity as more oil is solubilized in microemulsion. Addition of a polymer to the microemulsion system shifts the viscosity curve to higher values assuming negligible polymer/surfactant interactions and no salinity effect on the polymer coil. In reality, however, the polymer coil collapses as the salinity increases which results in vanishing polymer effect. Therefore the polymer-microemulsion viscosity behavior is a tradeoff between the gain of viscosity by solubilizing more oil and loss of viscosity from polymer coil collapse.	93
Figure 5.12: Viscosity of polymer-containing microemulsion is a non-linear combination of two hypothetical cases: “no salinity-effect” and “exaggerated salinity-effect”. In the no salinity-effect limit, the contribution of the polymer coil to the viscosity is high and independent of salinity while this contribution is negligible at the exaggerated salinity-effect limit. The combined behavior of the polymer-microemulsion system is also affected by the amount of polymer partitioning. For large polymer molecules the amount of partitioned polymer progressively decreases by getting closer to the end of Type II salinity.	96
Figure 5.13: Viscosity of a number of microemulsions with (orange markers) and without (black markers) polymer. The lines are the model calculations. The experimental data are measured by Upamali (2014).	97
Figure 5.14: Experimental Polymer solution viscosity at slug/polymer drive salinity and concentration (Fortenberry 2013) versus UTCHEM model.	104

Figure 5.15: Comparison of “ACP-1” coreflood data with simulation results for (a) cumulative oil recovery and oil cut, (b) pressure drop across the core, and (c) effluent pH. Favorable mobility ($MR = 1$) of ACP-1 coreflood resulted in a stable displacement and high oil recovery. Lines are the simulation results. The agreement between the experimental data and simulation results is evident.....	106
Figure 5.16: Simulation of tertiary chemical corefloods where variations in temperature and chemicals resulted in different performances. ACP-1 and ACP-2 are Alkali-Co-solvent-Polymer flooding and ALK is an alkaline flooding. “MR” refers to mobility ratio.....	107
Figure 5.17: Pressure drop for ACP-2 where the points show experimental results and the line is the simulation results. A leak in the pressure column was reported by Fortenberry (2013) at around 0.33 PV of chemical injection.	108
Figure 6.1: Temperature profile for a non-isothermal ASP coreflood simulation. Considering the composition dependency of microemulsion heat capacity removes the temperature oscillations. Value of λ (i.e. heat conductivity) changes the thermal Péclet number and thus the temperature profile.	111
Figure 6.2: Average reservoir temperature for single-phase water injection and hot waterflooding cases obtained from CMG-STARs and UTCHEM.	113
Figure 6.3: XZ cross-sectional temperature distribution for the hot water flooding case obtained from (a) CMG-STARs and (b) UTCHEM.	114
Figure 6.4: XZ cross-sectional temperature profile for an ACP chemical flood: (a) original UTCHEM (b) modified UTCHEM. Initial reservoir temperature is 203 °F. The profile is shown after 0.4 PV of fluid injection.....	115
Figure 7.1: Reservoir model and wellbore/electrode configuration. The wellbore arrangement allows for using 3-phase voltage during electrical heating and efficient flooding during fluid injection. The phase of each electrode is indicated by $\angle\theta$	119
Figure 7.2: Typical standard logs for the Bluesky formation (Shell Canada Limited 2009).....	124
Figure 7.3: Measured oil viscosity versus temperature. The data is adapted from (Fortenberry 2013).....	125
Figure 7.4: Validation of electrical heating simulation and gridding system by overall energy balance.	127

Figure 7.5: Voltage drop along the wellbore and the resulting temperature distribution. Note the non-uniform temperature increase along the wellbore..	128
Figure 7.6: Typical oil viscosity variations with depth and temperature for the Bluesky formation. Data is adapted from (Koci and Mohiddin 2007b; Larter et al. 2008).....	130
Figure 7.7: The default vertical flood (left) could be switched to a horizontal one (right) in the case of very low effective vertical permeability. The arrows schematically show the direction and magnitude of flow.	131
Figure 7.8: Fluid distribution effects on the performance of electrical heating. The graphs show XZ cross-sectional temperature distribution for (a) uniform water saturation, (b) variable resistivity-log-derived water saturation with $S_{w_ave} = 0.25$, and (c) variable resistivity-log-derived water saturation with $S_{w_ave} = 0.25$ including the presence of bottom water. Initial reservoir temperature is 80 and same amount of energy is injected for all the cases.....	135
Figure 7.9: Effect of initial water saturation and electrical operating conditions on the uniformity of the heating pattern. Variable (depicted by “var.” in the graph) water saturation inherently disturbs the balance of heating pattern which can be resolved by controlling the electrical operating conditions. With the presence of bottom water, however, the disturbance cannot be resolved.	136
Figure 7.10: XZ cross-section of two-layer reservoir model used to study the effects of permeability heterogeneities on the electrical heating and waterflooding. Base/cap shale are included in the simulation but not shown here.	137
Figure 7.11: Permeability heterogeneities effects on the heating performance where electrical heating for 360 days is flowed by a hot waterflood. While the electrical heating performance is not greatly altered by the permeability heterogeneities, that of waterflooding is strongly affected. (a) As k_v/k_h decreases, the lack of water injectivity causes the vertical flow pattern to be inefficient. For the case of $k_v/k_h=0.01$ water injection becomes impossible. (b) Switching to a horizontal flow pattern greatly recovers the efficacy of the process for the $k_v/k_h=0.01$ case. The vertical separation of the wells is slightly decreased in the horizontal flow, which is evident by the better performance of the electrical heating.	138
Figure 7.12: Field-scale simulation of chemical flood performance after reservoir temperature is raised to 150 °F corresponding to $\mu_o \sim 1000$ cP. Equivalent end-point mobility ratios shown in the graph are obtained by varying the amount of polymer used.	143

Figure 7.13: Optimization iteration summary in terms of best before-tax discounted NPV (top) and the optimum normalized design parameter set (bottom). The optimization took 23 iterations.....	145
Figure 7.14: Cost breakdown versus the number of simulations invoked by the optimization algorithm. Note that each optimization iteration involves a couple of simulation runs. The optimum solution corresponds to the last simulation.	146
Figure 7.15: Oil recovery for the optimum solution.	146
Figure 7.16: Temperature profile at the end of electrical heating (top) and of waterflooding (bottom) for the optimum solution.....	147
Figure 7.17: Oil saturation at the end of waterflood (top) and chemical flood (bottom) for optimum solution.	147

Chapter 1: Introduction

Despite the possible greater complexity, hybrid processes may help overcome the technical challenges of heavy oil production. For many shaley thin oil deposits, steam injection is not feasible. A hybrid process that involves moderate reservoir heating and chemical enhanced oil recovery is proposed, in which the same set of horizontal wells is used for injection of both energy and fluids. The reservoir heating is performed by means of electrical resistive heating and hot waterflooding.

This process is a three-stage scheme. This process, in its basic form, is a three-stage scheme. The first stage is electrical heating, in which the reservoir temperature is raised just enough to create fluid injectivity. No significant oil should be produced in this stage to prevent produced fluids from removing the generated heat from the reservoir. Due to the moderate efficiency of heating the reservoir electrically and no oil production, the time length of this stage would be short. After electrical heating has created sufficient fluid injectivity, high-rate high-pressure hot water injection accelerates the raise in temperature of the reservoir and assists oil production. The water injection extracts energy from the hot sand near the injection wells and transports it deep into the reservoir and also displaces oil towards the producers. At the end of hot waterflooding the oil viscosities are low enough for a chemical flood to be performed where oil can efficiently be mobilized and displaced at low pressure gradients. Recent developments in the application of chemical EOR to heavy oil have shown that Alkali-Co-solvent-Polymer (ACP) flooding is a promising process and hence, it will be investigated in this work.

A key aspect of surfactant-aided chemical EOR is the rheology of forming microemulsions, in which oil and water are separated by many interfaces that move and deform with the flow. Macroscopic rheology of these complex fluids to a large extent is determined by the dynamic properties of the interface. Highly-ordered interfaces are associated with lamellar-like microstructure and high macroscopic viscosities, while simple fluid-like interfaces are associated with disordered sponge-like microstructures and low viscosities. Under some conditions viscous microemulsions with complex rheology behavior form that generally show longer equilibrium times and limited transportability. To prevent the formation of these viscous fluids, a number of rheology alteration methods have been established: the addition of co-solvent and branched co-surfactant, and the variation of temperature. However, unsolved questions regarding the true nature of the alteration mechanisms and their effects on the rheological properties still remain. For example, it is not clear why the addition of a small amount of co-solvent would greatly alter the rheology of a viscous bicontinuous microemulsion.

The objective of this study is threefold. First goal is to provide theoretical explanations for the abovementioned microemulsion rheology alteration methods and develop a rheology model that can be used to calculate the rheology of Winsor-type microemulsions. The rheology model should accounts for phase composition, shear rate, and qualitatively for the rheology alteration methods. The second goal is to use realistic simulation for the proper evaluation of the proposed hybrid process. To do so, the electrical heating part of simulations were performed using the CMG-STARS (Computer Modelling Group 2011) simulator and chemical flooding part of the simulations were

performed using UTCHEM (Bhuyan et al. 1990; Delshad et al. 1996, 2011; Mohammadi et al. 2009) in a unified sequence. UTCHEM is the reference simulator for study of chemical EOR processes and was developed at the University of Texas at Austin. Its features include an energy balance and some temperature-dependent fluid properties. Our first few attempts to use UTCHEM to simulate non-isothermal chemical processes, however, have revealed the need for the energy balance module modification which will be addressed. Our third goal is to investigate the feasibility of the proposed recovery process through optimization. This would involve the identification of the key design parameters that dictate the performance of the proposed hybrid process.

This dissertation is organized in eight chapters, including this introductory chapter. Chapter 2 provides a consistent and thorough background of the microemulsion systems and their properties. Chapter 3 describes the experimental rheological observations and presents the theoretical explanations that justify the underlying alteration mechanisms. A model for describing the rheology of microemulsions is presented in Chapter 4, along with model validation against experimental data. Chapter 5 discusses the rheology of microemulsions when polymer is present and shows the polymer partitioning is governed by size exclusion. The findings are then used to postulate how polymer partitioning alters the microemulsion rheological behavior.

The modifications of energy balance module of UTCHEM are presented in Chapter 6. Chapter 7 presents a detailed description of the hybrid thermal-chemical process proposed in this work. It also provides the thermal and electrical properties of the rock and fluids which determine the energy transport. The simulation model and the

effects of heterogeneities will also be discussed. An economic optimization is presented at the end. Finally, Chapter 8 gives a brief summary and critique of the findings and identifies areas for further research.

Chapter 2: Background

2.1 INTRODUCTION

Microemulsions are thermodynamically stable fluid mixtures of oil, water and amphiphilic compound(s) that may also contain other components (Reed and Healy 1977). Stability implies that once equilibrated, their structure does not change with time, nor does it depend on how they are prepared (Israelachvili 1994). Unlike macroemulsions, microemulsions form spontaneously. Although microemulsions do not always scatter light, they do scatter x-rays and neutrons (Komura 2007).

The amphiphilic compounds include surfactant, co-surfactant and co-solvent, each of which each possesses hydrophilic (water-soluble) and lipophilic (oil-soluble) parts. Despite this basic similarity, they are used for different purposes in enhanced oil recovery, which is the main focus of this review. A good EOR surfactant has a strong and balanced attraction to both oil and water and thus prefers the oil/water interface. Its main role is to reduce the interfacial tension between oil and water.

Co-surfactants are used for a variety of purposes such as increasing the solubility of the primary surfactant in brine at or near the optimum salinity, reducing the viscosity of the microemulsion, reducing the surfactant retention in reservoir rocks and improving the robustness of the chemical flooding process. Additionally, it provides a tremendous degree of flexibility in tailoring the oil/water/surfactant phase behavior to obtain the required behavior such as the desired optimum salinity (Adkins et al. 2010; Flaaten et al. 2008; Jackson 2006; Levitt et al. 2006; Zhao et al. 2008). A synergistic interaction

between the surfactant and co-surfactant is sometimes observed. For example, the IFT may be lower for the mixture than for either component by itself.

Co-solvent is the smallest molecule among the three and in contrast with co-surfactant, it dissolves the interface. In other words, it partitions among the phases while staying around the interface. Co-solvents are used to improve the solubility of the surfactants in brine, reduce surfactant retention, reduce microemulsion viscosity, minimize formation of macroemulsions or reduce their viscosity, reduce the time required for the microemulsion to reach equilibrium, prevent the formation of gels and other condensed phases, and less often for various other specialized functions such as prevention of asphaltene precipitation. Co-solvents typically decrease oil and water solubilization ratios and increase the IFT at optimum salinity. While the aforementioned differences between co-surfactant and co-solvent are generally valid and helpful in understanding the complex world of microemulsions, some molecules perform somewhat in between. Additionally, in some fields co-surfactants and co-solvents are not distinguished from one another (for an example refer to Safinya et al. 1989).

The development of new and more complicated surfactants requires new measurements and examination of microemulsions. The purpose of this review is to provide a consistent and thorough background of the microemulsions and their properties.

2.2 OIL/WATER/SURFACTANT PHASE BEHAVIOR

Microemulsions gradually gained recognition as a class of fluid distinct from emulsions. However, it soon became clear that even in the context of microemulsion systems, oil/water/surfactant could form diverse and complex phases. For example, in the

presence of an anionic surfactant, i.e. a surfactant molecule with a fixed charge at its head, lower salinities yield oil dispersion in brine. This brine-rich microemulsion in equilibrium with excess oil is called *O/W microemulsion* or *Winsor Type I*. Increasing the salinity ultimately results in water dispersion in oil. This oil-rich microemulsion in equilibrium with excess brine is called *W/O microemulsion* or *Winsor Type II*. At intermediate salinities, the mixture separates into three coexisting phases over a range of surfactant concentrations. The intermediate surfactant-rich phase is called *Winsor Type III microemulsion* or sometimes *the middle phase microemulsion*. Depending on the overall composition, either an excess brine phase or an excess oil phase or both co-exist with the middle phase microemulsion. The excess phases may contain low surfactant concentrations on the order of the CMC. Later it was discovered that because of thermodynamically stable nature of microemulsions, this type of phase behavior is general. Therefore, it is convenient to characterize the microemulsions in terms of phase behavior. There are a number of different ways to demonstrate the phase behavior. Ternary diagrams are the most common ones. They consist of three components or pseudo-components and show the type of equilibrium phases and their numbers (i.e. multiphase vs. singular phases). Each ternary diagram is at fixed salinity, temperature, and pressure, and only concentrations of surfactant, oil, and water are varied. Figure 2.1.a shows a typical ternary diagram with presence of *Winsor Type III microemulsion*. The numbers represent the number of phases in each region of the diagram. “2” and “2” stand for *Winsor Type I* and *Winsor Type II*, respectively.

Increasing the surfactant concentration beyond that of the three-phase *Type III* region in Figure 2.1.a results in formation of a single phase microemulsion denoted by “L”. Further increase in surfactant concentration yields a lamellar liquid crystal phase denoted by “ L_{α} ”. This can be seen more clearly in the “fish diagram,” (Kahlweit et al. 1985) an example of which can be seen in Figure 2.1.b. A fish diagram is prepared at constant water-to-oil ratio (WOR). This resembles a plane-cut in stacks of a number of ternary diagrams at different temperatures or salinities to visualize the phase transitions. Surfactant amount is the other variable.

A third type of phase behavior diagram is a plot of solubilization ratios versus salinity or some other parameter of interest (Bourrel and Schechter 1988). For a fixed WOR and surfactant concentration, salinity is varied to demonstrate the performance of the surfactant formulation expressed in terms of solubilization ratios, defined as the volume of water or oil divided by the volume of pure surfactant present in the microemulsion phase (Reed and Healy 1977). Figure 2.1.c is an example of phase transition for an anionic surfactant (Levitt et al. 2006). Still another common and practical way to plot the phase behavior is the volume fraction diagram (Lake, 1989), which is a plot of the phase volumes versus salinity or other parameter of interest with all other variables held constant. Each of these diagrams is useful for different purposes. Solubilization ratios as a function of salinity are particularly helpful in developing surfactant formulations for EOR since salinity (or more generally electrolytes) is one of the most important variables and is easy to change.

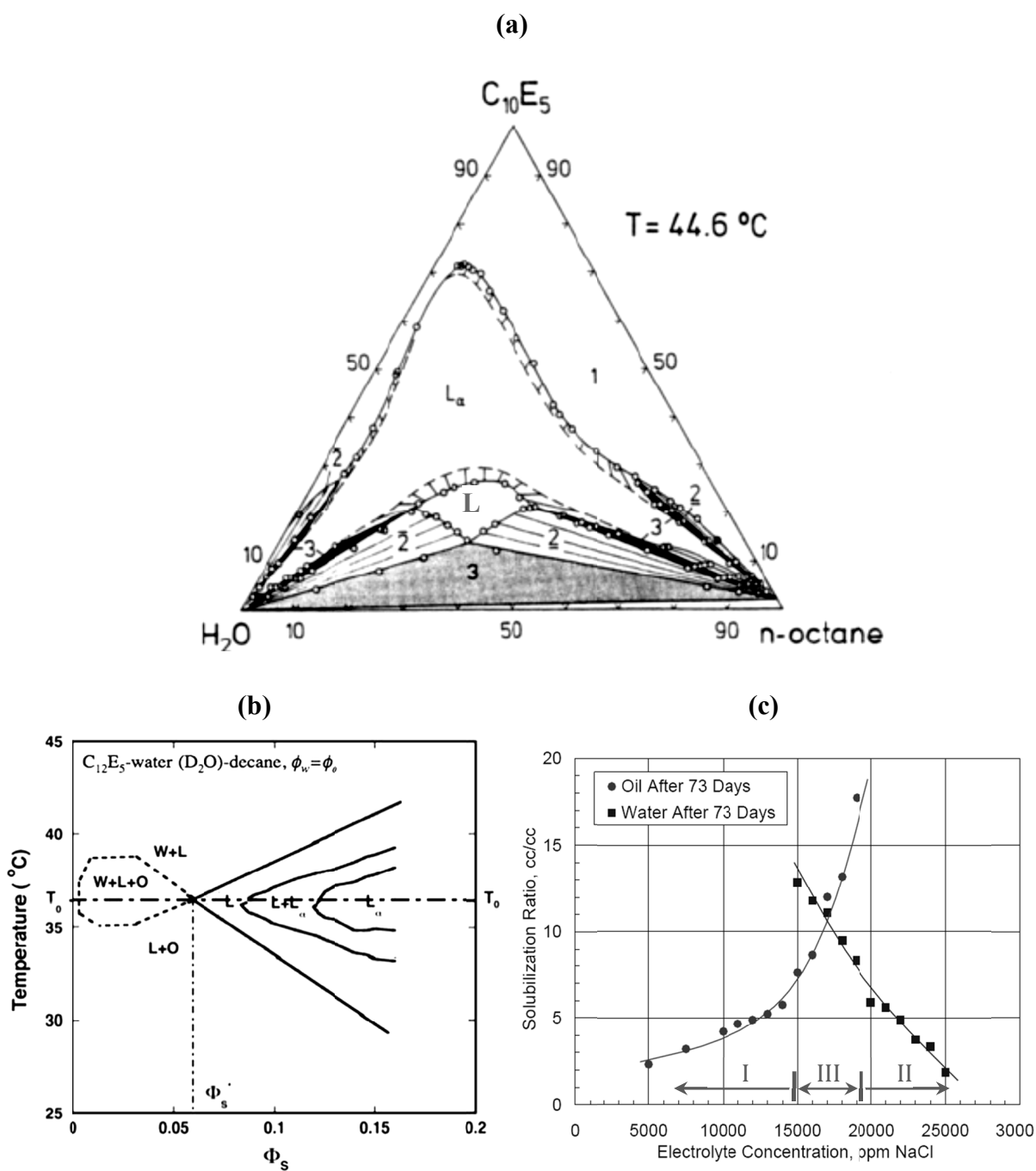


Figure 2.1: Phase behavior of surfactant/oil/water. (a) Experimental phase diagram of the ternary system $C_{10}E_5$ -water-octane from (Strey 1993; Daicic et al. 1995). (b) Fish diagram of the ternary system $C_{12}E_5$ -water-decane at equal volume fractions of water and oil. The diagram shows the number of phases as the surfactant volume fraction and temperature change. Symbol “L” denotes microemulsion and “ L_α ” lamellar liquid crystal phase. Note the transition as surfactant concentration is increased, denoted by “ $L + L_\alpha$ ” (Wennerström and Olsson 2009). (c) Solubilization ratios vs. salinity (Levitt et al. 2006).

2.3 THEORIES TO DESCRIBE THE PHASE TRANSITIONS

Once a decent understanding of the oil/water/surfactant phase behavior was established, many researchers tried to provide physical explanations and to quantify the phase transitions. The goal was to explain phase transitions brought about by increasing either electrolyte concentration (in the case of ionic surfactants) or temperature (for non-ionics) and many tried to come up with a single parameter to determine the type of microemulsion. In this section a brief summary of the theories will be presented.

2.3.1 Winsor R Ratio

Surfactant's interaction energies with bulk oil and water determine the tendency of interface toward either phase(s) and hence the type of microemulsion. In its simplest form, the R ratio (Winsor 1954; Shah and Schechter 1977; Bourrel and Schechter 1988) can be written as

$$R = \frac{A_{co}}{A_{cw}}, \quad (2.1)$$

where A_{co} indicates the interaction between the surfactant and the oil phase, and A_{cw} , the interaction between the surfactant and the water phase. When the interaction of the surfactant with the oil (respectively water) phase dominates, the $R > 1$ (respectively $R < 1$) and interface bends towards oil (respectively water). This preferable curvature towards oil results in an *Winsor Type II* (respectively *Winsor Type I*). When surfactant interactions with both bulk phases is similar and there is no preferential curvature, the R ratio is one and a three-phase behavior is exhibited, in which *Winsor Type III* microemulsion is in equilibrium with both water and oil excess phases.

2.3.2 Hydrophilic-Lipophilic Balance (HLB)

Employing the empirical rule which states that the phase in which the surfactant is more soluble will be the continuous phase of emulsion (Bancroft rule), the HLB was suggested to scale the tendency of a surfactant towards water or oil (Davies 1957; Griffin 1949). The main consequence of the HLB scale was recognition of the importance of surfactant molecule chemical structure, a matter that is still an area of research (refer to Solairaj et al. (2012) for an example). When it was realized that different chemical groups had different effects on the surfactant preferred curvature towards oil or water, each constitutive group was assigned a group number and the HLB of a given surfactant was calculated directly from its chemical formulae as follows:

$$HLB = 7 + \sum_i m_i H_i - \sum_i n_i L_i, \quad (2.2)$$

where H and L are group numbers of hydrophilic and lipophilic groups and m and n are their numbers, respectively. A $HLB < 10$ results in W/O microemulsion, $HLB > 10$ yields O/W microemulsion, and $HLB \approx 10$ corresponds to balanced microemulsion.

2.3.3 Phase Inversion Temperature

Shinoda and Arai (1964) observed that an O/W emulsion containing a nonionic surfactant containing ethylene oxide (EO) undergoes a phase inversion to become W/O by increasing temperature. The behavior is attributed to the reverse solubility of EO in water versus temperature. Based on this universal behavior, the authors defined the phase inversion temperature (PIT) at which surfactant has equal affinity for both phases. At

temperatures below PIT the emulsion is O/W and W/O at those higher. Salinity has a similar effect for emulsions/microemulsions containing anionic surfactants.

2.3.4 Packing Parameter

In an attempt to explain the observed physical properties of surfactant aggregates, Israelachvili et al. (1976) proposed the concept of the molecular packing parameter and demonstrated how the size and the shape of the aggregate at equilibrium can be predicted from a combination of molecular packing and thermodynamics. The authors defined the free energy μ_N^0 per amphiphile in the aggregate as

$$\mu_N^0 = \gamma a + \frac{2\pi e^2 D}{\epsilon a} + g, \quad (2.3)$$

where γ is interfacial tension, a interface area per amphiphile, e is electron charge, D is the Debye length, ϵ is dielectric constant, and g represents the self-energy of hydrocarbon term in water. The first term in Equation (2.3) represents the interfacial energy, the second term accounts for electrostatic self-energy associated with the (charged) head group, and the last term shows hydrophobic energy of the hydrocarbon chain.

The authors realized that in the absence of geometric limitations, spherical micelles will always be thermodynamically favored over other shapes like cylindrical micelles or bilayers (e.g. amphiphilic monolayers of alternating orientation embedded between alternating layers of the same solvent). Therefore they introduced the packing parameter as $v/a_0 l_c$, where v is the surfactant tail volume, l_c is the tail length, and a_0 is the equilibrium area per molecule at the aggregate surface. A particular value of the

molecular packing parameter can be translated via simple geometrical relations into specific shape and size of the equilibrium aggregate.

While the original purpose of the packing parameter was to explain the existence of non-spherical aggregates, Israelachvili (1994) later used the concept of packing parameter to describe the phase transition in emulsions (or microemulsion). In a similar fashion to the HLB theory, the author qualitatively considered the forces acting on different parts of a surfactant molecule sitting at the water-oil interface. The competition between the packing areas of the polar head and hydrocarbon tail of the surfactant molecules determines the overall packing shape of the surfactant molecules. Figure 2.2 shows aggregate structures that correspond to different packing parameters. Accordingly, a packing parameter of less than one (i.e. $v/a_0 l_c < 1$) corresponds to a O/W microemulsion while those of more than one (i.e. $v/a_0 l_c > 1$) corresponds to W/O microemulsion. *Type III* microemulsion has a unity packing parameter. Note that the packing parameter was the first theory suggesting that the packing shape of surfactant changes as transition from *Type I* to *Type II* takes place.

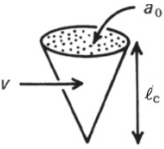

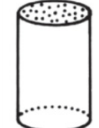
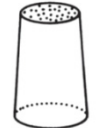


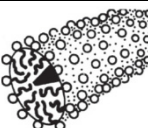
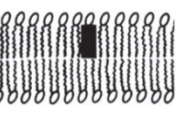
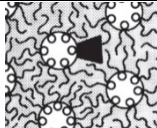

	Short single-tail; Lower ionic strength			Branched tail; Higher ionic strength	
Packing parameter	$<1/3$	$1/3-1/2$	~ 1	2-3	3
Surfactant packing shape	Cone 	Truncated cone 	Cylinder 	Inverted trunc. cone 	Inverted cone 
Aggregate structure					

Figure 2.2: Surfactant packing shape and associated schematic aggregate structures at different “packing parameter” or “shape factor”, $v/a_0 l_c$ (Israelachvili 1994, 2011).

2.3.5 Equivalent Alkane Carbon Number (EACN)

Using known pure hydrocarbons to assess performance of different surfactants is very appealing. It provides a convenient framework to understand their behavior and to measure their effectiveness in achieving low interfacial tensions. It also enables the identification of general trends in their performance and more efficient screening. With this in mind, Wade et al. (1977) used alkanes as the basis to assess different classes of surfactants. The authors characterized the hydrophobicity of an alkane by its number of carbon atoms, called alkane carbon number (ACN). Later it was shown that an equivalent alkane carbon number (EACN) can be assigned to mixtures of alkanes, alkyl benzenes, and alkyl cyclohexanes (Cash et al. 1977; Cayias et al. 1976). The EACN of the mixture is simply the molar-average of that of individuals (Equation (2.4)),

$$EACN = \sum_i x_i ACN_i . \quad (2.4)$$

The major advantage of this framework was revealed once Wade et al. (1977) realized that hydrocarbons with the same EACN have similar phase behavior under the same conditions. This similarity meant a crude oil can also be assigned an EACN by comparing its phase behavior with that of a known hydrocarbon. Once a crude's EACN is known, its phase behavior at different conditions can be predicted.

2.3.6 Hydrophilic-Lipophilic Deviation (HLD)

Despite its empirical nature, *HLD* (Salager et al. 1979; Bourrel et al. 1980; Salager and Antón 1999; Salager et al. 2000; Acosta et al. 2008) is among the more practical and successful frameworks to describe the phase behavior and to tune surfactant molecular structure. The affinity of the surfactant for the water and oil phases does not only depend on the surfactant, but also on the nature of the oil, electrolytes in water, the presence of co-solvents, temperature, and in some instances even pressure. The variation of Gibbs free energy when a surfactant molecule passes from oil to water, called the surfactant affinity difference (*SAD*), can be defined as

$$\frac{SAD}{RT} = \frac{\mu_w^* - \mu_o^*}{RT} = \frac{\Delta\mu_{o \rightarrow w}^*}{RT} = \ln \left(\frac{X_o}{X_w} \right) = \ln K , \quad (2.5)$$

where the μ^* indicates the standard chemical potential at some reference concentration, X is a dimensionless surfactant concentration, and K is the partitioning coefficient of surfactant between the bulk phases. It is convenient to define *HLD* as follows:

$$HLD = \frac{(SAD - SAD_{ref})}{RT} = \ln K - \ln K_{ref}, \quad (2.6)$$

where the reference state is taken as the surfactant concentration ratio (i.e. partitioning coefficient or K) between the very dilute excess oil and water phases at equilibrium with the *Type III* microemulsion. In this way $HLD = 0$ corresponds to *Type III* microemulsion and $HLD > 1$ (respectively $HLD < 1$) shows surfactant affinity for oil (respectively water) and therefore *Type II* (respectively *Type I*) microemulsion. In the lack of theoretical description for the partitioning coefficient, the following empirical correlations was proposed for HLD calculation:

$$HLD = \ln S - kACN + f(A) + \sigma - a_T(T - T_{ref}),$$

(for anionic surfactants)

(2.7)

$$HLD = \alpha - EON - kACN + bS + \varphi(A) + c_T(T - T_{ref}),$$

(for nonionic surfactants)

where S is the salinity in wt.% NaCl, ACN is the alkane carbon number of the oil, T is the temperature, $f(A)$ and $\varphi(A)$ are almost linear functions of the alcohol type and concentration. The characteristic parameter of the surfactant is σ for ionics, and $\alpha - EON$ for ethoxylated nonionic alcohols or phenols, EON being the average number of ethylene oxide group per surfactant molecule. Parameters a_T , b , c_T , and k are constants.

2.3.7 Membrane Theory

In mostly empirical or descriptive previous models described in this section, the value of a single parameter would indicate the type of microemulsion and the surfactant affinity for oil/water is at the heart of all models. Some have employed the importance of

surfactant molecule structure and relevant variables affecting the phase behavior to some degree (refer to *HLD* for example). However the lack of a phenomenological model is obvious. Furthermore, none of the previous models can describe the microstructure of the *Type III* microemulsion, which turned out to be crucial regarding its viscosity behavior.

The essential steps towards a phenomenological model arrived with the introduction of the membrane theory to describe microemulsions. In this approach, instead of focusing on a surfactant molecule the interface is modeled as an elastic membrane, making the total energy of the interface:

$$E = \int_{\text{membrane}} (\gamma + e_{\text{bend}}) dA, \quad (2.8)$$

where γ is interfacial tension and e_{bend} is the bending elastic energy per unit area of interface. Interfacial tension is the energy cost of increasing the interfacial area by one unit. At high interfacial tensions, the energy of an interface is mainly characterized by interfacial tension (Safran 1999) and oil and water are separated. Additional surfactant lowers the interfacial tension. At lower interfacial tensions the energy cost of increasing the area of an interface becomes very low. Under these circumstances the bending energy becomes important. Helfrich (1973) proposed the bending energy density to be

$$\begin{aligned} e_{\text{bend}} &= \frac{1}{2} \kappa (c_1 + c_2 - c_0)^2 + \bar{\kappa} c_1 c_2 \\ &= \frac{1}{2} \kappa (2H - c_0)^2 + \bar{\kappa} K, \end{aligned} \quad (2.9)$$

where c_1 and c_2 are the principal curvatures, κ is the bending modulus; $\bar{\kappa}$ is the saddle-splay modulus; $H = (c_1 + c_2)/2$ is the mean curvature, and $K = c_1 c_2$ is the Gaussian

curvature. c_0 is the spontaneous curvature that describes the tendency of the surfactant film to bend towards either water or oil (with the convention of a positive curvature toward water). Microemulsions are characterized by low interfacial tension. Their microstructure is therefore largely dictated by the spontaneous curvature and bending modulus (Safran 1999).

2.4 MICROSTRUCTURE

It is necessary but not sufficient to characterize microemulsion systems thermodynamically in terms of phase equilibria. These macroscopically homogeneous mixtures are composed of distinct water-rich and oil-rich domains at microscopic level. Their microstructure affects their properties and behavior. The following section provides a review on the microemulsion microstructure.

2.4.1 Dilute Microemulsions

For dilute O/W and W/O microemulsions, the structure is often that of globules or droplets (Langevin 1988). The droplet size polydispersity in microemulsion is and the average droplet radius can be calculated by

$$r_{ave} = \frac{3\phi}{C_s \Sigma^*}, \quad (2.10)$$

where ϕ is volume fraction of the dispersed phase, C_s is the volumetric density of surfactant molecules, and Σ^* is the average (saturated) area per surfactant molecule. Assuming the surfactant film to be incompressible, Σ^* is almost constant for a given system (Cazabat and Langevin 1981; Huang et al. 1987; Huh 1983). For single-chain surfactants generally $\Sigma^* \approx 20 - 50 \text{ \AA}^2$ (Huh 1983; Langevin 1988; Szleifer et al. 1988).

Figure 2.3 shows examples of average droplet variations with phase transitions. Note that in the *Type III* region the structures are not droplets.

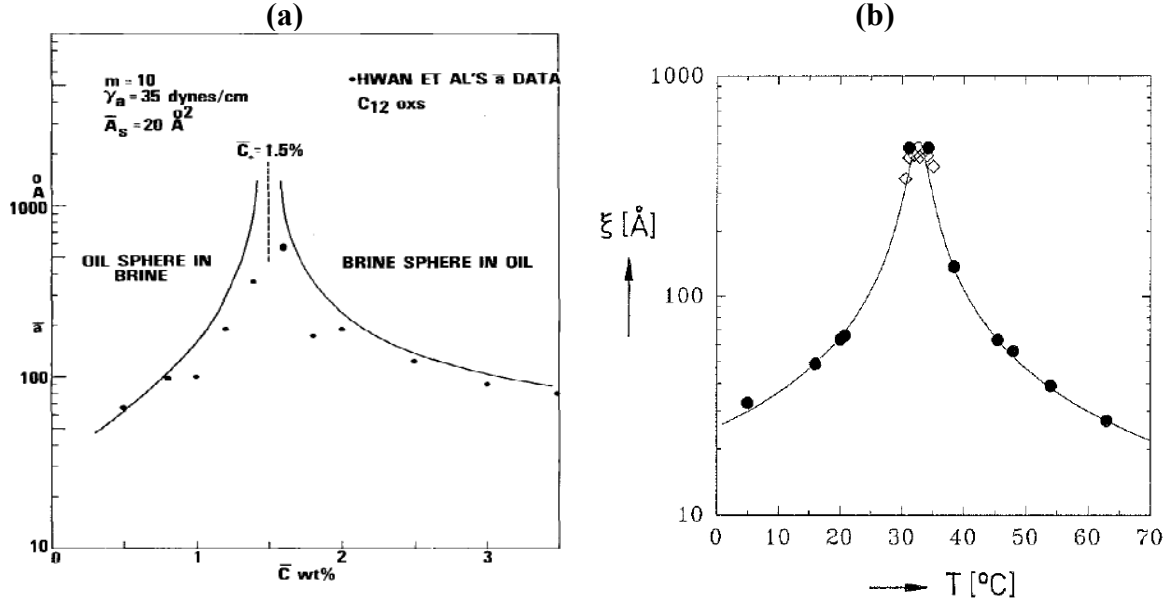


Figure 2.3: Variation of average droplet radius (or characteristic length for Type III microemulsion) with phase transition from *Type I* \rightarrow *III* \rightarrow *II*; (a) drop radius vs. salinity for an anionic surfactant (Huh 1983). (b) drop radius vs. temperature for nonionic surfactant (Strey 1994).

Measuring the self-diffusion coefficient also provides an indirect way of obtaining/infering the average droplet size in dilute microemulsions. The self-diffusion coefficient caused by the Brownian motion under zero chemical potential is given by the Stokes-Einstein equation:

$$D_0 = \frac{k_B T}{6\pi\eta r_{ave}}, \quad (2.11)$$

where k_B is the Boltzmann constant, T is temperature, and η is the viscosity of the continuous phase. Typical droplet size of dilute microemulsions (≈ 100 Å from Figure 2.3) gives D_0 to be in the order of 10^{-11} (m^2/s). However as the concentration of droplets increases the self-diffusion coefficient decreases because of the excluded volume

(Equation (2.12)) (Holmberg 2003). The amount of reduction depends on the intermolecular interactions. An attractive potential between the droplets suppresses the reduction while a repulsive one increases it,

$$D = D_0(1 - \alpha\phi), \quad (2.12)$$

α is the Virial coefficient account for the droplet interactions (Holmberg 2003).

2.4.2 Concentrated Microemulsions

2.4.2.1 Topological Relaxation

Self-diffusion refers to non-gradient diffusions. Collective or mutual diffusion, D_c , on the other hand, refers to the relaxation of fluctuations or gradients in concentration or chemical potential (Scalettar et al. 1988). At infinite dilution, the self- and collective-diffusion coefficients have the same value, D_0 . This "bare" diffusion coefficient could be used to infer the average droplet size in microemulsions. However, in concentrated regions, the droplets interact through mutual excluded volume and sometimes through longer-ranged potentials. These interactions not only differentiate D_0 and D_c but also can markedly change their volume fraction dependency.

Peter et al. (2001) and Hattori et al. (2007) report two diffusive relaxation modes in concentrated O/W microemulsions. In addition to the self-diffusion fast-mode process, the authors observe a slow collective diffusive relaxation mode with unusual scaling behavior. Peter et al. associated the slow-mode diffusion to thermally-activated topological relaxation by membrane fusion, which was first proposed by Milner et al. (1990). Hattori et al., however, attributed it to polydispersity relaxation. Appell et al.

(2005) makes a similar observations and suggested that the slow-mode diffusion arises from relaxation of the charge fluctuations. Whatever the explanation is, the main consequence is viscosity build up as the charged droplet concentration increases in O/W microemulsion or as the transition from *Type I* \rightarrow *III* is approaching.

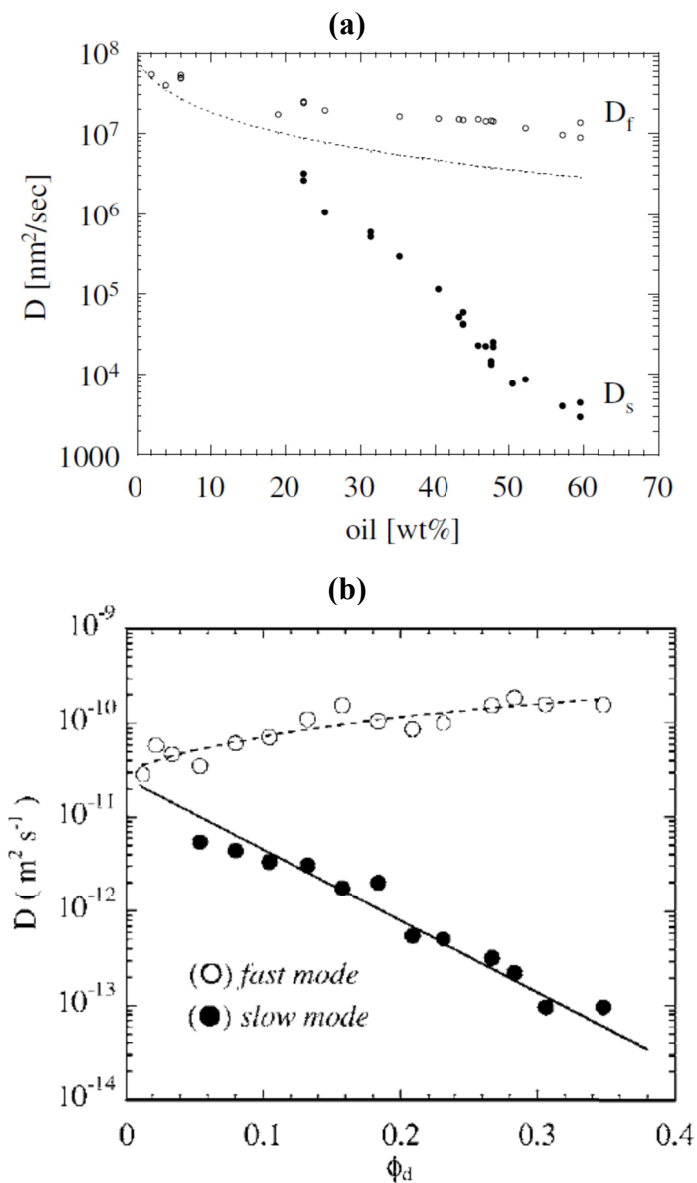


Figure 2.4: Fast- and slow-mode diffusion (a) O/W microemulsion containing SDS, octanol, octane, and brine (Peter et al. 2001). The dashed line represents the diffusion constant extracted from the Stokes-Einstein relation. (b) O/W microemulsion composed of brine, paraffin oil, AOT, and $C_{12}(EO)_4$ (Hattori et al. 2007).

2.4.2.2 Percolation

When the interaction potential between droplets is sufficiently attractive, an appreciable number of dimers and higher order aggregates can form (Langevin 1988). When the volume fraction, ϕ , of droplets is large enough, an infinite cluster appears: this corresponds to the percolation threshold, i.e. $\phi = \phi_p$ (Langevin 1988). In W/O microemulsions where the potential is attractive, a rapid increase in electrical conductivity is observed around ϕ_p (Figure 2.5). ϕ_p decreases with increasing attraction. Safran et al. (1985) suggested that the percolation is governed by a hopping mechanism that is facilitated by the interpenetration of surfactant layers (associated with attractive forces and flexible and fluid layers). In short, the occurrence of percolation reveals that cluster size, attractive interactions, and the rate of exchange of material between droplets through collisions increases (Feldman et al. 1995, 1996).

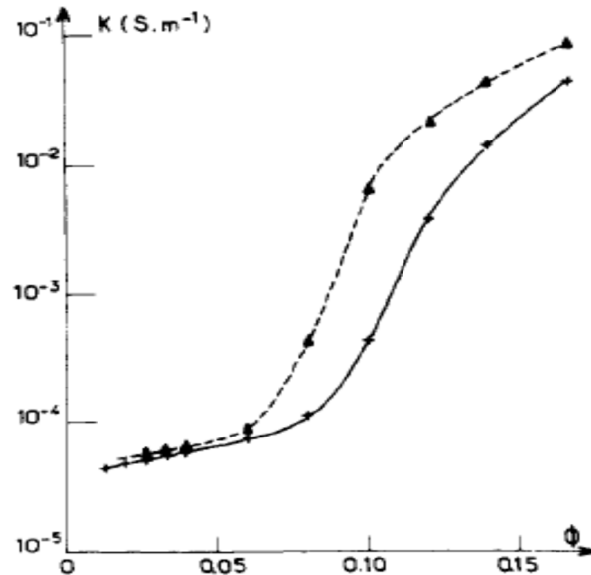


Figure 2.5: electrical conductivities of W/O microemulsion vs. droplet volume fraction. The left curve corresponds to more attractive droplets than the right curve (Langevin 1988).

2.4.3 Bicontinuous Microemulsion

Despite the intuitive microstructure of droplet microemulsions, discovering the Winsor Type III microstructure was the main focus of research related to microemulsions in the 70's and 80's (Langevin 1988). The first breakthrough was a theoretical one. Talmon and Prager (1978) proposed the use of space-filling models to describe the microemulsion thermodynamics and perceive their structures. The authors considered a subdivision of space into Voronoi polyhedrons that were filled at random with either oil or water according to a probability proportional to the volume fraction of each component (Langevin 1988). If the oil volume fraction ϕ_o is large, oil is the continuous phase and water polyhedrons are isolated: this represents the W/O structure (case a in Figure 2.6). If the water volume fraction is large, water is the continuous phase and oil polyhedrons are isolated: O/W structure (case c). In the intermediate range a bicontinuous structure is obtained (case b). Defining the percolation as the water volume fraction at which a infinite path of connected water polyhedrons first appears, the model gives $\phi_p = 0.16$, which agrees relatively well with the experimental values (Langevin 1992).

The Talmon and Prager model only accounted for entropy (and weakly for curvature) in the thermodynamic free energy model. However, it correctly predicted a disordered structure for a bicontinuous microemulsion with comparable oil and water fractions. In an attempt to understand why these structures do not collapse into ordered systems (lyotropic liquid crystals or crystals), de Gennes and Taupin (1982) introduced persistence length, ξ_k , to justify the importance of thermal undulations relative to bending energy of the interface. Fluid membranes undergo microscopically visible thermal

undulations or ripples. If the required energy to bend the interface is comparable to the thermal energy, the undulations destroy the long-range orientational correlation within a membrane. Because of these undulations, the interface is very wrinkled at scales larger than ξ_k while it is essentially flat at scales smaller than ξ_k . de Gennes and Taupin defined the persistence length in the following fashion:

$$\xi_k = a \exp\left(\frac{2\pi k}{k_B T}\right), \quad (2.13)$$

where a is a molecular scale, k is the local (or “bare”) bending elasticity, k_B is the Boltzmann constant, and T is temperature. The exponential dependence of the persistence length to the ratio of bending to thermal energies is noteworthy. Bending elasticities comparable to $k_B T$ yield a small ξ_k (~ 100 Å) and favor disordered bicontinuous structure, while those that are larger than $k_B T$ yield large small ξ_k (~ 500 Å) and favor liquid crystal phases (Jouffroy et al. 1982).

To build their model, de Gennes and Taupin (1982) and their coworkers (Jouffroy et al. 1982) proposed dividing the space into cubes, each of size ξ_k . Assuming that all of the surfactant is at the interface, the lattice configuration gives the area per surfactant molecule as

$$\Sigma = \frac{6v_s\phi(1-\phi)}{\xi_k\phi_s}, \quad (2.14)$$

where v_s is the volume of surfactant molecule and ϕ_s is the surfactant volume fraction. The free energy of the surfactant film has a simple form $F \propto (\Sigma - \Sigma^*)^2 / \Sigma^{*2}$ where Σ^* gives the minimum of the energy. In this model, the energy is defined per surfactant molecule and the interfacial tension vanishes at Σ^* . The model accounts for interfacial

tension, entropy of mixing, and curvature energy. The resulting free energy expressed in a reduced potential form is as below:

$$G_{\mu_s}(\phi) = 6\gamma(\Sigma)\xi_k^2\phi(1 - \phi) + k_B T[\phi\ln(\phi) + (1 - \phi)\ln(1 - \phi)] + \lambda f_3, \quad (2.15)$$

where μ_s is the surfactant chemical potential, $\gamma(\Sigma)$ is the interfacial tension, λ is the Bancroft constant, and f_3 represent the bending energy contribution. As seen in Equation (2.15) the only parameter to describe the system is the phase fractions. Through minimization of the free energy, the authors showed that the microemulsion equilibrium takes place at very low γ which is proportional to the persistence length, $\gamma \sim k_B T / \xi_k^2$. However the model failed to predict the presence of tree-phase equilibrium, which is the presence of Winsor Type III microemulsion.

In order to resolve this, Widom (1984) treated the size of the cubic lattice, ξ , as a variational parameter and enforced a penalty on the film free energy to keep the cube size larger than a molecular-size scale. For a fixed composition of W/O/S system the equilibrium would be at the ξ that minimizes the free energy. Widom's model successfully predicts three-phase equilibrium involving a middle-phase microemulsion. The model also predicted the structural length scale, ξ , for the balanced middle phase to be of 100 Å order, which is in accordance with experiments (Andelman et al. 1987).

Despite the success of Widom's model to capture the general picture of the phase behavior of W/O/S, Safran et al. (1986) and their coworkers Andelman et al. (1987) considered it to contain questionable assumptions and drawbacks. First, a variable area per surfactant molecule, Σ , was assumed, which is in contrast to the laboratory

measurements. Second, the characteristic length scale of bicontinuous microemulsions was predicted to be unrelated to the persistence length, ξ_k . Third, the characteristic length dependency on the bending properties of the surfactant film and bare oil-water interfacial tension, γ , seemed out of proportion (Andelman et al. 1987), as suggested by

$$\xi \sim a \left(\frac{k}{k_B T} \right)^{1/3} \left(\frac{\gamma a^2}{k_B T} \right)^{1/3} \exp \left(\frac{\gamma a^2}{3k_B T} \right). \quad (2.16)$$

Equation (2.16) shows a strong dependency on bare surface tension but only a weak dependency on the curvature. Experiments indicate that the properties of the middle phase are very sensitive to the properties of the surfactant, implying a strong dependence on the bending constant, k . For example, co-surfactants were thought to be needed to reduce k significantly while having very little effect on the bare surface tension γ (Andelman et al. 1987).

Employing all of the previous findings, Safran et al. (1986) proposed a model assuming a constant area per surfactant molecule (Many dynamic molecular simulations studies has supported this assumption (Feller and Pastor 1999)). The space is divided into cubes of size ξ determined by the volume fractions of surfactant, water, and oil. The persistence length, ξ_k , enters the model through the effective bending constant of the surfactant layer. The free energy per unit volume of the microemulsion phase is

$$f = \frac{1}{\xi^3} \left[s(\phi) + 8\pi P(\phi) k_{eff} \left(1 - \frac{2\xi(1-2\phi)}{\rho_0} \right) \right], \quad (2.17)$$

where $\phi = \phi_w + \phi_s/2$ with ϕ_w as water and ϕ_s as surfactant volume fractions. The lattice cube size is

$$\frac{\xi}{a} = z \left[\frac{\phi(1-\phi)}{\phi_s} \right], \quad (2.18)$$

where $z(= 6)$ is the coordination number in the lattice model and a is a molecular distance comparable to the in-plane spacing of two surfactant molecules or simply the length of the surfactant molecule. In Equation (2.17) the first term accounts for entropy and the second for curvature. Using random mixing approximations similar to the previous models, the entropy and total interface are respectively as follows:

$$s(\phi) = k_B T [\phi \ln(\phi) + (1-\phi) \ln(1-\phi)], \quad (2.19)$$

$$P(\phi) = \phi(1-\phi), \quad (2.20)$$

The effective bending constant is length-scale dependent because of the thermal fluctuations of the film and is related to the “bare” bending constant, k , as follows:

$$k_{eff}(\xi) = k + \frac{\alpha k_B T}{4\pi} \ln \left(\frac{\xi}{a} \right). \quad (2.21)$$

The prefix α depends on the method of calculation (Kleinert 1986). Finally the term $(1 - 2\xi(1 - 2\phi)/\rho_0)$ in Equation (2.17) accounts for the spontaneous radius of the curvature, ρ_0 , which reflects the tendency of the surfactant layer to bend towards either water or oil regions.

Equations (2.17)-(2.21) complete the specification of the model. The free energy is a function of two independent variables, ϕ and ϕ_s . Two phase behavior examples calculated by the model are shown in Figure 2.7. The model successfully predicts the presence of the middle-phase, which coexists with very dilute phases of surfactant in oil and surfactant in water. The free energy per unit volume of these dilute phases in water and oil respectively, \bar{f}_w and \bar{f}_o , is as follows:

$$\bar{f}_w = k_B T \left[\frac{\bar{\phi}_s (\log \bar{\phi}_s - 1) + \chi_w \bar{\phi}_s}{R^3} \right], \quad (2.22)$$

where $\chi_w = 8\pi k/k_B T$. Note that k refers to the micellar water (or oil for χ_o). At equilibrium with the middle-phase, $\bar{f}_w^* = T \exp(-\chi_w)/a^3$. Note that similar surfactant solubility in oil and water (i.e. $\bar{f}_w^* = \bar{f}_o^*$) results in a symmetric phase diagram while very asymmetric phase diagrams can result if $\bar{f}_w^* \neq \bar{f}_o^*$ (Figure 2.7). Safran et al. showed that it is only the entropy of mixing that stabilizes these dilute phases with respect to the microemulsion phases. Finally, the model predicts near the middle phase microemulsion that the scale of ξ is ξ_k while $\xi \approx a$ in the dilute micellar phases. Golubović and Lubensky (1990) later suggested adding a steric entropy term to the model to improve the structural length scale, ξ_k , of the middle phase. By way of persistence length, the theory established that microemulsions are, on a microscopic level, structured into random water-rich and oil-rich domains that are separated by an amphiphilic layer. However, the application of freeze fracture electron microscopy (FFEM) provided the conclusive evidence of this disordered microstructure (Bodet et al. 1988; Burauer et al. 2003; Jahn and Strey 1988; Vinson et al. 1991).

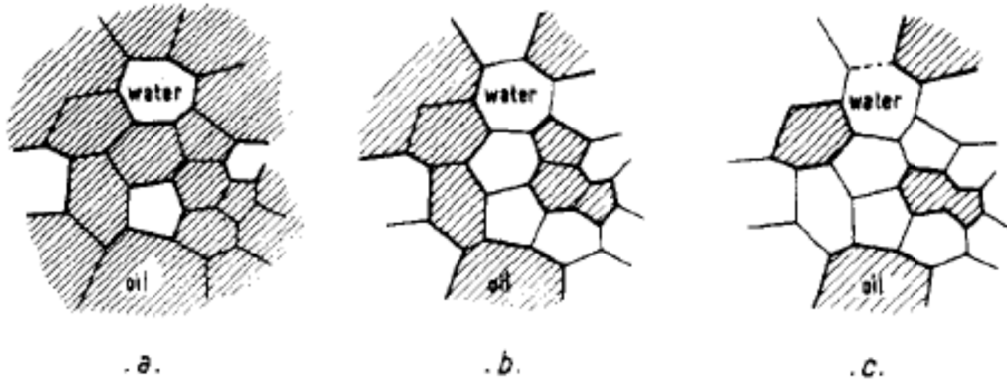


Figure 2.6: Voronoi polyhedrons of the Talmon-Prager model (Langevin 1988).

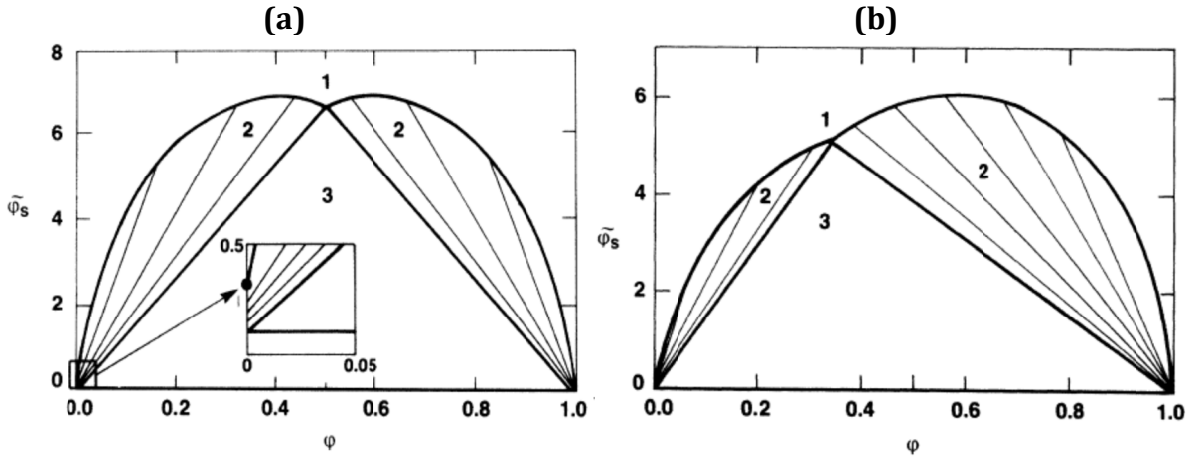


Figure 2.7: Phase diagram of a microemulsion with no spontaneous curvature ($\rho_0 \rightarrow \infty$). The volume fraction $\tilde{\phi}_s = \phi_s / \phi_m$, where ϕ_s is the volume fraction of surfactant, and $\phi_m = \exp(4\pi k / \alpha k_B T)$. The water volume fraction is ϕ_w and $\phi = \phi_w + \phi_s / 2$. The numbers indicate the number of coexisting phases and the tie lines in the two-phase region are shown. (a) $\bar{f}_w^* = \bar{f}_o^*$ Inset: The details of the tie lines at small volume fractions. (b) $\bar{f}_o^* = \bar{f}_w^* / 2$ (Safran et al. 1986).

In FFEM, microemulsion samples are rapidly frozen in a suitable cryogen (e.g. liquid ethane or propane), fractured, and replicated with a thin metal film (Burauer et al. 2003). The replica permits the discrimination between the water- and oil-rich domains and its morphology retains the sample's microstructure which can be seen by transmission electron microscopy (TEM). An example of a bicontinuous structure prepared by FFEM is presented in Figure 2.8 (Burauer et al. 2003). At equal volume

fractions of water and oil (Figure 2.8.b) one clearly sees two coexisting phases of equal structure, one of which is coarse-grained oil, the other fine-grained water. The structural peculiarities are the so-called saddle points. At these points the two principal radii of curvature r_1 and r_2 are equal but of opposite signs, leading to $c_1 = -c_2$ with $c_1 = 1/r_1$ and $c_2 = 1/r_2$. As a consequence, the mean curvature $H = (c_1 + c_2)/2$ of the amphiphilic layer is 0 and the Gaussian curvature $K = c_1 c_2$ is negative. This particular structure is the most frequently visualized structure of bicontinuous microemulsions. Turning towards the water-rich side (Figure 2.8.a), larger area fractions of the water-rich phase are visible with oil-rich domains that become increasingly branched tubes with circular cross sections. The same holds for the oil-rich side of the microstructure (Figure 2.8.c).

In summary, theory and experiments show that the surfactant film in the bicontinuous phase possesses zero mean curvature and negative Gaussian curvature, and its surface is locally minimized. Gózdź and Hołyst (1996) noted the resemblance of minimal surfaces to the bicontinuous structure and generated a 3D picture of the interface. A *minimal surface* is a surface that is locally area-minimizing, that is, a small piece has the smallest possible area for a surface spanning the boundary of that piece. Minimal surfaces necessarily have zero mean curvature and have a crystalline structure. The authors approximated the surfactant monolayer with a mathematical surface. Then Gózdź and Hołyst generated a number of different surfaces with different unit cells (Figure 2.9). It appeared that the gyroid-cell structures resembled the microemulsion in a

better fashion since they were most easily generated in the phase diagram close to the microemulsion stability region (Gózdź and Hołyst 1996).

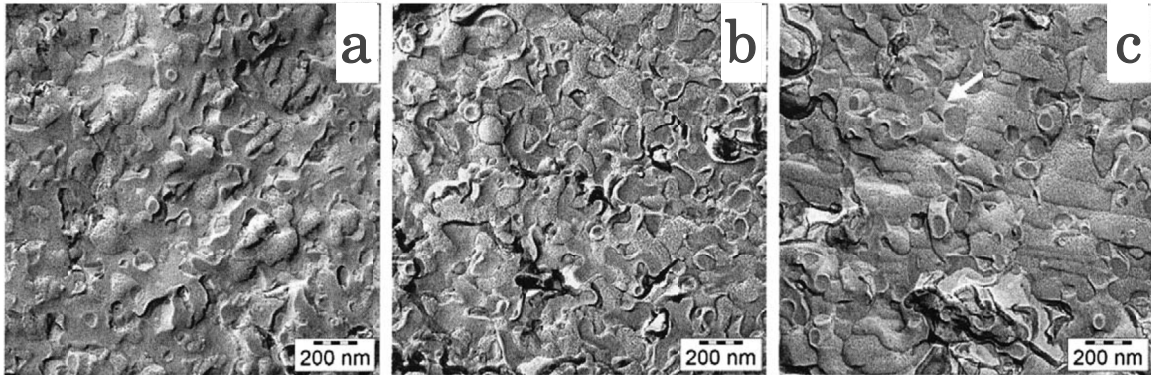


Figure 2.8: FFEM images ($10\,000\times$ instrument magnification) of freeze fractured microemulsions of the ternary system H₂O-*n*-octane-C₁₂E₅ at different WOR. (a) $\phi_w = 0.6$ (b) $\phi_w = 0.5$ (c) $\phi_w = 0.4$ The arrow in (c) indicates a saddle point (Burauer et al. 2003).

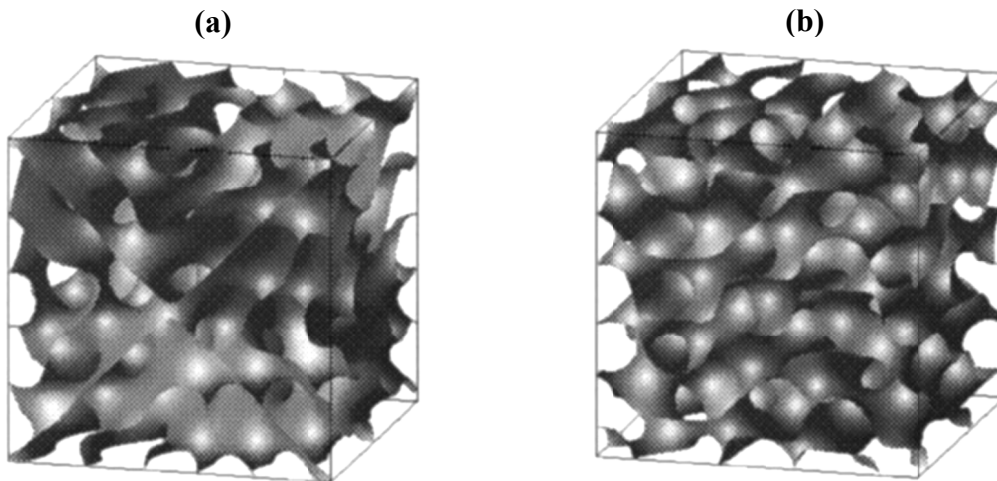


Figure 2.9: Periodic embedded minimal surfaces of non-positive Gaussian curvature: (a, b) unit cell is gyroid (Gózdź and Hołyst 1996).

Chapter 3: Microemulsion Rheology Alteration Mechanisms

The rheology of microemulsions can be altered by the addition of co-solvents and co-surfactants and by changing the temperature. This chapter describes a theoretical framework for understanding the relevant mechanisms.

3.1 BACKGROUND

Early research on microemulsions focused on macro- and micro-scale phenomena which led to the development of phase behavior diagrams and the characterization of a surfactant molecule affinity toward oil/water (Winsor 1954; Davies 1957; Griffin 1949; Shinoda and Arai 1964; Israelachvili et al. 1976; Wade et al. 1977; Cayias et al. 1976; Cash et al. 1977; Salager et al. 1979; Bourrel et al. 1980). With the introduction of the elastic membrane theory (Helfrich 1973) and the use of space-filling models (Talmon and Prager 1978; de Gennes and Taupin 1982; Jouffroy et al. 1982; Widom 1984; Andelman et al. 1987; Safran et al. 1986; Golubović and Lubensky 1990), the study of meso-scale (10-1000 nm) phenomena was greatly facilitated. The bicontinuous nature of the middle-phase or Winsor Type III microemulsion was established and de Gennes and Taupin (1982), for example, introduced the persistence length, ξ_k , to justify the importance of thermal undulations in the thermodynamic stability of the disordered bicontinuous microemulsions. Further confirmation of the microstructure was provided by direct imaging with freeze fracture electron microscopy (FFEM) (Bodet et al. 1988; Burauer et al. 2003; Jahn and Strey 1988; Vinson et al. 1991). With the availability of more sophisticated experimental methods, meso-scale features were probed, and interface

properties such as bending modulus, k , were determined experimentally (Binks et al. 1989; Farago et al. 1995; Gradzielski et al. 1996; Hellweg and Langevin 1998; Hellweg et al. 2001; Huang et al. 1987; Jahn and Strey 1988; Kawabata et al. 2004; Lisy and Brutovsky 2000). It was shown that the typical value of the bending modulus is $\sim 0.5k_B T$, and that larger k values are associated with larger meso-structural (50 – 200nm) features and vice versa.

Large meso-scale features are associated with a lamellar-like microstructure that possesses large zero-shear viscosity. Meanwhile, sponge or disordered bicontinuous microstructures lacking large meso-scale features typically show low viscosity. Even though viscosity does not intrinsically provide direct structural information (Cosgrove et al. 1995), the relation of viscosity to microstructure is well established for both bilayers and monolayers. For example, viscosity is used to differentiate ordered from disordered phases, such L_α from L_3 in bilayers (refer to Figure 4 in (Mahjoub et al. 1996) for an example). In addition to high viscosity, a fluid with a lamellar-like microstructure is characterized by shear thinning behavior, while fluids with a sponge or disordered bicontinuous microstructure behave Newtonian. Microemulsion rheological behavior, however, is more complex than this suggests.

While some Type III microemulsions behave as Newtonian fluids, others show shear-thinning behavior. Viscoelasticity evident from apparent viscosity hysteresis with shear rate sweep has also been reported. The complex rheology of viscous microemulsions makes them undesirable, as they generally show longer equilibrium

times and poor transport in porous media. As a result, different rheology alteration methods have been developed and relevant mechanisms have been suggested.

3.2 EXPERIMENTAL OBSERVATIONS

The experimental data presented in this section were obtained from Walker et al. (2012; Walker 2011). The authors used an ARES LS-1 rheometer to characterize the rheological behavior of a number of microemulsion samples for a specific crude oil and brine (Figure 3.1). All the samples are of Winsor Type III in equilibrium with excess oil and brine and have a bicontinuous microstructure ($\phi_o \sim 0.4$). The total surfactant and co-surfactant (if any) concentration is fixed at 0.3 wt%. An alcohol alkoxy sulfate (TDA-12EO-SO₄⁻) was used in these experiments with or without an internal olefin sulfonate, C_{19-23} IOS, as a co-surfactant and with and without a co-solvent (Table 3.1).

As evident in Figure 3.1, microemulsion “A,” created by only using only the primary surfactant at 55 °C, possesses a large zero-shear viscosity and shows shear-thinning behavior. To improve its rheological behavior, the authors added a branched internal olefin sulfonate (IOS) as co-surfactant to samples “B”, “C”, and “D” while keeping the total surfactant concentration the same at 0.3 wt%. In addition, sample “B” contains 1 wt% of iso-butyl alcohol (IBA) as co-solvent, while “C” contains Triethylene glycol monobutyl ether (TEGBE). No co-solvent was added to sample “D,” but the temperature was raised to 85 °C. It is worth mentioning that the viscosity of the crude decreases from ~ 70 cP at 55 °C to ~ 25 cP at 85 °C and the data shown in Figure 3.1 are reproducible (Dustin Walker 2011).

Table 3.1: Characteristics of the microemulsion samples

Sample	Co-surfactant	Co-solvent	Temperature
A	Branched IOS	-	55 °C
B	Branched IOS	IBA	55 °C
C	Branched IOS	TEGBE	55 °C
D	Branched IOS	-	85 °C

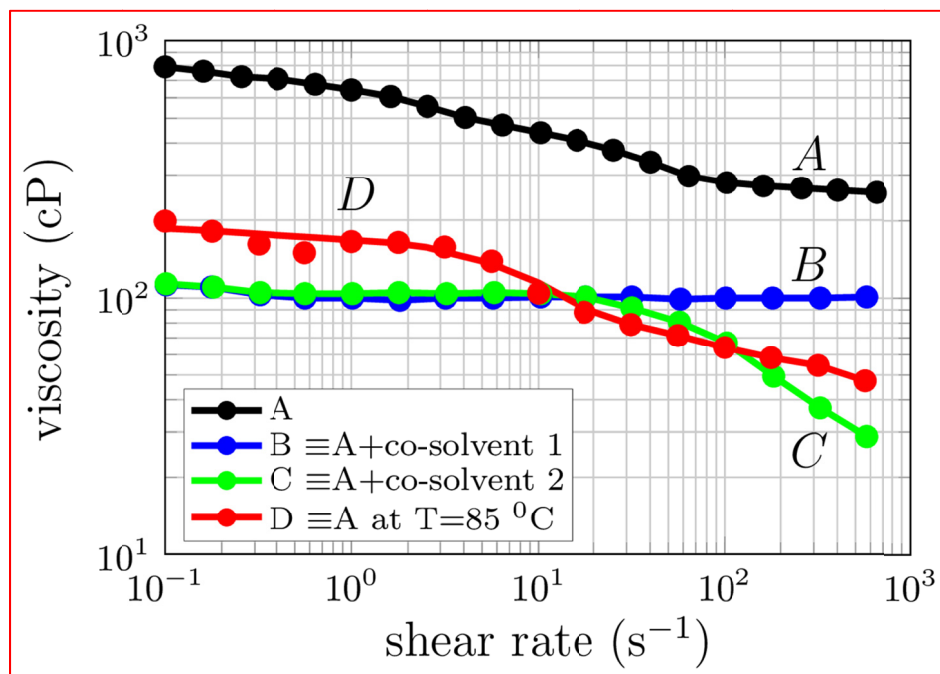


Figure 3.1: Rheology of microemulsion samples with $\phi_o \sim 0.4$ (Dustin Walker 2011). Microemulsion “A” is created by only using surfactant at 55 °C. Samples “B” and “C” are created by addition of 1wt% co-solvent to “A”. The composition of microemulsion “D” is similar to that of “A” but temperature is raised by 30 °C. Additionally, samples “B”, “C”, and “D” contain branched IOS as co-surfactant. Lines are for eye-guidance.

The most notable feature shown in Figure 3.1 is that the low-shear viscosity of microemulsion “A” is almost 10 times that of oil. Another notable feature is the shear thinning behavior of the microemulsion even at very low shear rates. It is highly likely that the interface in microemulsion “A” has a high bending modulus and that the sample possesses a lamellar-like microstructure or a large ξ_k . The addition of co-solvent and the increase of temperature both decreased the low-shear viscosity. The rheology is very

different, however. While the samples that contain co-solvent (“B” and “C”) show Newtonian-like behavior, sample “D” shows considerable shear-thinning behavior, and its apparent viscosity curve retains a shape similar to that of sample “A.” Two additional noteworthy features of Figure 3.1 are the shear thinning behavior of sample “C” at high shear rates and the shift of the onset of shear-thinning to higher shear rates for sample “D.” These different rheological behaviors can be explained in terms of the interface fluidity, as demonstrated in the next section.

3.3 THEORY

Although the terms co-surfactant and co-solvent are used interchangeably in various fields, we wish to make a distinction between the two molecules here. While co-surfactant increases the thermodynamic stability of the system by adsorption on the interface (i.e. moves the system away from emulsion towards microemulsion), co-solvent dissolves the interface (Kahlweit et al. 1991; Strey and Jonströmer 1992). In other words, it typically partitions between the aqueous domain and the interface (Kahlweit et al. 1991; Perez-Casas et al. 1997). A schematic demonstration of the distinction is presented in Figure 3.2. While co-surfactant binds to the interface (Figure 3.2.a), co-solvent acts as a ring around the interface (Figure 3.2.b). The contrast between the self-diffusivity of co-solvent and that of interface-bound molecules supports our generalization (Figure 3.3). The difference between the co-solvent and co-surfactant can be observed macroscopically through the reduction of surfactant efficiency in solubilizing oil/water by co-solvent (in contrast to the increase of surfactant efficiency by co-surfactant). We wish to emphasize that although the aforementioned differences between co-surfactant and co-solvent are

generally valid and helpful in understanding their behavior, some molecules perform somewhat in between the two and a clear distinction is absent.

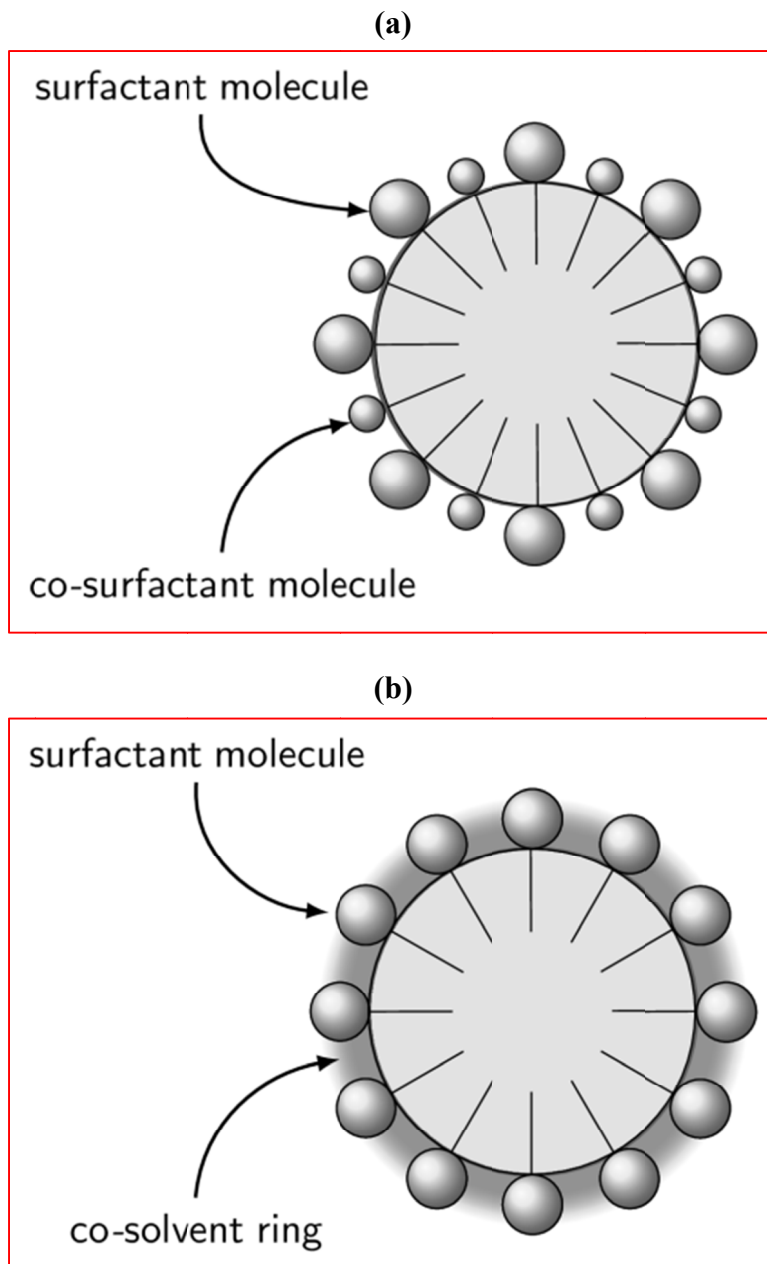


Figure 3.2: (a) Schematic representation of the arrangement of co-surfactant molecules. (b) Schematic representation of the arrangement of co-solvent molecules. In both cases the micelles core is filled with oil.

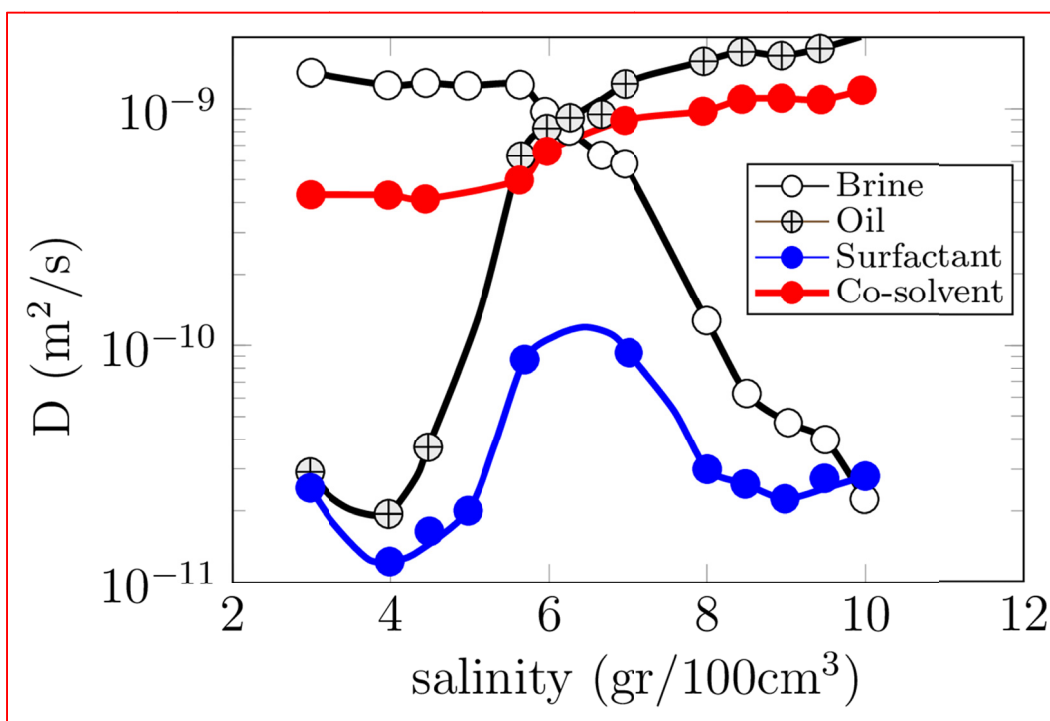


Figure 3.3: Component self-diffusion coefficients (at 20 °C) in microemulsions composed of sodium dodecyl sulfate (SDS) (1.99% by weight), butanol (3.96%), toluene (46.25%), and brine (46.8%) (Guering and Lindman 1985). While the self-diffusion coefficient of brine decreases with microemulsion phase evolution from Type *I* → *III* → *II*, that of oil increases. Surfactant (i.e. SDS) retains a comparatively low self-diffusion coefficient in all phase types whereas the co-solvent (i.e. butanol) self-diffusion coefficient remains close to that of the continuous phase. Lines are for eye-guidance.

3.3.1 Effect of Branched Co-surfactant

Using branched or twin-tailed surfactants to break the long-range interactions and lower the microemulsion viscosity is a well-documented procedure (Lelanne-Cassou et al. 1983; Levitt et al. 2006; Frank et al. 2007). Reducing the interface bending modulus is typically considered the main function of a branched surfactant (Bergström 2006; Rekvig et al. 2004). However, the role of interface concentration heterogeneity observed upon mixing surfactants with different affinities for oil/water is also very important. The concentration heterogeneity favors the creation of saddle-splay features which are

essential in the formation of low-viscosity “true” microemulsions and are induced by the mutual dependence of surfactant affinity and interface curvature.

The curvature correction to the surface tension is typically expressed by using the Tolman length, δ_0 , as follows:

$$\gamma(R) \simeq \gamma_\infty \left(1 - \frac{2\delta_0}{a} + \dots \right), \quad (3.1)$$

where γ_∞ is the surface tension for the planar interface. Tolman length is the distance between the equimolecular dividing surface and the surface of tension. The generalized Young-Laplace equation accordingly modifies Equation (3.2) (Anisimov and St. Pierre 2008),

$$\Delta P \equiv P'' - P' \simeq \frac{2\gamma_\infty}{a} \left(1 - \frac{2\delta_0}{a} + \dots \right), \quad (3.2)$$

where ΔP is the pressure difference across the interface. The sign and the value of δ_0 in Equation (3.2) have been debated. However most recent studies have shown that the Tolman length is negative for interface in microemulsions (Anisimov and St. Pierre 2008; Binder et al. 2011; Block et al. 2010; Blokhuis and Kuipers 2006; Ghoufi and Malfreyt 2011). Gurkov and Kralchevsky (1990) derived Equation (3.2) at an arbitrary dividing interface as follows, without the need to calculate the δ_0 ,

$$\Delta P \equiv P'' - P' \simeq \frac{2\gamma_\infty}{a} + \left(\frac{\partial\gamma}{\partial a} \right), \quad (3.3)$$

where $(\partial\gamma/\partial a) = (B/a^2)$ and B is called bending moment. Additionally, the authors demonstrated that the surface tension, γ (thermodynamic property), and surface dilation

energy, σ (mechanical property), for a sphere are related as follows and are exactly equal at the surface of tension where $B = 0$,

$$\gamma = \sigma + \frac{1}{2}BH, \quad (3.4)$$

where H is the mean curvature of the sphere. Kralchevsky et al. (1994) used the general form of Equation (3.4) within a general surface fundamental equation for an arbitrary shaped interface to arrive at Equation (3.5) for a mixed surfactant formulation.

$$\delta\gamma = -s_s\delta T - \sum_i \Gamma_i\delta\mu_i + B\delta H + \Theta\delta D, \quad (3.5)$$

where s_s is the excess surface density of energy; T , μ , and Γ_i are temperature, chemical potential, and number of surfactant molecules per unit area of the interface; B and Θ are bending and torsion moments; $H = (c_1 + c_2)/2$ and $D = (c_1 - c_2)/2$ where c_1 and c_2 are the principal curvatures. Note that Equation (3.5) is at an arbitrary dividing surface and reduces to the Gibbs surface tension equation at the surface of tension. The direct result of Equation (3.5) is the following equality:

$$\left(\frac{\partial\mu_i}{\partial H}\right)_\Gamma = \left(\frac{\partial B}{\partial\Gamma_i}\right)_{H,\Gamma_{j\neq i}}. \quad (3.6)$$

In other words, the change of the bending moment due to variations in interface composition is equivalent to changes of the chemical potential of components due to curvature change at constant overall composition. At constant overall composition, the bending moment is related to curvature energy by $B = (\partial e_c/\partial H)_\Gamma$. The curvature energy

of the interface per unit area is typically expressed by the Helfrich formulation (Equation (3.7)) (Helfrich 1973).

$$\begin{aligned}
e_c &= \frac{1}{2}k(c_1 + c_2 - c_0)^2 + \bar{k}c_1c_2, \\
&= \frac{1}{2}k(2H - c_0)^2 + \bar{k}K,
\end{aligned}
\tag{3.7}$$

where k is the bending modulus; \bar{k} is the saddle-splay modulus; H is the mean curvature, and $K = c_1c_2$ is the Gaussian curvature. c_0 is the spontaneous curvature that describes the tendency of the surfactant film to bend toward either water or oil (with the convention of a positive curvature toward water). The affinity of a mixed monolayer composing a reference area can be represented by (Kozlov and Helfrich 1992; Safran et al. 1991)

$$c_0 = \frac{\sum_i a_{s_i} \Gamma_i c_{0i}}{\sum_i a_{s_i} \Gamma_i},
\tag{3.8}$$

neglecting the monomer interactions. a_s stands for area per surfactant molecule and the subscript i indicates individual monomers.

Considering a mixture of branched and single-chain surfactants with the same head group and average size (i.e. $a_{s_1} \approx a_{s_2}$), combining Equations (6-8) and integrating leads to Equation (3.9)

$$\mu_i = \mu_i^0 + \frac{k_B T}{a_s \Gamma} \ln \left(\frac{\Gamma_i}{\Gamma} \right) - \frac{4k \delta c_{0ij} H}{\Gamma},
\tag{3.9}$$

where $\delta c_{0ij} \equiv c_{0i} - c_{0j}$ and $\Gamma = \sum_i \Gamma_i$. Note that in the derivation of Equation (3.9), monomers are assumed to be insoluble in oil/water (Israelachvili et al. 1976) and the

overall integral of Gaussian curvature is assumed to remain unchanged (for further information on the topic refer to (Safran 1999)). At chemical equilibrium, a Boltzmann distribution of the surfactant molecules is evident from Equation (3.9):

$$\Gamma_i \propto \exp\left(\frac{4ka_s\delta c_{0ij}H}{k_B T}\right). \quad (3.10)$$

If $\lambda \equiv \exp\left(\frac{4ka_s\delta c_{0ij}H}{k_B T}\right) > 1$, then the surface distribution of branched and single-chain monomers depends on their affinity for water/oil (an inherent property at fixed temperature, salinity, etc.) and curvature (an acquired property). More specifically, at salinities between the optimum salinities¹ of branched and single-chain monomers, $\delta c_{0ij} < 0$ and the concentration of branched monomers will be larger in the concave (i.e. $H < 0$) parts of the interface and vice versa. For a typical microemulsion with $a_s = 40 \text{ \AA}^2$ and $k/k_B T = 0.5$, the interface is wrinkled at scales greater than $\xi_k \sim 2 \text{ nm}$. Assuming $H \sim 0.1 \text{ nm}^{-1}$, $\lambda \sim 1.1$ for a typical values of $|\delta c_{0ij}| \sim 10^9 \text{ m}^{-1}$ (Frank et al. 2007). Therefore, the monomer type distribution is governed by the curvature as shown schematically in Figure 3.4. The curvature induced compositional heterogeneity has been reported for bilayers (Andelman et al. 1992; Hirose et al. 2012; Perlmutter and Sachs 2011; Schick 2012) and the strength of the coupling of the two has been suggested to be important when $\lambda_b = [k/k_B T] \left[k_B T (\delta c_{0ij})^2 / \gamma \right]^{1/2}$ is of order unity. Notice the similarity of λ and λ_b .

¹ The salinity at which a surfactant shows no preferred affinity for water/oil (Daicic et al. 1995)

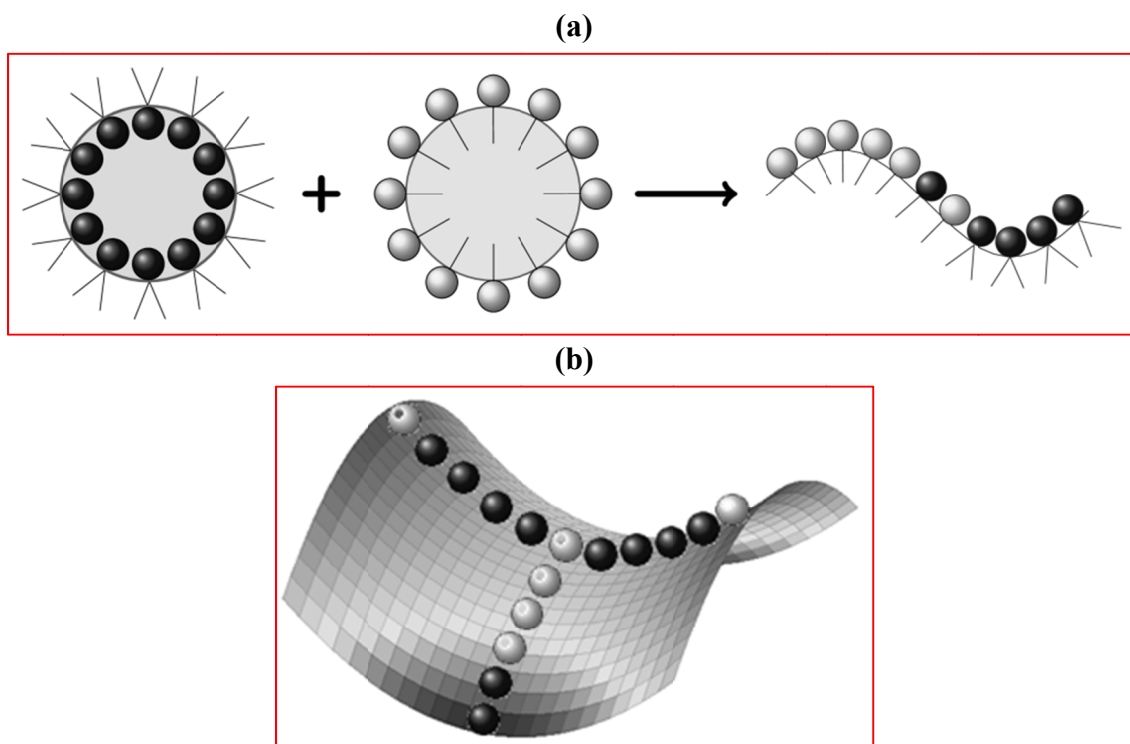


Figure 3.4: Schematic diagram demonstrating that the mixing of twin-tailed and single-chain surfactant results in the formation of saddle-splay structures at salinities between the optimum salinities of the two surfactants. Differences in the affinities of the two surfactants result in concentration heterogeneity at concave and convex parts of the resulting hyperboloid (a)2D, (b)3D.

The pattern presented in Figure 3.4 can be generalized for any mixture of surfactants as long as their optimum salinities differ. Thus, at salinities between the optimum salinities, one can expect to observe curvature induced compositional heterogeneity. This generalization may fail if the interface membrane bending modulus is very large. In that case, the interface remains essentially flat (i.e. $H = 0$) and the compositional heterogeneity predicted by Equation (3.10) disappears. A typical method to lower the bending modulus of the interface membrane is the addition of co-solvent. This method is the topic of the next section.

3.3.2 Effect of Co-solvent

Effective co-solvents are typically considered to have partial solubility in both water and oil with the ideal co-solvent partitioning equally between the water and oil; therefore their lowest chemical potential is around the interface in a microemulsion. Small alcohols, ethoxylated alcohols and glycols are generally considered to be effective co-solvents. It is well-documented that the addition of co-solvent reduces the bending modulus of a surfactant film (Strey and Jonströmer 1992; Safinya et al. 1989; Kegel et al. 1995; Di Meglio et al. 1985) and helps in creating saddle-splay structures (Porte et al. 1989; Moulik and Paul 1998; Safran 1991) which under certain conditions results in the formation of sponge or disordered bicontinuous phases (Morse 1994, 1997). However, the way in which co-solvent helps create handles is not adequately described. In this section, we wish to elaborate on those mechanisms with emphasis on the electrostatics.

In weak Coulomb regimes, such as microemulsions, the Poisson-Boltzmann equation describes experimental observations fairly well (Huh 1983; Mitchell and Ninham 1983; Hirasaki and Lawson 1986; Winterhalter and Helfrich 1992; Daicic et al. 1996). In this regime, the bare Coulomb potentials are screened and effective only at short ranges. Equation (3.11) represents the potential between two Z_c -valent point charges separated by distance r in a solvent with a static dielectric constant of ϵ , where e is the positive elementary charge,

$$W_c = \frac{Z_c^2 e^2}{4\pi\epsilon r}. \quad (3.11)$$

Relevant length scales that characterize the mean electrostatic potential in the Poisson-Boltzmann theory are the Bjerrum length (l_B) and the Gouy-Chapman length (b) which are defined as follows:

$$l_B \equiv \frac{e^2}{4\pi\epsilon k_B T}, \quad (3.12)$$

$$b \equiv \frac{e}{2\pi l_B |\sigma_0|}, \quad (3.13)$$

where σ_0 is surface charge density. The Bjerrum length ($\sim 0.7\text{nm}$ for 0.1M NaCl brine) measures the distance at which thermal energy balances the bare Coulomb potential of two unit charges, while Gouy-Chapman length (arising from the presence of a charged wall or interface in the case of microemulsions) is the length at which the cumulative counterions compensate half of the surface charge.

If Coulomb interactions are not screened, the Poisson-Boltzmann approach yields unreliable results (Moreira and Netz 2000). Moreira and Netz (2000) introduced the coupling parameter $\Xi \equiv 2\pi Z_c^3 l_B^2 \sigma_0$ to characterize the Coulomb regime where $\Xi < 1$ and $\Xi \gg 1$ represent weak and strong regimes, respectively. Figure 3.5.a shows the counterion distribution away from a charged surface for these coupling regimes. At the weak regime, the counterions feel the presence of other counterions and are dispersed. Meanwhile, at the strong regime, the counterions are collapsed on the surface. Figure 3.5.b demonstrates the difference in counterion density profiles with distance from the charged surface located at $z = 0$. The surface charge is half-compensated at $z/b = 1$ for the two regimes.

The strong Coulomb regime is often characterized by highly charged surfaces and/or very low temperatures. Another, less common, cause of the strong regime is the presence of a co-solvent with small dielectric constant (i.e. $\epsilon \ll \epsilon_w$). To demonstrate this phenomenon, let us consider the microemulsion presented in the previous section. Assuming an incompressible interface (Safran et al. 1986; Andelman et al. 1987; Cates et al. 1988; Murray et al. 1990; Feller and Pastor 1999) with a typical area per surfactant molecule of 40 \AA^2 (Murray et al. 1990; Kellay et al. 1993; Acosta et al. 2008), the Gouy-Chapman length and the coupling parameter are calculated for cases with and without co-solvent (Table 3.2). The static dielectric constant of co-solvents such as IBA (~ 18) (Dannhauser and Cole 1955) and TEGBE (~ 15) is much lower than that of water at room temperature (~ 80) and it is assumed that enough co-solvent is present to cover the interface. Effects of the salt concentration ($0.3M$) and temperature on the dielectric constants are qualitatively considered in Table 3.2.

Table 3.2: Comparison of the Gouy-Chapman length and Coulomb coupling for microemulsion samples “A” and “B”.

	Brine	Co-solvent
Temperature ($^{\circ}C$)	55	55
Dielectric constant (ϵ)	~ 67	~ 13
Area per surfactant molecule (\AA^2)	40	40
Degree of head-group ionization	0.4*	0.5**
σ_0 (C/m^2)	0.16	0.2
l_B (nm)	~ 0.8	~ 3.9
b (nm)	~ 0.21	~ 0.03
Ξ	~ 4	~ 120

* Typical ratio of head-ions that are ionized. Reported values can be found in (Benedouch et al. 1983; Hayter 1992; Reekmans et al. 1990).

** Even though the increase of head-ion ionization with co-solvent is considered (Sohrabi et al. 2010), the results are not sensitive to this modification and the main conclusions are still valid.

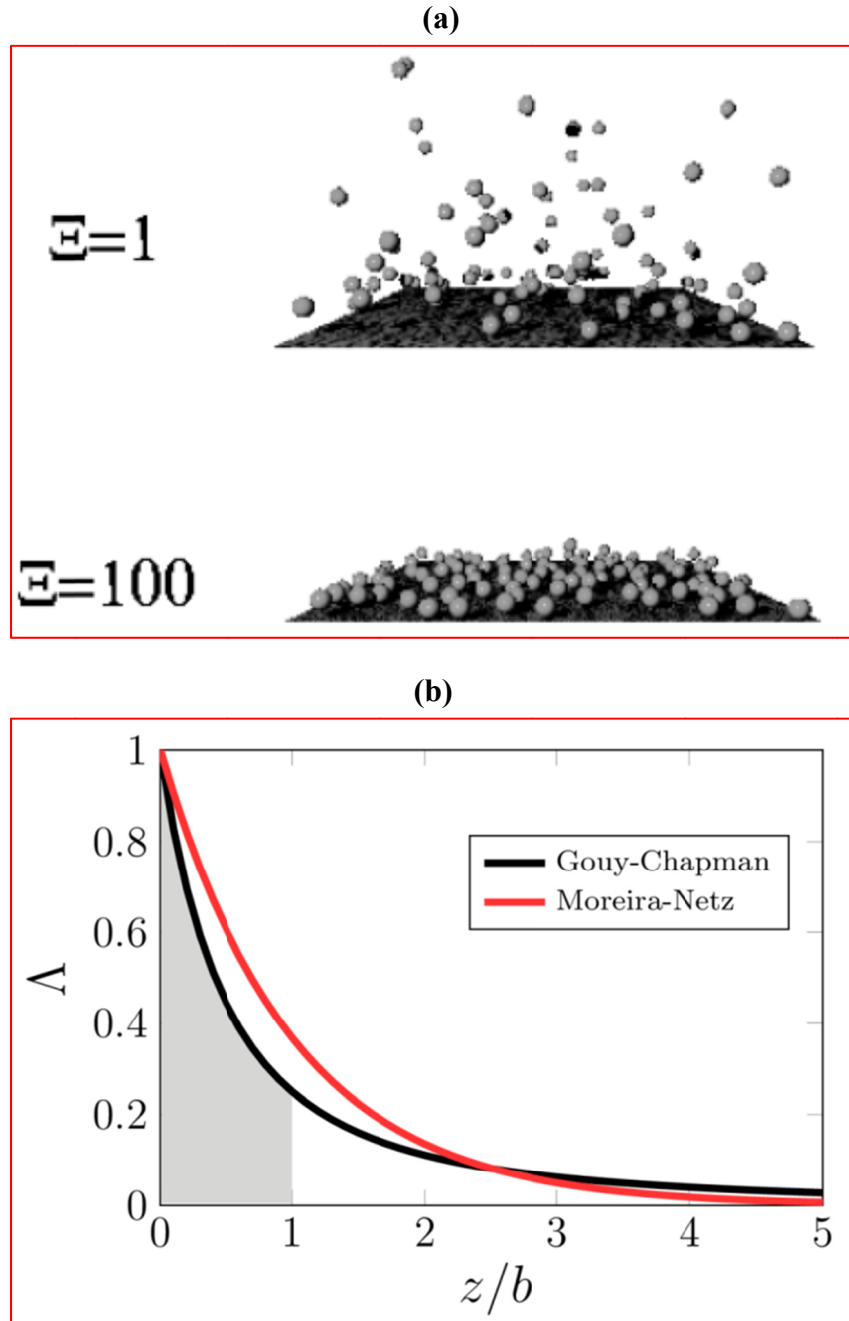


Figure 3.5: Snapshots of Monte-Carlo simulations demonstrating the distributions of counterions at different coupling parameters: $\Xi = 0.1$ or weak-coupling limit where Poisson-Boltzmann theory is accurate and $\Xi = 100$ or strong-coupling regime (Moreira and Netz 2000). (b) Reduced counterion distribution $\Lambda \equiv \rho_+(z)(2\pi l_B b^2)$ for weak Coulomb limit ($\Lambda = \frac{1}{(1+z/b)^2}$) compared to strong coupling limit ($\Lambda = \exp(-z/b)$). At $z = b$, the cumulated counterions (shadowed region) half-compensate the charge of the surface (Messina 2009).

As evident from Table 3.2, the presence of co-solvent shifts the Coulomb regime from a relatively weak ($\Xi \sim 4$) to a relatively strong ($\Xi \sim 120$) one. The shift of the Coulomb regime translates into a stronger in-plane electrostatic correlation of surfactant head groups. The enhanced in-plane correlation results from the stronger mutual repulsions between head-ions, which freeze out lateral degrees of freedom. Hence head-ions become laterally correlated and surrounded by a large correlation hole of size ξ_{el} (Naji et al. 2005). Note that ξ_{el} results from electrostatic interactions and is different from the persistence length, ξ_k . Pincus et al. (1990) derived a number of expressions for ξ_{el} , which is naturally $\xi_{el} \propto l_B$.

The reduced lateral degrees of freedom evident by large ξ_{el} stiffens the membrane (Andelman 1995; Pincus et al. 1990). However, for the microemulsions of the present study, this is only a local phenomenon instead of a mean-field. This locality arises for two reasons. First, a very small amount of co-solvent is used in the sample preparation. Note that the molar volume of co-solvent is much less than that of a surfactant. Second, only a fraction of surfactant head-groups are typically ionized (typically ~ 0.5). This charge and/or concentration heterogeneity nonetheless has a profound impact on the microstructure of the phase, as demonstrated below.

Lamellar phases composed of a stack of flexible membranes are stabilized by the entropically induced out-of-plane fluctuations of the stack, which cause a long-range repulsion between adjacent membranes. This undulation force (per unit area) is given by

$$f_u \sim \frac{k_B T}{k} \frac{k_B T}{d^2}, \quad (3.14)$$

where d is the repeat distance of the membranes. Upon dilution (i.e. increase of d), the lamellar phase often crumbles into a disordered bicontinuous phase in favor of more entropy. The two length scales ξ_k and d are adequate to describe this type of phase transition in most situations (d is often shown as ξ in lattice models). Around the transition from lamellar-like to bicontinuous microstructure, one can assume the characteristic length scales of the two microstructures are of the same order. For a bicontinuous microemulsion with $k/k_B T = 0.5$, $\xi_k \sim 2 \text{ nm}$, $\xi_{el} \sim 0.7 \text{ nm}$ and $d \sim 1 \text{ nm}$ (Teubner and Strey 1987). Therefore, the transition would happen around $d^* \sim 1\text{-}2 \text{ nm}$.

In the presence of co-solvent, however, ξ_{el} as the third length scale is also relevant. Although there is no long-range electrostatic repulsion between the membranes, the out-of-plane thermal undulations are suppressed by large enough ξ_{el} . In the presence of co-solvent, $\xi_{el} \sim \mathcal{O}(4 \text{ nm})$ and is greater than d . This means the undulation forces are reduced and so is the stability of the lamellar-like microstructure; it crumples at a $d < d^*$. The undulation forces can be conveniently modified to read

$$f_u^{normalized} \sim \frac{f_u}{\exp(\xi_{el}/\pi\xi_k)}. \quad (3.15)$$

With this treatment the undulation energy remains essentially unchanged in a weak Coulomb regime while will be reduced by a factor of 1.5-2 in a strong Coulomb regime.

To summarize, the presence of co-solvent strengthens the Coulomb regime because of its lower solvation capacity. The enhanced Coulomb interactions cause an in-plane head-ion electrostatic correlation, which reduces the undulation forces. This in turn destabilizes the membrane. The membrane relaxes by formation of a saddle structure to

reduce the in-plane tension in the spite of easy tilting. Finally it should be noted that in the presence of a small amount of co-solvent, the shift of Coulomb regime and saddle creation will nonetheless be local (rather than mean-field) to the area covered by the co-solvent. This non-uniform distribution of co-solvent facilitates the formation of the saddle-splay features necessary for the formation of disordered microemulsions (Figure 3.6). The inevitable result of this is significant reduction of low-shear viscosity, η_0 , as it scales as $\eta_0 \propto \xi^3$ (Hennes and Gompper 1996). The topological variations induced by the co-solvent could also explain the reduction in the solubilization capacity (i.e. solubilized volume of oil and water in the microemulsion) observed by many workers such as Levitt et al. (2006).

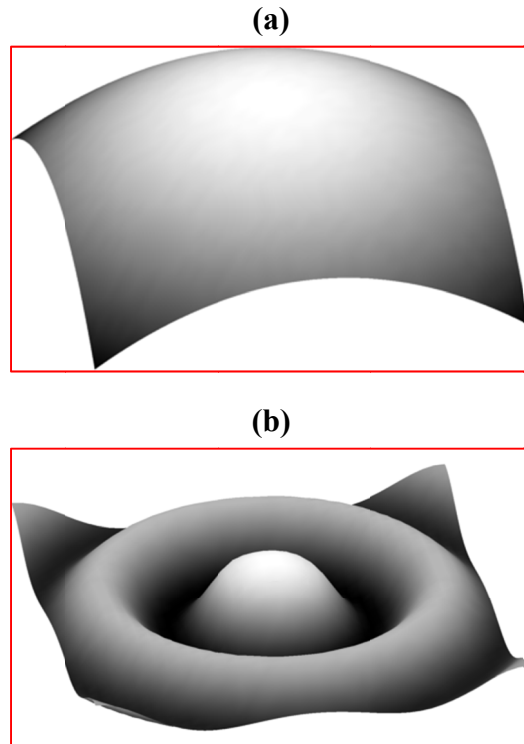


Figure 3.6: Schematic diagram demonstrating the curvature induced by non-uniform distribution of the co-solvent; (a) without (b) with co-solvent – the dark ring is covered by co-solvent.

An *ideal* interface possesses low bending modulus and high topography adaptation (i.e ability to adjust to the flow). Assuming two Newtonian fluids are separated by an ideal interface, the mixture will behave Newtonian as well. In microemulsions, brine and oil domains are separated by an amphiphilic interface. The addition of co-solvent not only reduces the bending modulus of the interface (hence increasing its fluidity) but also breaks the long-range interactions through charge and/or composition heterogeneity. In other words, co-solvent makes the interface more fluid or ideal. Therefore, the Newtonian-like behavior of samples “B” and “C,” in Figure 3.1, is a natural result of the addition of co-solvent. However, sample “C,” which contains bulkier TEGBE, shows a shear thinning behavior at high shear rates that closely resembles the shear induced $L_3 \rightarrow L_\alpha$ transition in bilayers (Mahjoub et al. 1996, 1998; Porcar et al. 2002; Tanaka et al. 2006). It is interesting to note that even though the lamellar-like microstructure reappears at high shear rates [sample C], the apparent viscosity remains small because of the reduced bending modulus. Increasing the concentration of the co-solvent will eliminate the shear thinning behavior at high shear rates (Walker 2011). The transition from lamellar-like microstructure to a disordered bicontinuous one has been experimentally observed by Hackett and Miller (1988) for microemulsions and by Mahjoub et al. (1996) for bilayers. Hackett and Miller used birefringence and viscosity measurements to differentiate the two microstructures while Mahjoub et al. used dynamic birefringence and viscosity measurements combined with in-situ X-ray scattering. Figure 3.7 illustrates how the viscosity changes when a lamellar structure changes to a

bicontinuous structure. The Newtonian behavior with the addition of co-solvent is evident in in Figure 3.7.

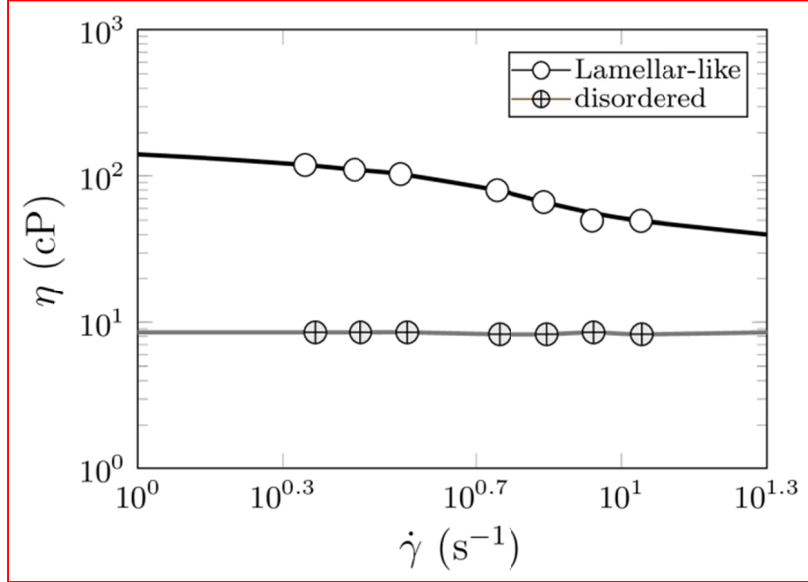


Figure 3.7.a: Example viscosity measurements where addition of co-solvent induced a lamellar microstructure conversion to a disordered bicontinuous one. The sample contains SDS/hexanol/brine/n-decane with $\phi_o = 0.5$ and $\phi_s \sim 0.02$ at $T = 30^\circ\text{C}$ (Hackett and Miller 1988). The lamellar-like sample contains 3.2 wt% hexanol while the microemulsion contains 3.6 wt%.

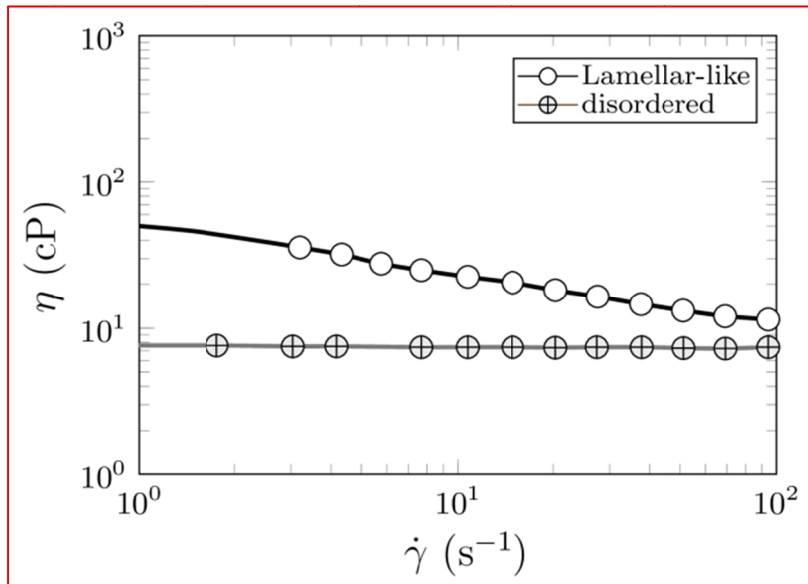


Figure 3.7.b: The data shows the rheology of CPCI/hexanol/brine with $\phi_{solvent} = 0.85$ at $T = 24^\circ\text{C}$ (Mahjoub et al. 1996). The ratio of co-solvent (hexanol) to surfactant (CPCL) is 1.075 for the L_α phase and 1.15 for the L_3 phase.

3.3.3 Effect of Temperature

Experiments have shown that the interface becomes more flexible with increasing temperature for microemulsions and bilayers² (Kawabata et al. 2004; Niggemann et al. 1995). This increase in flexibility can be explained as follows. The natural hydrogen bonding network of water is disturbed with increasing temperature. The disruption of the water hydrogen bonding network reduces its dielectric constant (Lu et al. 2001). As shown in the previous section, a reduced dielectric constant leads to an escalation in the electrostatic coupling parameter (Ξ) and a thinning of the interface. However, the increase in Ξ induced by the temperature is typically much smaller than that of the co-solvent (Table 3.3) due to increased interactions of the counterions at elevated temperatures. In other words, unlike with co-solvent, the thermal undulations are amplified at the elevated temperature, which causes the Bjerrum length to remain unchanged. Therefore, the amplified thermal undulations lead the collapsed counterions to increasingly separate from another, a phenomenon that causes an increase of area per surfactant molecule. In summary, the modest increase of Ξ is best physically described by the thinning of the interface transversely and by its expansion laterally. The thinning of the interface reduces the bending modulus only if microemulsion is in equilibrium with excess phases. In that case, the increase of area per surfactant molecule, which can be inferred from experimental observations (Sottmann et al. 1997), is compensated by solubilizing more oil/water. If a microemulsion is not in equilibrium with excess phases, increase in temperature stiffens the interface due to additional in-plane stresses.

² The role of temperature is linked to its net effect on the phase behavior. For some samples decreasing the temperature shifts the microstructure from lamellar-like to disordered and hence causes a similar rheology behavior as presented here.

Table 3.3: The Gouy-Chapman length and Coulomb coupling parameter the microemulsion sample “D”.

	Brine
Temperature ($^{\circ}\text{C}$)	85
Dielectric constant (ϵ)	~ 50
Area per surfactant molecule (\AA^2)	45*
Degree of head-group ionization	0.55
σ_0 (C/m^2)	0.20
l_B (nm)	~ 0.9
b (nm)	~ 0.14
Ξ	~ 7

* Slight increase of area per surfactant molecule with increasing the temperature is assumed.

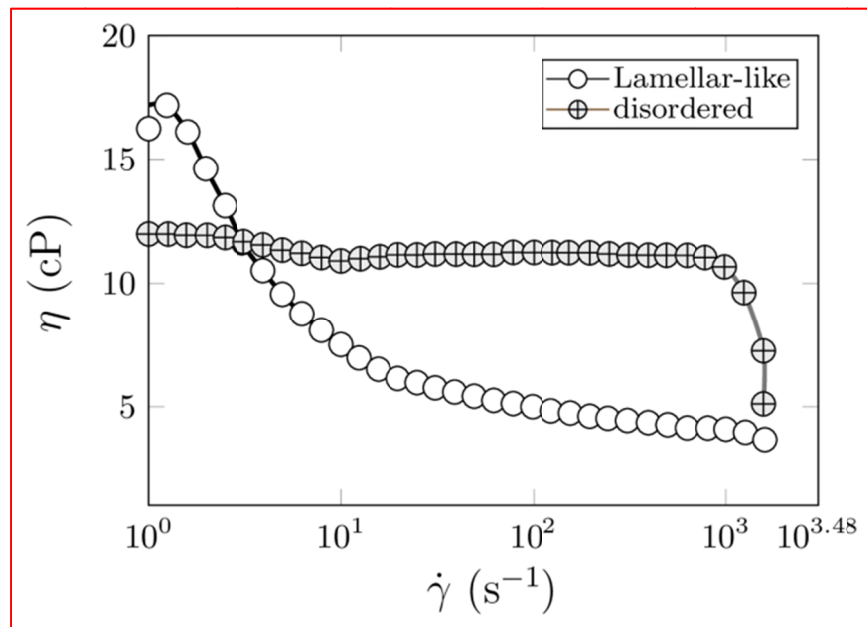


Figure 3.8: Effect of temperature on the rheology of a microemulsion composed of AOT/decane/brine with $\phi_o = 0.15$ and $\phi_s \sim 0.3$. The lamellar-like sample is at $T = 21.1^{\circ}\text{C}$ and the disordered at $T = 18.4^{\circ}\text{C}$ (Kotlarchyk et al. 1992).

There is another difference between the performance of co-solvent and temperature. While the addition of co-solvent provides great freedom for charge and/or composition heterogeneity, increasing the temperature modifies a mean-field property

(i.e. ε) and fails to provide heterogeneity in charge and/or composition. Therefore, increasing the temperature reduces the bending modulus of the interface but does not facilitate the formation of saddle-splay structures. In other words, temperature renormalizes the bending modulus but not the saddle-splay modulus – unless Ξ is increased enough to allow for the charge fluctuations.

The rheology of the microemulsion sample “D” in Figure 3.1 confirms the presence of long-range interactions at the elevated temperature because the sample rheology retains a shape similar to that of sample “A”. The shift of the apparent viscosity curve to lower values is most likely due to the decrease in viscosity of oil and water. However, the shift in the onset of shear thinning to a higher shear rate could be attributed to the higher fluidity of the interface. Similar observations for other samples have been reported.

Chapter 4: Microemulsion Rheology Model

A rheological model has been developed to describe the behavior of microemulsions. A key feature of the model is the treatment of the concentrated microemulsion as a bi-network. This provides accuracy and consistency in the calculation of the zero-shear viscosity, η_0 , of a microemulsion regardless of its type and microstructure.

4.1 LITERATURE REVIEW

Macroscopic rheology of complex fluids to a large extent is determined by the dynamic properties of the interface. In microemulsions, oil and water are separated by many interfaces that move and deform with the flow; variations in dynamic behavior of these interfaces may result in radically different bulk rheology of microemulsions with similar composition. Despite significant advances in modeling the stress-deformation behavior of interfaces in complex fluids (Gross and Reusken 2013; Sagis 2011), the numerical and theoretical challenges of coupling micro- and meso-scale dynamics have hindered the developing of a fluid-mechanical theory for macroscopic rheology of such fluids (Feng et al. 2005). The objective of this study was to develop a simple closed-form model for the rheology of microemulsions for use in numerical flow simulations. .

Rheological behavior of dilute microemulsions is similar to that of hard-sphere like dispersions and the interface properties such as bending modulus, k , play no significant role in this behavior. This is due to the preferred curvature of the surfactant monolayer towards oil or water which typically results in the formation of hard-sphere

micelles. However, for microemulsions that contain comparable amount of oil and water, the interface properties play a crucial role in the macroscopic rheology of microemulsion. Highly-ordered interfaces are associated with lamellar-like microstructures and high macroscopic viscosities, while simple fluid-like interfaces are associated with disordered sponge-like microstructures and low viscosities.

For weak affinity of surfactant monolayer for oil/water, the interface properties that shape the microstructure are bending and Gaussian moduli (Andelman et al. 1987). Due to the well-established link of microstructure and bulk rheology, it is safe to claim that these moduli determine the macroscopic rheology of microemulsions to the first order. This can be rationalized by noting that the formation of microemulsions is thermodynamically reversible and the path to their slightly-perturbed near-equilibrium microstructure should not involve significant dissipative shear forces. Under flow conditions, however, shear and dilatational moduli of the interface generally contribute to the macroscopic rheology with an additional elastic component in the presence of macromolecules at the interface (Espinosa and Langevin 2009; Hoffmann 1994; Koehler et al. 2000; Opawale and Burgess 1998; Sagi et al. 2013). Note that bending modulus accounts for out-of-plane deformations while elastic modulus for in-plane ones. Due to ultra-low interfacial tension in microemulsions and interface incompressibility (Milner and Safran 1987), the dilatational shear should be insignificant due to low energy cost of creating extra interface (Safran 1999; Barentin et al. 1999). An exception to this behavior may be observed for single-phase microemulsions where salinity and/or temperature variations create in-plane tensions and eventually phase separation. On the other hand,

the interface shear modulus may play a role in disordered to ordered microstructure at high shear rates.

The purpose of this study was to develop a unified rheology formulation that could be used to calculate the rheology of Winsor-type³ (Winsor 1954) microemulsions as they evolve from oil-in-water→bicontinuous→water-in-oil types. The differences between microemulsions with well-characterized hard-sphere colloid dispersions are highlighted in this development and some of their common behaviors are described. The unified rheology model developed here accounts for phase composition, shear rate, and qualitatively for the rheology alteration methods. The following section describes the mathematical model for rheology of microemulsions. Model validation by comparison with the experimental data of Walker et al. (2012; Walker 2011) and Lu et al. (2013) is given in the results section.

4.2 MODEL FORMULATION

Microemulsions are complex fluids and characterizing their behavior often involves adapting the findings from model systems, such as colloidal dispersions, stabilized suspensions, and polymeric solutions. We shall start with discussing the similarities and differences of microemulsion and model systems for slightly-perturbed near-equilibrium systems. Then, the role of steady shearing will be discussed. Finally the effects of rheology alteration methods will be discussed and the relevant modeling techniques are presented.

³ Characterized by a low surfactant concentration and are in equilibrium with excess phase(s).

4.2.1 Zero-shear Viscosity

Understanding zero-shear viscosity of colloidal dispersions provides invaluable insights to understanding that of microemulsions. However, caution should be taken in adapting the findings to microemulsions since there are fundamental differences between the two fluids. The viscosity of a hard-sphere dispersion increases with the volume fraction of the particles, ϕ , and eventually diverges at the random close packing, ϕ_m , “because the number of *contacting* particles becomes infinite and the short-time self-diffusivity, D_s^s , vanishes as the touching particles are *stuck* by the hydrodynamic lubrication forces” (Brady 1993). This can be better understood by looking at the self-diffusivity of particles. Crowding a dispersion slows down the particle diffusion due to hydrodynamic and thermodynamic interactions among the suspended particles (Ottewill and Williams 1987). At short times where a particle moves over only a very small fraction of its radius, the particle diffusion is felt by others through solvent or hydrodynamic interactions (Medina-Noyola 1988). The self-diffusivity relevant to this time scale is called the short-time self-diffusivity, D_s^s , which is smaller than Einstein-Stokes self-diffusivity of a single Brownian particle, D_0 , as a result of the hydrodynamic interactions (Medina-Noyola 1988). At longer times scales, a particle diffuses over such a distance that it feels a substantial potential interaction forces from the other particles in the form of (shielded) Coulomb, excluded volume, and van der Waals interactions (Imhof et al. 1994). The resulting long-time self-diffusivity, D_s^l , is slower than D_s^s , as the particle needs to distort the configuration of neighboring particles in order to diffuse. For hard-sphere and hard-sphere like particles, both D_s^s and D_s^l vanish with different rates in the

vicinity of the maximum close packing. The value of ϕ_m is not universal and depends on the particle's shape, size distribution, and packing protocol and varies between 0.524 – 0.71 (Mewis and Wagner 2012).

Expressing the zero-shear viscosity, η_0 , in terms of the high-frequency low amplitude viscosity, η'_∞ , and the excess viscosity, $\Delta\eta_0$ gives (Cheng et al. 2002):

$$\eta_0 = \eta'_\infty + \frac{k_B T}{6\pi a D_s^s} \Delta\eta_0, \quad (4.1)$$

where k_B is the Boltzmann constant, T is temperature, and a is the particle radius. η'_∞ and $\Delta\eta_0$ represent the hydrodynamic and thermodynamic contributions, respectively. Generally at ϕ_m , D_s^s vanishes and $\Delta\eta_0$ diverges as $(\phi_m - \phi)^{-1}$ leading to the net effect of viscosity divergence by $\eta_0 \sim (\phi_m - \phi)^{-2}$ (Brady 1993); which can be expressed by the generalized Krieger and Dougherty (1959) equation,

$$\eta_{r0} = \left(1 - \frac{\phi}{\phi_m}\right)^{-[\eta]\phi_m}, \quad (4.2)$$

where $\eta_{r0} \equiv \eta_0/\mu_s$; μ_s is solvent viscosity and $[\eta]$ is the intrinsic viscosity. Brady (1993) also showed that in the presence of long-range interactions between the particles, the short- and long-time self-diffusivities remain finite (Figure 4.1) and the viscosity singularity scales as $\eta_0 \sim (\phi_m - \phi)^{-1}$. In the case of microemulsions and other similar systems (Krishnamurthy et al. 2004), the long-range interactions are present as electrostatic potentials and the viscosity build-up at high volume fractions is smaller. Other forms of non-idealities compared to hard-sphere like systems, explained below, limit the application of Equation (4.2) for microemulsions.

Unlike in dispersions, increasing the volume fraction of oil (water) droplets in a *type I (type II)* microemulsion is done indirectly by changing a parameter such as salinity or temperature. In dilute and semi-dilute regions, the increase in volume fraction is accompanied by (1) an increase in droplets size (Huh 1983; Strey 1994), (2) modification of the droplet interactions and interface membrane properties. In other words, a hard-sphere is always a hard-sphere but micelles evolve as the volume fraction of the dispersed phase varies. At even higher dispersed phase concentrations, often topological relaxations in the form of membrane fusion (Peter et al. 2001; Milner et al. 1990; Appell et al. 2005; Hattori et al. 2007; Tlusty et al. 2000) and percolation induced by short-lived clusters (Safran et al. 1985; Feldman et al. 1996; Langevin 1988; Feldman et al. 1995; Arleth and Pedersen 2001) cause deviation from the simple droplet picture. Topological relaxation refers to microstructure evolution from a micellar or droplet form to a bicontinuous form evident by an exponential-type diffusivity. Electrical percolation is evident by a jump in electrical conductivity of a Type II or water-in-oil (W/O) microemulsion. In any case, at comparable amount of oil and water, either a phase separation (i.e. emulsification failure (Evilevitch et al. 2001)) or microstructure evolution to a bicontinuous microemulsion occurs (Langevin 1988), and a glass transition becomes irrelevant.

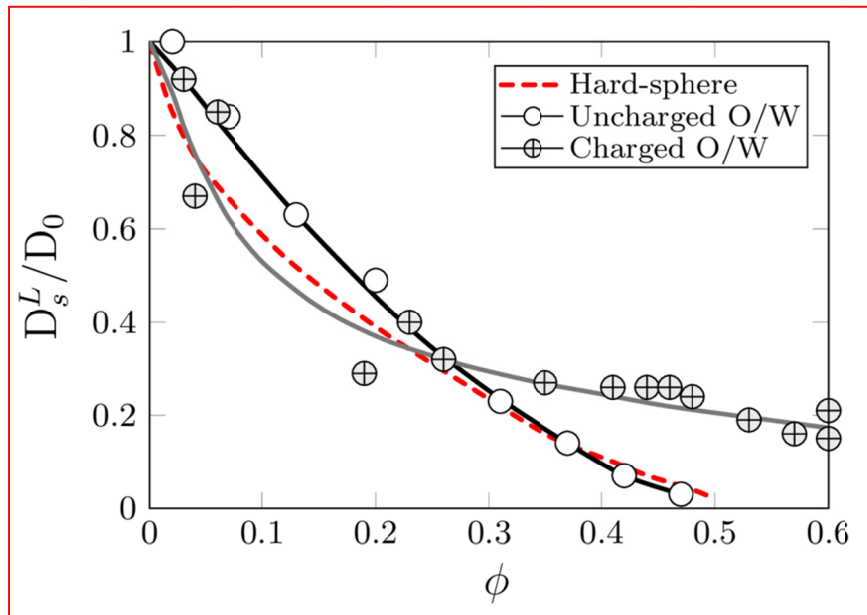


Figure 4.1: Normalized long-time self-diffusivity of hard-spheres (Ottewill and Williams 1987) and uncharged (Evilevitch et al. 2001) and negatively-charged (Peter et al. 2001) oil-in-water (O/W) droplet microemulsions. The behavior of uncharged microemulsion is hard-sphere-like while because of the long-range electrostatic potential of charged microemulsion, D_s^L (hence D_s^s) remains finite. This phenomenon makes the viscosity singularity less severe.

This research was focused on Winsor-type evolving microemulsions where an increase of the volume fraction (induced by changing salinity) of oil-in-water or Type I microemulsion results in the formation of a bicontinuous or Type III microemulsion and eventually to a water-in-oil or Type II microemulsion. This behavior is universal and has a direct implication on the viscosity of microemulsions where viscosity/stress relaxation adapts to the microstructure of the microemulsion. The relevant questions are what microemulsion property is physically reasonable and what form of equation can be used to describe the rheology for such diverse microstructures.

For droplet microemulsions the viscosity behavior resembles that of dispersions where a property of infinitely dilute region, $[\eta]$, is adequate to describe the system

behavior (Leaver and Olsson 1994). Note that $[\eta]$ in Equation (4.2) is independent of ϕ and equal to 2.5 for mono-dispersed hard-spheres (de Kruif et al. 1985) as defined by

$$[\eta] \equiv \lim_{\phi \rightarrow 0} \frac{\eta_{r0} - 1}{\phi}. \quad (4.3)$$

The physical implication of Equation (4.3) is that the rate of dispersion viscosity build-up with crowding is proportional to $[\eta]$ (i.e. $\partial\eta_{r0}/\partial\phi \propto [\eta]$). For dispersions this is reasonable as the size and shape of particles remains unchanged, unlike in microemulsions where both can vary. Therefore instead of Equation (4.3), we define the intrinsic property of the interface, adapting the form of inherent viscosity of a polymer molecule, to read

$$[\eta] = \lim_{\phi \rightarrow 0} \frac{\ln \eta_{r0}}{\phi}. \quad (4.4)$$

The immediate result of this treatment is that the viscosity of microemulsion is in an exponential form with ϕ as follows:

$$\eta_{r0} = \exp([\eta]\phi). \quad (4.5)$$

In order to examine the validity of Equation (4.5), comparisons were made against experimental measurements of viscosity for O/W and water-in-oil (W/O) dilute microemulsions (Berg et al. 1987; Leaver and Olsson 1994) by setting $[\eta] = 2.5$ as in the hard-sphere case. As seen in Figure 4.2.a, the model prediction fits the experimental data reasonably well. For the sake of completeness, comparisons were also made with experimental data for concentrated droplet microemulsions (Leaver and Olsson 1994; Peyrelasse et al. 1988) up to emulsification failure (Figure 4.2.b). In order to account for

the crowing effects, a Mooney-type exponent (which has shown to work well for dense microemulsions by (Majolino et al. 1990)) in the form of $(1 + \phi)^{[\eta]}$ was introduced to the right-side of Equation (4.5). The advantage of this form for the Mooney exponent is that Equation (4.5) remains a single-parameter model. The model predictions are aligned with experimental measurements as evident in Figure 4.2. It is interesting to note that the uncharged O/W microemulsion of Leaver and Olsson (1994) behaved similar to hard-sphere in the vicinity of phase separation while W/O microemulsions which possess a *soft* potential do not show the sudden viscosity build-up. These behaviors are in line with the earlier discussions. In any case, the resemblance of droplet microemulsions behavior to dispersions is a direct result of strong affinity of surfactant monolayer towards either water or oil, making the interface membrane properties essentially irrelevant. In the lack of strong interface preference, microemulsions with comparable amount of oil and water are bicontinuous with disordered sponge-like or ordered cubic or lamellar-like microstructures depending on the bending and Gaussian moduli of the interface. For these microemulsions neither the form of Equation (4.5) nor the $[\eta]$ is appropriate.

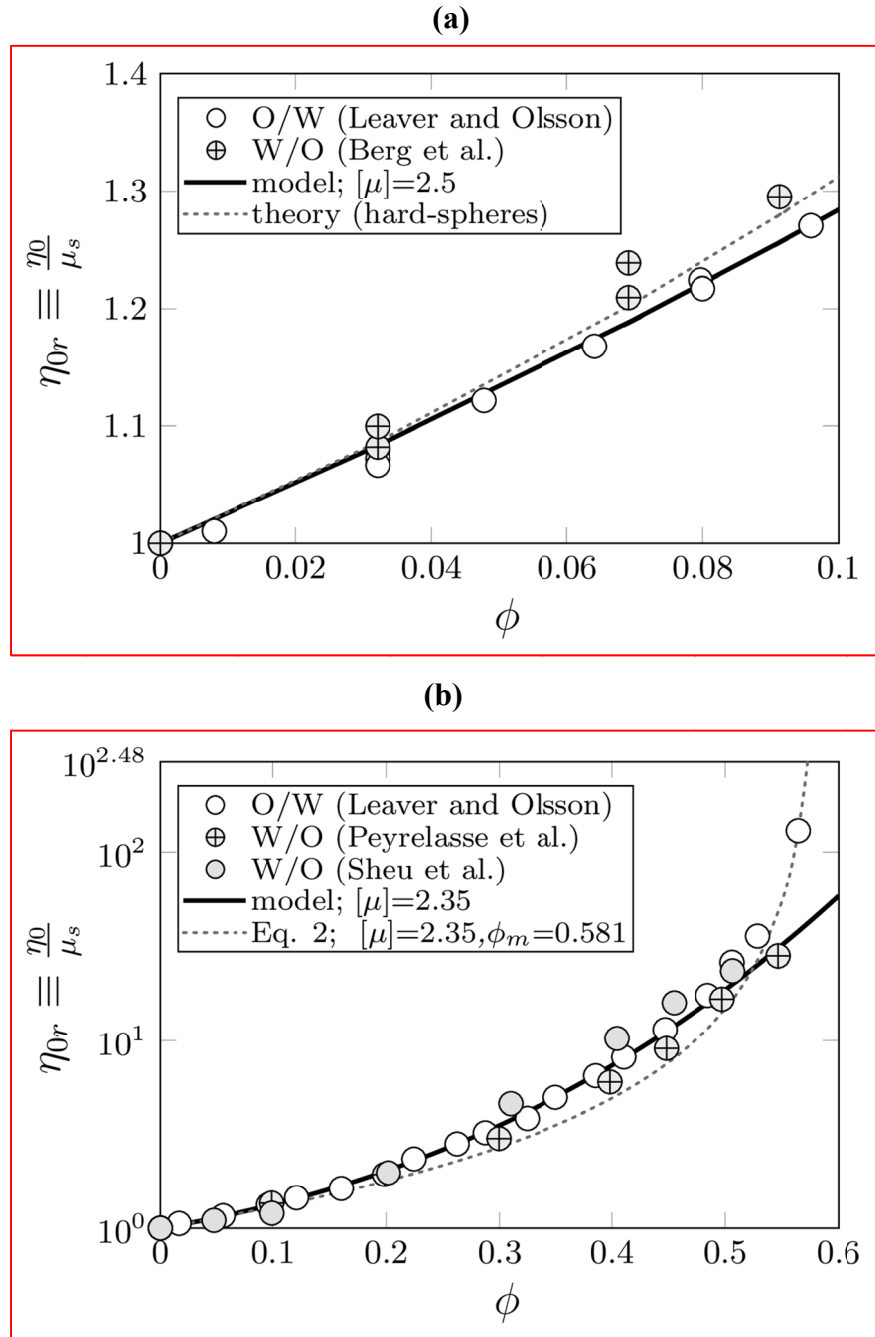


Figure 4.2: Relative zero-shear viscosity of droplet microemulsions. (a) Dilute O/W (Leaver and Olsson 1994) and W/O (Berg et al. 1987) microemulsions. For the sake of comparison, the theory prediction ($\eta_{0r} = 1 + 2.5\phi + 6.2\phi^2$) for hard-spheres (Batchelor 1977) is included. (b) Concentrated O/W (Leaver and Olsson 1994) and W/O (Peyrelasse et al. 1988; Sheu et al. 1989) microemulsions. At high concentrations the O/W viscosities deviate from the model prediction. Emulsification failure occurs at $\phi_m = 0.581$ (Leaver and Olsson 1994) which was used in the generalized Krieger and Dougherty (Equation (4.2)) and included in the graph for comparison.

For bicontinuous microemulsions characterized by short-range ordering, Pätzold and Dawson (1996) showed that the deformation of correlated random interfaces, even under a small shear, gives rise to excess stresses, $\Delta\eta$, given by

$$\Delta\eta \propto \xi^3 \frac{\pi^2 + \alpha^2}{4\pi^2 + \alpha^2}, \quad (4.6)$$

where $\alpha = d/\xi$; d and ξ are characteristic periodicity and correlation lengths (Andelman et al. 1987; Teubner and Strey 1987). Equation (4.6) suggests that interface film bending contribution must have the dominant role in producing these excess stresses (Pätzold and Dawson 1996), as $\xi \sim \xi_k$ for disordered bicontinuous microemulsions (Safran et al. 1986). It should be noted that the full stress is characterized by the bare Newtonian oil/water viscosities and $\Delta\eta$ resulting from the many interfaces deformation. The stress relaxation in this random two-domain network separated by an interface resembles a parallel network, which suggests that its bulk fluidity (i.e. inverse of viscosity) can be approximated as the sum of the fluidity of the individual domains, in analogy to co-continuous polymer blends (Nielsen 1974; Veenstra et al. 2000; Willemsse et al. 1999; Yu et al. 2010). In other words, the fluidity of each domain (water or oil), can be used to determine the bulk fluidity as follows:

$$f_{ME} = \phi' f_I + \phi f_{II}, \quad (4.7)$$

where ϕ is taken to be oil volume fraction in the microemulsion, $\phi' = 1 - \phi$, and $f = 1/\eta_0$. f_{ME} is the fluidity of the microemulsion and f_I and f_{II} are the fluidity of the water and oil domains, respectively. The viscosity of each domain is obtained by $\eta_0 = \mu_s \exp(\nu\phi)$, which as shown above, works well where hydrodynamic interactions

are moderate. This model includes the contribution of the bare viscosities and a corrective term for the difficulty to deform the interface which is characterized by $\nu \propto k/k_b T$. Inserting $\eta_0 = \mu_s \exp(\nu\phi)$ for each fluid into Equation (4.7) and rearranging the terms gives:

$$\eta_0 = \frac{\mu_o \exp(\nu' \phi) \exp(\nu \phi')}{\phi \exp(\nu' \phi) + \lambda_r \phi' \exp(\nu \phi')} \quad (4.8)$$

where $\lambda_r = \mu_o/\mu_w$. The only adjustable parameter in Equation (4.8) is ν , which closely resembles the bending modulus of the interface and ranges from 0.25 to 2. In order to extend the application of Equation (4.8) to the entire range of ϕ , we chose ν' to be different from ν based on the experimental observation that the maximum low-shear viscosity often occurs near the phase boundary of a bicontinuous microemulsion (Gradzielski and Hoffmann 1999). The corresponding phase fraction is denoted as ϕ_m at which $\partial\eta_{r0}/\partial\phi = 0$. This can be used to calculate ν' by iteratively solving

$$\frac{1 + (1 - \phi_m)\nu'}{1 + \phi_m\nu} = \frac{1}{\lambda_r} \exp[\phi_m\nu' - (1 - \phi_m)\nu]. \quad (4.9)$$

Typically, ϕ_m is $0.3 \leq \phi_m \leq 0.5$ for low surfactant concentrations. In the absence of laboratory data, $\phi_m = 0.35$ is an adequate estimation. Co-solvent increases ϕ_m . Equation (4.8) goes to the correct limits, i.e. $\lim_{\phi \rightarrow 0} \eta_0 = \mu_w$ and $\lim_{\phi \rightarrow 1} \eta_0 = \mu_o$.

The adequacy of Equation (4.8) to cover the entire range of ϕ , corresponding to Types I, III, and II microemulsions, is demonstrated in the results section. However, it

should be noted that the microstructures and dynamics are very different for each of these types of microemulsion. .

4.2.2 Effect of Shear Rate

Dilute Type I and Type II microemulsions behave as Newtonian fluids while more concentrated ones show shear thinning behavior as the micelles align to the flow field in a fashion similar to dispersions. The rheology of Type III microemulsions is more complex. While some Type III microemulsions are Newtonian, others are shear-thinning. The controlling factor is the fluidity of the interface. Taking into account the microstructure evolution with shear rate, Pätzold and Dawson (1996) showed that for a bicontinuous microemulsion the excess viscosity, $\Delta\eta$, resulting from deformation of myriad interfaces, reduces with shear rate indicating a shear thinning characteristic. Additionally, the shear-thinning becomes stronger in the highly structured systems (with larger k) and the onset of shear-thinning shifts to higher shear rates with a more flexible interface (Pätzold and Dawson 1996). This can be understood by picturing two Newtonian fluids separated by an ideal interface with a low bending modulus and high topology adaptation (i.e. ability to adjust to the flow). Then the mixture will behave Newtonian as well. In contrast, microemulsions with large bending modulus possessing long-range interactions tend to have large zero-shear viscosities and shear-thinning characteristics.

The common practice to describe the shear thinning behavior of complex fluids is to use the Cross model (Cross 1965),

$$\frac{\eta(\phi, \dot{\gamma}) - \eta_{\infty}(\phi)}{\eta_0(\phi) - \eta_{\infty}(\phi)} = \frac{1}{1 + \left(\alpha \frac{\dot{\gamma}}{\dot{\gamma}_h}\right)^{P_{\alpha}-1}}, \quad (4.10)$$

where concentration-dependent low- and high shear rate viscosities (η_0 and η_{∞} respectively) set the limits of apparent viscosity, η . η_{∞} is often close to the viscosity of the solvent or continuous phase (de Kruif et al. 1985). Unless a rheology alteration method is employed (next section), $\alpha=1$. For flow simulations of interest in this research, all types of microemulsions may be present and a formulation to adequately compute η_0 and η_{∞} is essential. While η_0 is obtained from Equation (4.8), estimating η_{∞} is not straightforward since it depends on the type of the microemulsion, its composition, its microstructure and its internal interactions. To demonstrate this dependency, a comparison was made using the experimental steady-shear viscosity of two bicontinuous microemulsions with $\phi_o \sim 0.4$ (Walker 2011) with more crowded dispersions (Figure 4.3). The dispersions are of hard-sphere (Cheng et al. 2011), charged-stabilized (Foss and Brady 2000; Van der Werff and De Kruif 1989), and polymer brush-stabilized (Wagner and Brady 2009) types. Since the experimental data are reported as a function of shear rate, the generalized Stokes-Einstein equation (Cheng et al. 2002; Cebula et al. 1981; Evilevitch et al. 2001) was used to calculate the Péclet number $Pe = 6\pi\eta_0 a \dot{\gamma} / k_B T$ at the low shear limit. a and $\dot{\gamma}$ are the particle radius and shear rate, respectively. The calculations yielded $D_s^L \sim 10^{-14} \text{ m}^2/\text{s}$, which is typical for dispersions with $\eta_0 \sim 1000 \text{ cP}$. The microemulsion samples are characterized with large zero-shear viscosities and possess long-range features. This can be inferred from the extent that

microemulsions retained their viscosity despite their lower crowding compare to the dispersions. As expected, dispersions with higher particle concentration and interacting potentials better retain viscosity with Péclet numbers due to excluded volume interactions as it would be the case of droplet microemulsion.

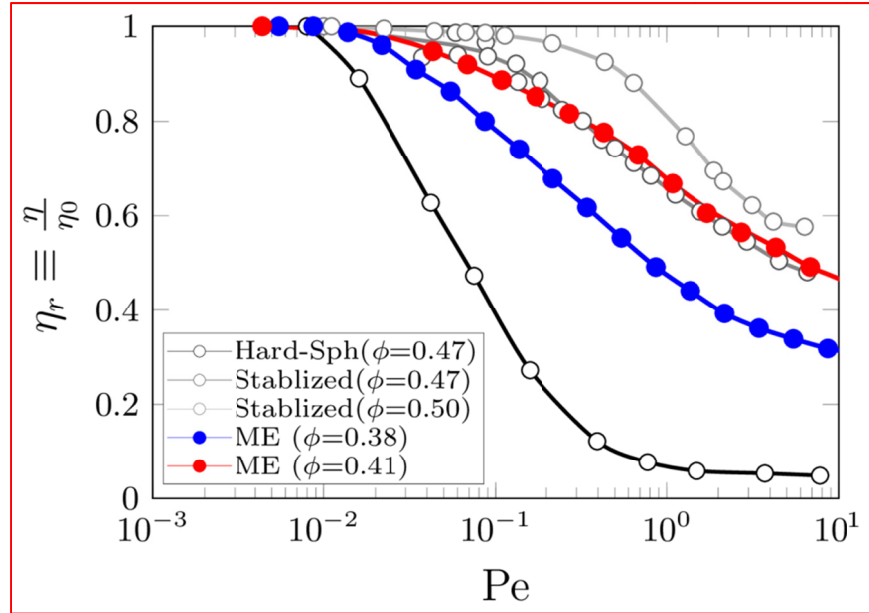


Figure 4.3: Comparison of normalized experimental steady shear viscosity of dispersions and microemulsions (ME) as a function of Péclet number. Dispersion data are characterized as Brownian with $\phi = 0.47$ (Cheng et al. 2011), charge stabilized with $\phi = 0.47$ (Foss and Brady 2000; Van der Werff and De Kruif 1989), and stabilized by polymer brush with $\phi = 0.5$ (Wagner and Brady 2009). Microemulsion data are adapted from (Dustin Walker 2011). Despite their lower concentration, microemulsions behave similar to hard-spheres. All lines are for eye-guidance.

Trivially in dilute O/W microemulsion $\eta_\infty \sim \mu_w$ while in dilute W/O case $\eta_\infty \sim \mu_o$. However, in the concentrated regions a rough approximation should be employed. A useful, but empirical, approximation may be defines as

$$\eta_\infty = (\phi\mu_o + \phi'\mu_w)(f_0 + f_1), \quad (4.11)$$

where the trivial solvent viscosities are obtained in the O/W and W/O dilution limits and correction terms f_0 and f_1 qualitatively represent the hydrodynamic and thermodynamic interactions, respectively. f_0 and f_1 may be in any form but the following forms are shown to be useful:

$$f_0 = (1 - \phi\phi')^{\nu}, \quad (4.12)$$

$$f_1 = c(\phi\phi'[0.1 + (\phi - \phi_m)(\phi' - \phi_m)])^2. \quad (4.13)$$

c in Equation (4.13) is a constant, scaling the interactions. Even though Equations (4.11-14) are rough approximations, they make the application of the Cross model possible for the entire range of ϕ which is essential for the flow simulation of microemulsions where phase type varies. The final remark of this section is to point out that microemulsions may experience the disordered-to-ordered transition of microstructure at high shear rates (Harting et al. 2007; Tanaka et al. 2006), which could add more complexity to the calculations.

4.2.3 Effects of Co-solvent, Branched Co-surfactant, and Temperature

Rheology alteration methods break the long-range interactions in microemulsions and cause the interface to be more flexible. The stress relaxation in a microemulsion is governed by its microstructure, which in turn is mainly determined by the interface bending and saddle-splay moduli. The bending modulus (k) measures the energy cost of bending while the saddle-splay modulus (\bar{k}) measures the difficulty in making saddle-splay features. Co-solvents are very efficient in modifying both moduli and hence in reducing the zero-shear viscosity and shear-thinning characteristics, if any, of

microemulsions. The addition of branched co-surfactant favors the creation of saddle-splay features while a modest increase in temperature mainly modifies the bending modulus of the interface. Despite the lower efficiency of branched co-surfactants and temperature variations compared to co-solvent, reducing the zero-shear viscosity and increasing the onset of shear thinning is often observed with these rheology alteration methods.

The net effect of rheology alteration methods can be captured by using parameter α , which is reduced to less than 1 by the rheology alteration methods. The reduction of α translates to less dependency of the apparent viscosity on shear rate and hence to increase of onset of the shear thinning. Note that in the case of an efficient co-solvent, α is zero, which corresponds to Newtonian behavior. Lacking sufficient experimental data, we speculate that α would vary with co-solvent/branched co-surfactant concentration as shown schematically in Figure 4.4.

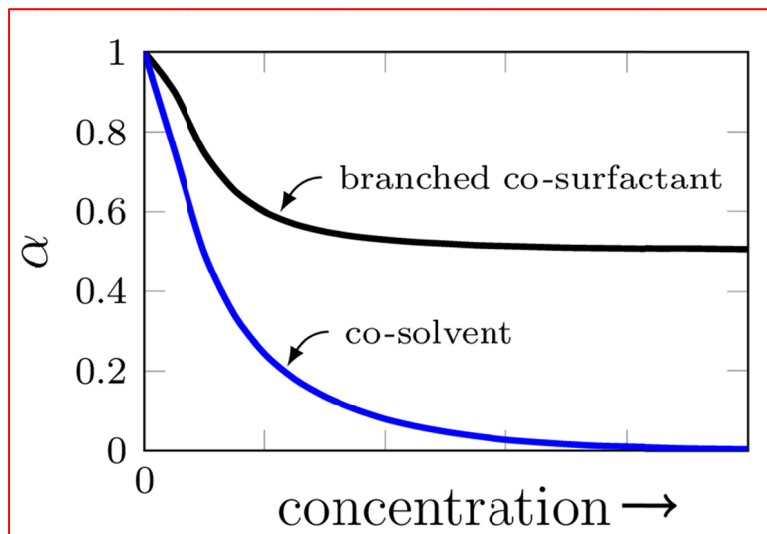


Figure 4.4: Increase of onset of shear-thinning behavior by the addition of co-solvent and/or branched co-surfactant. In the presence of enough good co-solvent the sample loses its rheology dependency to shear rate (i.e. $\alpha = 0$) and behaves Newtonian.

4.3 RESULTS

To validate the model presented in the preceding section, comparisons were made between the model and the experimental data of Walker (2011) and Lu et al. (2013) (Table 4.1). Walker measured the microemulsion viscosity for four different samples designated A, B, C and D. The primary surfactant in all four samples was TDA-12EO-sulfate and the co-surfactant was twin-tailed C₁₉₋₂₃ internal olefin sulfonate (IOS). The combined surfactant and co-surfactant concentration was 0.3 wt%. Iso-butyl alcohol (IBA) co-solvent was added to sample B and Triethylene glycol monobutyl ether (TEGBE) co-solvent was used in sample C. Sample D is the same as A, but the temperature was raised to 85 °C. Table 4.2 shows the composition of the brine used in the Walker (2011) samples. The parameters used in the model calculations are summarized in Table 4.3. The Lu et al. (2013) formulation contained C₁₃₋₁₃PO-sulfate as the primary surfactant and C₂₀₋₂₄ internal olefin sulfonate (IOS) as the co-surfactant.

Figure 4.5.a compares the measured and calculated apparent viscosity for samples A, B, and D. Note that by changing salinity, a number of samples were created with each of the formulations. The shear rate is fixed at 100 s⁻¹ so the viscosity build-up with the droplet crowding and finally phase-type shift from oil-in-water to Type III becomes evident. Figure 4.5.b shows the steady-shear viscosity of samples with a $\phi \sim 0.4$. Note that each sample represents one subset. Subset 1 is characterized by large viscosities and shear thinning behavior at crowded Type I and Type III phases. Addition of a co-solvent to the formulation greatly reduces the viscosity and results in a Newtonian-like behavior, as evident by subset 2 and samples “B” and “C” behavior. Subset 4, which is

characterized by a higher temperature, shows a behavior similar to the subset 1. The viscosity values are, however, shifted to much lower values as the oil viscosity itself decreases by a factor of ~ 3 and the onset of shear-thinning is shifted to higher shear rates. A 3D image of the microemulsion rheology is shown in Figure 4.7 based on the Walker (2011) data.

The Lu et al. data and the model calculations are presented in Figure 4.6. The variation of viscosities as phase type shifts from dilute Type I to Type III to Type II is shown in Figure 4.6.a. In the dilute regions the rate of viscosity build-up is small, whereas in the concentrated regions the rate is large due to percolation. Unlike dispersions, microemulsions retain finite viscosities by adapting a bicontinuous microstructure. The asymmetry in the viscosity curve is a result of difference in micelle coverage in Types I and II (charged and shell respectively). It is evident from Figure 4.6.b that the dilute samples are Newtonian while bicontinuous ones show shear thinning behavior.

Table 4.1: Differences of the microemulsion samples

	Sample(s)	Amphiphilic Formulation (%wt)	Oil/Brine	T (°C)	Oil Viscosity (cP)
Walker (2011)	A	0.1% TDA-12EO SO ₄ ⁻ 0.2% C ₁₉₋₂₃ IOS ^{**}	O1/SSRB [*]	55 °C	68
	B	0.1% TDA-12EO SO ₄ ⁻ 0.2% C ₁₉₋₂₃ IOS ^{**} 1% IBA ^{***}	O1/SSRB	55 °C	68
	C	0.1% TDA-12EO SO ₄ ⁻ 0.2% C ₁₉₋₂₃ IOS ^{**} 1% TEGBE ^{****}	O1/SSRB	55 °C	68
	D	0.1% TDA-12EO SO ₄ ⁻ 0.2% C ₁₉₋₂₃ IOS	O1/SSRB	85 °C	25
Lu et al. (2013)	all	0.5% C ₁₃₋₁₃ PO SO ₄ ⁻ 0.5% C ₂₀₋₂₄ IOS 2% IBA; 0.5% Na ₂ CO ₃	O2/NaCl	38 °C	~5

^{*} Softened synthetic reservoir brine
^{**} Internal olefin sulfonate
^{***} Iso-butyl alcohol
^{****} Triethylene glycol monobutyl ether

Table 4.2: Softened synthetic reservoir brine used in Walker (2011) samples

Ion	Concentration (ppm)
Na ²⁺	12,429
HCO ₃ ⁻	793
SO ₄ ²⁻	12
Cl ⁻	18,700
Total salinity	31,934

Table 4.3: Model parameters

	Subset	ν	m	$\dot{\gamma}_h$	c_{int}	ϕ_m
Walker et al.	1	2.5	1.7	6	8000	0.35
	2	0.3	1.7	6	500	0.47
	3	0.3	1.7	6	30	0.47
	4	2.1	1.7	7	4800	0.33
Lu et al.	1	2	1.8	50	2000	0.45

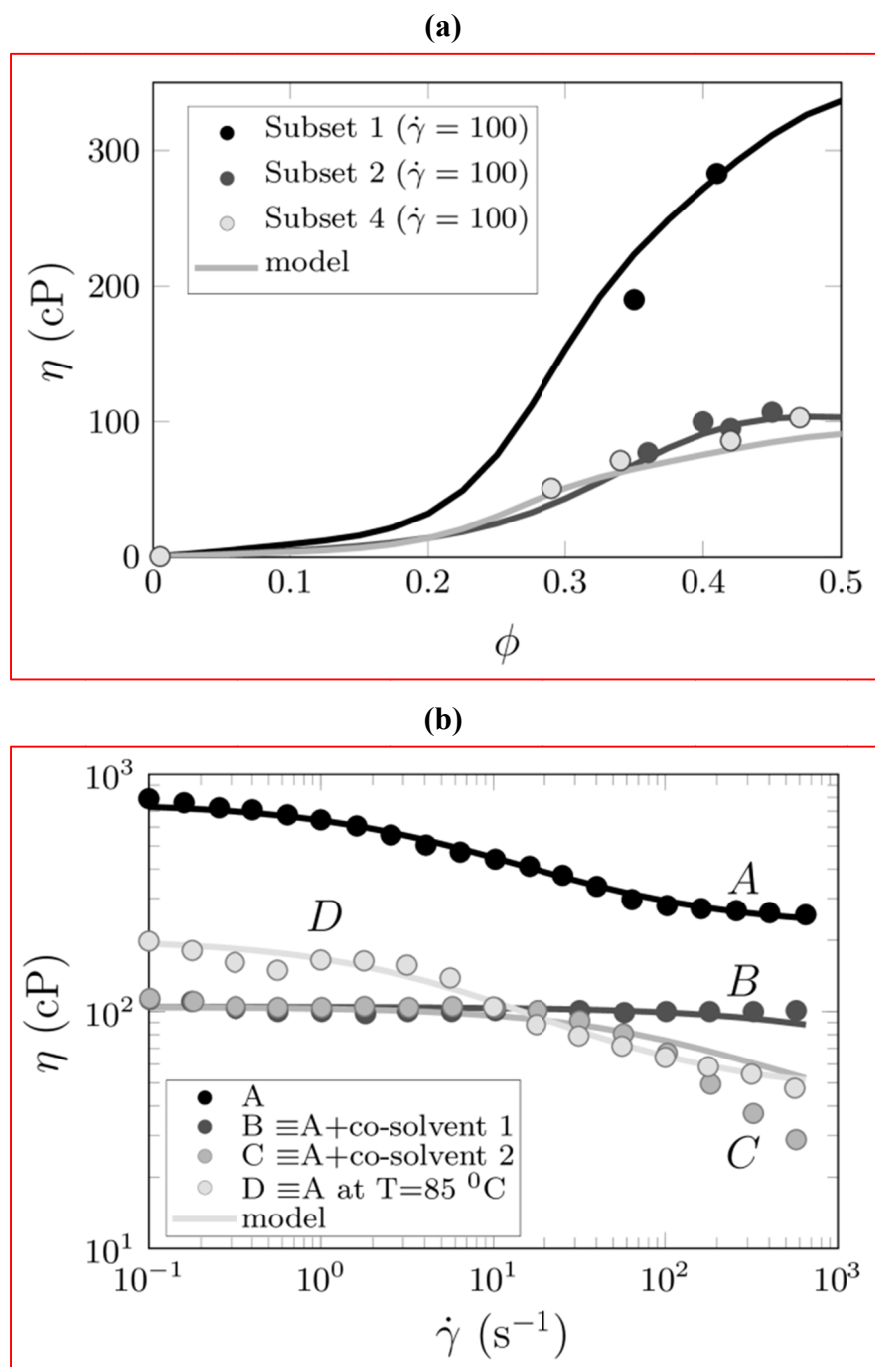


Figure 4.5: Comparison of calculated and measured apparent viscosity. The experimental data are adapted from (Dustin Walker 2011). (a) Apparent viscosity versus oil volume fraction in microemulsion at $\dot{\gamma} = 100 \text{ s}^{-1}$. (b) Steady-shear rheology of microemulsion samples with $\phi_o \sim 0.4$. Note that each sample represents a different subset here. Within each subset, salinity is the only variable to create the phase shift. Sample “A” is created by only using surfactant at $55 \text{ }^\circ\text{C}$, while samples “B” and “C” contain 1 wt% co-solvent. Sample “D” contains no co-solvent but the temperature was raised to $85 \text{ }^\circ\text{C}$.

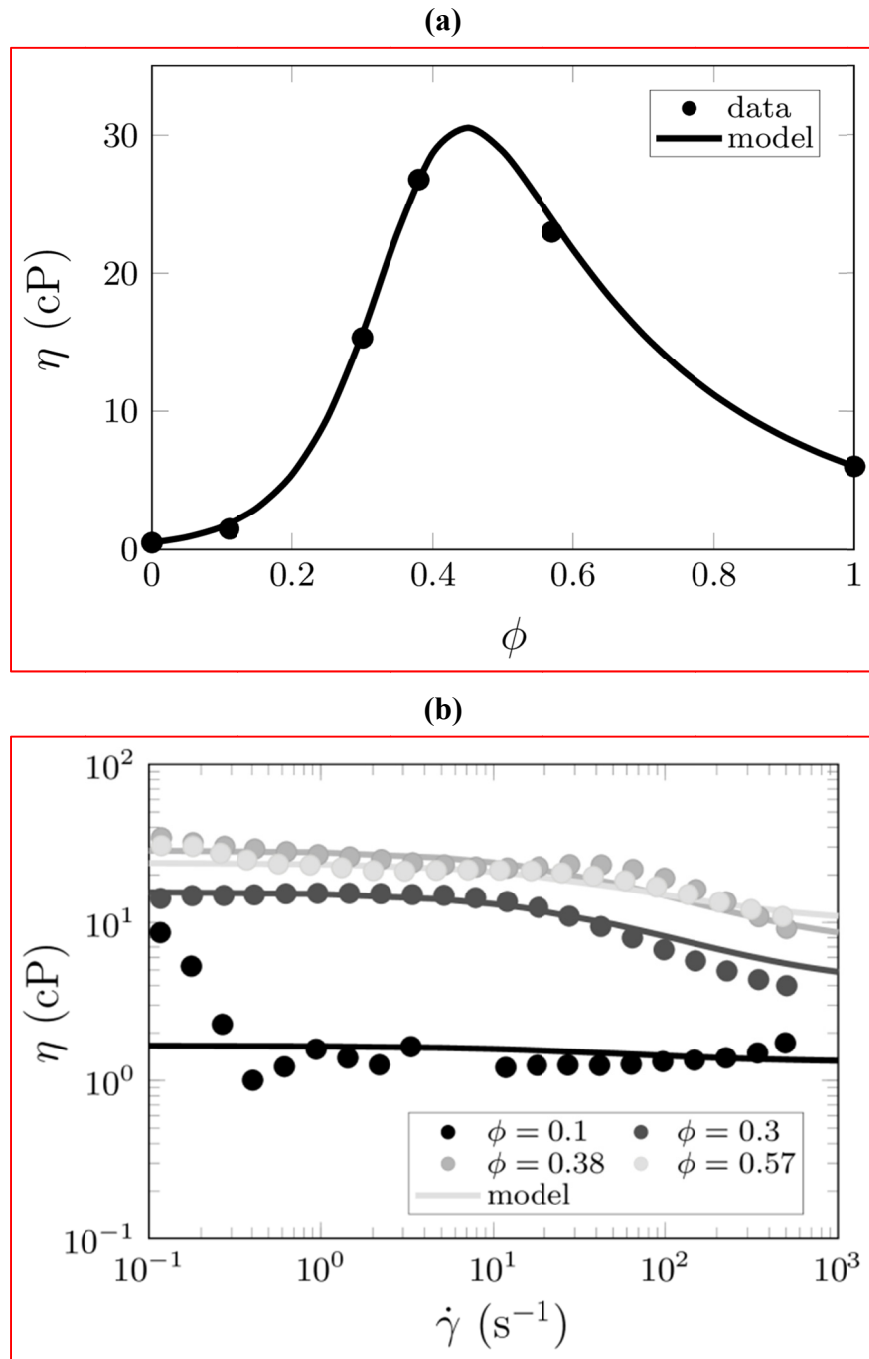


Figure 4.6: Comparison of calculated and measured apparent viscosities for data from (Lu et al. 2013). (a) Apparent viscosity versus oil volume fraction in microemulsion at $\dot{\gamma} = 10 \text{ s}^{-1}$. (b) Steady-shear rheology of microemulsion samples with different oil volume fractions. Since the phase shift is caused by only varying the salinity, only one set of model parameters are adequate to describe the behavior of all the samples.

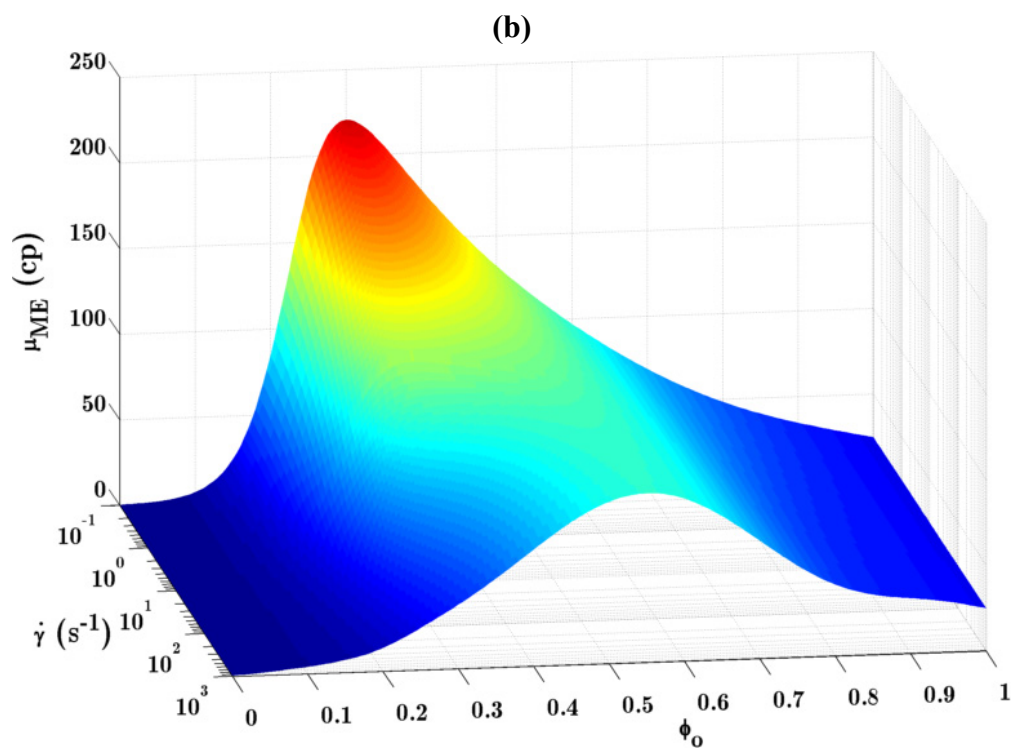
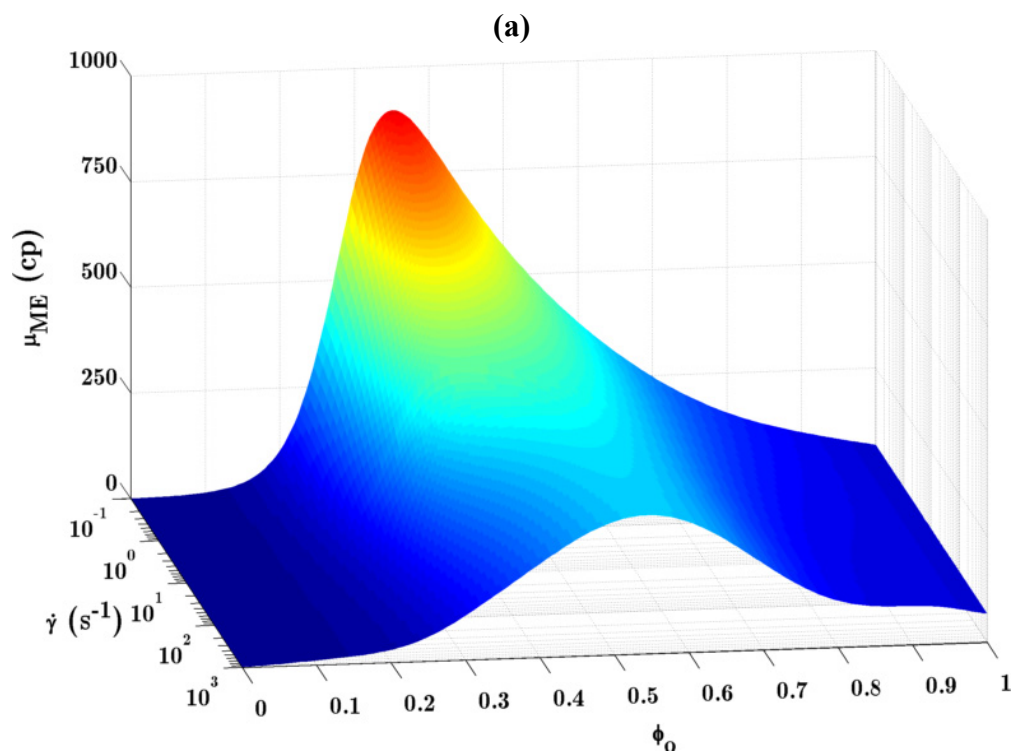


Figure 4.7: (full caption next page)

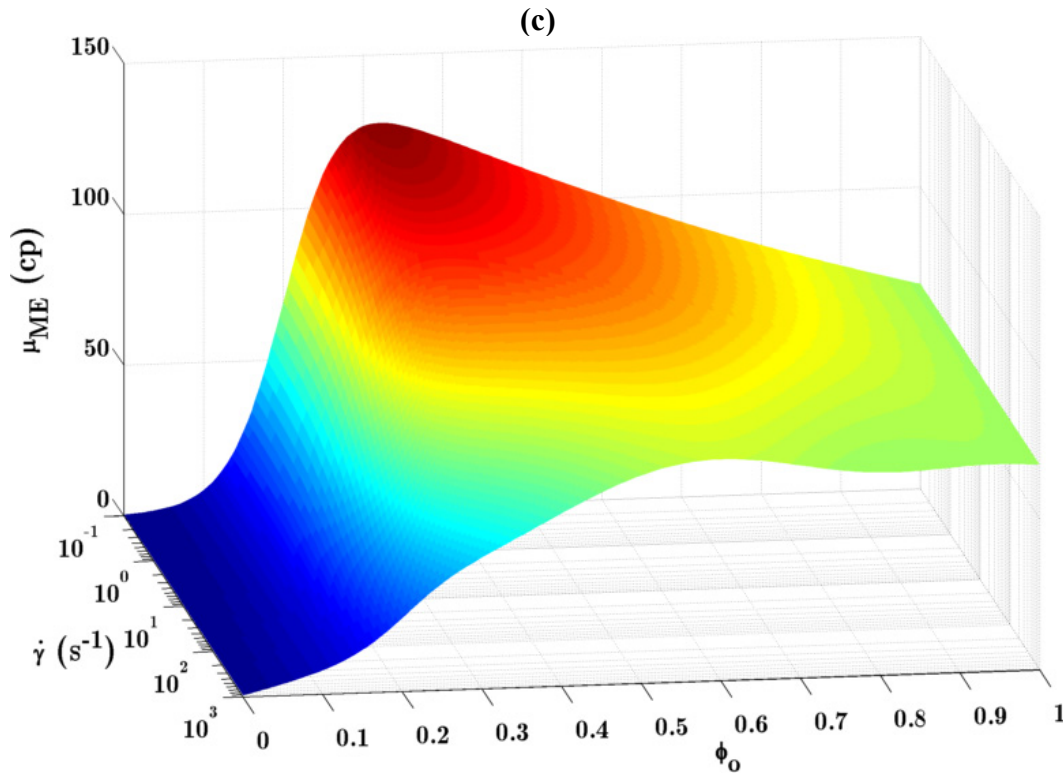


Figure 4.7: Example 3D microemulsion rheology versus shear rate and ϕ based on Walker et al. (2012; Dustin Walker 2011) data.

In spite of the similarities in the rheology behavior presented in Figures 4.5 and 4.6, subtle differences are evident. For example, note the differences in the onset and severity of the shear thinning behavior of the concentrated samples. The observed behavior confirms that shear thinning is more profound in the highly structured microemulsions and the onset of shear-thinning shifts to higher shear rates with a more flexible interface and smaller values of λ_r . Despite its simple form, the model presented here captures these features. Additionally, ν used in the model to fit the data shows an interesting trend with the maximum zero-shear viscosity, η_{0m} ; which is η_0 at ϕ_m . η_{0m} is system dependent and therefore is normalized by the oil viscosity for consistency in

comparing different experimental data. Figure 4.8 shows plots the experimental data versus ν . As ν increases, the maximum zero-shear viscosity becomes larger. This behavior also confirms that $\nu \propto k/k_B T$ as suggested before. It is interesting to note that, for example, sample “A” has a large $\nu = 2.5$ while $\nu = 0.3$ for samples “B” and “C” that contain co-solvent.

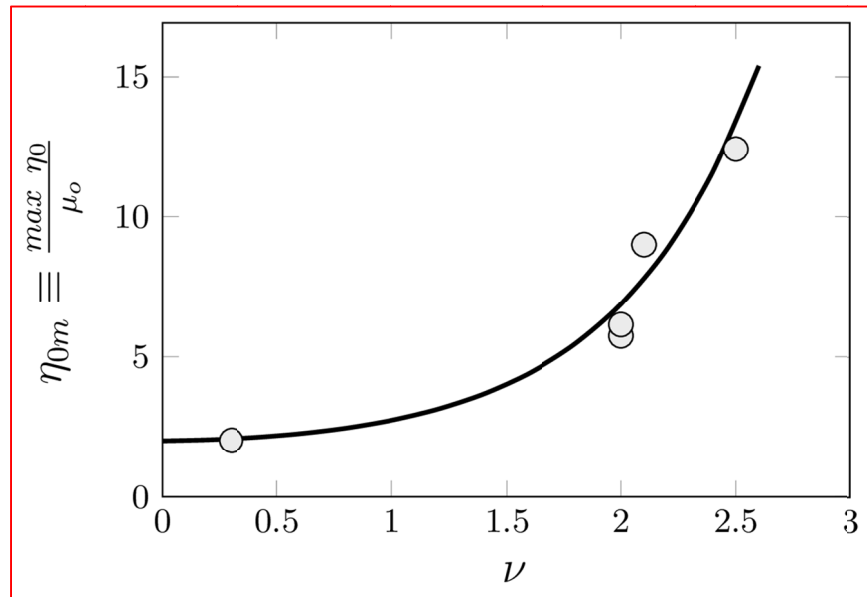


Figure 4.8: Variation of maximum zero-shear viscosity, η_{0m} , as a function of the intrinsic interface property, ν . η_{0m} values are experimental data and ν is the relevant model parameter. Note that ν closely resembles the interface bending modulus, k , and it varies between $0.3 \leq \nu \leq 2.5$.

Chapter 5: Microemulsion Rheology in the Presence of Polymer

The microemulsion viscosity model described in the previous chapter was next expanded to include water-soluble polymer. This model was then implemented in UTCHEM, a multicomponent and multiphase chemical flooding simulator developed by The University of Texas at Austin (Bhuyan et al. 1990; Delshad et al. 1996, 2011; Mohammadi et al. 2009). Then several corefloods showing the large impact of microemulsion viscosity on ACP flooding performance were modeled.

5.1 SURFACTANT/POLYMER INTERACTIONS IN AQUEOUS SOLUTION

A stable aqueous surfactant solution remains clear and single phase at equilibrium. However, increasing salinity of anionic surfactants causes a phase separation. The onset salinity of phase separation evident by solution cloudiness is called the aqueous stability limit or critical electrolyte concentration (CEC) (Pope et al. 1982). Adding polymer to the surfactant solution usually lowers the aqueous stability limit. The phase separation at high salinities (i.e. higher than CEC) is one of two types: associative or segregative (Holmberg 2003). Associative separation (also known as coacervation) results from strong attractions where segregative separation occurs in the lack of attractions (Figure 5.1). For the case of the typical polymers and surfactants used in chemical EOR, the separation is often segregative, which results in the formation of surfactant-rich and polymer-rich phases (Pope et al. 1982).

The cloudiness of a phase-separating solution is attributed to the formation of the connected micellar network (Holmberg 2003) (Figure 5.2). At these salinities the packing parameter of the surfactant is $\frac{1}{3} < \frac{v}{a_0 l_c} < 1$ and branched cylindrical micelles form. The surfactant-rich phase that ultimately forms could have the microstructure of a lamellar or cubic phase (Figure 5.3). Polymer generally shifts the onset of phase separation to lower salinities (Figure 5.4). This could be explained by noticing that the presence of polymer often facilitates the formation of micellar aggregates (Figure 5.5) with a critical association concentration (CAC) smaller than the critical micelle concentration (CMC). The CAC occurs at the onset of surfactant association to the polymer (i.e. binding) and CMC is the onset of micelle formation.

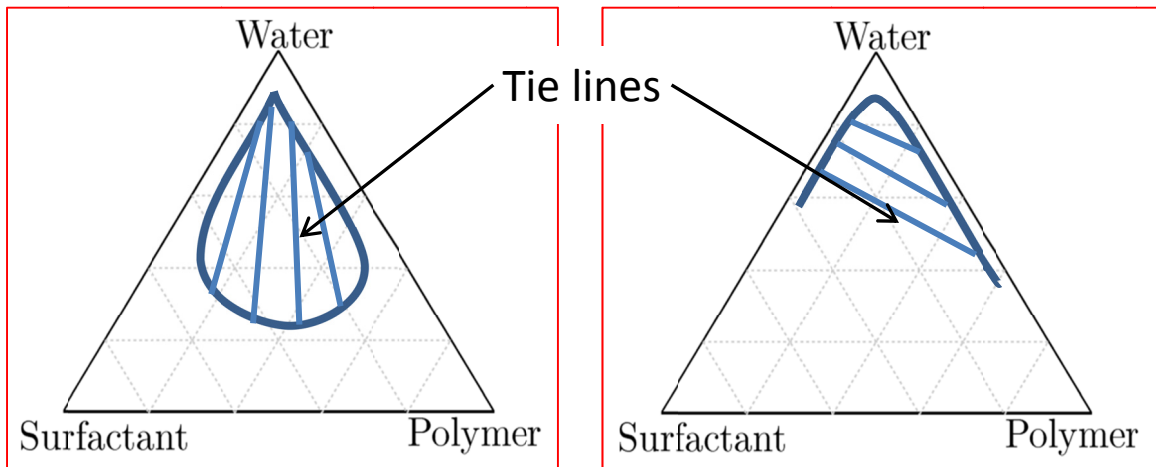


Figure 5.1: Associative (left) and segregative (right) surfactant/polymer phase separation at salinities higher than aqueous solubility limit, adapted from Holmberg (2003).

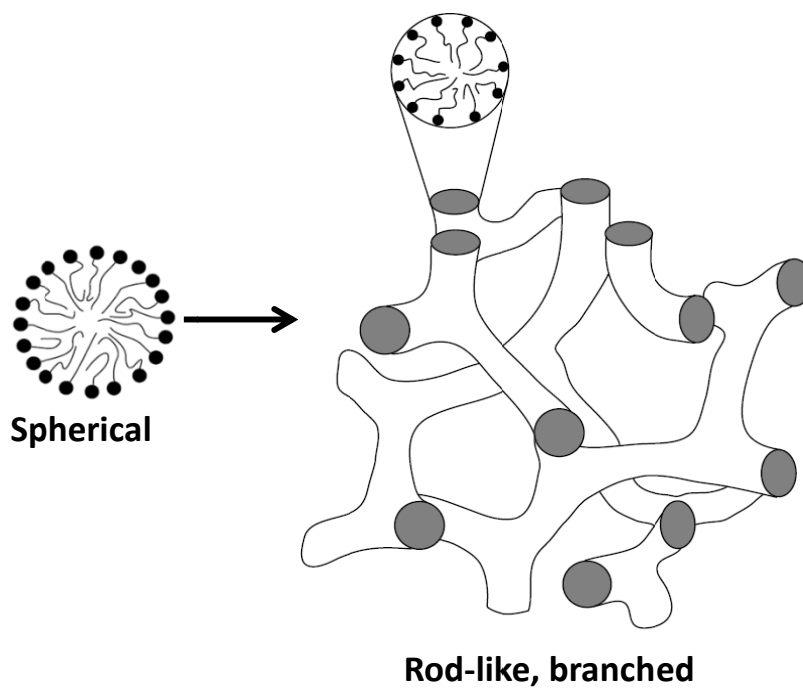


Figure 5.2: Formation of branched micelles in a cloudy solution (Holmberg 2003).

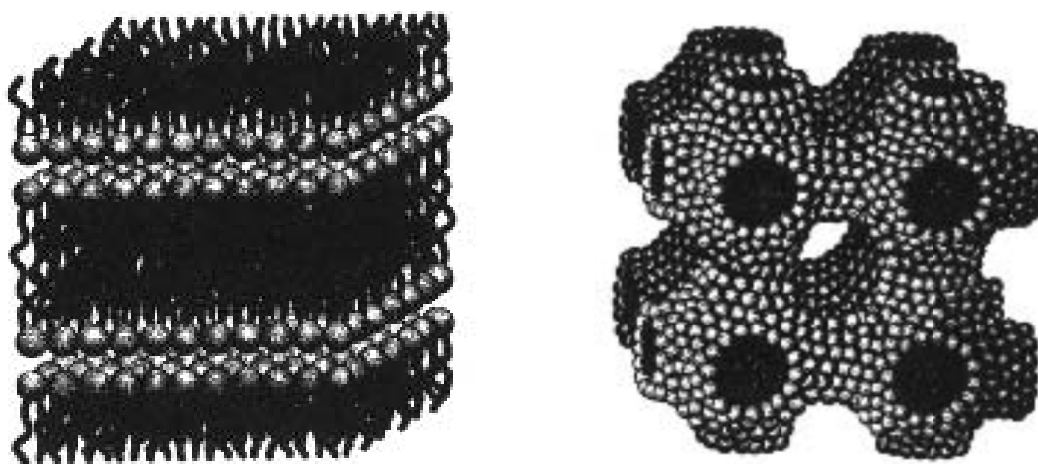


Figure 5.3: Lamellar (left) and cubic (right) phase microstructures (Holmberg 2003).

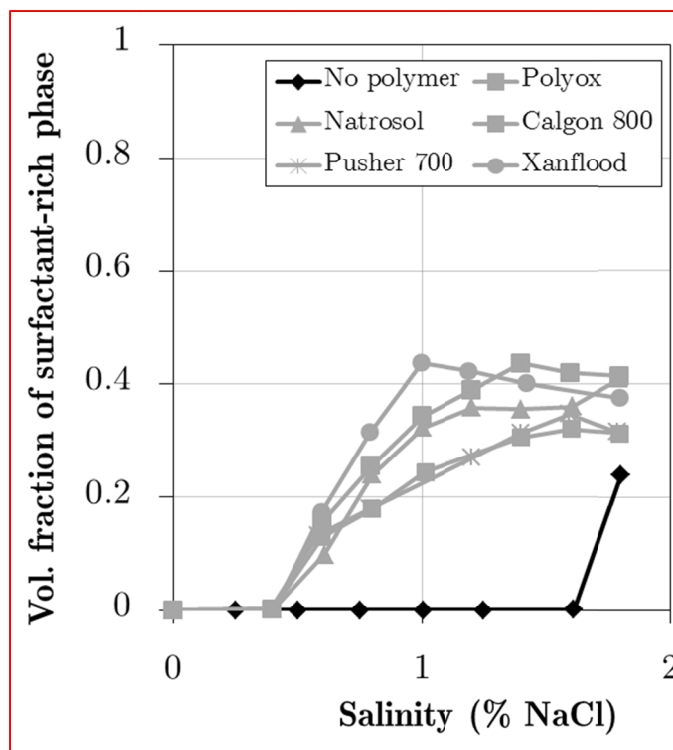


Figure 5.4: Onset salinity of phase separation is shifted to the left in the presence of polymer (Pope et al. 1982).

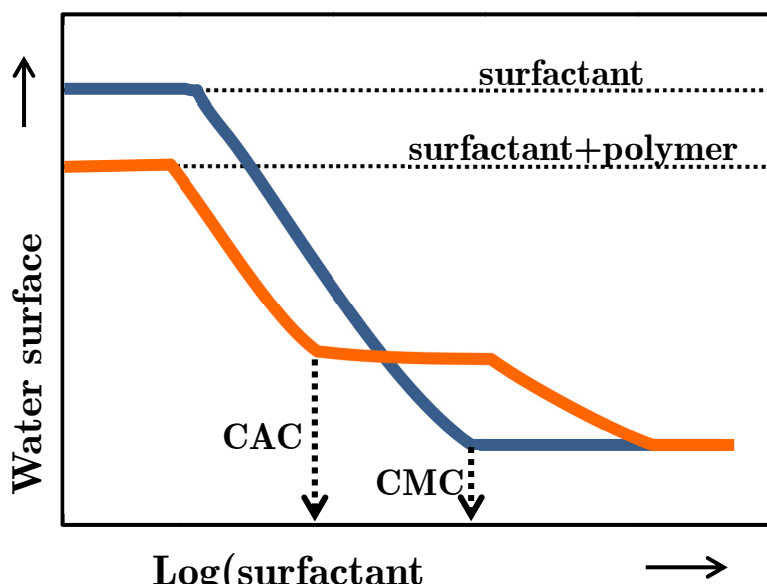


Figure 5.5: Schematic graph of water surface tension in the presence of polymer (Holmberg 2003).

5.2 SIZE OF POLYMER COIL

Polymer coils adjust their size with salinity (Sorbie 1991). The coil size can be expressed by the radius of gyration, R_g , which is the root mean square distance of any point in the coil from its center of mass (Teraoka 2002). In this context, a polymer coil roughly occupies a sphere of radius equal to R_g .

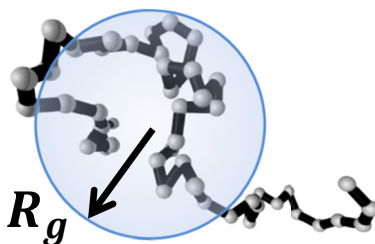


Figure 5.6: radius of gyration of a polymer coil.

The radius of gyration is typically a strong function of polymer molecular weight and can be expressed as

$$R_g \cong a\bar{M}^b, \quad (5.1)$$

where \bar{M} is the average molecular weight of the polymer molecule and a and b are constants. In order to investigate if Equation (5.1) holds for polyacrylamide, radius of gyration data for polyacrylamide polymer and polyacrylamide co-polymers (Table 5.1) were collected from the literature (Ball and Pitts 1984; Jia et al. 2009; Mihcakan and C.W. 1986; Omari et al. 1989). Figure 5.7 shows that there is indeed a power-law correlation between the radius of gyration and molecular weight for these polymers. However, at a fixed molecular weight, R_g also varies with salinity and degree of hydrolysis (COO- fraction).

Table 5.1: Polyacrylamide gyration radius data

Polymer	Molecular weight, \bar{M}	Gyration Radius (<i>nm</i>)	Salt concentration (<i>gr. l⁻¹</i>)
PAM ^a	36×10^6	640	–
PAM ^a	36×10^6	480	15 <i>Na₂CO₃</i>
PAM ^a	17×10^6	440	–
PAM ^a	17×10^6	350	15 <i>Na₂CO₃</i>
HPAM 30% ^b	14×10^6	300	–
PAM ^c	7.3×10^6	150	20 <i>NaCl</i>
HPAM 30% ^c	7×10^6	190	20 <i>NaCl</i>
PAM ^a	6.5×10^6	270	–
PAM ^a	6.5×10^6	240	15 <i>Na₂CO₃</i>
PAM ^c	6.35×10^6	210	20 <i>NaCl</i>
PAM ^c	4.8×10^6	110	20 <i>NaCl</i>
PAM ^c	4.5×10^6	100	20 <i>NaCl</i>
PAM ^c	2.1×10^6	70	20 <i>NaCl</i>
PAM-AMP ^d	0.23×10^6	19.7	–
PAM-AMP ^d	0.09×10^6	11.1	–

^aBall, J.T. and Pitts, M.J. (1984); ^bMihcakan, I.M. and C.W., V. (1986); ^cOmari, A., et. al., (1989); ^dJia, Z.-P., et. al., (2009).

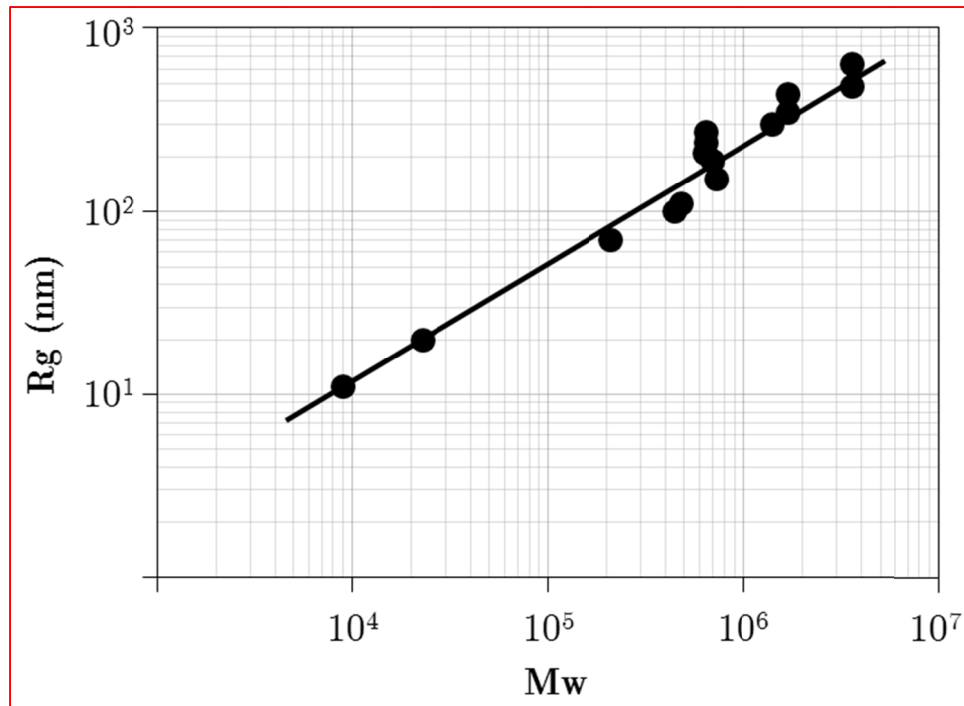


Figure 5.7: Polyacrylamide gyration radius in brine versus its molecular weight. The data are adapted from (Ball and Pitts 1984; Jia et al. 2009; Mihcakan and C.W. 1986; Omari et al. 1989).

5.3 POLYMER PARTITIONING IN MICROEMULSION SYSTEMS

HPAM and PAM-co-AMPS polymer coil shrinkage in brine at higher salinities is well understood. In microemulsions (i.e. oil is present), however, their behavior is affected by the presence of amphiphilic molecules. The surfactant-polymer (SP) compatibility should be established through aqueous stability tests prior to use in chemical EOR. Once the SP compatibility is established, the behavior of polymer is very similar to its behavior in brine. Polymers used in chemical EOR are water-soluble and therefore would be expected to be compatible with Type I microemulsions since they are water external. However, near the transition to Type III behavior, a polymer-rich phase sometimes forms that is not present without polymer. For Types III and II

microemulsions, the polymer partitions between the excess water and microemulsion. The extent of partitioning is governed by the size of the polymer coil and microemulsion characteristic domain size. Kabalnov et al. (1996) defined the polymer partition coefficient as

$$\chi \stackrel{\text{def}}{=} \frac{C_p^{ME}}{C_p^W}, \quad (5.2)$$

where C_p^W and C_p^{ME} are the polymer concentrations in water and the water domains of the microemulsion, respectively. By definition, χ is $0 \leq \chi \leq 1$ where $\chi = 1$ means equal partitioning between excess brine and the brine in the microemulsion. In UTCHEM notation, Equation (5.2) becomes $\chi \stackrel{\text{def}}{=} C_{p3}/C_{p1}$. Kabalnov et al. showed that for a balanced⁴ C12E5-water-decane-dextran microemulsion, if the polymer molecule size is greater than 50 nm the partitioning is essentially zero (Figure 5.8).

The extent of partitioning can also be inferred from viscosity measurements. For example, Pope et al. (1982) measured the viscosity of microemulsions formed from octane-brine-TRS1080⁵ surfactant, with and without the presence of a xanthan gum polymer (Figure 5.9). While the viscosity of the Type I microemulsion was much higher with xanthan gum added, xanthan gum had little effect on the viscosity of Type III and Type II microemulsions. This indicates little partitioning of xanthan gum into Type III and Type II microemulsions and is likely due in part to its rigidity. Based on Figure 5.8, polymer partitioning decreases with an increase in its molecular weight. A schematic depiction of polymer partitioning is given in Figure 5.10.

⁴ Balanced microemulsion is a type III at optimum salinity.

⁵ TRS1080 is an anionic surfactant.

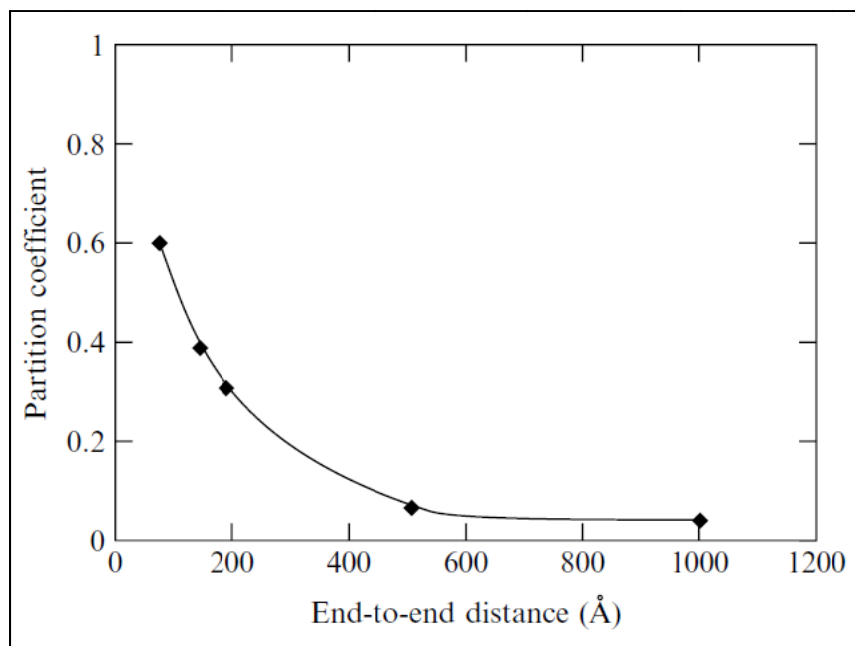


Figure 5.8: Polymer partitioning for a balanced $C_{12}E_5$ -water-decane-dextran microemulsion (Kabalnov et al. 1996).

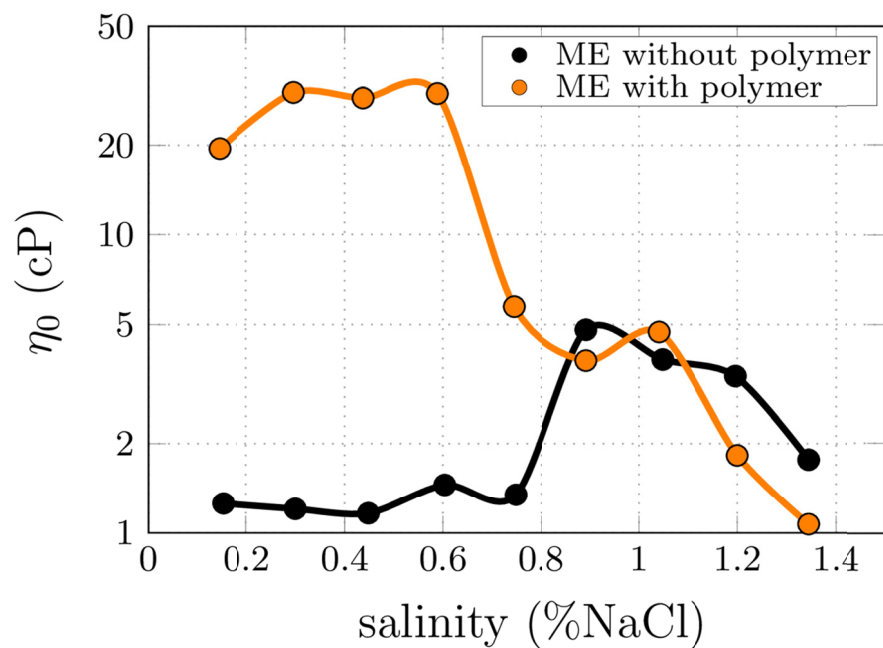
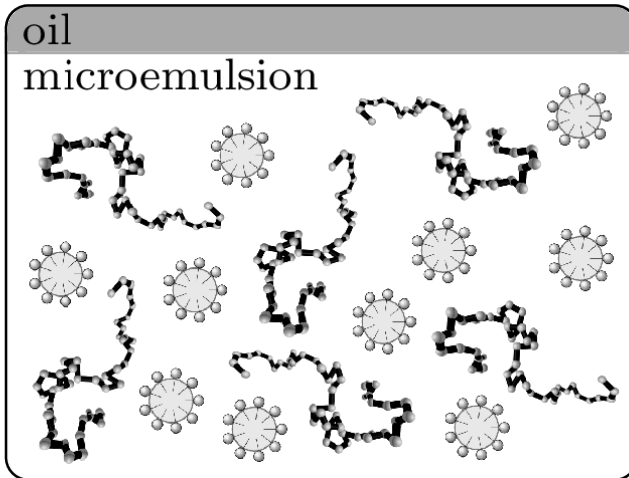
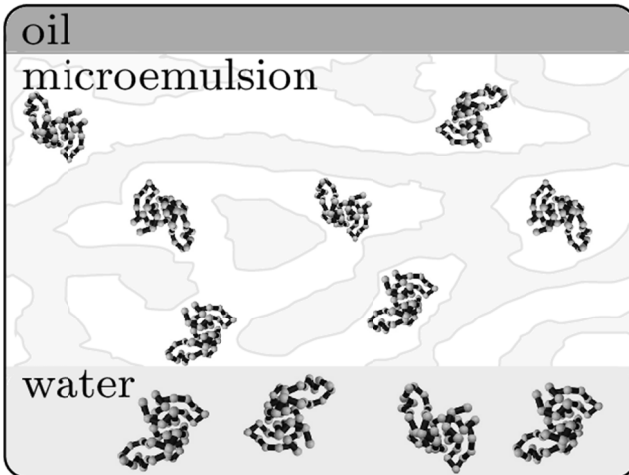


Figure 5.9: Microemulsion viscosity for octane-brine-TRS1080-XANFLOOD system as phase type changes from *Type I* → *III* → *II* (Pope et al. 1982).



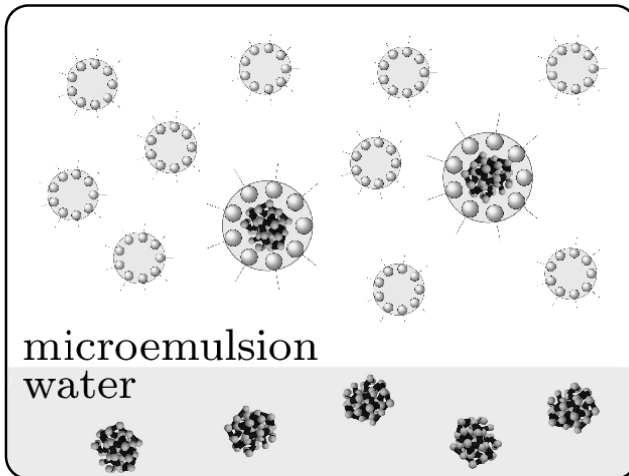
$$R_g \approx 100 \text{ (nm)}$$

$$R_m \approx 20 \text{ (nm)}$$



$$R_g \approx 50 \text{ (nm)}$$

$$\xi \approx 100 \text{ (nm)}$$



$$R_g \approx 20-40 \text{ (nm)}$$

$$R_m \approx 30-50 \text{ (nm)}$$

Figure 5.10: Schematic depiction of polymer-microemulsion microstructure and polymer partitioning as the microemulsion type evolves. Typical polymers used in chemical EOR are only water-soluble and therefore Type I microemulsion contains the entire polymer that is present. In Type III and II systems, polymer partitions between the microemulsion phase and the excess brine. The partitioning is mainly governed by the size exclusion mechanism which implies low partitioning if polymer has a large gyration radius compared to micro-emulsion characteristic domain size.

5.4 INCLUSION OF POLYMER IN THE RHEOLOGY MODEL

Polymer partitioning affects the rheology of microemulsions in a complicated way. To explain this behavior, let us consider the difference in behavior of a Type I microemulsion (no polymer) and a polymer solution (no oil). Increasing salinity causes the formation of more micelles with larger sizes (Figure 5.11.a), which increases the viscosity of the polymer-free microemulsion. On the other hand, an increase in salinity causes a reduction in the viscosity of an anionic polymer solution (no surfactant) due to a decrease in its radius of gyration at higher salinities (Figure 5.11). The combined effect is depicted schematically in Figure 5.11.b.

Increasing salinity eventually leads to the formation of bicontinuous and Type II microemulsions. For these microemulsions, the extent of partitioning, polymer-surfactant interactions, and polymer concentration have an impact on the rheology of microemulsion (Taghavifar et al. n.d.).

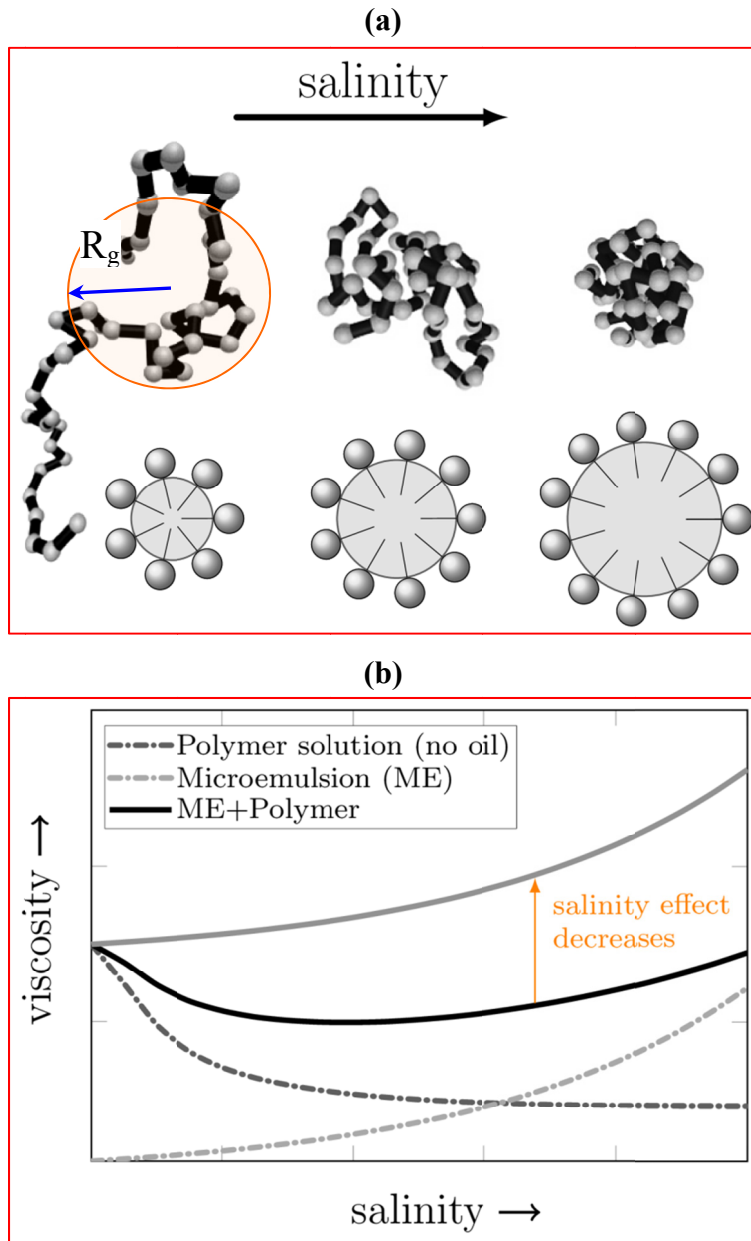


Figure 5.11: (a) Schematic demonstration of salinity effect on the polymer gyration radius and oil-in-water (O/W) micelle size in the Type I salinity window. As salinity increases the polymer coil shrinks while the micelle size grows. (b) Schematic illustration of the effect of polymer on the zero-shear viscosity of a Type I microemulsion. Without the polymer, the viscosity of the microemulsion increases with increasing salinity as more oil is solubilized in microemulsion. Addition of a polymer to the microemulsion system shifts the viscosity curve to higher values assuming negligible polymer/surfactant interactions and no salinity effect on the polymer coil. In reality, however, the polymer coil collapses as the salinity increases which results in vanishing polymer effect. Therefore the polymer-microemulsion viscosity behavior is a tradeoff between the gain of viscosity by solubilizing more oil and loss of viscosity from polymer coil collapse.

There are two methods to model the effect of polymer on the rheology of microemulsions. If the partitioning of the polymer between the equilibrium phases is known, then simply replacing the viscosity ratio in Equation (4.8) according to Equation (5.3),

$$\lambda_{rp} = \frac{\mu_o}{\mu_p}, \quad (5.3)$$

would be sufficient. In Equation (5.3), μ_p is the polymer solution viscosity at the salinity and polymer concentration in the water domains in the microemulsion. This method is very useful when the polymer viscosity and partitioning is known. If the polymer partitioning is not known a priori, an amalgamation model can be used for the viscosity calculations. Let us assume polymer solution is a “simple” fluid with the viscosity of μ_p . By “simple” we mean it does not have a microstructure and its viscosity is fairly independent of salinity, similar to water. If instead of water the microemulsion samples are prepared with this simple fluid, then Equation (4.8) can be used to calculate the viscosity of microemulsion. However, the polymer solution does have a microstructure in which polymer coils expand and shrink according to the salinity. Now let us assume that under exaggerated impact of salinity, the polymer coils collapse to spheres of virtually zero radius. In this case the polymer solution is identical to water and the typical viscosity behavior of microemulsions with water is retrieved. Experimental results have shown that the behavior is in between that of these two hypothetical cases (Figure 5.12). Therefore the zero-shear viscosity can be model by the effective partitioning parameter, δ , as follows:

$$\eta_0 = (1 - \delta)\eta_{0|\lambda_{rw}} + \delta\eta_{0|\lambda_{rp}}, \quad (5.4)$$

where $\eta_{0|\lambda_r}$ is the zero-shear viscosity at λ_r ; $\lambda_{rw} \equiv \mu_o/\mu_w$ and $\lambda_{rp} \equiv \mu_o/\mu_p$. Note that λ_{rw} and λ_{rp} are associated with hypothetical “exaggerated salinity-effect” and “no salinity-effect” cases, respectively. δ for the typical polymers could be obtained as follows:

$$\delta = (1 - \phi)^{\frac{|s_p|}{\delta_0^5}}, \quad (5.5)$$

where s_p is the typical salinity parameter of polymeric solution viscosity model and $\delta_0 \sim 0.5$ is the fraction of the polymer that partitions into the microemulsion at optimum salinity. Typically $\delta \sim 10$ and it ranges from 5 to 15.

To demonstrate the capability of the model, a comparison with experimental data is shown in Figure 5.13 where the viscosity of a number of microemulsions was measured with and without the presence of polymer. The chemical formulation used in the sample preparation is given in Table 5.2. The samples are created by a Na_2CO_3 scan. The polymer was hydrolyzed polyacrylamide FP 3330S. The polymer concentration was 3000 ppm. As seen in Figure 5.13, the viscosity in the Type I and early Type III regions is higher with polymer than without polymer. However, the viscosity is the same with and without polymer in the optimum type III region and beyond. This behavior can be attributed to low polymer partitioning in these regions.

Table 5.2: Chemical formulation for Upamali (2014) microemulsion samples

Chemical Formulation	Oil	T (°C)	Oil Viscosity (cP)
0.65% C ₂₈ -25PO-45EO COO ⁻ 0.4% Enordet 0332 45% Enordet 0392; 1% EDTA	O3	78 °C	~7

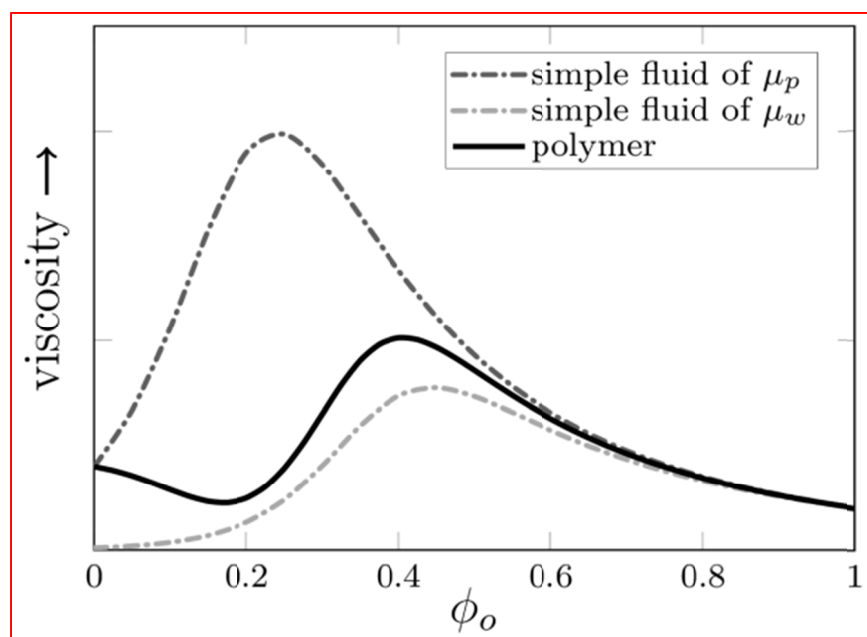


Figure 5.12: Viscosity of polymer-containing microemulsion is a non-linear combination of two hypothetical cases: “no salinity-effect” and “exaggerated salinity-effect”. In the no salinity-effect limit, the contribution of the polymer coil to the viscosity is high and independent of salinity while this contribution is negligible at the exaggerated salinity-effect limit. The combined behavior of the polymer-microemulsion system is also affected by the amount of polymer partitioning. For large polymer molecules the amount of partitioned polymer progressively decreases by getting closer to the end of Type II salinity.

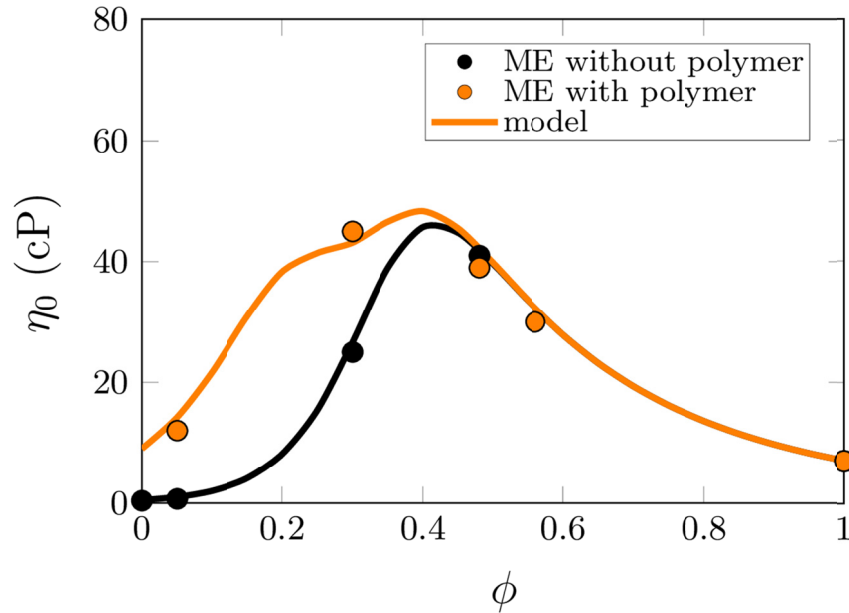


Figure 5.13: Viscosity of a number of microemulsions with (orange markers) and without (black markers) polymer. The lines are the model calculations. The experimental data are measured by Upamali (2014).

5.5 RESULTS

To validate the rheological model implementation in UTCHEM, comparisons were made with the experimental data of Fortenberry et al. (2013) for a series of heavy oil corefloods operated at different temperatures. The performance of a heavy oil coreflood, among other things, depends on the mobility control and the experimental temperature. The role of temperature is significant since it: (1) changes the oil viscosity and (2) modifies the phase behavior and interactions with chemicals, as demonstrated by Fortenberry et al. (2013) through activity diagrams (Nelson et al. 1984). Therefore, the

corefloods were chosen to be at different temperatures so the simulation modeling would not merely be a mobility control exercise.

All the corefloods are performed with a heavy oil of API 12° (crude #2 in Fortenberry et al. 2013) in tertiary recovery mode with a $S_{row} \sim 0.5$ in Bentheimer cores with brine permeabilities of ~ 2.5 D and porosities of ~ 0.23 . Table 5.3 summarizes the corefloods' specifications. "ACP-1" and "ACP-2" are Alkali-Co-solvent-Polymer floods while "ALK" is an alkaline flood with no mobility control and no co-solvent. Experiment ACP-1 was performed at 50 °C where the oil viscosity is ~ 1000 cP. The coreflood was designed to have a mobility ratio of 1. Experiment ACP-2 was similar to ACP-1 except it was done at a lower temperature where the oil viscosity is ~ 5000 cP. The third coreflood, ALK, was at an elevated temperature and hence lower oil viscosity ($\mu_o = 220$ cP) but with no mobility control and a mobility ratio of 20.

The simulations were performed using the geochemical module of UTCHEM, which is specifically designed for pH-sensitive processes such as ACP and alkaline flooding (Bhuyan et al. 1990; Delshad et al. 1996; Mohammadi et al. 2009). The ACP-1 coreflood was used to set up the base simulation model, which then was used for ACP-2 and ALK coreflood simulations. Due to the similarities of the corefloods, most simulation parameters are the same for the three corefloods. However, accounting for the temperature/co-solvent effects on (1) the shift of optimum salinity window, and (2) the rheological behavior, distinguishes the simulation models from each other. The optimum salinity windows are reported in Fortenberry et al. (2013) and the rheology model parameters are shown in Table 5.4. The polymer rheology parameters were obtained by

fitting experimental measurements (Fortenberry 2013) (Figure 5.14). It is worth noting the effect of temperature and co-solvent on the parameters. An increase in temperature magnifies the adverse effects of salinity on the polymer contribution to viscosity, as evident by the increase of salinity parameter, S_p , at higher temperatures. Additionally, at the elevated temperature of ACP-1, the intrinsic property of the interface, ν , is 1.9 compared to $\nu = 2.3$ at 25 °C for ACP-2, which translates to a lower microemulsion-to-oil viscosity ratio, η_{me}/μ_o , at ACP-1 conditions. The UTCHEM simulation input files are given in Appendix B. To simulate the ACP experiments, the generation of soap was modeled by considering the partitioning of acid component between oil and aqueous phase and its dissociation as follows



The partitioning coefficient, K_D , and the dissociation coefficient, K_a , were assumed to be 8.15e-12 and 3.15-03, respectively. The optimum salinity window for the soap was obtained directly from the observed activity diagram of Fortenberry (2013). Very high solubilization ratios observed with the crude oil indicated a highly reactive crude. Therefore, a high concentration of 0.06 *ml/ml oil* for acid component in oil was assumed, based on the typical data reported by Meredith et al. (2000).

Figure 5.15 shows the ACP-1 coreflood performance along with simulation results. Cumulative oil recovery, oil cut, pressure drop across the core, and effluent pH were used to validate the simulation model. Good mobility control and efficient

chemicals resulted in a stable displacement and high tertiary oil recovery for this coreflood. Unlike in ACP-1 coreflood, the displacement is not stable in the ACP-2 and ALK corefloods and the oil recovery took much longer (Figure 5.16). Even though the corefloods were performed in a vertical configuration, the simulations were done horizontally. The difference between a vertical and horizontal flood is small due to the small density difference between the oil and brine (i.e. 0.02 g/cc) and thus a small Bond number compared to the capillary number. The Bond number is given by Equation (5.8) and the capillary number is given by Equation (5.9).

$$N_B = \frac{k\Delta\rho g}{\gamma}, \quad (5.8)$$

$$N_c = \frac{k\Delta p}{\gamma L}, \quad (5.9)$$

where k is permeability, γ is interfacial tension, L is the length of core, and ρ is density. Using a permeability of 2000 mD and interfacial tension of 0.001 mN/m, the Bond number is $\sim 2 \times 10^{-4}$. The capillary number with the pressure drop in psi is,

$$N_c = 0.05\Delta p. \quad (5.10)$$

Among the three corefloods, the alkali flood has the least pressure drop which is 0.85 psi. Using this value the capillary number is $\sim 4 \times 10^{-2}$ which gives a ratio of $N_c/N_B \sim 200$. Since the capillary number is around two orders of magnitude greater the Bond number, neglecting the gravity effects is a reasonable assumption for the alkali flood. The ratio of capillary to Bond numbers is even greater than 200 for the ACP-1 and ACP-2 corefloods since they have a greater pressure drop while the Bond number

remains essentially unchanged. Therefore, neglecting the effects of gravity is justified there too. A summary of coreflood input parameters is given in Table 5.6.

Figure 5.16 shows the results in terms of cumulative tertiary oil recovery and oil cut for the three corefloods. A more detailed comparison of experimental data and simulation results can be found in Table 5.5, where the final oil recovery (after 2.5 PV), oil breakthrough time, (micro)emulsion breakthrough time, and maximum pressure drop are reported. It is interesting to note that the ACP-2 coreflood reached the same final tertiary oil recovery as ACP-1 despite its higher mobility ratio. This surprising performance, however, came with two drawbacks: (1) a slower oil recovery rate that resulted in ~20% lower recovery at 1 PV for ACP-2 and (2) an unsustainable pressure drop with a maximum pressure drop of 18.5 *psi/ft* (Figure 5.17), which is too high for field applications. The reported maximum pressure drop is obtained from the simulation since the experimental data is missing due to a leak in the polymer drive column during the coreflood, as shown in Figure 5.17.

The ALK coreflood used no polymer and no co-solvent. As expected, the oil recovery performance was much poorer than for the stable ACP-1 coreflood. The relative performance of an alkali flood in the field would be even worse than in a coreflood, especially when done at a constant injection rate in a homogeneous core such as Bentheimer sandstone. The adverse effects of fingering in a 3D heterogeneous reservoir are much worse than in a homogeneous core.

Table 5.3: Corefloods' specifications

	ACP-1	ACP-2	ALK*
Mobility ratio	1	5	20
Temperature (°C)	50	25	68
Oil viscosity (cP)	~1000	~5000	220
Slug			
Co-solvent (wt%)	1	1	<i>none</i>
Polymer (ppm)	4100	4100	<i>none</i>
Alkali (ppm)	10000	10000	4000
Velocity (ft/day)	0.48	0.5	0.96
Polymer drive			
Polymer (ppm)	3700	3700	<i>none</i>
Alkali (ppm)	5000	5000	2500

* ALK stands for alkaline flood.

Table 5.4: Rheology model parameters

	ACP-1	ACP-2	ALK
Polymer solution			
A_{p1}	80	80	—
A_{p2}	200	200	—
A_{p3}	28000	28000	—
S_p	-0.39	-0.3	—
$\dot{\gamma}_h$	0.35	2.0	3.5
P_α	1.6	1.6	1.6
Microemulsion			
ν	1.9	2.3	2
ν'	5	6	3.9
η_p^0 (cP)*	2000	2000	50
c_{int}	0	0	0

* η_p^0 is used in Equation (5.4) to calculate λ_{rp} .

Table 5.5: Comparison of corefloods' performances and simulation results (numbers in parentheses)

	ACP-1		ACP-2		ALK	
Oil recovery (%)	~96	(99) §	~96	(~91)	46	(~43)
Oil bank BT* (PV)	0.25	(0.25)	0.25	(0.25)	0.3	(0.5)
(micro)emulsion BT (PV)	0.86	(0.88)	0.40	(0.45)	0.3	(0.45)
Max. pressure drop (psi/ft)	4.5	(4.5)	>17.5	(18.5)	1.7†	(0.85)

§ The numbers in parentheses are the simulation results.

* BT stands for breakthrough.

† Signs of core plugging were observed.

Table 5.6: Summary of coreflood input parameters

Length (ft)	1
Number of grids in x, y, z directions	100x1x1
Gridblock sizes in x, y, z directions (ft)	0.01x0.1351x0.1351
Components simulated	Water, oil, surfactant, polymer, anion, calcium, co-solvent, sodium, calcium, magnesium, carbonate, hydrogen, petroleum acid
Average porosity	~0.23
Permeability (md)	~2000
Initial water saturation	~0.5
Residual water saturation	0.15
Residual oil saturation	~0.5
Endpoint relative permeability for water	0.025
Endpoint relative permeability for oil	1
Relative permeability exponent for water	2
Relative permeability exponent for oil	2
Elements modeled in geochemistry	Calcium, magnesium, carbon (as carbonate), sodium, hydrogen, acid (petroleum), chlorine
Independent fluid species	H^+ , Na^+ , Ca^{2+} , Mg^{2+} , CO_3^{2-} , HA_o , H_2O
Dependent fluid species	$Ca(OH)^+$, $Mg(OH)^+$, $Ca(HCO_3)^+$, $Mg(HCO_3)^+$, A^- , OH^- , HCO_3^- , $H_2CO_3^0$, $CaCO_3^0$, $MgCO_3^0$, HA_w
Solid species	$CaCO_3$, $MgCO_3$, $Ca(OH)_2$, $Mg(OH)_2$
Cation exchange	$\overline{H^+}$, $\overline{Na^+}$, $\overline{Ca^{2+}}$, $\overline{Mg^{2+}}$

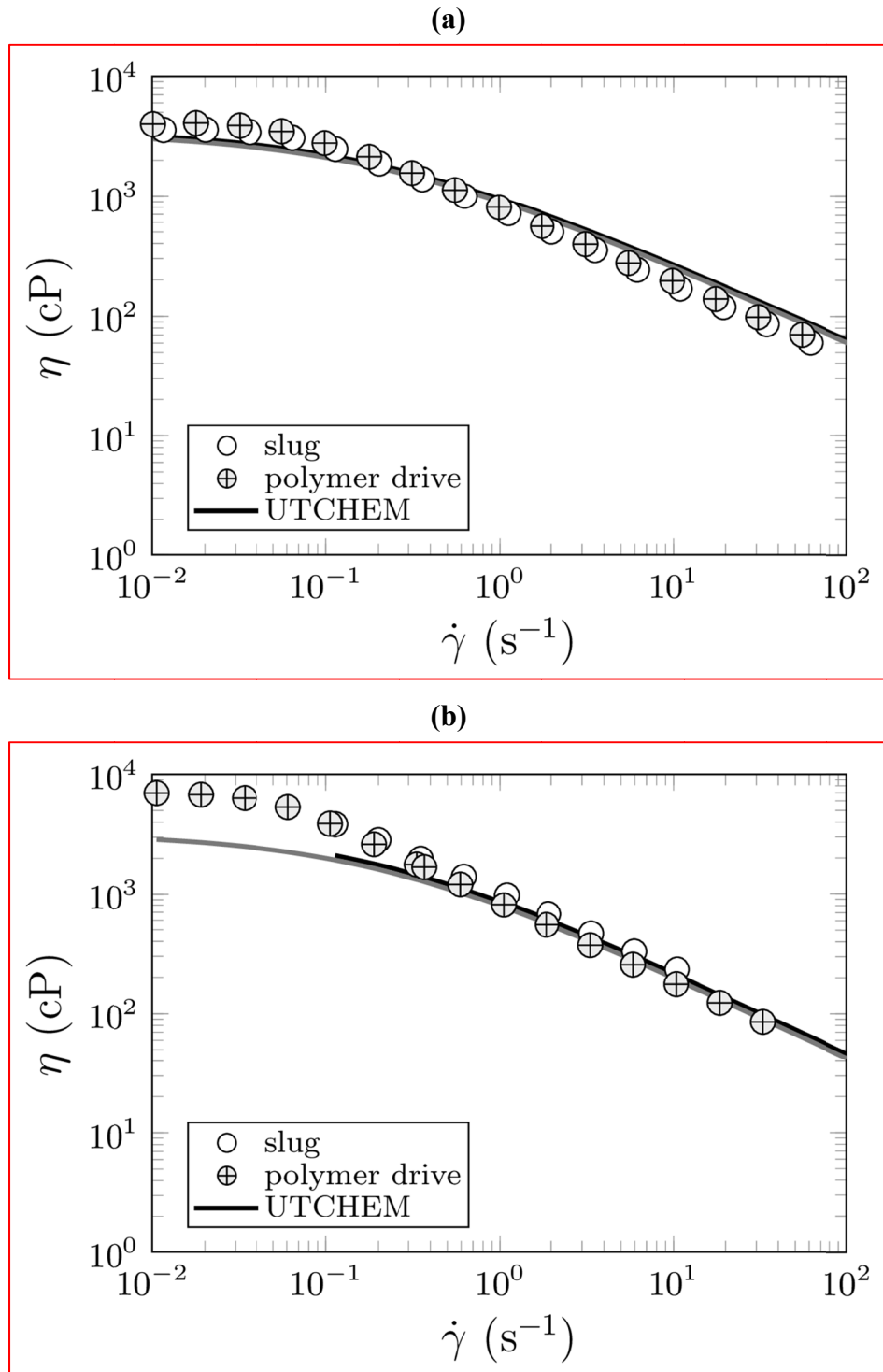


Figure 5.14: Experimental Polymer solution viscosity at slug/polymer drive salinity and concentration (Fortenberry 2013) versus UTCHEM model.

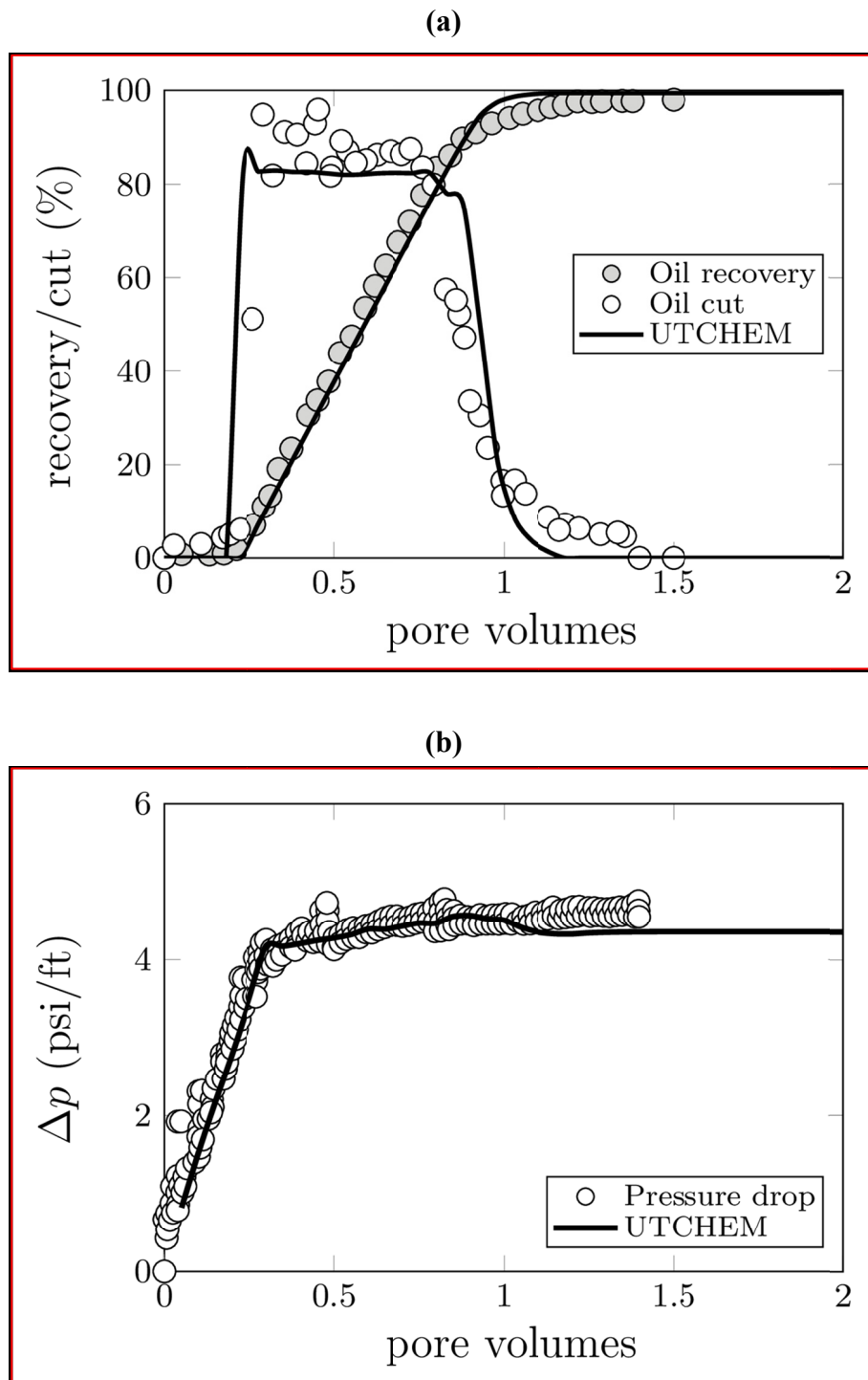


Figure 5.15: (full caption next page)

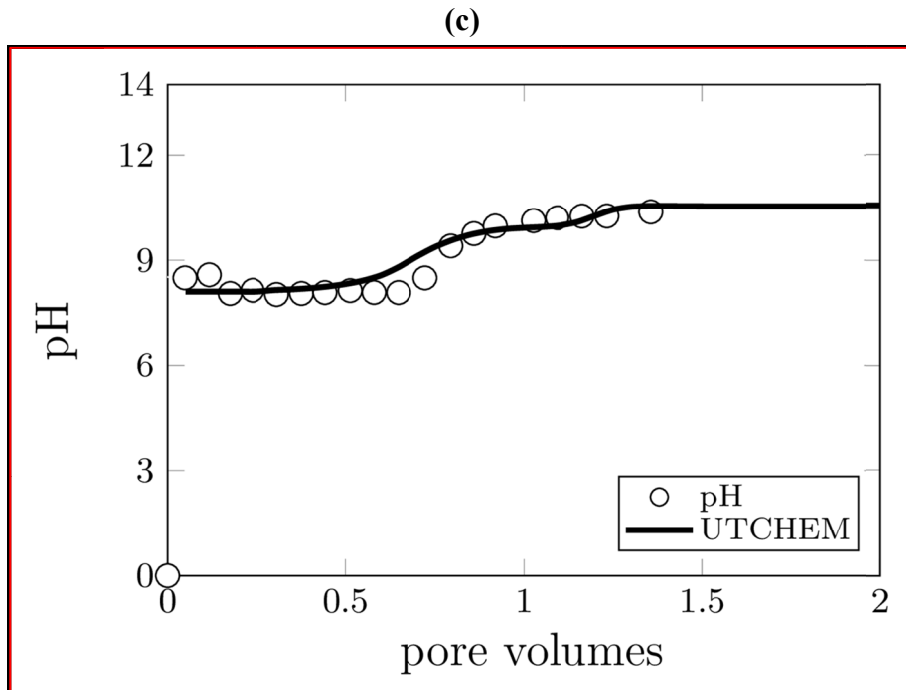


Figure 5.15: Comparison of “ACP-1” coreflood data with simulation results for (a) cumulative oil recovery and oil cut, (b) pressure drop across the core, and (c) effluent pH. Favorable mobility ($MR = 1$) of ACP-1 coreflood resulted in a stable displacement and high oil recovery. Lines are the simulation results. The agreement between the experimental data and simulation results is evident.

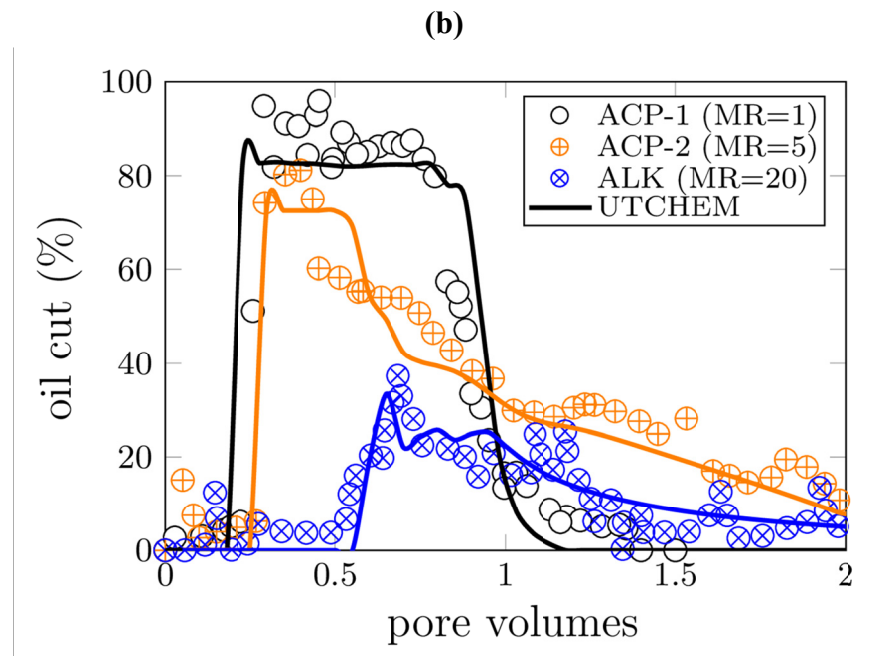
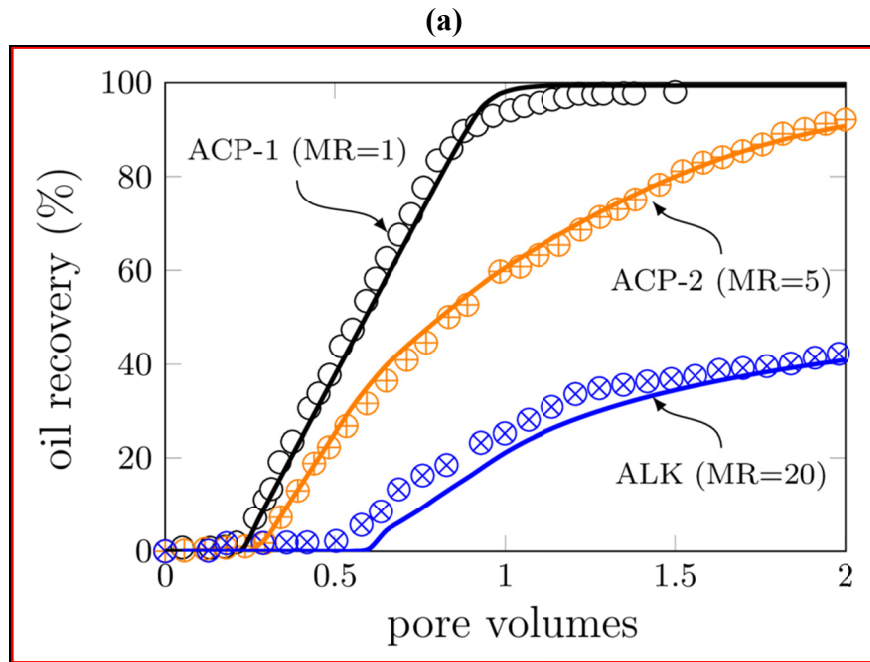


Figure 5.16: Simulation of tertiary chemical corefloods where variations in temperature and chemicals resulted in different performances. ACP-1 and ACP-2 are Alkali-Co-solvent-Polymer flooding and ALK is an alkaline flooding. “MR” refers to mobility ratio.

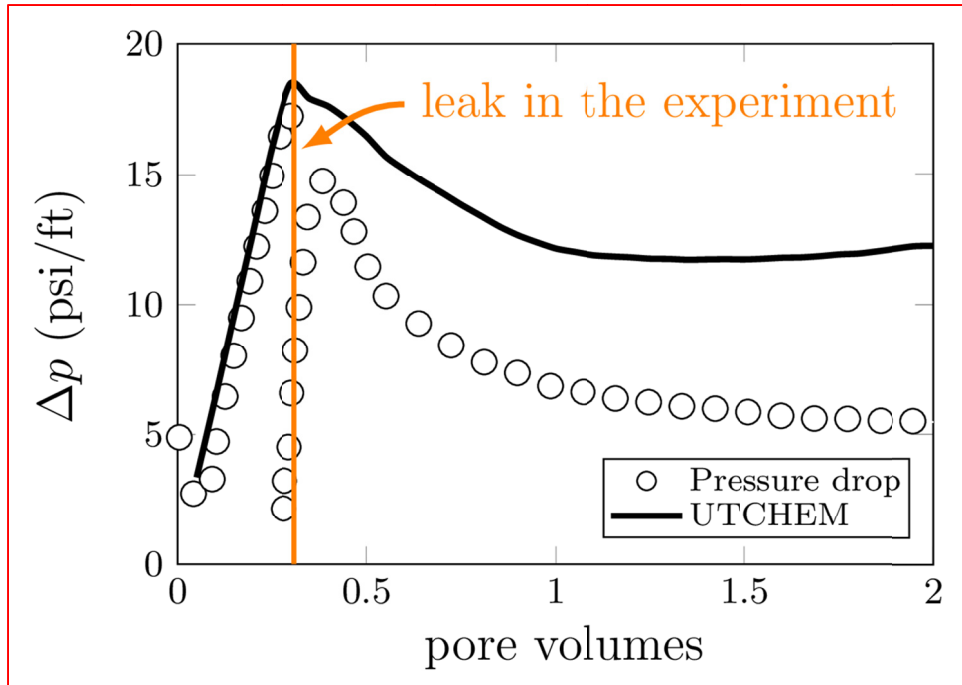


Figure 5.17: Pressure drop for ACP-2 where the points show experimental results and the line is the simulation results. A leak in the pressure column was reported by Fortenberry (2013) at around 0.33 PV of chemical injection.

Chapter 6: UTCHEM Thermal Module Modification and Verification

Thermal module of UTCHEM numerically solves the energy conservation equation to account for heat conduction and convection in the reservoir and heat losses to the over burden and under burden in addition to the coupled mass conservation equations. Prior to use for field scale simulations, the module was modified and verified as discussed below.

6.1 VARIABLE TEMPERATURE INPUT

Originally UTCHEM only allowed for a constant initial reservoir temperature. Therefore, an initialization flag, *ITEMP*, was introduced in the input section to allow for variable initial reservoir temperature. *ITEMP* = 4 corresponds to a variable temperature profile in the initialization and requires temperature data for each gridblock in the reservoir, unlike in *ITEMP*=0 where a constant temperature is required. The *ITEMP* flag is only required when the thermal module flag, *IENG* = 1.

6.2 THERMAL CONDUCTIVITY

Energy transports through the porous reservoir rock as well as the fluids in the pores. The energy balance used in UTCHEM (Delshad et al. 2000) can be written as follows:

$$\begin{aligned} \frac{\partial}{\partial t} \left[(1 - \varphi) \rho_r C_{vr} + \varphi \sum_{l=1}^{n_l} \rho_l S_l C_{vl} \right] T + \vec{\nabla} \cdot \left(\sum_{l=1}^{n_l} \rho_l C_{pl} u_l T - \lambda_T \vec{\nabla} T \right) \\ = q_H - Q_L, \end{aligned} \quad (6.1)$$

In Equation (6.1), T is the reservoir temperature; u is the volumetric fluid flux (Darcy velocity) in the porous medium; ρ and φ refer to density and porosity respectively; subscripts r and l refer to rock and phase number; S is saturation and n_l is the number of phases; C_v and C_p are the heat capacities at constant volume and pressure, and λ_T is the thermal conductivity. q_H accounts for the energy sources and sinks and Q_L for the heat losses outside the reservoir. The thermal conductivity term in the energy balance was modified to read:

$$\lambda_T = (1 - \varphi) \lambda_r + \varphi \sum_{l=1}^{n_l} S_l \lambda_l. \quad (6.2)$$

6.3 MICROEMULSION HEAT CAPACITY

The bulk heat capacity of the porous control volume is calculated as follows:

$$C_{vb} = (1 - \varphi) \rho_r C_{vr} + \varphi \sum_{l=1}^{n_l} \rho_l S_l C_{vl}, \quad (6.3)$$

which requires the heat capacity of each phase, C_{vl} . The heat capacities of oil and water are constants provided by the user. That of microemulsion, however, depends on its composition and is hence variable. Assuming a zero enthalpy of mixing, this composition dependency can be accounted for on a unit-mass basis by

$$C_{v_ME} = \frac{\sum_i \rho_i C_{i_ME} C_{vi}}{\sum_i \rho_i C_{i_ME}}, \quad (6.4)$$

where subscript i sums over oil and water present in microemulsion with concentrations C_{i_ME} . An example thermal Alkali-Surfactant-Polymer (ASP) coreflood simulation with UTCHEM shows this treatment removes the oscillations in the temperature profile as shown in Figure 6.1.

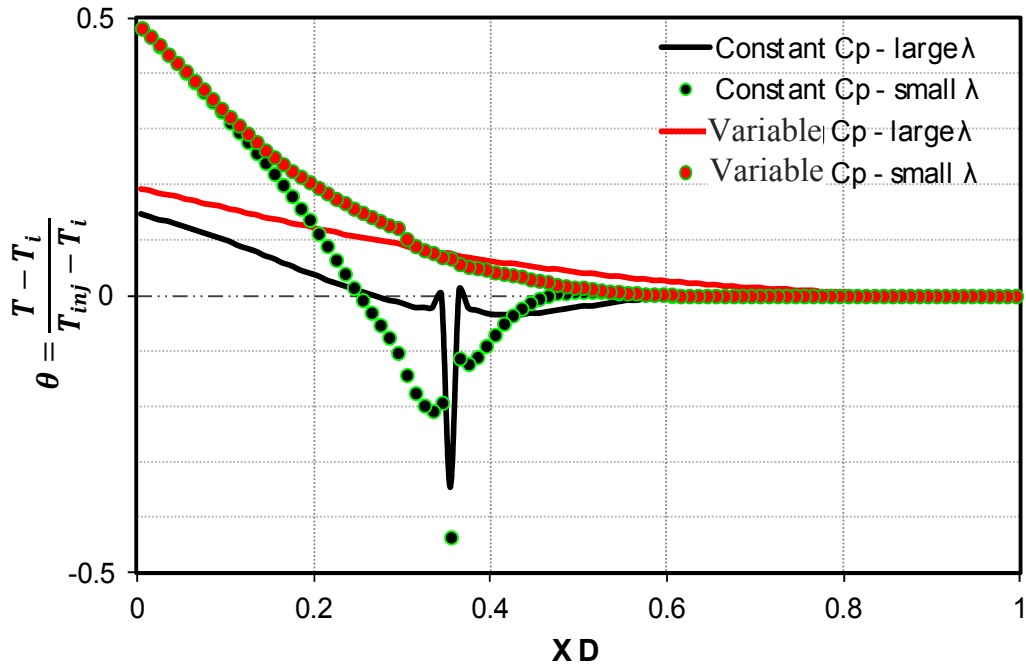


Figure 6.1: Temperature profile for a non-isothermal ASP coreflood simulation. Considering the composition dependency of microemulsion heat capacity removes the temperature oscillations. Value of λ (i.e. heat conductivity) changes the thermal Péclet number and thus the temperature profile.

6.4 COMPARISON WITH CMG-STARS

In order to validate the UTCHEM thermal module comparisons were made with CMG-STARS (Computer Modelling Group 2011) for two cases: (1) a single-phase hot water injection, (2) a hot waterflooding case. In the former, water is injected in a water-

saturated reservoir while oil is present in the later. Three wells including one injector and two producers are considered. The simulation model parameters for the single-phase hot water injection are shown in Table 6.1. Waterflooding was performed with the same set of parameters, except the initial oil saturation was set to 0.55. The simulation results obtained from UTCHEM and CMG-STARs are shown in Figure 6.2 and Figure 6.3. Figure 6.2 shows the average reservoir temperature and Figure 6.3 shows the XZ cross-sectional temperature profile.

6.5 CHEMICAL FLOODING EXAMPLE

An example simulation of an ACP flood is provided for demonstrating the importance of the modifications considered above. The ACP flood is done in the same setting as above with one injector (refer to Figure 6.4) and two producers. The chemical slug and polymer drive specifications are provided in Table 6.2. The slug size is 0.25 PV and the polymer drive is 1.25 PV. The negative normalized temperatures with the original UTCHEM (shown in Figure 6.4.a) are resolved using the modified module (Figure 6.4.b).

Table 6.1: Simulation model parameters for the single-phase hot water injection

Reservoir dimensions (ft)	41×600×54
Number of Gridblocks	41×1×27
Porosity	0.25
Permeability (D)	2×2×1
Initial pressure (psi)	420
Initial temperature (°F)	203
Injection water temperature (°F)	212
Injection rate (ft ³ /day)	500
Initial water saturation	1.0

Table 6.2: The ACP flood model parameters

Initial temperature (°F)	203
Injection water temperature (°F)	212
Oil viscosity (cP)	65
Slug	
Co-solvent (wt%)	1
Polymer (ppm)	3500
Alkali (ppm)	10000
Polymer drive	
Polymer (ppm)	4100
Alkali (ppm)	5000

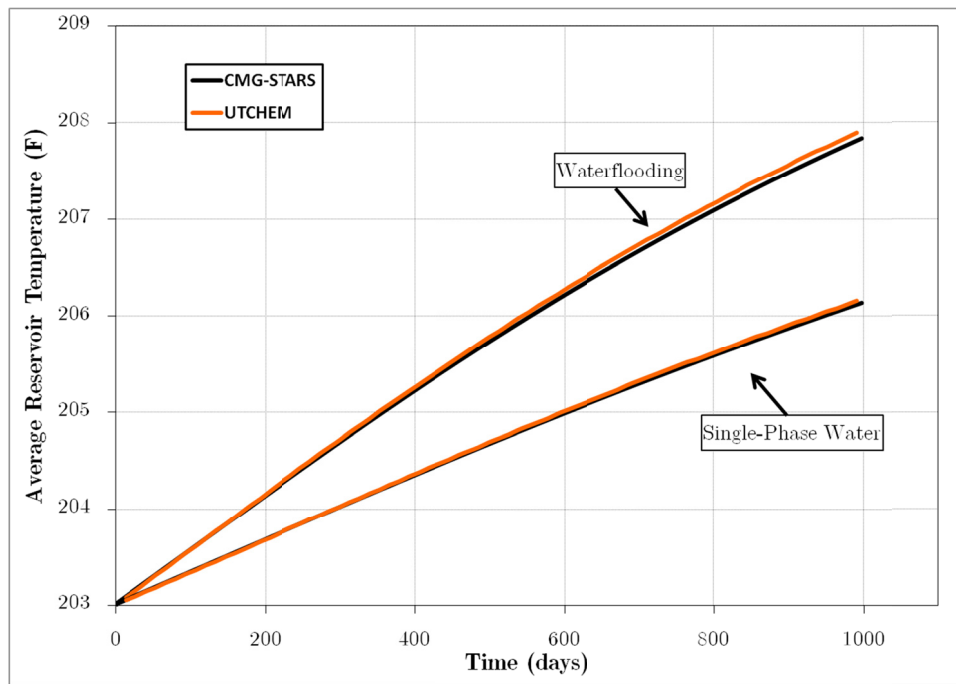


Figure 6.2: Average reservoir temperature for single-phase water injection and hot waterflooding cases obtained from CMG-STARS and UTCHEM.

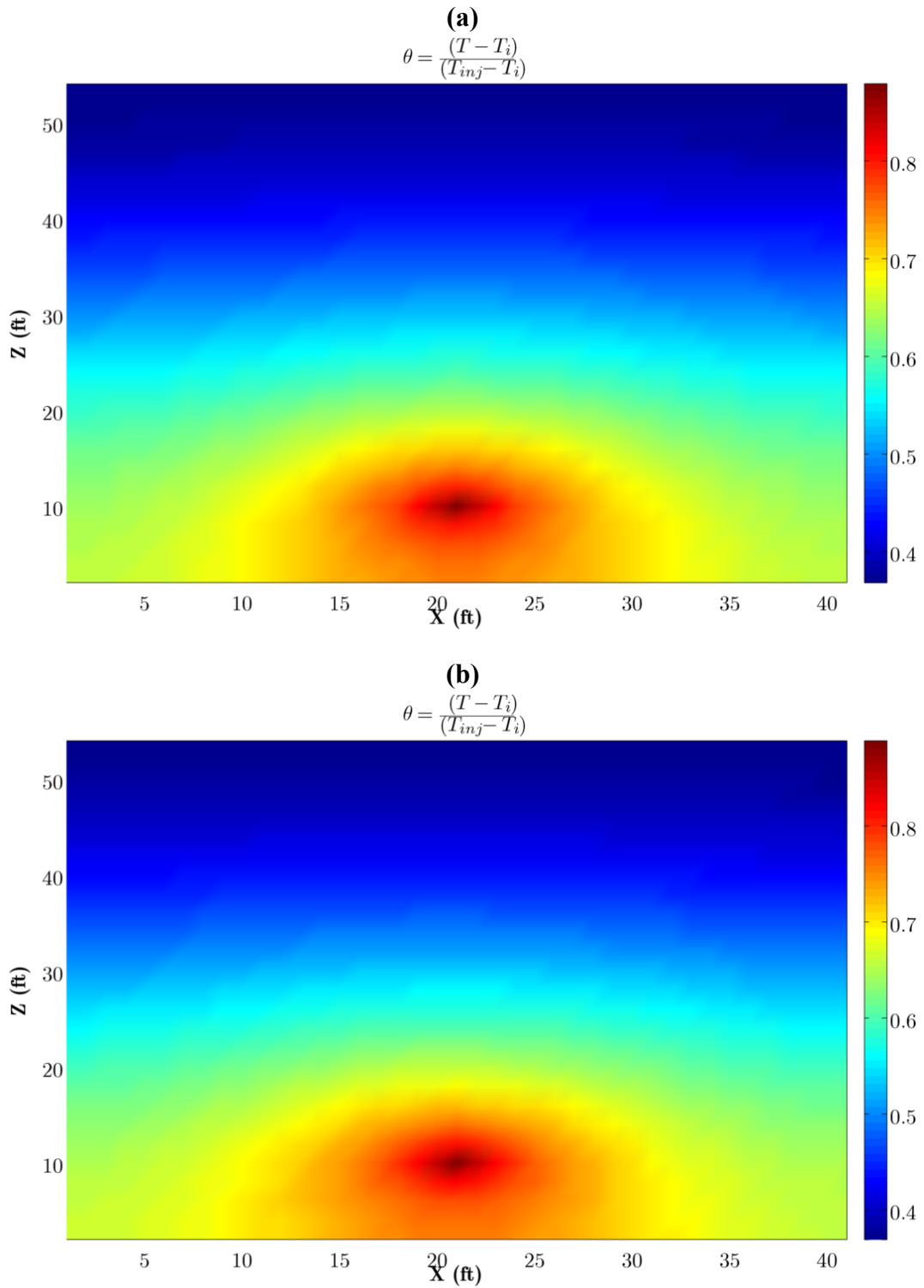


Figure 6.3: XZ cross-sectional temperature distribution for the hot water flooding case obtained from (a) CMG-STARS and (b) UTCHEM.

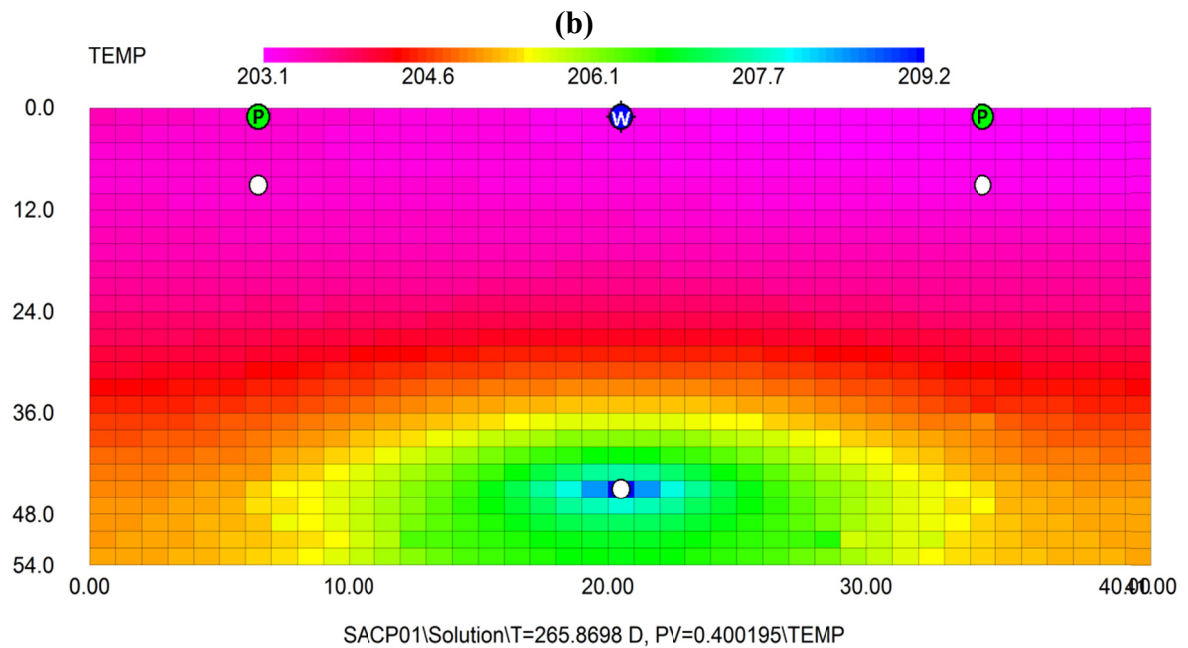
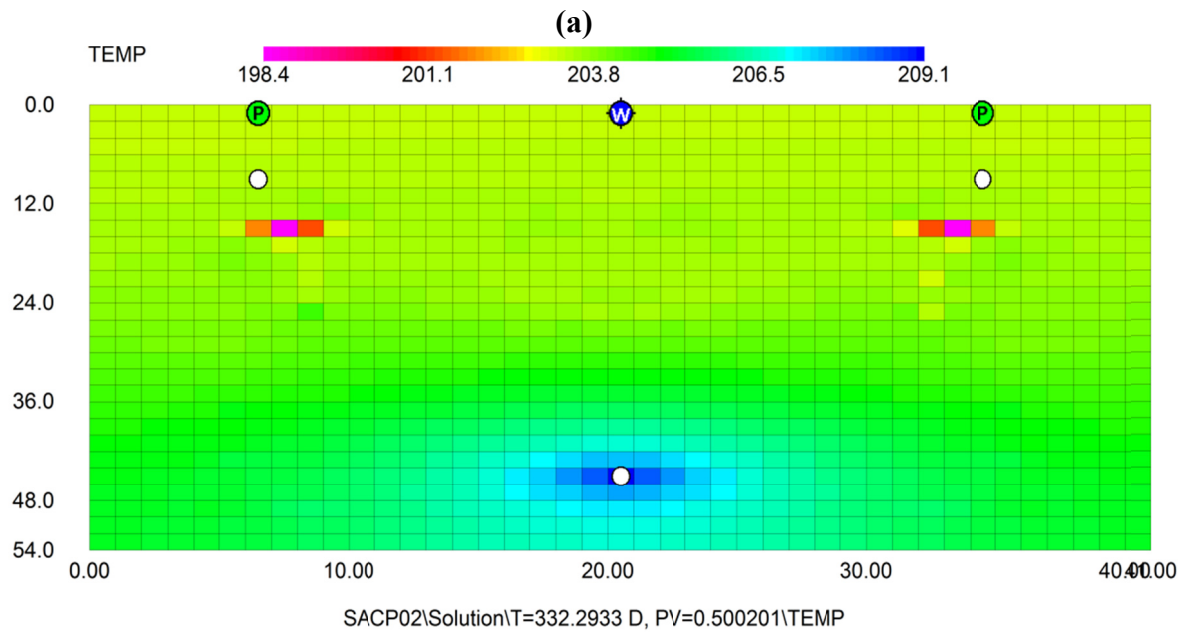


Figure 6.4: XZ cross-sectional temperature profile for an ACP chemical flood: (a) original UTCHEM (b) modified UTCHEM. Initial reservoir temperature is 203 °F. The profile is shown after 0.4 PV of fluid injection.

Chapter 7: HTCP Development and Optimization

For many shaley thin oil deposits in Canada steam injection is not feasible. A hybrid process that involves moderate heating without steam coupled with chemical enhanced oil recovery is proposed and discussed in this chapter as an alternative method of enhanced oil recovery.

7.1 LITERATURE REVIEW

Heavy oil recovery methods range from cold production to complex thermal EOR technologies. The most common thermal recovery methods use steam to heat the oil in place (Shah et al. 2010; Al-Bahlani and Babadagli 2009; Ardali et al. 2012), but under certain common conditions steam injection is not feasible or economic. Hybrid processes based on electrical heating have been proposed where water (McGee and Vermeulen 2007), a gas (Zhong et al. 2011), or a solvent (Zhu and Zeng 2012) is injected during or after the electrical heating. In this paper, we focus on a new hybrid process that combines moderate electrical heating with chemical EOR.

Recent research in the application of chemical EOR to heavy oil at The University of Texas resulted in the development of a new process called Alkali-Co-solvent--Polymer (ACP) flooding. The alkali reacts with acids in the crude oil to form soap, which reduces the interfacial tension. Polymer is used to increase the water viscosity for mobility control. Co-solvent is used to optimize the phase behavior and prevent the formation of highly viscous emulsions. Fortenberry et al. (2013) evaluated the ACP

flooding process in a series of core floods at moderately elevated temperatures using heavy oils in the range of 5000 to 300,000 *cP* at 22 °C. The ACP floods recovered almost all of the oil from these cores. A moderate increase in temperature has the benefit of reducing the oil viscosity so that the oil can be displaced at flow rates and pressure gradients that are feasible in oil reservoirs.

These observations form the foundation for the development of the hybrid process presented here, in which ACP is combined with moderate reservoir heating by means of electrical resistance heating and hot water flooding. This combination is necessary to effectively deal with challenges of heavy oil production. Electromagnetic heating can be divided into low-frequency resistive heating and high-frequency dielectric heating (Chhetri and Islam 2008; Sahni et al. 2000). In low-frequency resistive heating (Hiebert et al. 1983; Pizarro and Trevisan 1990; Sierra et al. 2001), the flow of an alternating current through the reservoir brine dissipates (ohmic) heat and raises the reservoir temperature while in high-frequency heating the adaptive alignment of dipoles to the alternating electric field dissipates heat (Sahni et al. 2000; Mutyala et al. 2010). We investigated the use of low-frequency electrical resistive heating (ERH) where horizontal wells serve as both electrodes and injectors/producers (McGee and Vermeulen 1996). In this approach, current is forced through the reservoir by imposing a potential gradient between the horizontal wells. Electrode locations, lengths and spacing are essential in determining the temperature profiles that will develop in the formation (McGee and Vermeulen 2007) and require careful engineering design for efficient heating of the oil

rich parts of the reservoir (McGee et al. 1999). These principles will be discussed in the following sections.

7.2 RECOVERY SCHEME AND WELLBORE/ELECTRODE CONFIGURATIONS

The proposed enhanced oil recovery process, in its basic form, is a three-stage scheme. The first stage is electrical heating. In this stage the reservoir temperature is raised just enough to create fluid injectivity. Unlike in McGee and Vermeulen (1996) approach, no significant oil should be produced in this stage to prevent produced fluids from removing the generated heat from the reservoir (Rice et al. 1992). Additionally, this approach increases the pressure and energy of the formation prior to production, which results in higher ultimate oil recovery (McGee and Vermeulen 2007). Due to the moderate efficiency of heating the reservoir electrically (Das 2008) and no oil production, the time length of this stage would be short and will often be less than 4 months. In addition, the electrical operating conditions should be chosen to avoid near-wellbore water vaporization (McGee and Vermeulen 2007). An electrode configuration that would facilitate a more uniform heating and hence less risk of near-wellbore water vaporization is presented in Figure 7.1. Oliveira et al. (2009) showed that this electrode configuration combined with standard three-phase electric power is very efficient compared to other configurations. Another advantage of this repeated *triad* configuration is efficient oil displacement in the chemical EOR phase once fluid injection is started.

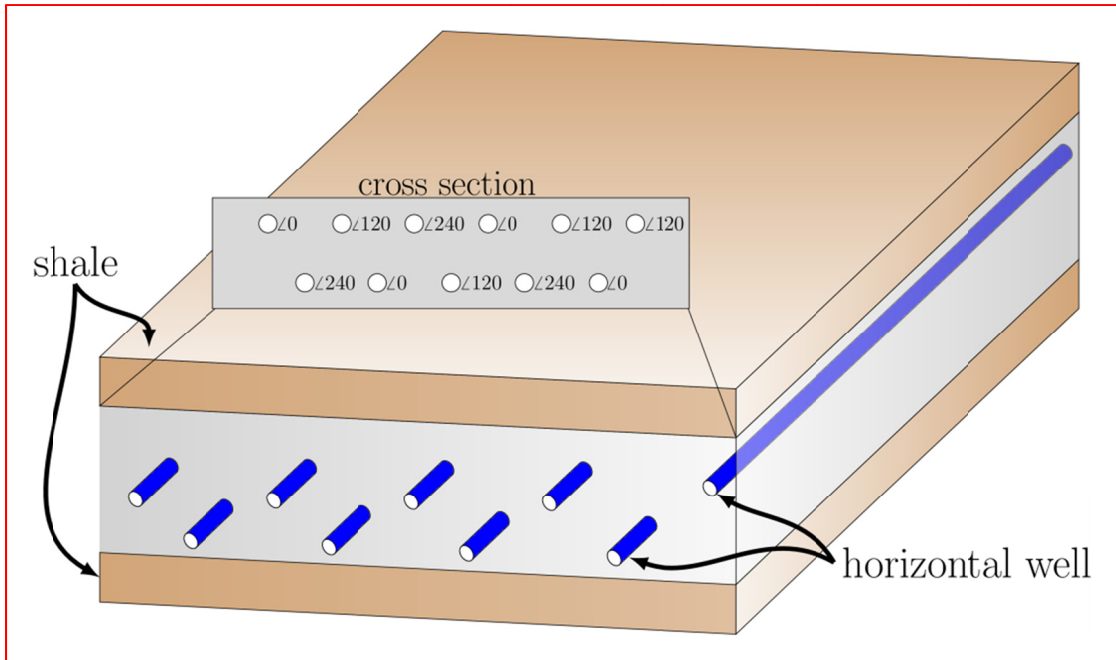


Figure 7.1: Reservoir model and wellbore/electrode configuration. The wellbore arrangement allows for using 3-phase voltage during electrical heating and efficient flooding during fluid injection. The phase of each electrode is indicated by $\angle\theta$.

After electrical heating has created sufficient fluid injectivity, high-rate high-pressure hot water injection accelerates the increase in temperature of the reservoir and at the same time oil production starts at the producers. The water injection extracts energy from the hot sand near the wells and transports it deep into the reservoir and also displaces oil towards the producers. The injection rate must be high to quickly increase the reservoir temperature, a principle demonstrated in our own optimization studies as well as those done by Zhao and Gates (2013) for a similar case. Simultaneous production avoids excessive pressures and helps with the project economics. Achieving relatively low bottom-hole pressures in production wells has also been shown to improve the oil recovery (Rangel-German et al. 2004). Viscosity reduction, oil expansion, and unstable oil displacement by water are the recovery mechanisms with potential recovery factors in

the range of 5-25 %OOIP. Because most of the oil recovery comes before water breakthrough as evident from flattened recovery curves upon water breakthrough as shown in Luo and Torabi (2013) and Levitt et al. (2011), further waterflooding produces very little oil. Thus the duration of this stage is kept below two pore volumes to avoid hot water circulating through the reservoir without producing much oil.

At the end of hot waterflooding, the oil viscosities are low enough for a chemical flood to be performed where oil can efficiently be mobilized and displaced at low pressure gradients. As mentioned earlier, ACP flooding is the most promising chemical EOR technique in heavy oils; it is inexpensive, robust and fully customizable to individual reservoirs, while producing as much oil as surfactant-based methods such as ASP flooding.

7.3 ROCK AND FLUID PROPERTIES

The success or failure of any thermal recovery process is governed by energy transport as oil viscosity must be reduced for any fluid flow to occur. In this regard, not only average reservoir temperature but also temperature distribution is important. Therefore, in this work, special consideration was paid to thermal and electrical properties used in the simulations. Electrical properties become important as they affect the magnitude and distribution of resistive heating. The rock and fluid properties are published values from the Bluesky formation in the Peace River Basin in Alberta, Canada (Koci and Mohiddin 2007a; 2007 b).

7.3.1 Thermal Properties

Energy transports through both fluids and solids. Therefore, for a fluid-saturated porous medium, the heat capacity and thermal conductivity are averaged over the solid and fluids.

7.3.1.1 Heat capacity

The average heat capacity, C_v , is averaged as follows:

$$C_v = (1 - \varphi)C_{vr} + \varphi \sum_{l=1}^{n_l} S_l C_{vl} \quad (7.1)$$

where φ is the porosity and C_v is the volumetric heat capacity in $BTU/ft^3^\circ F$, subscripts r and l refer to rock and fluid phase number; S is saturation and n_l is the number of phases. Heat capacities of water, oil and reservoir rock are 62.4, 30.25 and 35.31, respectively. Base and cap rock heat capacity is 31.8. Heat capacity of the casing is 50 with a temperature dependency coefficient of 0.0235 ($1/^\circ F$) (Davis 1994; Dobrosavljević and Maglić 1992).

7.3.1.2 Heat conductivity

Unlike heat capacity, the calculation of bulk heat conductivity is not straight forward. Three common approaches are

- volumetric averaging:

$$\lambda_b = (1 - \varphi)\lambda_r + \varphi \sum_{l=1}^{n_l} S_l \lambda_l \quad (7.2)$$

- geometric mean:

$$\lambda_b = \lambda_f^\phi \lambda_r^{(1-\phi)} \quad (7.3)$$

- Anand et al.'s empirical correlation (Anand et al. 1973):

$$\lambda_b = \lambda_f \left(\frac{\lambda_r}{\lambda_f} \right)^b ; \quad b = 0.28 - 0.757 \log \phi - 0.057 \log \left(\frac{\lambda_r}{\lambda_f} \right) \quad (7.4)$$

λ is conductivity and $\lambda_f = \sum_l S_l \lambda_l$ (assuming no gas is present). Using thermal conductivities of $\lambda_{r=quartz} = 108$ (Horai 1971), $\lambda_{water} = 8.88$, and $\lambda_{oil} = 1.8$ in *BTU/ft.day.°F* with $\phi = 0.25$ and $S_w = 0.25$ in Equations (2 through 4) results in significantly different λ_b values of 82, 46, and 33.0, respectively. To resolve the issue, comparisons were made against field measurements of ~ 34 *BTU/ft day.°F* (Seto and Bharatha 1991; Bachu 1993) for sandstones with similar porosities and water saturation, which agrees with the calculations from Anand et al.'s correlation. Therefore this correlation was used. The shale (base/cap rock) thermal conductivity is taken to be ~ 16 *BTU/ft day.°F* (Bachu 1993).

7.3.2 Electrical Conductivity

Bulk electrical conductivity, C_b , which is the inverse of bulk resistivity, R_b , can be obtained from resistivity logs or the Archie's law in the case of clean sands by

$$\frac{1}{C_b} \equiv R_b = \frac{a R_w}{\phi^m S_w^n}, \quad (7.5)$$

where R_b and R_w are the formation (bulk) and brine resistivity respectively. For Bluesky formation typical standard logs are shown in Figure 7.2. As indicated by the deep

resistivity log, the bulk formation resistivity varies across the reservoir column but the average value is around 90 (*ohm.m*), which corresponds to $S_{w_ave} = 0.25$; obtained from Equation (7.5) using $a = 1$, $m = 1.8$, $n = 2.15$, and $R_w = 0.32$ (*ohm.m*) for the Bluesky formation. The shale (base/cap rock) resistivity is often distinctively low (5 *ohm.m* here), which corresponds to high electrical conductivity due to clay cation exchange capacity and bound water.

In the absence of clay in the formation, the conductivity comes from the brine only. Therefore, the temperature dependence of bulk electrical conductivity can be accounted for by considering the brine conductivity variation with temperature (Sorensen and Glass 1987) as

$$C_w = \begin{cases} C_{w@T_{ref}}[1 + 0.026(T - T_{ref})] & \text{if } (T \leq 100 \text{ }^\circ\text{C}) \\ C_{w@T_{ref}}[2.98 + 0.002(T - 100)] & \text{if } (T > 100 \text{ }^\circ\text{C}), \end{cases} \quad (7.6)$$

where T_{ref} is a reference temperature and $C_{w@T_{ref}}$ is brine conductivity at T_{ref} . Updated C_w then can be used in Equation (7.5) to obtain the bulk conductivity. A similar temperature dependence can be used to obtain the shale (base/cap rock) conductivity at different temperatures. Temperature-dependent casing conductivities in the range of $(0.1-0.2) \times 10^7$ (*siemens/m*) (Davis 1994; Dobrosavljević and Maglić 1992) were used in the simulation. The casing conductivity determines the voltage drop along the wellbore.

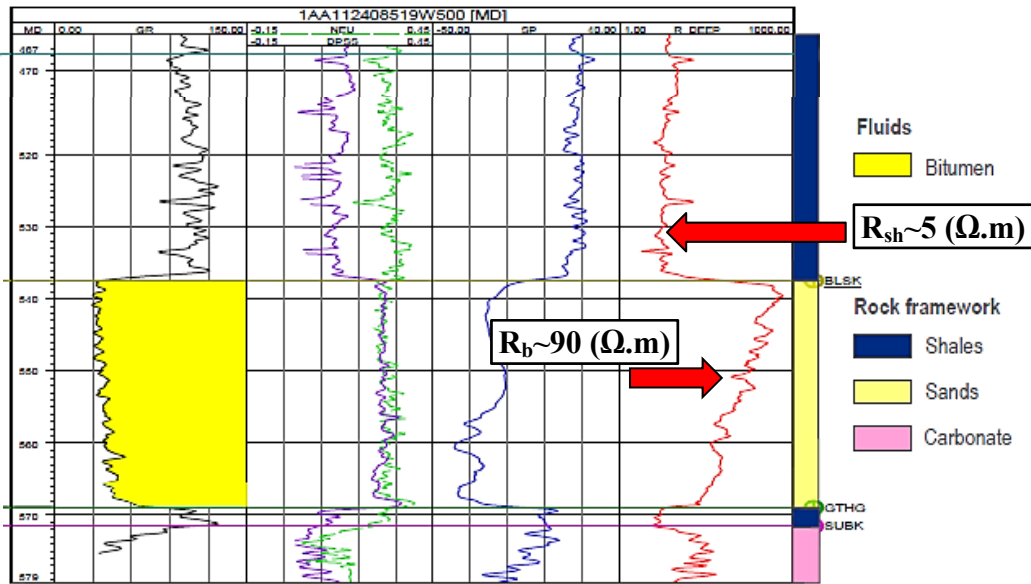


Figure 7.2: Typical standard logs for the Bluesky formation (Shell Canada Limited 2009).

7.3.3 Oil Viscosity

The oil viscosity in the simulation model is ~ 5000 cP at reservoir temperature. Figure 7.3 shows the oil viscosity versus temperature (Fortenberry 2013). Solution gas has been shown to improve heavy oil recovery upon heating (Rangel-German et al. 2004) and is qualitatively accounted for by considering an oil thermal expansion coefficient of $\sim 9 \times 10^{-4}$ 1/°F.

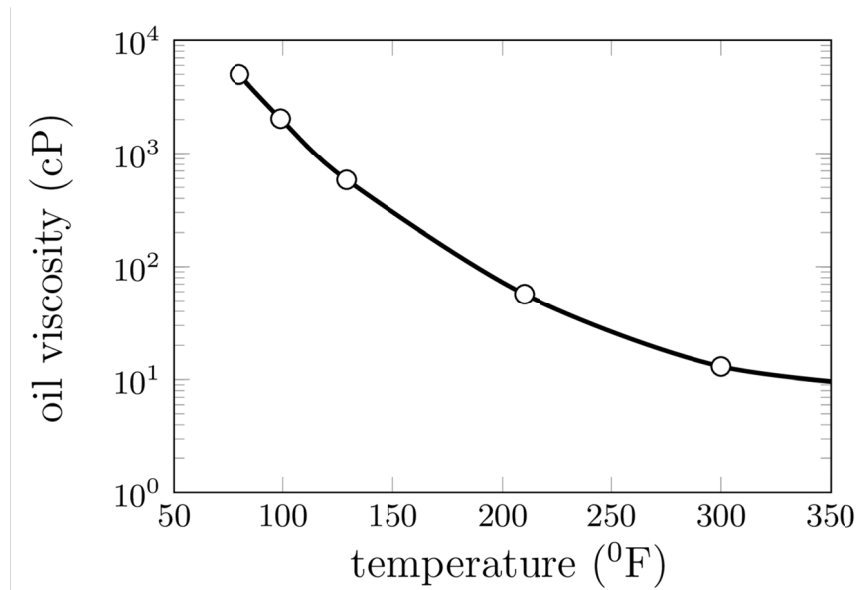


Figure 7.3: Measured oil viscosity versus temperature. The data is adapted from (Fortenberry 2013).

7.4 SIMULATION MODEL

Realistic simulation is a necessary tool for the proper evaluation of the proposed hybrid process. The electrical heating simulations were performed using the CMG-STARS (Computer Modelling Group 2011) simulator and the chemical flooding simulations were performed using the UTCHEM simulator (Bhuyan et al. 1990; Delshad et al. 1996; Mohammadi et al. 2009) in a unified sequence. The simulation model was then verified by the overall energy balance in the CMG-STARS simulation and by coreflood results for the chemical flooding part. The reservoir model containing ~ 5 MMbbl oil is shown in Figure 7.1. The horizontal well spacing between two adjacent wells is ~ 50 meter. Originally a $167 \times 5 \times 33$ grid was used for the simulations. To reduce the simulation time, the number of gridblocks was then reduced to $167 \times 1 \times 33$ without losing much accuracy. Base and cap rocks are included in the

model as the presence of shale affects the electrical heating process. It should be emphasized that base/cap rocks (i.e. shale) should always be present in in any realistic simulation of electrical heating as they modify the electrical current flow and constrain the flow of heat.

7.4.1 Electrical Heating

Electrical power is supplied to the horizontal electrodes (i.e. wellbore casing) that are in electrical contact with the reservoir formation. In the simulation model, the electric potentials were applied at the grid block faces that contain the casings. As a result of this treatment, the simulation of electrical heating can be sensitive to grid block size. For example, as noted by Das (2008), the amount of ohmic heat dissipation can decrease by increasing grid block sizes. The key to avoiding possible unphysical results is to ensure that the energy balance is respected as the process unfolds. This was verified in the present simulation study by appropriate choice of gridblock sizes. In this sense, without any heat losses, the plot of overall energy input versus bulk reservoir temperature increase should be a straight light with a slope equal to $C_{v,b}$ as

$$\Delta H = C_{v,b} V_b \Delta T \quad (7.7)$$

where ΔH is the overall energy (enthalpy) added to the reservoir, V_b is bulk reservoir volume, and $\Delta T (\equiv T_{ave} - T_i)$ is the average reservoir temperature increase. $C_{v,b}$ is known *a priori* and can be used to judge the simulation accuracy. Figure 7.4 shows such a validation.

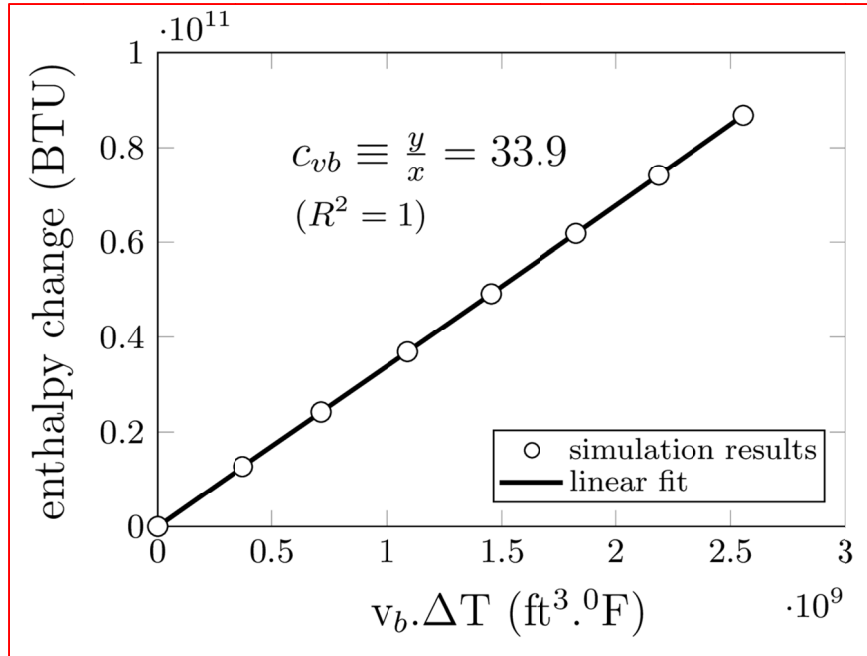


Figure 7.4: Validation of electrical heating simulation and gridding system by overall energy balance.

Once the simulation model is verified different aspects of the process can be explored. For example, Figure 7.5 shows the voltage drop along the wellbore and the resulting temperature distribution. Because of the voltage drop, the temperature increase is not the same along the wellbore. Another issue with using the casing of long horizontal wells as electrodes is the excessive heating of the casing. In this case, the casing temperature increases such that the near wellbore water vaporization is inevitable. Although this phenomenon was not observed in the simulation studies here, using casings made of steel grades with high electrical conductivities could reduce the excessive heating.

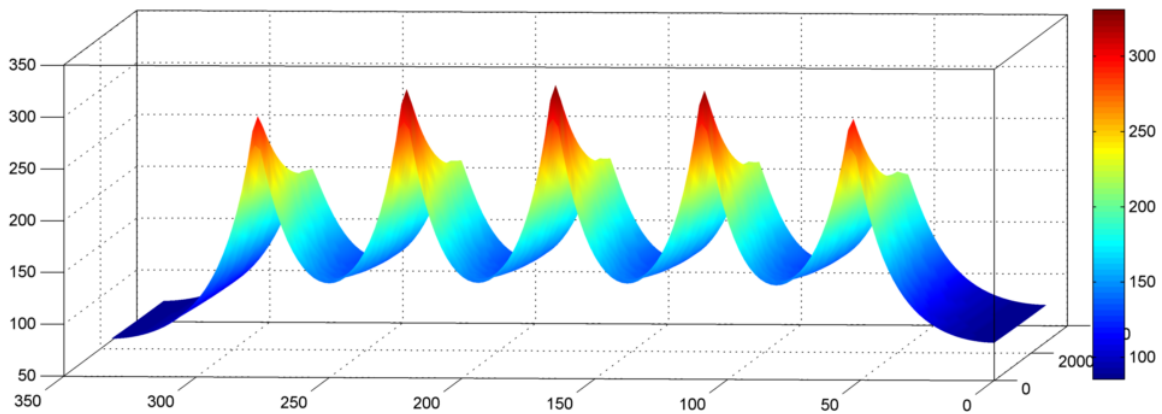
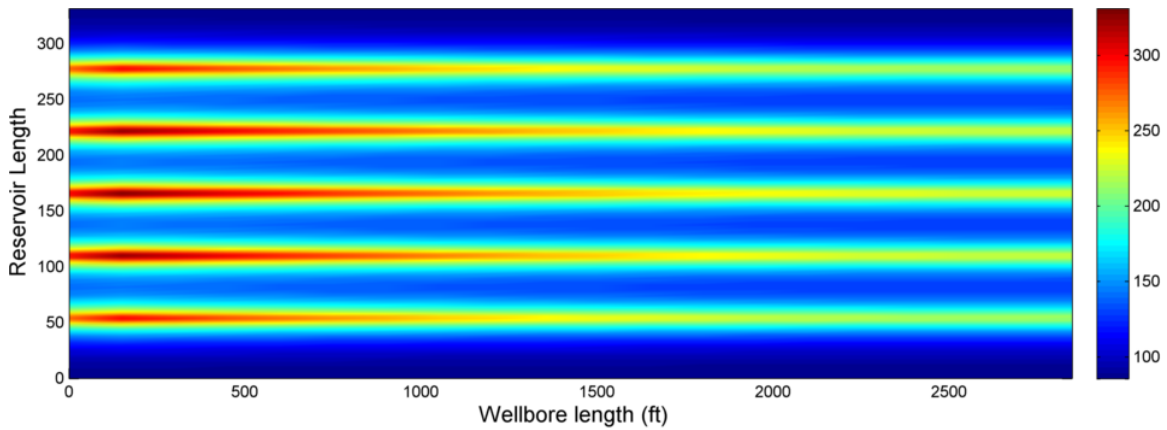


Figure 7.5: Voltage drop along the wellbore and the resulting temperature distribution. Note the non-uniform temperature increase along the wellbore.

7.4.2 Chemical Flooding

The chemical EOR simulations were performed using the geochemical module of UTCHEM, which is specifically designed for pH-sensitive processes such as ACP and alkaline flooding (Bhuyan et al. 1990; Delshad et al. 1996; Mohammadi et al. 2009). The chemical parameters were estimated from the experimental data of Fortenberry et al. (2013). The details can be found in Chapter 5.

7.4.3 Effects of Heterogeneities

Heterogeneities in terms of fluid/rock distribution and properties complicate the implementation of any recovery technology. In typical heavy oil and oil sand reservoirs, oil viscosity not only varies across the field but also within the reservoir column. For the Bluesky formation, the compositional gradient in the reservoir column and biodegradation causes a viscosity increase with depth, which is most significant when there is a bottom water zone (Larter et al. 2008). In this case, the oil viscosity of ~ 5000 cP sharply increases near the bottom of the reservoir to $\sim 2 \times 10^5$ cP at 22 °C (Larter et al. 2008). However, this viscosity difference with depth decreases to values of about 500 to 1000 cP with a moderate increase of temperature to 52 °C (Koci and Mohiddin 2007b) (Figure 7.6). A viscosity difference of this order is not expected to greatly alter the performance of HTCP with mobility control.

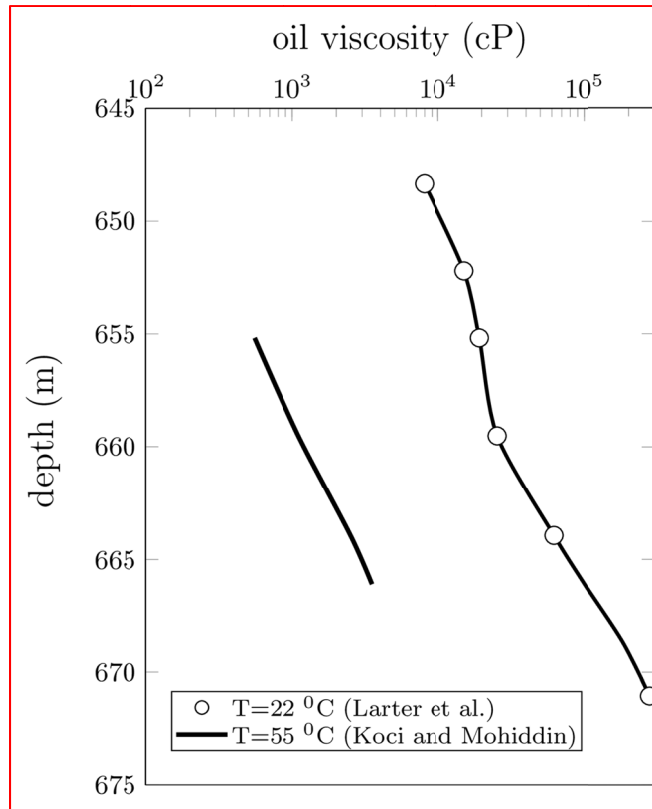


Figure 7.6: Typical oil viscosity variations with depth and temperature for the Bluesky formation. Data is adapted from (Koci and Mohiddin 2007b; Larter et al. 2008).

A second type of common heterogeneity is the presence of horizontal shale baffles in the reservoir. For steam injection processes, they hinder the steam rise in the formation and reduce the recovery efficiency (Shin and Choe 2009; Yang and Butler 1992). For electrical heating, however, the presence of shale baffles encourages uniform heating and, as shown by Glandt and Chia-Fu (1992), does not affect the recovery greatly. In the present work, the default well configuration is to have injectors near the bottom of the reservoir and producers near the top, which results in a vertical upward displacement (Figure 7.7a). In the case of severe blockage of vertical fluid flow by shale baffles, the HTCP floods could be performed horizontally without changing the

well pattern (Figure 7.7b). In this way the symmetry and potential performance of the pattern will be preserved as shows in Figure 7.11b.

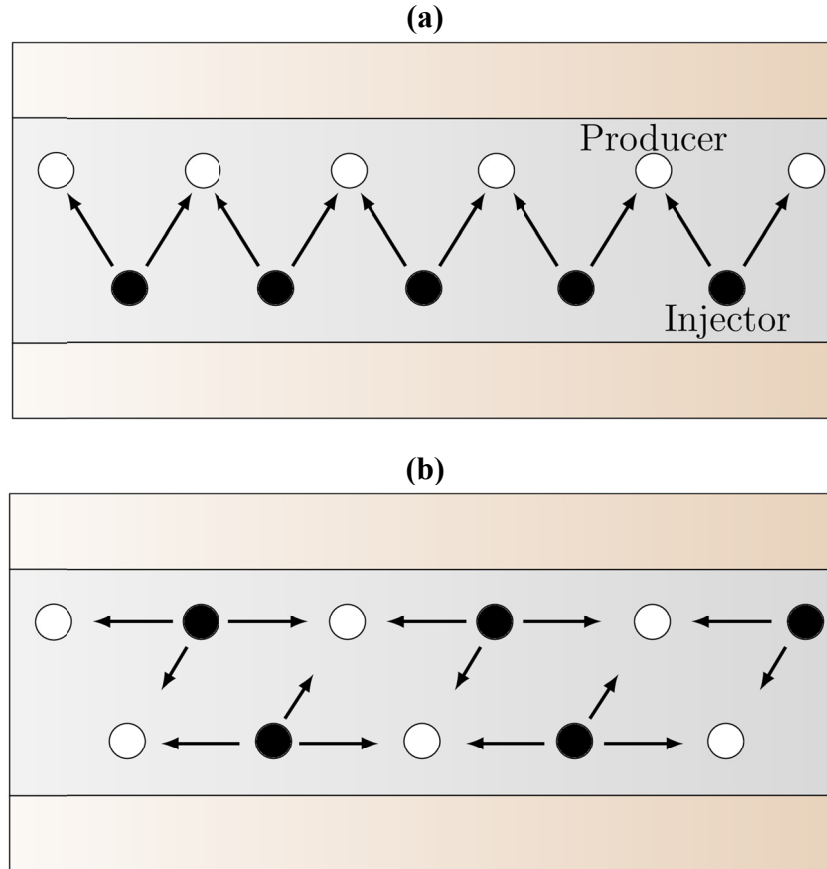


Figure 7.7: The default vertical flood (left) could be switched to a horizontal one (right) in the case of very low effective vertical permeability. The arrows schematically show the direction and magnitude of flow.

Variation of fluid saturations in the reservoir column and presence of bottom water zone is the third common type of heterogeneity. Experimental work of Oskouei et al.(2012) showed that increasing the initial water saturation lowers the recovery and energy efficiency of steam-assisted-gravity-drainage (SAGD) and several researchers have shown the adverse effects of bottom water (Chang et al. 1992; Masih et al. 2012; Saskoil and Butler 1990). In order to investigate how the water/oil distribution alter the

electrical heating performance, the deep resistivity log measurements (Figure 7.2) along with Equation (7.5) were used to compute the initial water saturation across the reservoir column. The water saturation increases with depth, as is typical, and averages to about 0.25. Three scenarios were defined in which

- a) Water saturation is fixed and equal to 0.25.
- b) Log-derived water saturation with an average value of 0.25 is used. Water saturation increases with depth.
- c) Log-derived water saturation with an average value of 0.25 is used with a bottom layer of water. The lower row of electrodes is placed in the bottom water.

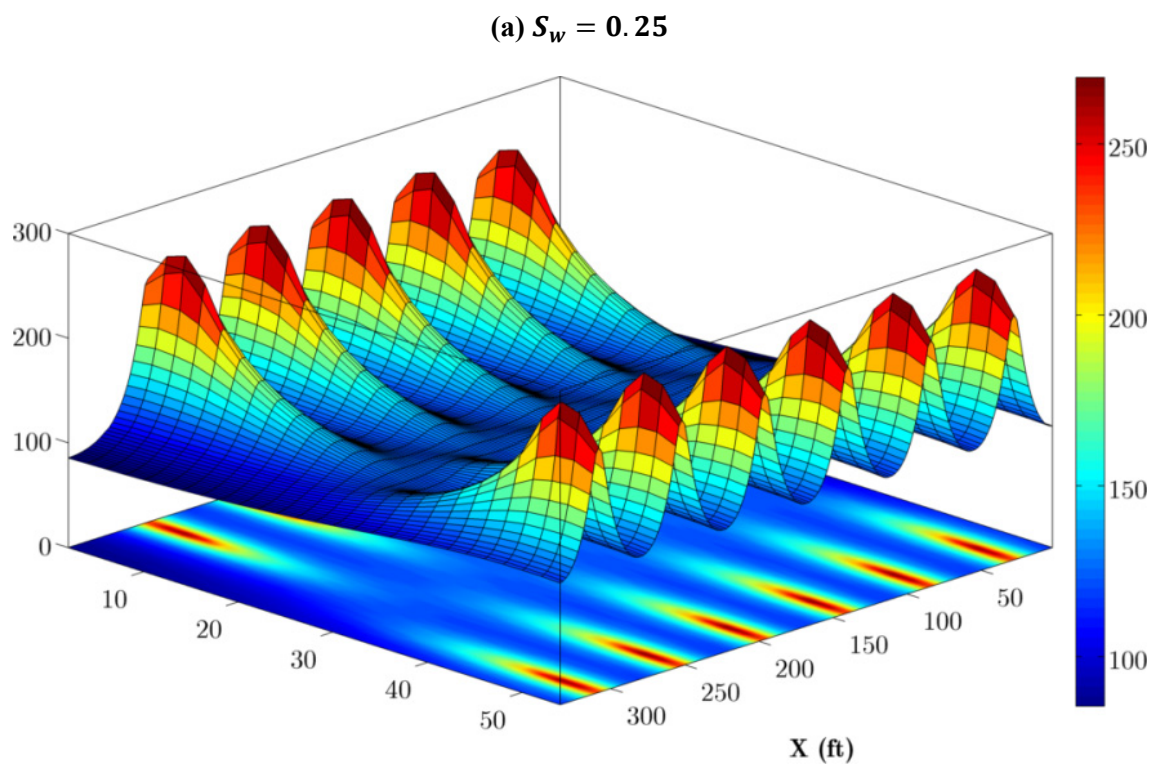
Figure 7.8 shows the simulated XZ vertical cross-sectional temperature distributions for the three scenarios after a fixed amount of energy is injected. For the uniform S_w case (Figure 7.8.a), the symmetry in heating pattern is evident where temperature forms peaks around the electrodes (11 electrodes correspond to 11 peaks) and smear out toward the middle of the reservoir. Variable water saturation inherently changes the temperature distribution (Figure 7.8.b) because (1) power distribution among the electrodes will not be uniform (refer to the next section) (2) even if a uniform power distribution is imposed, more heat is dissipated at the upper portions of the reservoir due to higher resistivities. In Figure 7.8.b a uniform power distribution among electrodes was imposed, which made the heating pattern similar to uniform S_w with slightly hotter upper electrodes. The presence of bottom water, however, changes the overall pattern, as shown in Figure 7.8.c. The conductivity in bottom water is high enough to significantly reduce the heat dissipation and leave the bottom portion of the reservoir unheated. This observation dictates that electrode/wellbore position should be elevated in the reservoir as much as possible away from the bottom water. Even though the salinity of injected brine

is assumed to be uniform, its variation has been shown to impact the final temperature profile (Bogdanov et al. 2010).

A remedy for imbalanced heating with non-uniform fluid distribution can be found in the efficient ERH design proposed by McGee and Vermeulen (2007; McGee 2008), in which uniform electrical power distribution between the electrodes is achieved through voltage phase and magnitude regulations. In other words, imposing proper electrical operating conditions (EOC) could resolve the imbalanced heating by controlling the amount of energy that is emitted from each electrode/wellbore. To understand the role of EOC, an analogy with fluid injection operating conditions, given in Table 7.1, is useful. Unlike the current EOC, the power EOC provides little control over the heating process and normally results in imbalanced heating. Figure 7.9 shows the effect of electrical operating conditions for the cases shown in Figure 7.8. The standard deviation, as a measure of uniform heating, was calculated by

$$s = \left(\frac{1}{N-1} \sum_{i=1}^N (x_i - \bar{x})^2 \right)^{1/2}, \quad (7.8)$$

where x is the temperature with a mean value of \bar{x} . As seen in Figure 7.9, variable water saturation disturbs the balance of heating pattern, which can be resolved by controlling the electrical operating conditions. With the presence of bottom water, however, the disturbance cannot be resolved and reservoir heating is uneven regardless of EOC. These results also show that for a homogenous reservoir with uniform fluid distributions, the choice of EOC is irrelevant. However, for field application it becomes important to select the most appropriate EOC for the sake of process robustness.



(b) log-derived water saturation with $S_{w_ave} = 0.25$

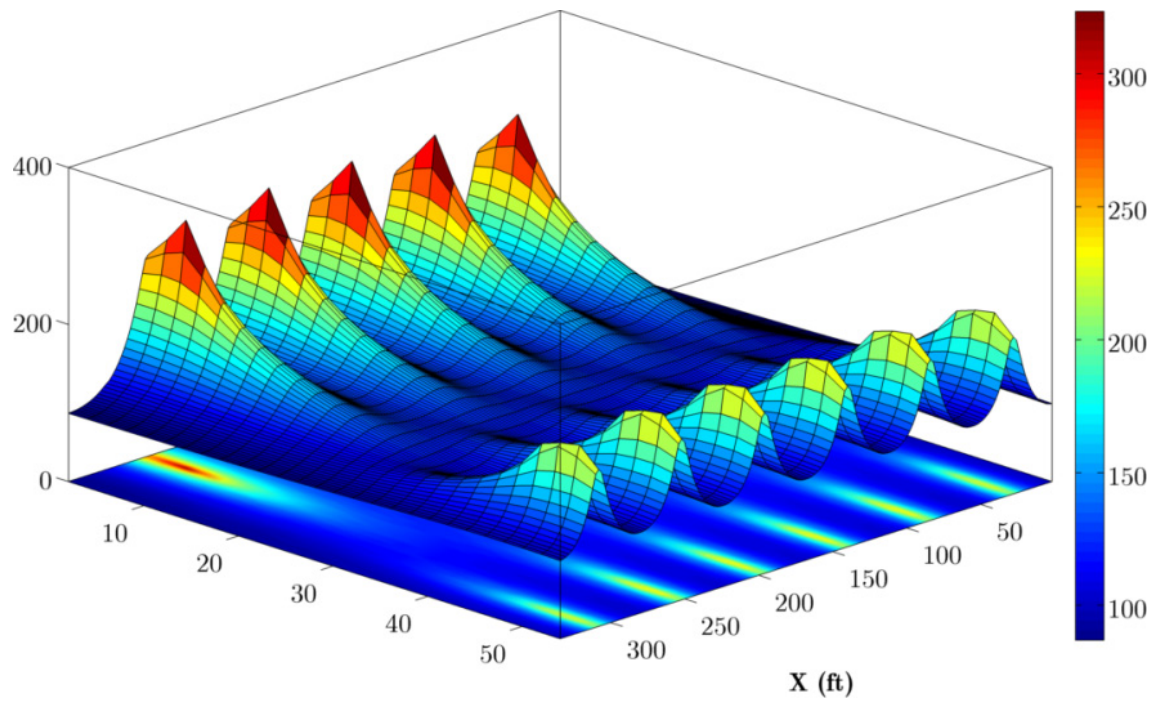


Figure 7.8: (full caption next page)

(b) log-derived water saturation with $S_{w_ave} = 0.25$ and bottom water

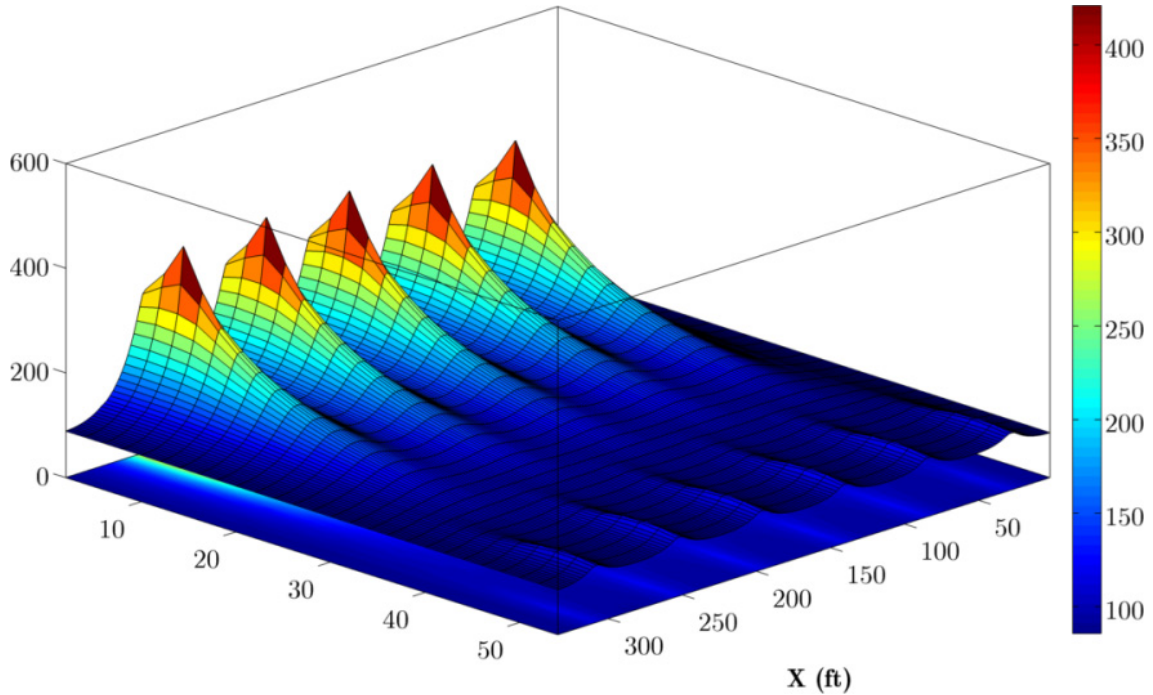


Figure 7.8: Fluid distribution effects on the performance of electrical heating. The graphs show XZ cross-sectional temperature distribution for (a) uniform water saturation, (b) variable resistivity-log-derived water saturation with $S_{w_ave} = 0.25$, and (c) variable resistivity-log-derived water saturation with $S_{w_ave} = 0.25$ including the presence of bottom water. Initial reservoir temperature is 80 and same amount of energy is injected for all the cases.

Table 7.1: Analogy of electrical and fluid injection operating conditions

Electrical Operating Conditions	Fluid Injection Operating Conditions
<i>Power (global):</i> Layers (sections) with lower resistivity will get higher current. Heating is very imbalanced.	<i>Total field injection rate (global):</i> Wells drilled in higher permeability sections get most of the injected fluid. This results in a non-uniform flood.
<i>Current (local):</i> The amount of energy dissipated through each electrode cannot be larger than a specified value and the heating is more uniform.	<i>Well injection rate (local):</i> Every well has an upper limit on its injection rate. The effect of permeability contrast on the flood is less profound.

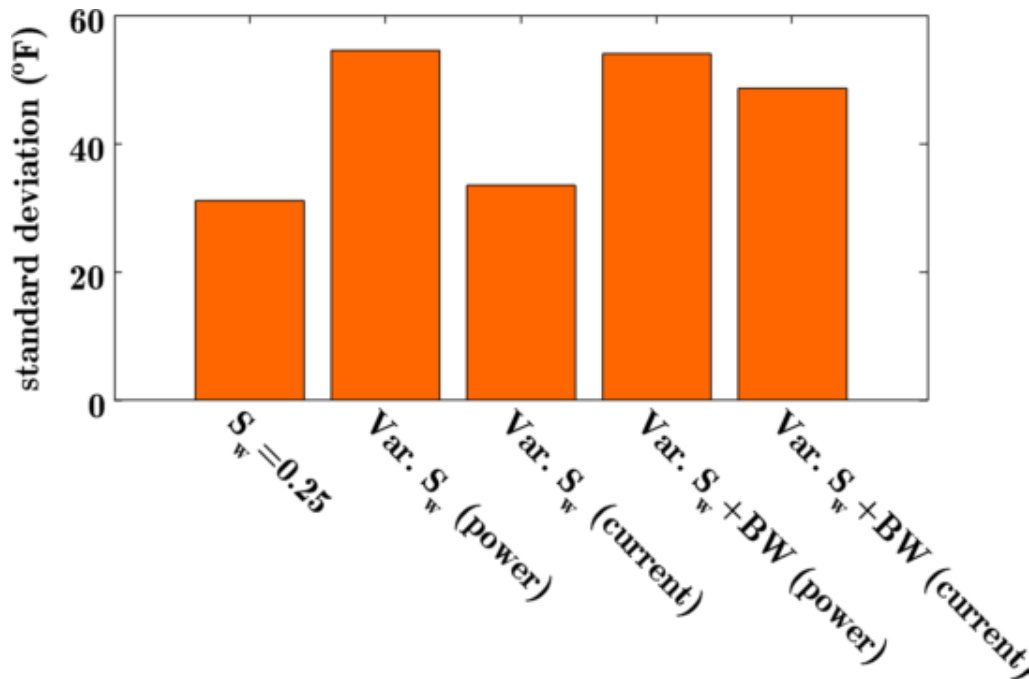


Figure 7.9: Effect of initial water saturation and electrical operating conditions on the uniformity of the heating pattern. Variable (depicted by “var.” in the graph) water saturation inherently disturbs the balance of heating pattern which can be resolved by controlling the electrical operating conditions. With the presence of bottom water, however, the disturbance cannot be resolved.

In addition to fluid distribution, permeability variations can also impact the heating performance. To demonstrate this, a two-layer model (Figure 7.10) of the Bluesky formation was considered with a log-derived fluid distribution and a bottom water zone. A series of simulations were performed in which electrical heating for 360 days was followed by hot waterflooding. Injection water temperature was 212 °F. Figure 7.11.a shows the average reservoir temperature versus time. The vertical-to-horizontal permeability ratio, k_v/k_h , was varied from 0.5 to 0.01, which are the core-derived and history-matched values for the Bluesky formation, respectively (Koci and Mohiddin 2007a). While the electrical heating appeared to be less dependent on k_v/k_h , very little or no temperature increase occurred during the hot water flood for very low

k_v/k_h due to low injectivity. For $k_v/k_h = 0.01$, injectivity is essentially zero and the reservoir actually cools down due to heat losses to the over and underburden shales. The limited injectivity occurs because of reaching the maximum injection pressure which is 200 *psi* below the fracturing pressure of ~ 1800 *psi* (Koci and Mohiddin 2007a). In order to improve the injectivity for the case of $k_v/k_h = 0.01$, horizontal waterflooding (Figure 7.11.b) was investigated. For horizontal flow, maximum vertical well spacing is not essential for oil recovery as in the vertical flood and therefore the wells were moved toward the middle of the formation. This resulted in a slightly better performance of electrical heating. More importantly, the horizontal flood resulted in a significant improvement of the performance of the waterflood (Figure 7.7b). These results suggest that the wellbore/electrode pattern employed here provides robustness essential for field applications.

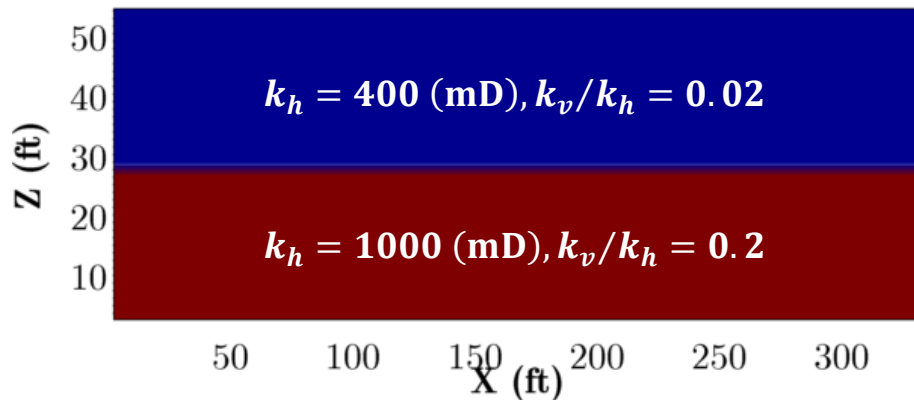


Figure 7.10: XZ cross-section of two-layer reservoir model used to study the effects of permeability heterogeneities on the electrical heating and waterflooding. Base/cap shale are included in the simulation but not shown here.

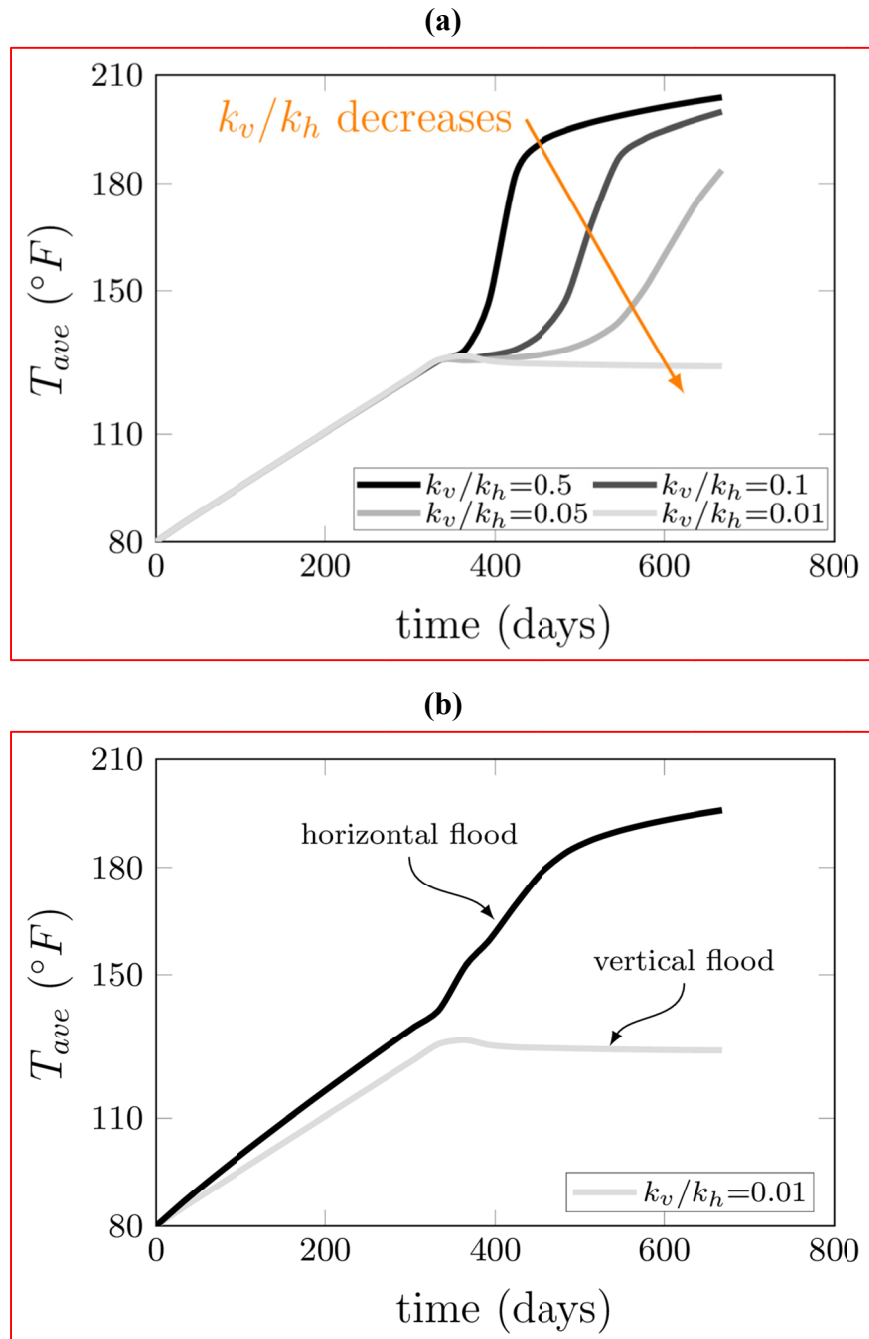


Figure 7.11: Permeability heterogeneities effects on the heating performance where electrical heating for 360 days is flowed by a hot waterflood. While the electrical heating performance is not greatly altered by the permeability heterogeneities, that of waterflooding is strongly affected. (a) As k_v/k_h decreases, the lack of water injectivity causes the vertical flow pattern to be inefficient. For the case of $k_v/k_h=0.01$ water injection becomes impossible. (b) Switching to a horizontal flow pattern greatly recovers the efficacy of the process for the $k_v/k_h=0.01$ case. The vertical separation of the wells is slightly decreased in the horizontal flow, which is evident by the better performance of the electrical heating.

7.5 OPTIMIZATION

This section deals with process optimization in which the net present value (NPV) (the *objective function*) is maximized by adjusting *design parameters* (Gill et al. 1981). The design parameters dictate the process performance. Once identified, proper constraints/dependency should be imposed on them. For example, polymer concentration cannot be negative so this is a necessary constraint on the optimization. For the problem at hand, the design parameters were selected to be: method of heating, duration of the heating, ACP slug size and composition, polymer drive size, and polymer concentration in the polymer drive. Table 7.2 summarizes the design parameters and relevant constraints.

The *NPV* is calculated as

$$NPV = \sum_{i=1}^n \frac{C_i}{(1+r)^i} - C_0, \quad (7.9)$$

where C_i is cash flow at the time of i , r is the discount rate, and C_0 is the undiscounted capital expense. The cash flow is obtained by

$$C = \text{revenue} - \underbrace{(\text{operational} + \text{elec. power} + \text{heating water} + \text{chemicals})}_{\text{costs}}. \quad (7.10)$$

An annual discount rate of 10% and an oil price of 75 \$/bbl (all values are in US dollars) was assumed. Since the royalties and taxes vary from place to place and time to time, the gross revenue was used in the cash flow calculation for simplicity. The unit prices used for cost calculations are shown in Table 7.3. To obtain operational expenses,

it was assumed that cost of water injection is 0.3 \$/bbl and water injection temperature is 212 °F throughout the process.

Table 7.2: Design parameters for optimization

	Denoted by	l^*	u^{**}
Thermal process			
Electrical power (kW)	q	5000	20000
Water injection rate (bbl/day.ft)	Q_w	0.33	4
Length of electrical heating (months)	t_e	1	6
Length of waterflooding (months)	t_{wf}	2	12
Chemical flooding			
Slug size (PV)	t_s	0.2	0.5
Alkali concentration (ppm)	c_a	4500	20000
Co-solvent concentration (wt%)	c_c	0	3
Polymer concentration (ppm)	c_p	1000	4100
Polymer drive size (PV)	t_{pd}	0.5	2
Polymer drive concentration (ppm)	c_{pd}	1000	4100

* l refers to the lower bound.

** u refers to the upper bound.

Table 7.3: Unit prices for cost calculations

Alkali (\$/lb)	0.07
100% active co-solvent (\$/lb)	1.3
100% active polymer (\$/lb)	1.6
Natural gas (\$/MMBTU)	4.5
Electricity (\$/kW.h)	0.07

After setting the objective function and design parameters, the MATLAB pattern search algorithm (The Mathworks Inc. 2010). was used to search for the design parameters which would yield the maximum efficiency. The search algorithm uses a set of vectors $\{v_k\}$, i.e. pattern, to determine which set of points, i.e. mesh, to search at each iteration. Once mesh points are set, the objective function is evaluated over the mesh to

try to find a point that yields a lower objective function value than the incumbent (Audet and Dennis 2004). After finding the local minimum, the search continues to find a possible candidate over the entire pattern that gives a lower value for the objective function. Once a candidate is found, the search process is reiterated. The overall optimization involves a sequence invoking CMG-STARs and UTCHEM as follows:

while x is not the optimum design parameter set

generate a new x

update simulation models for the new x

execute CMG-STARs to simulate the electrical heating & waterflooding

read grid properties (p, T, S_w) once STARs is finished and initialize the UTCHEM grid system

execute UTCHEM to simulate the chemical flood

generate performance report (oil recovery, etc.) using CMG-Report and UTCHEM-history

calculate NPV corresponding to the new x

check if (negative)NPV is minimum; if yes, assign x as the optimum parameter set

Prior to the field optimization, the adequacy of the simulation model should be checked. The field-scale simulations in the next section serve to illustrate this. The final remark is that although the duration of electrical heating is determined by the lower and upper bounds given in Table 7.2, the heating is stopped if the connate water is vaporized and then waterflooding is started. Injection water temperature is 212 °F throughout the entire process.

7.5.1 Field-scale Sensitivity Analysis

Since the optimization process requires robust and representative simulations, the adequacy of the simulation model should be checked prior to optimizations. The

validation of simulation model is performed in the previous section against the chemical corefloods of Fortenberry et al. (2013) and the overall energy balance. Here, a sensitivity analysis of the field process is performed to establish the adequacy of the model. Figure 7.12 shows an example of chemical flood performance conducted after ERH and hot waterflood where average reservoir temperature was raised to ~ 150 °F, corresponding to an average oil viscosity of ~ 1000 *cP*. An equivalent end-point mobility ratio was calculated for each flood using the average value of oil viscosity at the start of chemical flood. The oil viscosity is, however, non-uniform ranging from 50 *cP* in the vicinity of wellbore to 5000 *cP* at the reservoir edges. The simulated oil recoveries, as expected, are lower than the coreflood values as shown in Figure 5.16. For example, for the case of alkaline flooding (corresponding to a mobility ratio $MR_{eq}^0 \sim 100$ in Figure 7.12), the simulated oil recovery in the field is only ~ 20 %OOIP compared to ~ 46 %OOIP in the coreflood.

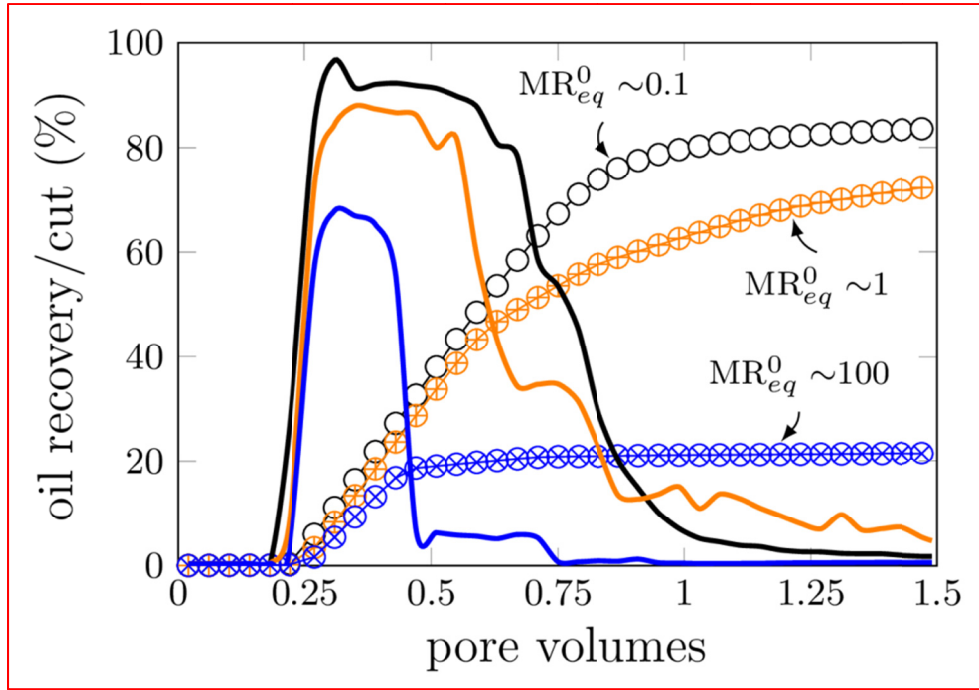


Figure 7.12: Field-scale simulation of chemical flood performance after reservoir temperature is raised to 150 °F corresponding to $\mu_o \sim 1000$ cP. Equivalent end-point mobility ratios shown in the graph are obtained by varying the amount of polymer used.

7.5.2 Results

The parameter set is organized and normalized as follows⁶:

$$x = \{t_s, c_a, c_c, c_p, t_{pd}, c_{pd}, q, t_e, Q_w, t_{wf}\}, \quad x^N = \frac{x - l}{u - l}, \quad (7.11)$$

where x^N represents the normalized set. The optimization iteration summary is shown in Figure 7.13 in terms of objective function (i.e. NPV) and the normalized design parameter set. The optimum NPV is $\sim \$225$ million, which corresponds to a cost of ~ 13 \$/bbl produced oil. The cost breakdown versus the number of simulations (invoked by the optimization algorithm) is shown in Figure 7.14. This cost, however,

⁶ Refer to Table 7.2 for parameter notations and bounds l and u .

does not include the capital costs (see Equation (7.10)), which were not considered in the optimization because the number of wells was fixed. If changed, the drilling/completion costs should be a part of the optimization. Reliable data were not available, but using a rough estimate of \$2.5 *million* per well (Burrowes et al. 2011), the total cost increases to ~23 \$/*bbl produced oil*. Analyzing the cost data reveals that well expenses dominate the spending. Because of smaller inter well spacing compared to processes such as SAGD, the well costs are greater, but so is the oil recovery. However, the number of wells is an optimization problem itself and should be investigated in a future study.

Analyzing the optimum design set (Figure 7.13) shows the results are in line with the recovery scheme presented above. Short electrical heating and high-rate waterflooding are evident from the optimum parameter set. The optimum reservoir temperature at the start of the chemical flood was around 165 °F. The optimum slug and polymer drive sizes were ~0.25 PV and ~1 PV, respectively. A convenient verification of the optimum solution could be obtained by analyzing the chemical slug composition. Intuitively one knows that the optimum recovery should be achieved when the chemical flood is performed at the optimum salinity, as too low alkali concentration fails to reduce IFT and too high alkali concentration increases the slug costs. The optimum case has an alkali concentration of 14000 *ppm* which is in the experimental range of optimum salinity at the slug temperature and co-solvent concentration of 1 *wt%* from Fortenberry et al. (2013). However, alkali consumption depends on the clay type and content (cation exchange capacity) of the actual formation and will usually be higher than in the clean cores used by Fortenberry et al. (2013). The alkali concentration may need to be 20,000

to 40,000 ppm to satisfy consumption. The alkali is inexpensive, so the total operating expenses will not increase very much, but there may be logistical issues depending on the location. The polymer concentrations in the slug and the polymer drive are ~ 3000 ppm and ~ 3500 ppm, respectively. The recovery performance of the optimum design is presented in Figure 7.15 with temperature and oil saturation profiles shown in Figure 7.16 and Figure 7.17.

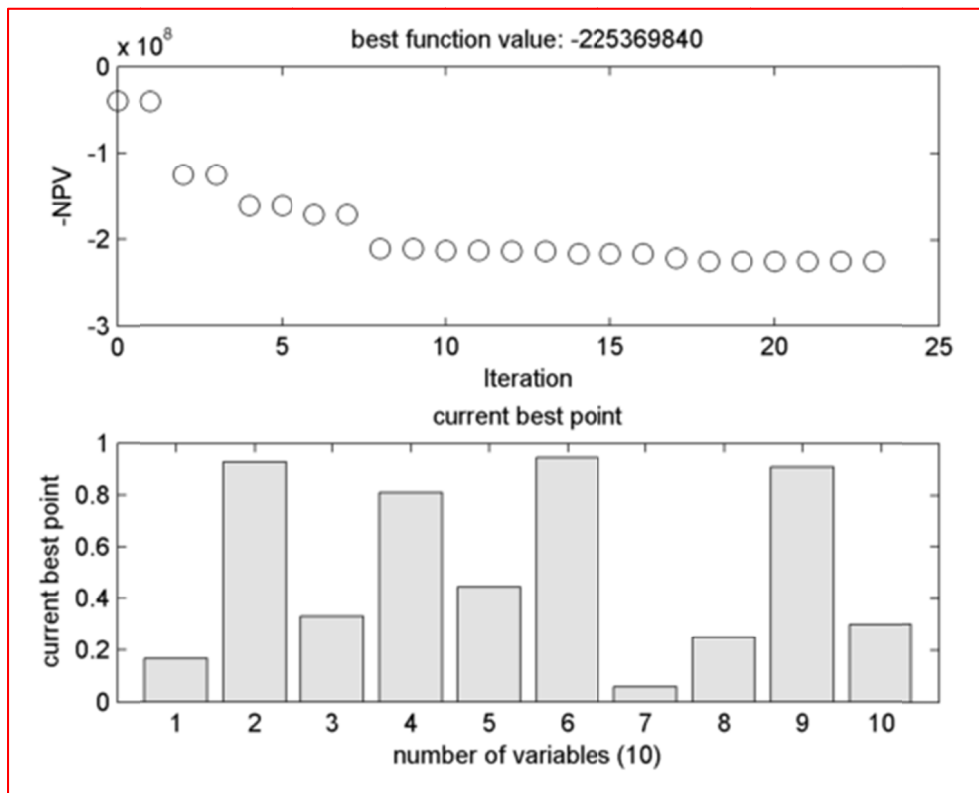


Figure 7.13: Optimization iteration summary in terms of best before-tax discounted NPV (top) and the optimum normalized design parameter set (bottom). The optimization took 23 iterations.

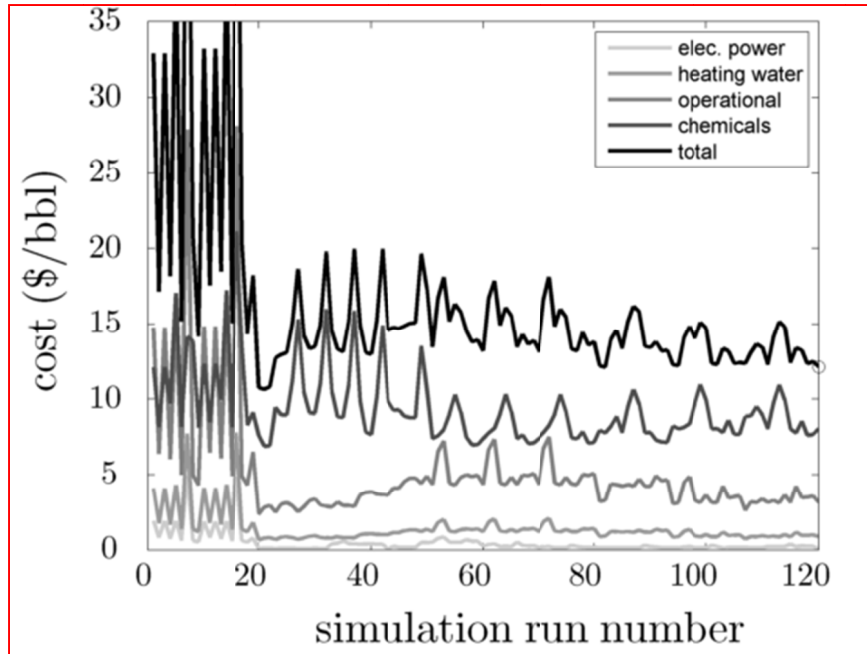


Figure 7.14: Cost breakdown versus the number of simulations invoked by the optimization algorithm. Note that each optimization iteration involves a couple of simulation runs. The optimum solution corresponds to the last simulation.

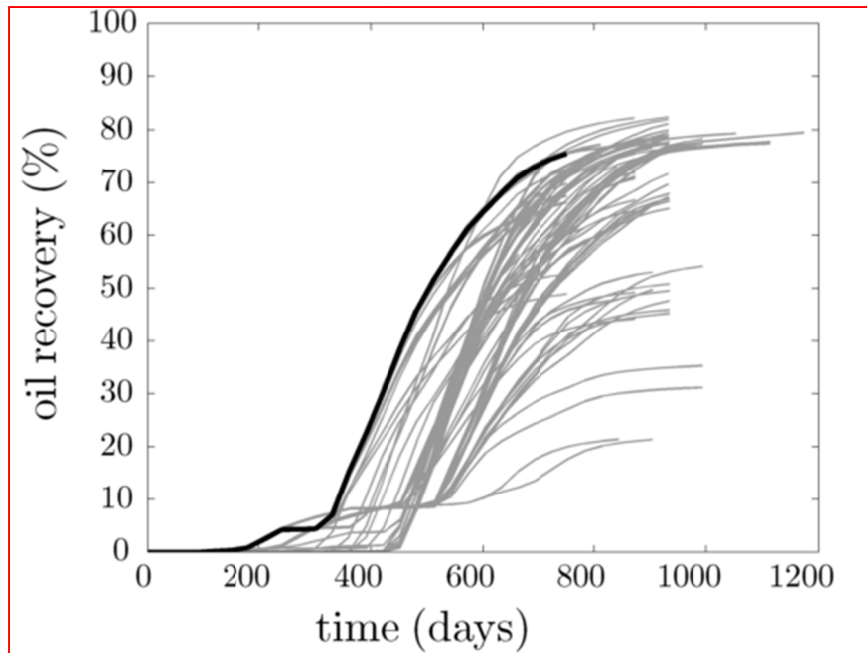


Figure 7.15: Oil recovery for the optimum solution.

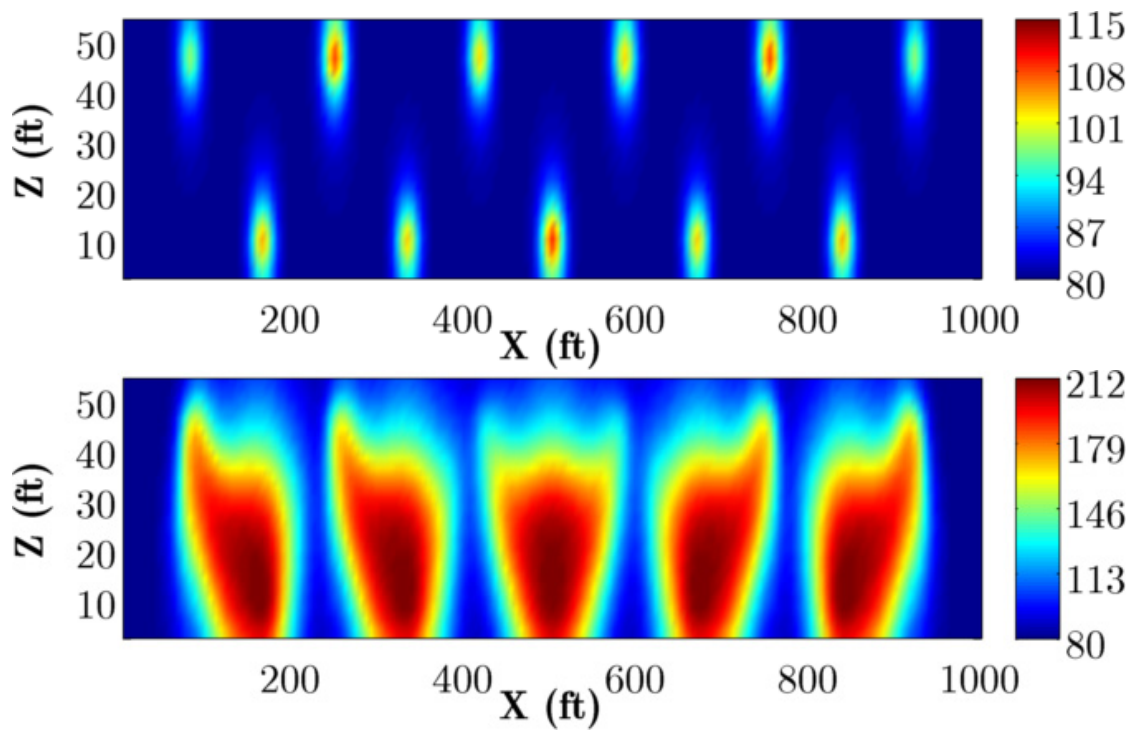


Figure 7.16: Temperature profile at the end of electrical heating (top) and of waterflooding (bottom) for the optimum solution.

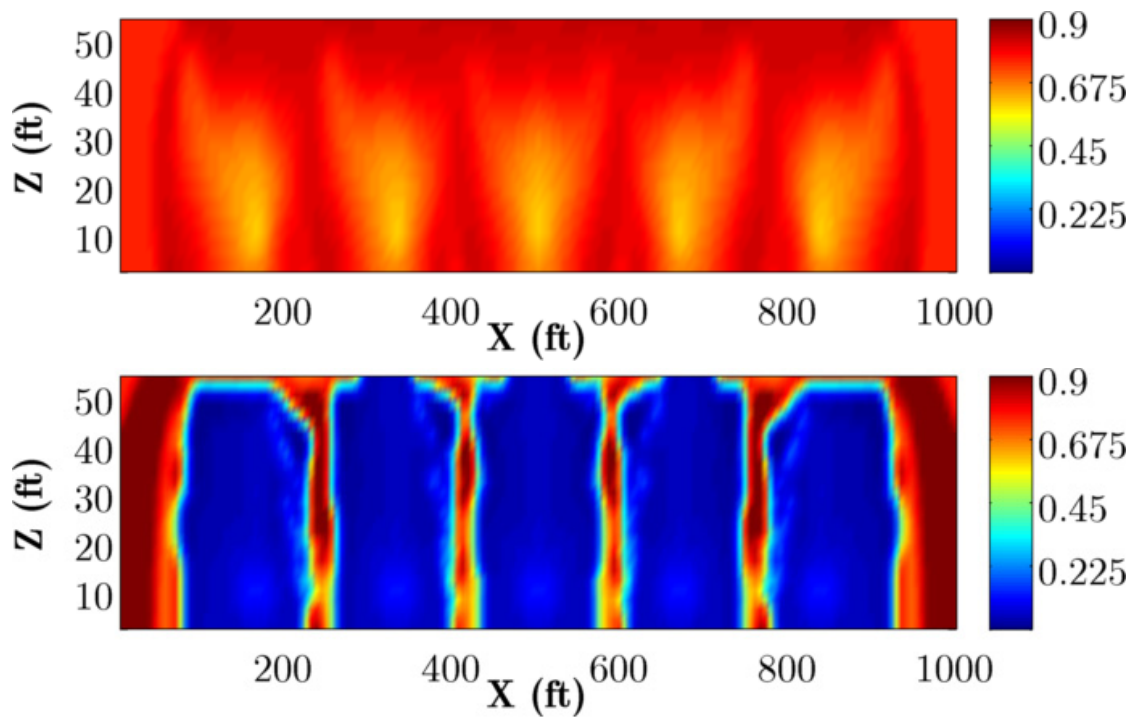


Figure 7.17: Oil saturation at the end of waterflood (top) and chemical flood (bottom) for optimum solution.

Chapter 8: Summary, Conclusions and Recommendations

8.1 SUMMARY AND CONCLUSIONS

A consistent theoretical framework was proposed to describe the mechanisms of microemulsion rheology alteration methods, specifically the addition of co-solvents and branched co-surfactants and the increase in temperature. This framework was used to explain the rheological measurements of Walker (2011). Walker measured the shear viscosity of microemulsions with different co-solvents and temperature. Branched co-surfactants in mixed surfactant formulations greatly facilitate the formation of saddle-splay features (i.e. increase \bar{k}) through concentration heterogeneity resulting from the mutual dependence of surfactant affinity and curvature. Co-solvents reduce the bending modulus by thinning the interface and increasing the saddle-splay modulus by stimulating charge and/or composition fluctuations in the interface membrane. Temperature reduces the bending modulus but typically leaves the saddle-splay modulus unchanged.

Reduction of the bending modulus and increase of the saddle-splay modulus are essential for breaking the long-range interactions and improving the rheology of microemulsions. Because addition of co-solvent modifies both moduli, it is the most effective method in breaking the long-range interactions, often yielding a Newtonian microemulsion. Unlike addition of co-solvent, increase in temperature and addition of branched co-surfactant typically only modifies one of the moduli; therefore, their main effect on rheology is to increase the onset of shear thinning.

A model was developed to describe the shear viscosity of microemulsions that follow a Winsor-type phase behavior. It was argued that the similar rheological behavior of dilute droplet microemulsions and dispersions arises from the strong preference of the monolayer to either oil or water. It is in the lack of strong preference of interface film for water/oil that the interface properties become relevant. The equilibrium microstructure and hence bulk zero-shear viscosity of bicontinuous microemulsions is to the first-order determined by the bending modulus of surfactant monolayer. Although explicit parameterization of the influence of microstructure on the bulk rheology is a difficult task, a qualitative link between the two was obtained. By considering a bicontinuous microemulsion to be a bi-network, a unified formulation to compute the bulk zero-shear viscosity was derived. Comparisons with experimental data revealed that this formulation describes the behavior of the whole range of microemulsions fairly well and that the viscosity is correlated with the bending modulus of the interface. As with shear rate, a modified Cross's model fits the experimental data and that the shear-thinning effect is more pronounced in the highly structured systems and the onset of shear-thinning shifts to higher shear rates with a more flexible interface.

Accurate predictions and realistic simulations under a wide range of reservoir conditions will be an essential element in design and optimization of chemical EOR projects. In order to facilitate these, the microemulsion rheological model discussed above, was implemented in UTCHEM. The implementation was validated through comparisons with experimental data for three corefloods using chemicals to recover

heavy oil. Simulation results showed good agreement with these experimental data and captured the essential dynamics of the recovery process.

In the second part of this dissertation, a hybrid process was developed that combines electrical heating, hot waterflooding and chemical EOR to address the challenges of injectivity and oil production from heavy oil reservoirs. The design of the process was based on (1) an efficient well pattern that allowed for vertical and horizontal flood as needed, (2) an effective electrical heating method that facilitates balanced heating, and (3) alkali-co-solvent-polymer flooding, which is relatively inexpensive and robust. By numerical simulations, it was shown that hybrid thermal-chemical processes (HTCP) make a promising alternate/option for reservoirs where steam injection is not feasible or economical. Additionally, it was shown that a moderate temperature increase is sufficient for the process to work. Key design parameters were identified to be: the design parameters were selected to be: method of heating, duration of the heating, ACP slug size and composition, polymer drive size, and polymer concentration in polymer drive. The optimization revealed that short electrical heating and high-rate high-pressure waterflooding are necessary to minimize the energy use and operational expenses. The optimum slug and polymer drive sizes were ~ 0.25 PV and ~ 1 PV, respectively. It was shown that the well costs dominate the expenditure and the overall cost of the optimized process is in the 20-30 $\$/bbl$.

8.2 RECOMMENDATIONS

It is recommended that further research be undertaken in the following areas:

Experimental determination of interface moduli

The bending and Gaussian moduli of an interface are in principle directly accessible by neutron spin-echo spectroscopy (NSES) (Hellweg and Langevin 1998). In practice, however, the NSES results should be combined with either small-angle neutron scattering (SANS) or with dynamic light scattering (DLS) data to make reliable estimates of the interface moduli (Hellweg and Langevin 1998). It would be interesting to experimentally assess these properties for the surfactants commonly used in the chemical EOR and further confirm the rheology alteration mechanisms presented here.

Variation of rheology model parameters with alteration methods

Increasing the onset of shear thinning behavior of microemulsions is often observed with rheology alteration methods. This effect can be captured in the rheology model of Chapter 4 by using parameter α which equals to 1 and is reduced by the rheology alteration methods. The reduction of α is, however, only qualitatively described in this work. Experimental measurements are needed to quantify the reduction of α with the alteration methods. Additionally, improving the prediction capabilities of the rheology model to make automated parameter adjustment is a prerequisite for the scale up and successful simulation of field-scale chemical flooding; as reservoir heterogeneities may cause formation of different types of complex fluids at different places in the reservoir.

Polymer partitioning

More information on polymer partitioning would help to establish a greater degree of accuracy on the rheology of microemulsion systems that contain polymer. Experimental work needs to examine the link between the two more closely. Establishing

reliable and accurate methods to measure polymer concentration in brine or dilute Type I microemulsion is an essential step in achieving this goal. Further, a study should be undertaken to investigate the effects of temperature and pH variations on the polymer partitioning and the consequences on microemulsion rheology behavior.

Dynamic rheology measurements

In addition to steady-shear measurements, dynamic rheology measurements should be performed to assess the possible viscoelasticity behavior of microemulsions. This would be of more interest when hydrophobically-modified polymers are present since they often help forming complex interfaces with viscoelastic properties. In this case interface shear and dilatational moduli cannot be ignored in describing the macroscopic rheology behavior of microemulsions.

Optimization

Although the current study demonstrated the economic feasibility of the hybrid thermal-chemical processes, it has certain limitations in its optimization approach. First, the optimization process was time consuming and computationally expensive. It would be desirable to design surrogate models such as those suggested by Carrero et al. (2007) to lower the number of simulations and hence the overall optimization time. Second, heterogeneities were left out of the optimization study and their presence is expected to change the optimum scenario obtained here. A future study investigating changes of the optimum scenario/design with reservoir heterogeneities would be very interesting. Third, the optimization was performed for a fixed number of wells. The lack of reliable well costs did not permit a meaningful comparison when the number of wells varied. Further

work needs to be done to obtain reliable well costs and establish the overall optimization design by including the cost of wells in the net present value calculations.

Comparison with other recovery methods

It would be interesting to compare the performance of the hybrid thermal-chemical process presented here to other recovery methods, including the well-established thermal methods such as steam injection and SAGD processes and the hybrid processes that have been suggested by other researchers.

Appendix A

The simulation input files (UTCHEM and CMG-STARS) for hot waterflooding case of Chapter 6 are given in this appendix.

```
CC*****
CC
CC BRIEF DESCRIPTION OF DATA SET : UTCHEM (VERSION 2011_1) *
CC
CC*****
CC HOT WATERFLOOD UTCHEM and CMG - SEAL Project 06/02/2012 *
CC
CC LENGTH (FT) :          PROCESS : waterflooding *
CC THICKNESS (FT) :      INJ. RATE (FT3/DAY) : *
CC WIDTH (FT) :          *
CC POROSITY : 0.30       COORDINATES : CARTESIAN *
CC GRID BLOCKS : 41x1x27 PERMEABILITY : *
CC DATE : 06/02/2012 *
CC
CC
CC*****
CC
CC*****
CC
CC RESERVOIR DESCRIPTION *
CC
CC*****
CC
CC Run number
*---- RUNNO
ENGB02
CC
CC Title and run description
*---- title(i)

CC
CC SIMULATION FLAGS
*---- IMODE IMES IDISPC ICWM ICAP IREACT IBIO ICOORD ITREAC ITC IGAS IENG
      1 4 0 0 0 0 0 1 0 0 0 1
CC
CC no. of gridblocks,flag specifies constant or variable grid size,unit
*---- NX NY NZ IDXYZ IUNIT
      41 1 27 0 0
CC
CC CONSTANT GRID BLOCK SIZE IN X-Y DIRECTIONS (FT)
```

```

*---DX      DY  DZ
  1      600  2
CC
CC total no. of components,no. of tracers,no. of gel components
*---n no ntw nta ngc ng noth
  7  0  0  0  0  0  0
CC
CC Name of the components
*--- SPNAME(I),I=1,N
WATER
OIL
SURFACTANT
POLYMER
ANION
CALCIUM
ALC1
CC
CC FLAG INDICATING IF THE COMPONENT IS INCLUDED IN CALCULATIONS OR NOT
*---ICF(KC) FOR KC=1,N
  1  1  1  1  1  1  0  1  1  1  1  1
CC
CC*****
CC
CC  OUTPUT OPTIONS
CC
CC*****
CC
CC
CC FLAG FOR PV OR DAYS
*---ICUMTM ISTOP IOUTGMS
  1  1  0
CC
CC FLAG INDICATING IF THE PROFILE OF KCTH COMPONENT SHOULD BE WRITTEN
*--- IPRFLG(KC),KC=1,N
  1  1  1  1  1  1  1  0  1  1  1  1  1
CC
CC FLAG FOR PRES.,SAT.,TOTAL CONC.,TRACER CONC.,CAP.,GEL, ALKALINE PROFILES
*--- IPPRES IPSAT IPCTOT IPBIO IPCAP IPGEL IPALK IPTEMP IPOBS
  1  1  1  0  0  0  1  1  0
CC
CC FLAG FOR WRITING SEVERAL PROPERTIES TO UNIT 4 (Prof)
*--- ICKL IVIS IPER ICNM ICSE IHYSTP IFOAMP INONEQ
  0  1  1  0  0  0  0  0
CC
CC FLAG for variables to PROF output file
*--- IADS IVEL IRKF IPHSE
  0  0  1  0
CC
CC*****
CC
CC  RESERVOIR PROPERTIES
CC
CC*****

```

```

CC
CC
CC MAX. SIMULATION TIME ( DAYS)
*---- TMAX
      1.5
CC
CC ROCK COMPRESSIBILITY (1/PSI), STAND. PRESSURE(Psia)
*---- COMPR      PSTAND
      0.          420
CC
CC FLAGS INDICATING CONSTANT OR VARIABLE POROSITY, X,Y,AND Z PERMEABILITY
*---- IPOR1 IPERMX IPERMY IPERMZ IMOD  ITRNZ  INTG
      0  0  0  0  0  0  0
CC
CC CONSTANT POROSITY OVER RESERVOIR
*---- POR(I),FOR I=1 TO NX*NY*NZ
      0.25
CC
CC CONSTANT PERMEABILITY OVER RESERVOIR
*---- PERMX(I),FOR I=1 TO NX*NY*NZ
      2000
CC
CC Y DIRECTION PERMEABILITY IS DEPENDENT ON X DIRECTION PERMEABILITY
*---- CONSTANT PERMEABILITY MULTIPLIER FOR Y DIRECTION PERMEABILITY
      2000
CC
CC CONSTANT PERMEABILITY OVER RESERVOIR
*---- PERMZ(I),FOR I=1 TO NX*NY*NZ
      1000
CC
CC FLAG FOR CONSTANT OR VARIABLE DEPTH, PRESSURE, WATER SATURATION,INITIAL
AQUEOUS PHASE cOMPOSITIONS
*----DEPTH IPRESS ISWI ICWI
      0  0  0  -1
CC
CC CONSTANT DEPTH (FT)
*---- D111
      0
CC
CC CONSTANT PRESSURE (PSIA)
*---- PRESS1
      420
CC
CC CONSTANT INITIAL WATER SATURATION
*---- SWI
      0.45
CC
CC BRINE SALINITY AND DIVALENT CATION CONCENTRATION (MEQ/ML)
*---- C50  C60
      0.3419  1.E-6
CC
CC*****
CC

```



```

CC PHYSICAL PROPERTY DATA *
CC *
CC*****
CC
CC
CC OIL CONC. AT PLAIT POINT FOR TYPE II(+)AND TYPE II(-), CMC
*---- c2plc c2prc epsme ihand
      0 1 0.003 0
CC
CC FLAG INDICATING TYPE OF PHASE BEHAVIOR PARAMETERS
*---- IFGHBN
      0
CC SLOPE AND INTERCEPT OF BINODAL CURVE AT ZERO, OPT., AND 2XOPT SALINITY
CC FOR ALCOHOL 1
*----HBNS70 HBNC70 HBNS71 HBNC71 HBNS72 HBNC72
      0.0 .062 0.036 0.034 0.0 0.25
CC
CC SLOPE OF BINODAL WITH TEMP., SLOPE OF SALINITY WITH TEMP. (1/F)
*---- HBNT0 HBNT1 HBNT2 CSET(0.00415)
      0.000 0.000 0.000 0.00
CC SLOPE AND INTERCEPT OF BINODAL CURVE AT ZERO, OPT., AND 2XOPT SALINITY
CC FOR ALCOHOL 2
*----HBNS80 HBNC80 HBNS81 HBNC81 HBNS82 HBNC82
      0. 0. 0. 0. 0. 0.
CC
CC LOWER AND UPPER EFFECTIVE SALINITY FOR ALCOHOL 1 AND ALCOHOL 2
*----CSEL7 CSEU7 CSEL8 CSEU8
      0.28 0.6 0. 0.
CC
CC THE CSE SLOPE PARAMETER FOR CALCIUM AND ALCOHOL 1 AND ALCOHOL 2
*----BETA6 BETA7 BETA8
      0.0 0.1 0.
CC
CC FLAG FOR ALCOHOL PART. MODEL AND PARTITION COEFFICIENTS
*----IALC OPSK7O OPSK7S OPSK8O OPSK8S
      0 0. 0. 0. 0.
CC
CC NO. OF ITERATIONS, AND TOLERANCE
*----NALMAX EPSALC
      20 0.0001
CC
CC ALCOHOL 1 PARTITIONING PARAMETERS IF IAIC=1
*----AKWC7 AKWS7 AKM7 AK7 PT7
      4.671 1.79 48. 35.31 0.222
CC
CC ALCOHOL 2 PARTITIONING PARAMETERS IF IALC=1
*----AKWC8 AKWS8 AKM8 AK8 PT8
      0. 0. 0. 0. 0.
CC
CC IFT MODEL FLAG
*----IFT
      1
CC

```

```

CC INTERFACIAL TENSION PARAMETERS
*--- CHUH  AHUH
    0.3  10.0
CC
CC LOG10 OF OIL/WATER INTERFACIAL TENSION
*---XIFTW
    1.4
CC
CC
*---IMASS icor
    0  0
cc
cc
*--- iwalt iwalf
    0  0
CC
CC CAPILLARY DESATURATION PARAMETERS FOR PHASE 1, 2, AND 3
*---ITRAP T11  T22  T33
    0  565.  6000.  2200.
CC
CC RELATIVE PERM and pc model
*---IPERM  IRTYPE
    0  0
CC
CC FLAG FOR CONSTANT OR VARIABLE REL. PERM. PARAMETERS
*---ISRW IPRW IEW
    0  0  0
CC
CC CONSTANT RES. SATURATION OF PHASES 1,2,AND 3 AT LOW CAPILLARY NO.
*---S1RWC S2RWC S3RWC
    0.28 .45 0.28
CC
CC CONSTANT ENDPOINT REL. PERM. OF PHASES 1,2,AND 3 AT LOW CAPILLARY NO.
*---P1RW P2RW P3RW
    0.042 1.0 1.
CC
CC CONSTANT REL. PERM. EXPONENT OF PHASES 1,2,AND 3 AT LOW CAPILLARY NO.
*---E1W E2W E3W
    2.4 1.3 1.3
CC
CC WATER AND OIL VISCOSITY , RESERVOIR TEMPERATURE
*---VIS1 VIS2 TEMPV
    0.29 60.0 203.
CC
CC VISCOSITY-TEMP PARAMETERS 5326.8
*---BVI(1) BVI(2)
    0.0 5000.
CC Mu_p: the polymer viscosity in equation 5.4; delta_0: equation 5.5; c: equation 4.13
CC COMPOSITIONAL PHASE VISCOSITY PARAMETERS
*--- Nu  Nu_prime Mu_p delta_0 c
    0.0865 0.9 0. 1. 0.
CC
CC PARAMETERS TO CALCULATE POLYMER VISCOSITY AT ZERO SHEAR RATE

```

```

*----AP1  AP2  AP3
      30.0  160.0  2700
CC
CC PARAMETER TO COMPUTE CSEP,MIN. CSEP, AND SLOPE OF LOG VIS. VS. LOG CSEP
*----BETAP CSE1  SSLOPE
      1  0.01  -0.15
CC
CC PARAMETER FOR SHEAR RATE DEPENDENCE OF POLYMER VISCOSITY
*----GAMMAC GAMHF  POWN  IPMOD  ishear  rweff  GAMHF2
      1.0  1.e6  1.643  0  0  0.25  0
CC
CC FLAG FOR POLYMER PARTITIONING, PERM. REDUCTION PARAMETERS
*----IPOLYM EPHI3 EPHI4  BRK  CRK  RKCUT
      1  1.  0.92  0.  0.4  10
CC
CC SPECIFIC WEIGHT FOR COMPONENTS 1,2,3,7,AND 8 , AND GRAVITY FLAG
*----DEN1 DEN2  DEN23  DEN3  DEN7 DEN8  IDEN
      0.433 0.416  0.416  0.42  0.24 0  1
CC
CC FLAG FOR CHOICE OF UNITS ( 0:BOTTOMHOLE CONDITION , 1: STOCK TANK)
*----ISTB
      0
CC
CC COMPRESSIBILITY FOR VOL. OCCUPYING COMPONENTS 1,2,3,7,AND 8
*----COMPC(1) COMPC(2) COMPC(3) COMPC(7) COMPC(8)
      0.0 0.0  0.  0.  0.
CC
CC CAPILLARY PRESSURE PARAMETERS, WATER-WET OR OIL-WET PC CURVE FLAG
*----ICPC IEPC IOW
      0  0  0
CC
CC
*----CPC
      0.00
CC
CC
*----EPC
      2.
CC
CC MOLECULAR DIFFUSIVITY OF KCTH COMPONENT IN PHASE 1 (D(KC),KC=1,N)
*----D(1) D(2) D(3) D(4) D(5) D(6) D(7) D(8) D(9) D(10) D(11)
      13*0.
CC
CC MOLECULAR DIFFUSIVITY OF KCTH COMPONENT IN PHASE 2 (D(KC),KC=1,N)
*----D(1) D(2) D(3) D(4) D(5) D(6) D(7) D(8) D(9) D(10) D(11)
      13*0.
CC
CC MOLECULAR DIFFUSIVITY OF KCTH COMPONENT IN PHASE 3 (D(KC),KC=1,N)
*----D(1) D(2) D(3) D(4) D(5) D(6) D(7) D(8) D(9) D(10) D(11)
      13*0.
CC
CC LONGITUDINAL AND TRANSVERSE DISPERSIVITY OF PHASE 1 (FT)
*----ALPHAL(1)  ALPHAT(1)

```

```

0.0    0.000
CC
CC LONGITUDINAL AND TRANSVERSE DISPERSIVITY OF PHASE 2 (FT)
*----ALPHAL(2)  ALPHAT(2)
0.0    0.000
CC
CC LONGITUDINAL AND TRANSVERSE DISPERSIVITY OF PHASE 3 (FT)
*----ALPHAL(3)  ALPHAT(3)
0.0    0.000
CC
CC FLAG TO SPECIFY ORGANIC ADSORPTION CALCULATION
*----IADSO
0
CC
CC SURFACTANT AND POLYMER ADSORPTION PARAMETERS
*----AD31 AD32  B3D  AD41  AD42  B4D  IADK, IADS1, FADS REFK
0.0 0.0 1000. 0.0 0.0 100.0 0 0 0 0 10
CC
CC
*----
0 0 0 300
CC
CC INITIAL TEMPERATURE
*--- ITEMP
0
CC
CC INITIAL TEMPERATURE
*--- TEMPI (F)
203
CC
CC ROCK DENSITY, CONDUCTIVITY, HEAT CAPACITY
*---- DENS  CRTC  CVSPR  CVSPL(1) CVSPL(2) CVSPL(3)
34.56 33.6 1 1.0 0.5 1.
CC
CC HEATLOSS FLAG, ANALYTICAL SOLUTION
*---- IHLOS IANAL
0 0
CC
CC*****
CC
CC WELL DATA
CC
CC*****
CC
CC
CC FLAG FOR BOUNDARIES
*--- IBOUND IZONE
0 0
CC
CC TOTAL NUMBER OF WELLS, WELL RADIUS FLAG, FLAG FOR TIME OR COURANT NO.
*---- NWELL IRO ITSTEP  NWREL
3 2 1 3
CC

```

```

CC WELL ID,LOCATIONS,AND FLAG FOR SPECIFYING WELL TYPE, WELL RADIUS, SKIN
*---- IDW IW JW IFLAG RW SWELL IDIR IFIRST ILAST IPRF
  1  1  2  2  0.078  0  1  7  7  0
CC
CC WELL NAME
*---- WELNAM
Prod-1
CC
CC ICHEK , MAX. AND MIN. ALLOWABLE BOTTOMHOLE PRESSURE AND RATE
*---- ICHEK PWFMIN PWFMAX QTMIN QTMAX
  0  0  4000  0  9000
CC
CC WELL ID,LOCATIONS,AND FLAG FOR SPECIFYING WELL TYPE, WELL RADIUS, SKIN
*---- IDW IW JW IFLAG RW SWELL IDIR IFIRST ILAST IPRF
  2  1  2  2  0.078  0  1  35  35  0
CC
CC WELL NAME
*---- WELNAM
Prod-2
CC
CC ICHEK , MAX. AND MIN. ALLOWABLE BOTTOMHOLE PRESSURE AND RATE
*---- ICHEK PWFMIN PWFMAX QTMIN QTMAX
  0  0  4000  0  9000
CC
CC WELL ID,LOCATIONS,AND FLAG FOR SPECIFYING WELL TYPE, WELL RADIUS, SKIN
*---- IDW IW JW IFLAG RW SWELL IDIR IFIRST ILAST IPRF
  3  1  23  1  0.008  0  1  21  21  0
CC
CC WELL NAME
*---- WELNAM
Inj-1
CC
CC ICHEK , MAX. AND MIN. ALLOWABLE BOTTOMHOLE PRESSURE AND RATE
*---- ICHEK PWFMIN PWFMAX QTMIN QTMAX
  0  0  4000  0  9000
CC
CC ID, BOTTOM HOLE PRESSURE FOR PRESSURE CONSTRAINT WELL (IFLAG=2 OR 3)
*---- ID PWF
  1  420
CC
CC ID, BOTTOM HOLE PRESSURE FOR PRESSURE CONSTRAINT WELL (IFLAG=2 OR 3)
*---- ID PWF
  2  420
CC
CC ID,INJ. RATE AND INJ. COMP. FOR RATE CONS. WELLS FOR EACH PHASE (L=1,3)
*---- ID QI(M,L) C(M,KC,L)
  3  500 1.  0.  0.0  0.0  0.000001  0.000001  0.0  0.  0.000001  0.1887  0.1887  110.011  0.0
  3  0.  13*0.
  3  0.  13*0.
CC
CC
*---- ID, INJ. TEMP (F)
  3  212

```

```

CC
CC CUM. INJ. TIME , AND INTERVALS (PV OR DAY) FOR WRITING TO OUTPUT FILES
*---- TINJ CUMPR1 CUMHI1 WRHPV WRPRF RSTC
      0.25  0.05  0.02  0.02  0.05  1000000000000000
CC
CC THE INI. TIME STEP,CONC. TOLERANCE,MAX.,MIN. time steps
*---- DT  DELC(I)      DTMAX      DTMIN
      0.00001 0.05 0.05 0.05 0.05 0.05 0.05 0.05  0.2 .001
cc
cc
*--- IBMODE
      0
CC
CC IRO, ITIME, NEW FLAGS FOR ALL THE WELLS
*---- IRO ITIME IFLAG(M),M=1,NWELL
      2  1  2 2 1
CC
CC NUMBER OF WELLS CHANGES IN LOCATION OR SKIN OR PWF
*----NWEL1
      0
CC
CC NUMBER OF WELLS WITH RATE CHANGES, ID
*----NWEL2 ID
      1  3
CC
CC ID,INJ. RATE AND INJ. COMP. FOR RATE CONS. WELLS FOR EACH PHASE (L=1,3)
*---- ID  QI(M,L)  C(M,KC,L)
      3  500  1.  0.  0.0  0.0  0.000001  0.000001  0.  0.  0.0000001  0.094  0.094  111.043  0.00000001
      3  0.  13*0.
      3  0.  13*0.
CC
CC
*--- ID, INJ. TEMP (F)
      3  212
CC
CC CUM. INJ. TIME , AND INTERVALS (PV OR DAY) FOR ERITING TO OUTPUT FILES
*----TINJ CUMPR1 CUMHI1 WRHPV WRPRF RSTC
      1.5  0.05  0.02  0.02  0.05  1000000000000000
CC
CC FOR IMES=2, ITIME=1, INI. DT ,CONC. TOLERANCE, MAX.,MIN. COURANT NUMBERS
*----DT  DCLIM(KC=1,16)      CNMAX  CNMIN
      0.00001 0.05 0.05 0.05 0.05 0.05 0.05 0.05  0.5 .001

```

```

**          OVERVIEW
**          =====
**  PURPOSE: Hot waterflooding case of Chapter 6.
**  ===== INPUT/OUTPUT CONTROL =====
RESULTS SIMULATOR STARS
*interrupt *stop
*title1 "
*title2 '1P_WF.dat'
*inunit *field  ** output same as input
*wprn *grid 20
*outprn *grid sw viso visw temp pres HEATCAP OBHLOSS THCONDUCT
*outprn res all
*outprn *well *all
*wprn *iter 20
wprn sector 2
wsrf sector 2
wsrf grid 0
*outsrf grid sw viso visw temp pres HEATCAP OBHLOSS THCONDUCT CMPDENW CMPDENO
outsrf special blockvar temp 7 1 26
      blockvar temp 35 1 26
      blockvar temp 21 1 5
OBHLOSSCUM
OBHLOSSRATE
** ===== GRID AND RESERVOIR DEFINITION =====
*grid *cart 41 1 27
*di *CON 1
*dj *con 600
*dk *CON 2
*por *con 0.25
*permi *con 2000
*permj *equalsi
*permk *equalsi / 2
*SECTORARRAY 'Reservoir' *KVAR 27*2
end-grid
** ===== ROCK PROPERTIES =====
*ROCKTYPE 1  ** reservoir rock
*cpor 0
*prpor 420
*rockcp 34.56
*thconr 33.6
*thconw 8.
*thcono 1.8
*thcong 0.0
**HLOSSPROP *OVERBUR 31.8 16.64 *UNDERBUR 31.8 16.64
**HLOSST 80.
*THTYPE *KVAR 27*1
** ===== FLUID DEFINITIONS =====
*model 2 2 2  ** Components are water and dead oil. Most water
      ** properties are defaulted (=0). Dead oil K values
      ** are zero, and no gas properties are needed.

```

```

*compname  'Water' 'OIL'
**
*cmm      18.02  600
*pcrit    3206.2  0
*tcrit    705.4  0
*cpl1     18.02  300
*cpl2     0.0    0.0
*cpl3     0.0    0.0
*cpl4     0.0    0.0
*massden  62.4   60.
*cp       0.     0.
*ct1      0.     0.

```

```

*visctable
**   Temp
81   0   5000
99   0   2037
129  0   584
210  0   57
300  0   13
400  0   8
430  0   7

```

```

*prsr 420
*temr 0.
*psurf 14.7
*tsurf 70

```

```

** ===== ROCK-FLUID PROPERTIES =====

```

```

*rockfluid
*swt ** Water-oil relative permeabilities
** Sw   Krw   Krow
** ---- -
0.28  0           1.
0.33  0.000733676 0.76626077
0.38  0.003872365 0.54803804
0.43  0.010246966 0.348467859
0.48  0.020438464 0.172923716
0.53  0.034916626 0.033928613
0.55  0.042       .0

```

```

** ===== INITIAL CONDITIONS =====

```

```

*initial
*pres *con 420
*temp *con 203
*SW *con 0.45

```

```

** ===== NUMERICAL CONTROL =====

```

```

*numerical
*dtmax 100
*norm  press 50 satur 0.2 temp 50
*north 100
*itermax 100
**SDEGREE 2
*run

```



```

** ===== RECURRENT DATA =====
*DATE 2014 01 01
*DTWELL 0.001
*DTMAX 5
  well 1 'Producer 1'
  well 2 'Producer 2'
  well 3 'Injector 1'
  producer 'Producer 1' 'Producer 2'
  operate *min bhp 420  ** Starting liquid rate is 100 BPD
    ** wrad  geofac  wfrac  skin
  *geometry j 0.08  0.249  1  0
  perf *GEO 'Producer 1'
  7 1:1 26 1.
  perf *GEO 'Producer 2'
  35 1:1 26 1.
  injector mobweight *implicit 'Injector 1'
  *incomp water 1.0 0.0
  *QUAL 0.0
  *TINJW 212.0
*operate *max stw 89.0472
*operate max bhp 4000
  ** wrad  geofac  wfrac  skin
  *geometry j 0.079  0.249  1  0
  *perf *GEO 'Injector 1'
  21 1:1 5 1.
  *OPEN 'Producer 1' 'Producer 2'
  *OPEN 'Injector 1'
  wprn grid time
  wsrf grid time

time 0.001
time 66.46  **0.1 PV
time 332.24  **0.5 PV
time 664.37  **1.0 PV
time 996.4  **1.5 PV
STOP

```

Appendix B

The input files for ACP-1, ACP-2, and ALK Corefloods are given here.

```
CC*****
CC
CC BRIEF DESCRIPTION OF DATA SET : UTCHEM (VERSION 2011_1) *
CC
CC*****
CC ALKALI-COSOLVENT-POLYMER Coreflood (ACP-1 or ACP2.4) *
CC
CC
CC
CC PROCESS : 1D ALKALINE/SURFACTANT/POLYMER *
CC
CC
CC COORDINATES : CARTESIAN *
CC
CC
CC GRID BLOCKS : 100X1X1 *
CC DATE : 05/05/2014 *
CC
CC*****
CC
CC*****
CC
CC PART1 : RESERVOIR DESCRIPTION *
CC
CC*****
CC
CC
*---- RUNNO
ACP-24
CC
CC
*----TITLE

CC
CC SIMULATION FLAGS
*---- IMODE IMES IDISPC ICWM ICAP IREACT IBIO ICOORD ITREAC ITC IGAS IENG
      1 4 0 0 0 3 0 1 0 0 0 0
CC
CC NUMBER OF GRID BLOCKS AND FLAG SPECIFIES CONSTANT OR VARIABLE GRID SIZE
*----NX NY NZ IDXYZ IUNIT
      100 1 1 0 0
CC
CC CONSTANT GRID BLOCK SIZE IN X-Y DIRECTIONS (FT)
*----DX DY DZ
      0.00953 0.1351 0.1351
CC
```

```

CC TOTAL NO. OF COMPONENTS, NO. OF TRACERS,NO. OF GEL COMPONENTS
*---N NO NTW NTA NGC NG NOTH
  13 0 0 0 5 0 0
CC
CC
*--- SPNAME(I),I=1,N
WATER
OIL
SURFACTANT
POLYMER
ANION
CALCIUM
ALC1
NONE
MG
CO3
Na
Hydr.
Acid
CC
CC FLAG INDICATING IF THE COMPONENT IS INCLUDED IN CALCULATIONS OR NOT
*---ICF(KC) FOR KC=1,N
  1 1 1 1 1 1 1 0 1 1 1 1 1
CC
CC*****
CC
CC PART2 : OUTPUT OPTIONS
CC
CC*****
CC
CC
CC FLAG FOR PV OR DAYS
*---ICUMTM ISTOP IOUTGMS
  1 1 0
CC
CC FLAG INDICATING IF THE PROFILE OF KCTH COMPONENT SHOULD BE WRITTEN
*---IPRFLG(KC),KC=1,N
  1 1 1 1 1 1 1 0 1 1 1 1 1
CC
CC FLAG FOR PRES,SAT.,TOTAL CONC.,TRACER CONC.,CAP.,GEL, ALKALINE PROFILES
*---IPPRES IPSAT IPCTOT IPTBIO IPCAP IPGEL IPALK IPTEMP IPOBs
  1 1 1 0 0 0 1 0 0
CC
CC FLAG FOR WRITING SEVERAL PROPERTIES
*---ICKL IVIS IPER ICNM ICSE IFOAM IHYST INONEQ
  1 1 1 1 1 0 0 0
CC
CC FLAG FOR WRITING SEVERAL PROPERTIES TO PROF
*---IADS IVEL IRKF IPHSE
  1 1 1 1
CC
CC*****
CC

```

```

CC PART3 : RESERVOIR PROPERTIES *
CC *
CC*****
CC
CC
CC MAX. SIMULATION TIME ( PV )
*---- TMAX
    2.5
CC
CC ROCK COMPRESSIBILITY (1/PSI), STAND. PRESSURE(PSI)
*----COMPR    PSTAND
    0.    0.
CC
CC FLAGS INDICATION CONSTANT OR VARIABLE POROSITY, X,Y,AND Z PERMEABILITY
*----IPOR1 IPERMX IPERMY IPERMZ IMOD ITRNZ INTG
    0  0  3  3  0  0  0
CC
CC CONSTANT POROSITY
*----PORC1
    0.231
CC
CC CONSTANT X-PERMEABILITY (MILIDARCY)
*----PERMX(I)
    3505.0
CC
CC CONSTANT Y-PERMEABILITY MULTIPLIER
*----FACTY
    1.
CC
CC CONSTANT Z-PERMEABILITY MULTIPLIER
*----FACTZ
    1.
CC
CC FLAG FOR CONSTANT OR VARIABLE DEPTH, PRESSURE,WATER SATURATION
*----DEPTH IPRESS ISWI ICWI
    0  0  0  -1
CC
CC DEPTH OF THE FIRT GRID BLOCK
*----DEPTH(I)
    0.0
CC
CC INITIAL CORE PRESSURE
*----PRESS
    14.47
CC
CC INITIAL WATER SATURATION
*----SWI
    0.4
CC
CC CONSTANT CHLORIDE AND CALCIUM CONCENTRATIONS (MEQ/ML)
*----C50    C60
    0.34  1.E-006
CC

```

```

CC*****
CC
CC PART4 : PHYSICAL PROPERTY DATA
CC
CC*****
CC
CC
CC OIL CONC. AT PLAIT POINT FOR TYPE II(+)AND TYPE II(-), CMC
*---- C2PLC C2PRC EPSME IHAND
      0.  1.  .0010510093751  0
CC
CC FLAG INDICATING TYPE OF PHASE BEHAVIOR PARAMETERS
*---- IFGHBN
      0
CC SLOPE AND INTERCEPT OF BINODAL CURVE AT ZERO, OPT., AND 2XOPT SALINITY
CC FOR ALCOHOL 1
*----HBNS70 HBNC70 HBNS71 HBNC71 HBNS72 HBNC72
      0.0 .062 0.036 0.034 0.0 0.15
CC SLOPE AND INTERCEPT OF BINODAL CURVE AT ZERO, OPT., AND 2XOPT SALINITY
CC FOR ALCOHOL 2
*----HBNS80 HBNC80 HBNS81 HBNC81 HBNS82 HBNC82
      0.  0.  0.  0.  0.  0.
CC
CC LOWER AND UPPER EFFECTIVE SALINITY FOR ALCOHOL 1 AND ALCOHOL 2
*----CSEL7 CSEU7 CSEL8 CSEU8
      0.28 0.6 0.  0.
CC
CC THE CSE SLOPE PARAMETER FOR CALCIUM AND ALCOHOL 1 AND ALCOHOL 2
*----BETA6 BETA7 BETA8
      0.0 0.  0.
CC
CC FLAG FOR ALCOHOL PART. MODEL AND PARTITION COEFFICIENTS
*----IALC OPSK7O OPSK7S OPSK8O OPSK8S
      0 0.  0.  0.  0.
CC
CC NO. OF ITERATIONS, AND TOLERANCE
*----NALMAX EPSALC
      20  0.0001
CC
CC ALCOHOL 1 PARTITIONING PARAMETERS IF IAIC=1
*----AKWC7 AKWS7 AKM7 AK7  PT7
      4.671 1.79 48. 35.31 0.222
CC
CC ALCOHOL 2 PARTITIONING PARAMETERS IF IALC=1
*----AKWC8 AKWS8 AKM8 AK8  PT8
      0.  0.  0.  0.  0.
CC
CC IFT MODEL FLAG
*----IFT
      1
CC
CC INTERFACIAL TENSION PARAMETERS
*---- CHUH  AHUH

```

```

0.3  10.0
CC
CC LOG10 OF OIL/WATER INTERFACIAL TENSION
*---XIFTW
  1.3
CC
CC
*---IMASS icor
  0  0
cc
cc
*--- iwalt iwalf
  0  0
CC
CC CAPILLARY DESATURATION PARAMETERS FOR PHASE 1, 2, AND 3
*---ITRAP T11  T22  T33
  2  300.  2800.  300.
CC
CC RELATIVE PERM and pc model
*---IPERM  IRTYPE
  0  0
CC
CC FLAG FOR CONSTANT OR VARIABLE REL. PERM. PARAMETERS
*---ISRW IPRW IEW
  0  0  0
CC
CC CONSTANT RES. SATURATION OF PHASES 1,2,AND 3 AT LOW CAPILLARY NO.
*---S1RWC S2RWC S3RWC
  0.15  0.60  0.15
CC
CC CONSTANT ENDPOINT REL. PERM. OF PHASES 1,2,AND 3 AT LOW CAPILLARY NO.
*---P1RW P2RW P3RW
  0.025  1.0  0.025
CC
CC CONSTANT REL. PERM. EXPONENT OF PHASES 1,2,AND 3 AT LOW CAPILLARY NO.
*---E1W E2W E3W
  2.  2.  2.
CC
CC RES. SATURATION OF HPASES 1,2,AND 3 AT HIGH CAPILLARY NO.
*---S1RC S2RC S3RC
  0.0  0.0  0.0
CC
CC ENDPOINT REL. PERM. OF PHASES 1,2,AND 3 AT HIGH CAPILLARY NO.
*---P1RC P2RC P3RC
  1.  1.0  1.
CC
CC REL. PERM. EXPONENT OF PHASES 1,2,AND 3 AT HIGH CAPILLARY NO.
*---E13CW E23C E31C
  1.  1.0  1.
CC
CC WATER AND OIL VISCOSITY , RESERVOIR TEMPERATURE
*---VIS1 VIS2 TEMPV
  0.56  970.0  0.

```

```

CC Mu_p: the polymer viscosity in equation 5.4; delta_0: equation 5.5; c: equation 4.13
CC COMPOSITIONAL PHASE VISCOSITY PARAMETERS
*---- Nu      Nu_prime Mu_p delta_0 c
      1.9      4.5  2000.  1.  0.0
CC
CC PARAMETERS TO CALCULATE POLYMER VISCOSITY AT ZERO SHEAR RATE
*----AP1  AP2  AP3
      80.0  200.0  28000
CC
CC PARAMETER TO COMPUTE CSEP,MIN. CSEP, AND SLOPE OF LOG VIS. VS. LOG CSEP
*----BETAP CSE1  SSLOPE
      1  0.01  -0.39
CC
CC PARAMETER FOR SHEAR RATE DEPENDENCE OF POLYMER VISCOSITY
*----GAMMAC GAMHF  POWN  IPMOD  ishear rweff GAMHF2
      4.0  0.35  1.6  0  0  0.25  0
CC
CC FLAG FOR POLYMER PARTITIONING, PERM. REDUCTION PARAMETERS
*----IPOLYM EPHI3 EPHI4  BRK  CRK  RKCUT
      1  1.  1.  1.  0.4  1.
CC
CC SPECIFIC WEIGHT FOR COMPONENTS 1,2,3,7,AND 8 , AND GRAVITY FLAG
*----DEN1 DEN2  DEN23  DEN3  DEN7 DEN8  IDEN
      0.43353 0.33353  0.33353  0.35353 0.346  0  1
CC
CC FLAG FOR CHOICE OF UNITS ( 0:BOTTOMHOLE CONDITION , 1: STOCK TANK)
*----ISTB
      0
CC
CC COMPRESSIBILITY FOR VOL. OCCUPYING COMPONENTS 1,2,3,7,AND 8
*----COMPC(1) COMPC(2) COMPC(3) COMPC(7) COMPC(8)
      0.0  0.0  0.  0.  0.
CC
CC CAPILLARY PRESSURE PARAMETERS, WATER-WET OR OIL-WET PC CURVE FLAG
*----ICPC IEPC IOW
      0  0  0
CC
CC
*----CPC
      0.00
CC
CC
*----EPC
      2.
CC
CC MOLECULAR DIFFUSIVITY OF KCTH COMPONENT IN PHASE 1 (D(KC),KC=1,N)
*----D(1) D(2) D(3) D(4) D(5) D(6) D(7) D(8) D(9) D(10) D(11)
      13*0.
CC
CC MOLECULAR DIFFUSIVITY OF KCTH COMPONENT IN PHASE 2 (D(KC),KC=1,N)
*----D(1) D(2) D(3) D(4) D(5) D(6) D(7) D(8) D(9) D(10) D(11)
      13*0.
CC

```

CC MOLECULAR DIFFUSIVITY OF KCTH COMPONENT IN PHASE 3 (D(KC),KC=1,N)

*---D(1) D(2) D(3) D(4) D(5) D(6) D(7) D(8) D(9) D(10) D(11)

13*0.

CC

CC LONGITUDINAL AND TRANSVERSE DISPERSIVITY OF PHASE 1 (FT)

*---ALPHAL(1) ALPHAT(1)

0.001 0.00

CC

CC LONGITUDINAL AND TRANSVERSE DISPERSIVITY OF PHASE 2 (FT)

*---ALPHAL(2) ALPHAT(2)

0.01 0.0

CC

CC LONGITUDINAL AND TRANSVERSE DISPERSIVITY OF PHASE 3 (FT)

*---ALPHAL(3) ALPHAT(3)

0.01 0.0

CC

CC FLAG TO SPECIFY ORGANIC ADSORPTION CALCULATION

*---IADSO

0

CC

CC SURFACTANT AND POLYMER ADSORPTION PARAMETERS

*---AD31 AD32 B3D AD41 AD42 B4D IADK, IADS1, FADS REFK

1.0 2.0 1000. 2.0 0.2 100.0 0 0 0 1

2 1 300

7.0 11.0 11.0 0.25

.2 .24

1

0.01 0.01 0.025

7 18 4 4 3 1

7 1 4 12

5 4 1 2 3

0 0 0

6

CALCIUM 2.00

MAGNESIUM 2.00

CARBON (AS CARBOBATES) -2.00

SODIUM 1.00

HYDROGEN (REACTIVE) 1.00

ACID (PETROLEUM) -1.00

CHLORINE -1.00

HYDROGEN ION

SODIUM ION

CALCIUM ION

MAGENSIUM ION

CARBONATE ION

PETROLEUM ACID IN OIL

WATER

CALCIUM MONOHYDROXIDE ION

MAGNESIUM MONOHYDROXIDE ION

CA (HC03) +

MG (HCO3) +

PETRLEUM ACID ANION

HYDROXIDE ION

BICARBONATE ION
 DISSOLVED CARBON MONOHYDROXIDE
 AQUEOUS CALCIUM CARBONATE
 AQUEOUS MAGNESIUM CARBONATE
 PETROLEUM ACID IN WATER
 CALCIUM CARBONATE(SOLID)
 MAGNESIUM CARBONATE (SOLID)
 CALCIUM HYDROXIDE (SOLID)
 MAGNESIUM HYDROXIDE(SOLID) (*
 SORBED HYDROGEN ION
 SORBED SODIUM ION
 SORBED CALCIUM ION
 SORBED MAGNESIUM ION (*)
 SURF. ASSOCIATED SODIUM ION
 SURF. ASSOCIATED CALCIUM ION
 SURF. ASSOCIATED MAGNESIUM ION

4

0. 0. 1. 0. 0. 0. 0. 1. 0. 1. 0. 0. 0. 0. 0. 0.
 1. 0. 0.
 0. 0. 0. 1. 0. 0. 0. 0. 1. 0. 1. 0. 0. 0. 0. 0.
 0. 1. 0.
 0. 0. 0. 0. 1. 0. 0. 0. 0. 1. 1. 0. 0. 1. 1.
 1. 1. 0.
 0. 1. 0. 0. 0. 0. 0. 0. 0. 0. 0. 0. 0. 0. 0.
 0. 0. 0.
 1. 0. 0. 0. 0. 1. 2. 1. 1. 1. 1. 0. 1. 1. 2.
 0. 0. 1.
 0. 0. 0. 0. 0. 1. 0. 0. 0. 0. 0. 1. 0. 0. 0.
 0. 0. 1.
 1. 0. 1. 0.
 0. 1. 0. 1.
 1. 1. 0. 0.
 0. 0. 0. 0.
 0. 0. 2. 2.
 0. 0. 0. 0.
 0. 0. 1. 0.
 0. 0. 0. 1.
 0. 0. 0. 0.
 0. 1. 0. 0.
 1. 0. 0. 0.
 0. 0. 0. 0.
 0. 1. 0.
 0. 0. 1.
 0. 0. 0.
 1. 0. 0.
 0. 0. 0.
 0. 0. 0.
 1.0 0.0 0.0 0.0 0.0 0.0 0.0 0.0 0.0 0.0 0.0 0.0
 0.0 0.0
 0.0 1.0 0.0 0.0 0.0 0.0 0.0 0.0 0.0 0.0 0.0 0.0
 0.0 0.0
 0.0 0.0 1.0 0.0 0.0 0.0 0.0 0.0 0.0 0.0 0.0 0.0
 0.0 0.0

```

0.0 0.0 0.0 1.0 0.0 0.0 0.0 0.0 0.0 0.0 0.0 0.0
0.0 0.0
0.0 0.0 0.0 0.0 1.0 0.0 0.0 0.0 0.0 0.0 0.0 0.0
0.0 0.0
0.0 0.0 0.0 0.0 0.0 1.0 0.0 0.0 0.0 0.0 0.0 0.0
0.0 0.0
0.0 0.0 0.0 0.0 0.0 0.0 1.0 0.0 0.0 0.0 0.0 0.0
0.0 0.0
-1.0 0.0 1.0 0.0 0.0 0.0 0.0 0.0 0.0 0.0 0.0 0.0
0.0 0.0
-1.0 0.0 0.0 1.0 0.0 0.0 0.0 0.0 0.0 0.0 0.0 0.0
0.0 0.0
1.0 0.0 1.0 0.0 1.0 0.0 0.0 0.0 0.0 0.0 0.0 0.0
0.0 0.0
1.0 0.0 0.0 1.0 1.0 0.0 0.0 0.0 0.0 0.0 0.0 0.0
0.0 0.0
-1.0 0.0 0.0 0.0 0.0 1.0 0.0 0.0 0.0 0.0 0.0 0.0
0.0 0.0
-1.0 0.0 0.0 0.0 0.0 0.0 0.0 0.0 0.0 0.0 0.0 0.0
0.0 0.0
1.0 0.0 0.0 0.0 1.0 0.0 0.0 0.0 0.0 0.0 0.0 0.0
0.0 0.0
2.0 0.0 0.0 0.0 1.0 0.0 0.0 0.0 0.0 0.0 0.0 0.0
0.0 0.0
0.0 0.0 1.0 0.0 1.0 0.0 0.0 0.0 0.0 0.0 0.0 0.0
0.0 0.0
0.0 0.0 0.0 1.0 1.0 0.0 0.0 0.0 0.0 0.0 0.0 0.0
0.0 0.0
0.0 0.0 0.0 0.0 0.0 1.0 0.0 0.0 0.0 0.0 0.0 0.0
0.0 0.0
0.0 0.0 0.0 0.0 0.0 0.0 0.0 1.0 0.0 0.0 0.0 0.0
0.0 0.0
0.0 0.0 0.0 0.0 0.0 0.0 0.0 0.0 1.0 0.0 0.0 0.0
0.0 0.0
0.0 0.0 0.0 0.0 0.0 0.0 0.0 0.0 0.0 1.0 0.0 0.0
0.0 0.0
0.0 0.0 0.0 0.0 0.0 0.0 0.0 0.0 0.0 0.0 1.0 0.0
0.0 0.0
0.0 0.0 0.0 0.0 0.0 0.0 0.0 0.0 0.0 0.0 0.0 1.0
0.0 0.0
0.0 0.0 0.0 0.0 0.0 0.0 0.0 0.0 0.0 0.0 0.0 0.0
1.0 0.0
0.0 0.0 0.0 0.0 0.0 0.0 0.0 0.0 0.0 0.0 0.0 0.0
0.0 1.0
0.0 0.0 1.0 0.0 1.0 0.0 0.0
0.0 0.0 0.0 1.0 1.0 0.0 0.0
-2.0 0.0 1.0 0.0 0.0 0.0 0.0
-2.0 0.0 0.0 1.0 0.0 0.0 0.0
1.0 1.0 2.0 2.0 -2.0 0.0 0.0 1.0 1.0 1.0 1.0 -1.0
-1.0 -1.0 0.0 0.0 0.0 0.0
1.0 1.0 2.0 2.0
0.10000000000000000E+01 0.10000000000000000E+01 0.10000000000000000E+01
0.10000000000000000E+01 0.10000000000000000E+01 0.10000000000000000E+01

```

```

0.100000000000E+01 0.166000000000E-12 0.363000000000E-11
0.241000000000E+12 0.207000000000E+12 0.1166063286003E-10
0.531000000000E-13 0.149000000000E+10 0.289000000000E+15
0.326000000000E+04 0.140000000000E+04 0.4506870369215E-02
0.793000000000E-05 0.520000000000E-05 0.270000000000E+02
0.0 2.0 -1.0 0.0 0.0 0.0 0.0 -2.0 1.0 0.0 0.0
0.0 0.0
0.0 2.0 0.0 -1.0 0.0 0.0 0.0 -2.0 0.0 1.0 0.0
0.0 0.0
-1.0 1.0 0.0 0.0 0.0 0.0 1.0 -1.0 0.0 0.0 0.0
0.0 0.0
-1.0 -1.0 0.0
0.3998796365232E-10
0.541000000000E-05 0.700000000000E-04 0.473150000000E+23
0.560450000000E+17
1.0 2.0 2.0
0.500000000000E+00 0.940000000000E+00
0.0 2.0 -1.0 0.0 0.0 0.0 0.0 0.0 0.0 -2.0
1.0 0.0
0.0 2.0 0.0 -1.0 0.0 0.0 0.0 0.0 0.0 -2.0
0.0 1.0
0.2327068943879E-03 0.1306566292887E-13 0.1019027255524E-19
0.340000000000E+00 0.4841272648115E-03
0.200000000000E-09
0.4859230648115E-03
0.3399999999000E+00
0.110000000000E+03
0.8599979010258E-03
0.1391855001858E+00
0.6974400226488E-08 0.3397672930056E+00 0.2393849454367E-03
0.9931008091451E-10 0.2259958323666E-05 0.1991400020990E+00
0.5489999148289E+02
0.000000000000E+00 0.000000000000E+00 0.000000000000E+00
0.000000000000E+00
0.2216246730032E-16 0.3998794148985E-10 0.6575604579067E-28
0.1788802307699E-34
0.9996990913079E+00 0.9535479815337E+00
0.2587301587302E-08 0.350000000000E+03
CC
CC*****
CC
CC PART5 : WELL DATA
CC
CC*****
CC
CC
CC FLAG FOR BOUNDARIES
*--- IBOUND IZONE
0 0
CC
CC TOTAL NUMBER OF WELLS, WELL RADIUS FLAG, FLAG FOR TIME OR COURANT NO.
*---- NWELL IRO ITSTEP NWREL
2 2 1 2

```

```

CC
CC WELL ID,LOCATIONS,AND FLAG FOR SPECIFYING WELL TYPE, WELL RADIUS, SKIN
*----IDW IW JW IFLAG RW SWELL IDIR IFIRST ILAST IPRF
  1 1 1 1 .003 0. 3 1 1 0
CC
CC WELL NAME
*---- #1
INJECTOR
CC
CC MAX. AND MIN. ALLOWABLE BOTTOMHOLE PRESSURE AND RATE
*----ICHEK PWFMIN PWFMAX QTMIN QTMAX
  0 0. 20000. 0. 200.
CC
CC WELL ID,LOCATIONS,AND FLAG FOR SPECIFYING WELL TYPE, WELL RADIUS, SKIN
*----IDW IW JW IFLAG RW SWELL IDIR IFIRST ILAST IPRF
  2 100 1 2 .003 0. 3 1 1 0
CC
CC WELL NAME
*---- #2
PRODUCER
CC
CC MAX. AND MIN. ALLOWABLE BOTTOMHOLE PRESSURE AND RATE
*----ICHEK PWFMIN PWFMAX QTMIN QTMAX
  0 0. 20000. 0. 0.
CC
CC ID,INJ. RATE AND INJ. COMP. FOR RATE CONS. WELLS FOR EACH PHASE (L=1,3)
*----ID QI(M,L) C(M,KC,L)
  1 0.0019 0.99 0. 0.0 0.41 0.000001 0.000001 0.01 0. 0.000001 0.18 0.18 111. 0.000001
  1 0. 13*0.
  1 0. 13*0.
CC
CC ID, BOTTOM HOLE PRESSURE FOR PRESSURE CONSTRAINT WELL (IFLAG=4)
*----ID PWF
  2 14.47
CC
CC CUM. INJ. TIME , AND INTERVALS (PV OR DAY) FOR ERITING TO OUTPUT FILES
*----TINJ(PV) CUMPR1 CUMHI1 WRHPV WRPRF RSTC
  0.25 0.05 0.05 0.05 0.05 5.
CC
CC FOR IMES=2, ITIME=1, INI. DT ,CONC. TOLERANCE, MAX.,MIN. COURANT NUMBERS
*----DT DCLIM(KC=1,16) CNMAX CNMIN
  0.000001 0.05 0.05 0.05 0.05 0.05 0.05 0.05 0.05 0.05 0.05 0.05 0.05 0.05 0.1 .0001
cc
cc
*--- ibmod
  0
CC
CC IRO, ITIME, NEW FLAGS FOR ALL THE WELLS
*---- IRO ITIME IFLAG(M),M=1,NWELL
  2 1 1 2
CC
CC NUMBER OF WELLS CHANGES IN LOCATION OR SKIN OR PWF
*----NWEL1

```

```

0
CC
CC NUMBER OF WELLS WITH RATE CHANGES, ID
*----NWEL2 ID
1 1
CC
CC ID,INJ. RATE AND INJ. COMP. FOR RATE CONS. WELLS FOR EACH PHASE (L=1,3)
*----ID QI(M,L) C(M,KC,L)
1 0.0019 1. 0. 0.0 0.37 0.000001 0.000001 2*0. 0.0000001 0.09 0.09 111. 0.000001
1 0. 13*0.
1 0. 13*0.
CC
CC CUM. INJ. TIME , AND INTERVALS (PV OR DAY) FOR ERITING TO OUTPUT FILES
*----TINJ CUMPR1 CUMHI1 WRHPV WRPRF RSTC
2.5 0.05 0.05 0.05 0.05 5
CC
CC FOR IMES=2, ITIME=1, INI. DT ,CONC. TOLERANCE, MAX.,MIN. COURANT NUMBERS
*----DT DCLIM(KC=1,16) CNMAX CNMIN
0.00001 0.05 0.05 0.05 0.05 0.05 0.5 0.05 0.05 0.05 0.05 0.05 0.05 0.05 0.2 .0001

```

```

CC*****
CC
CC BRIEF DESCRIPTION OF DATA SET : UTCHEM (VERSION 2011_1)
CC
CC*****
CC ALKALI-COSOLVENT-POLYMER Coreflood (ACP-2 or ACP2.5)
CC
CC
CC PROCESS : 1D ALKALINE/SURFACTANT/POLYMER
CC
CC COORDINATES : CARTESIAN
CC
CC GRID BLOCKS : 100X1X1
CC DATE : 05/05/2014
CC
CC*****
CC
CC*****
CC
CC PART1 : RESERVOIR DESCRIPTION
CC
CC*****
CC
CC
*--- RUNNO
ACP-25
CC
CC
*---TITLE

CC
CC SIMULATION FLAGS
*--- IMODE IMES IDISPC ICWM ICAP IREACT IBIO ICOORD ITREAC ITC IGAS IENG
      1 4 0 0 0 3 0 1 0 0 0 0
CC
CC NUMBER OF GRID BLOCKS AND FLAG SPECIFIES CONSTANT OR VARIABLE GRID SIZE
*---NX NY NZ IDXYZ IUNIT
      100 1 1 0 0
CC
CC CONSTANT GRID BLOCK SIZE IN X-Y DIRECTIONS (FT)
*---DX DY DZ
      0.00953 0.1351 0.1351
CC
CC TOTAL NO. OF COMPONENTS, NO. OF TRACERS,NO. OF GEL COMPONENTS
*---N NO NTW NTA NGC NG NOTH
      13 0 0 0 5 0 0
CC
CC
*--- SPNAME(I),I=1,N
WATER

```

```

OIL
SURFACTANT
POLYMER
ANION
CALCIUM
ALC1
NONE
MG
CO3
Na
Hydr.
Acid
CC
CC FLAG INDICATING IF THE COMPONENT IS INCLUDED IN CALCULATIONS OR NOT
*----ICF(KC) FOR KC=1,N
  1 1 1 1 1 1 1 0 1 1 1 1
CC
CC*****
CC
CC PART2 : OUTPUT OPTIONS
CC
CC*****
CC
CC
CC FLAG FOR PV OR DAYS
*----ICUMTM ISTOP IOUTGMS
  1 1 0
CC
CC FLAG INDICATING IF THE PROFILE OF KCTH COMPONENT SHOULD BE WRITTEN
*----IPRFLG(KC),KC=1,N
  1 1 1 1 1 1 1 0 1 1 1 1
CC
CC FLAG FOR PRES,SAT.,TOTAL CONC.,TRACER CONC.,CAP.,GEL, ALKALINE PROFILES
*----IPPRES IPSAT IPCTOT IPTBIO IPCAP IPGEL IPALK IPTEMP IPOBs
  1 1 1 0 0 0 1 0 0
CC
CC FLAG FOR WRITING SEVERAL PROPERTIES
*----ICKL IVIS IPER ICNM ICSE IFOAM IHYST INONEQ
  1 1 1 1 1 0 0 0
CC
CC FLAG FOR WRITING SEVERAL PROPERTIES TO PROF
*----IADS IVEL IRKF IPHSE
  1 1 1 1
CC
CC*****
CC
CC PART3 : RESERVOIR PROPERTIES
CC
CC*****
CC
CC
CC MAX. SIMULATION TIME ( PV )
*---- TMAX

```

```

2.5
CC
CC ROCK COMPRESSIBILITY (1/PSI), STAND. PRESSURE(PSI)
*----COMPR    PSTAND
    0.    0.
CC
CC FLAGS INDICATION CONSTANT OR VARIABLE POROSITY, X,Y,AND Z PERMEABILITY
*----IPOR1 IPERMX IPERMY IPERMZ IMOD ITRNZ INTG
    0  0  3  3  0  0  0
CC
CC CONSTANT POROSITY
*----PORC1
    0.21
CC
CC CONSTANT X-PERMEABILITY (MILIDARCY)
*----PERMX(I)
    2366.0
CC
CC CONSTANT Y-PERMEABILITY MULTIPLIER
*----FACTY
    1.
CC
CC CONSTANT Z-PERMEABILITY MULTIPLIER
*----FACTZ
    1.
CC
CC FLAG FOR CONSTANT OR VARIABLE DEPTH, PRESSURE, WATER SATURATION
*----IDEPTH IPRESS ISWI ICWI
    0  0  0  -1
CC
CC DEPTH OF THE FIRT GRID BLOCK
*----DEPTH(I)
    0.0
CC
CC INITIAL CORE PRESSURE
*----PRESS
    14.47
CC
CC INITIAL WATER SATURATION
*----SWI
    0.35
CC
CC CONSTANT CHLORIDE AND CALCIUM CONCENTRATIONS (MEQ/ML)
*----C50    C60
    0.34  1.E-006
CC
CC*****
CC
CC PART4 : PHYSICAL PROPERTY DATA
CC
CC*****
CC
CC

```



```

CC OIL CONC. AT PLAIT POINT FOR TYPE II(+)AND TYPE II(-), CMC
*---- C2PLC C2PRC EPSME IHAND
    0.  1.  .0010510093751  0
CC
CC FLAG INDICATING TYPE OF PHASE BEHAVIOR PARAMETERS
*---- IFGHBN
    0
CC SLOPE AND INTERCEPT OF BINODAL CURVE AT ZERO, OPT., AND 2XOPT SALINITY
CC FOR ALCOHOL 1
*----HBNS70 HBNC70 HBNS71 HBNC71 HBNS72 HBNC72
    0.0 .062  0.036  0.034  0.0  0.15
CC SLOPE AND INTERCEPT OF BINODAL CURVE AT ZERO, OPT., AND 2XOPT SALINITY
CC FOR ALCOHOL 2
*----HBNS80 HBNC80 HBNS81 HBNC81 HBNS82 HBNC82
    0.  0.  0.  0.  0.  0.
CC
CC LOWER AND UPPER EFFECTIVE SALINITY FOR ALCOHOL 1 AND ALCOHOL 2
*----CSEL7 CSEU7 CSEL8 CSEU8
    0.28  0.6  0.  0.
CC
CC THE CSE SLOPE PARAMETER FOR CALCIUM AND ALCOHOL 1 AND ALCOHOL 2
*----BETA6 BETA7 BETA8
    0.0  0.  0.
CC
CC FLAG FOR ALCOHOL PART. MODEL AND PARTITION COEFFICIENTS
*----IALC OPSK7O OPSK7S OPSK8O OPSK8S
    0  0.  0.  0.  0.
CC
CC NO. OF ITERATIONS, AND TOLERANCE
*----NALMAX EPSALC
    20  0.0001
CC
CC ALCOHOL 1 PARTITIONING PARAMETERS IF IAIC=1
*----AKWC7 AKWS7 AKM7 AK7  PT7
    4.671  1.79  48.  35.31  0.222
CC
CC ALCOHOL 2 PARTITIONING PARAMETERS IF IALC=1
*----AKWC8 AKWS8 AKM8 AK8  PT8
    0.  0.  0.  0.  0.
CC
CC IFT MODEL FLAG
*----IFT
    1
CC
CC INTERFACIAL TENSION PARAMETERS
*---- CHUH  AHUH
    0.3  10.0
CC
CC LOG10 OF OIL/WATER INTERFACIAL TENSION
*----XIFTW
    1.3
CC
CC

```

```

*---IMASS icor
  0  0
cc
cc
*--- iwalt iwalf
  0  0
CC
CC CAPILLARY DESATURATION PARAMETERS FOR PHASE 1, 2, AND 3
*---ITRAP T11    T22    T33
  2  300.  2800.  300.
CC
CC RELATIVE PERM and pc model
*---IPERM  IRTYPE
  0  0
CC
CC FLAG FOR CONSTANT OR VARIABLE REL. PERM. PARAMETERS
*---ISRW IPRW IEW
  0  0  0
CC
CC CONSTANT RES. SATURATION OF PHASES 1,2,AND 3 AT LOW CAPILLARY NO.
*---S1RWC S2RWC S3RWC
  0.15 0.60 0.15
CC
CC CONSTANT ENDPOINT REL. PERM. OF PHASES 1,2,AND 3 AT LOW CAPILLARY NO.
*---P1RW P2RW P3RW
  0.025 1.0 0.025
CC
CC CONSTANT REL. PERM. EXPONENT OF PHASES 1,2,AND 3 AT LOW CAPILLARY NO.
*---E1W E2W E3W
  2.  2.  2.
CC
CC RES. SATURATION OF HPASES 1,2,AND 3 AT HIGH CAPILLARY NO.
*---S1RC S2RC S3RC
  0.0 0.0 0.0
CC
CC ENDPOINT REL. PERM. OF PHASES 1,2,AND 3 AT HIGH CAPILLARY NO.
*---P1RC P2RC P3RC
  1.  1.0  1.
CC
CC REL. PERM. EXPONENT OF PHASES 1,2,AND 3 AT HIGH CAPILLARY NO.
*---E13CW E23C E31C
  1.  1.0  1.
CC
CC WATER AND OIL VISCOSITY , RESERVOIR TEMPERATURE
*---VIS1 VIS2 TEMPV
  .9  4700.0  0.
CC Mu_p: the polymer viscosity in equation 5.4; delta_0: equation 5.5; c: equation 4.13
CC COMPOSITIONAL PHASE VISCOSITY PARAMETERS
*--- Nu    Nu_prime Mu_p delta_0 c
  2.3    6.    2000.  0.01  0.0
CC
CC PARAMETERS TO CALCULATE POLYMER VISCOSITY AT ZERO SHEAR RATE
*---AP1 AP2 AP3

```

```

80.0 200.0 28000
CC
CC PARAMETER TO COMPUTE CSEP,MIN. CSEP, AND SLOPE OF LOG VIS. VS. LOG CSEP
*----BETAP CSE1 SSLOPE
1 0.01 -0.3
CC
CC PARAMETER FOR SHEAR RATE DEPENDENCE OF POLYMER VISCOSITY
*----GAMMAC GAMHF POWN IPMOD ishear rweff GAMHF2
4.0 2.0 1.6 0 0 0.25 0
CC
CC FLAG FOR POLYMER PARTITIONING, PERM. REDUCTION PARAMETERS
*----IPOLYM EPHI3 EPHI4 BRK CRK RKCUT
1 1. 1. 1. 0.4 1.
CC
CC SPECIFIC WEIGHT FOR COMPONENTS 1,2,3,7,AND 8 , AND GRAVITY FLAG
*----DEN1 DEN2 DEN23 DEN3 DEN7 DEN8 IDEN
0.43353 0.33353 0.33353 0.35353 0.346 0 1
CC
CC FLAG FOR CHOICE OF UNITS ( 0:BOTTOMHOLE CONDITION , 1: STOCK TANK)
*----ISTB
0
CC
CC COMPRESSIBILITY FOR VOL. OCCUPYING COMPONENTS 1,2,3,7,AND 8
*----COMPC(1) COMPC(2) COMPC(3) COMPC(7) COMPC(8)
0.0 0.0 0. 0. 0.
CC
CC CAPILLARY PRESSURE PARAMETERS, WATER-WET OR OIL-WET PC CURVE FLAG
*----ICPC IEPC IOW
0 0 0
CC
CC
*----CPC
0.00
CC
CC
*----EPC
2.
CC
CC MOLECULAR DIFFUSIVITY OF KCTH COMPONENT IN PHASE 1 (D(KC),KC=1,N)
*----D(1) D(2) D(3) D(4) D(5) D(6) D(7) D(8) D(9) D(10) D(11)
13*0.
CC
CC MOLECULAR DIFFUSIVITY OF KCTH COMPONENT IN PHASE 2 (D(KC),KC=1,N)
*----D(1) D(2) D(3) D(4) D(5) D(6) D(7) D(8) D(9) D(10) D(11)
13*0.
CC
CC MOLECULAR DIFFUSIVITY OF KCTH COMPONENT IN PHASE 3 (D(KC),KC=1,N)
*----D(1) D(2) D(3) D(4) D(5) D(6) D(7) D(8) D(9) D(10) D(11)
13*0.
CC
CC LONGITUDINAL AND TRANSVERSE DISPERSIVITY OF PHASE 1 (FT)
*----ALPHAL(1) ALPHAT(1)
0.001 0.00

```

```

CC
CC LONGITUDINAL AND TRANSVERSE DISPERSIVITY OF PHASE 2 (FT)
*----ALPHAL(2)  ALPHAT(2)
    0.04    0.0
CC
CC LONGITUDINAL AND TRANSVERSE DISPERSIVITY OF PHASE 3 (FT)
*----ALPHAL(3)  ALPHAT(3)
    0.01    0.0
CC
CC FLAG TO SPECIFY ORGANIC ADSORPTION CALCULATION
*----IADSO
    0
CC
CC SURFACTANT AND POLYMER ADSORPTION PARAMETERS
*----AD31 AD32  B3D  AD41  AD42  B4D  IADK, IADS1, FADS  REFK
    1.0 2.0 1000. 2.0 0.2 100.0 0 0 0 0 1
2 1 300
7.0 11.0 11.0 0.25
.17 .26
1
0.01 0.01 0.03
7 18 4 4 3 1
7 1 4 12
5 4 1 2 3
0 0 0
6
CALCIUM                2.00
MAGNESIUM              2.00
CARBON (AS CARBOBATES) -2.00
SODIUM                 1.00
HYDROGEN (REACTIVE)    1.00
ACID (PETROLEUM)      -1.00
CHLORINE               -1.00
HYDROGEN ION
SODIUM ION
CALCIUM ION
MAGENSIUM ION
CARBONATE ION
PETROLEUM ACID IN OIL
WATER
CALCIUM MONOHYDROXIDE ION
MAGNESIUM MONOHYROXIDE ION
CA (HC03) +
MG (HCO3) +
PETRLEUM ACID ANION
HYDROXIDE ION
BICARBONATE ION
DISSOLVED CARBON MONOHYDROXIDE
AQUEOUS CALCIUM CARBONATE
AQUEOUS MAGNESIUM CARBONATE
PETROLEUM ACID IN WATER
CALCIUM CARBONATE(SOLID)
MAGNESIUM CARBONATE (SOLID)

```

CALCIUM HYDROXIDE (SOLID)
 MAGNESIUM HYDROXIDE(SOLID) (*
 SORBED HYDROGEN ION
 SORBED SODIUM ION
 SORBED CALCIUM ION
 SORBED MAGNESIUM ION (*
 SURF. ASSOCIATED SODIUM ION
 SURF. ASSOCIATED CALCIUM ION
 SURF. ASSOCIATED MAGNESIUM ION

4
 0. 0. 1. 0. 0. 0. 0. 1. 0. 1. 0. 0. 0. 0. 0.
 1. 0. 0.
 0. 0. 0. 1. 0. 0. 0. 0. 1. 0. 1. 0. 0. 0. 0.
 0. 1. 0.
 0. 0. 0. 0. 1. 0. 0. 0. 0. 1. 1. 0. 0. 1. 1.
 1. 1. 0.
 0. 1. 0. 0. 0. 0. 0. 0. 0. 0. 0. 0. 0. 0. 0.
 0. 0. 0.
 1. 0. 0. 0. 0. 1. 2. 1. 1. 1. 1. 0. 1. 1. 2.
 0. 0. 1.
 0. 0. 0. 0. 0. 1. 0. 0. 0. 0. 0. 1. 0. 0. 0.
 0. 0. 1.
 1. 0. 1. 0.
 0. 1. 0. 1.
 1. 1. 0. 0.
 0. 0. 0. 0.
 0. 0. 2. 2.
 0. 0. 0. 0.
 0. 0. 1. 0.
 0. 0. 0. 1.
 0. 0. 0. 0.
 0. 1. 0. 0.
 1. 0. 0. 0.
 0. 0. 0. 0.
 0. 1. 0.
 0. 0. 1.
 0. 0. 0.
 1. 0. 0.
 0. 0. 0.
 0. 0. 0.
 1.0 0.0 0.0 0.0 0.0 0.0 0.0 0.0 0.0 0.0 0.0 0.0
 0.0 0.0
 0.0 1.0 0.0 0.0 0.0 0.0 0.0 0.0 0.0 0.0 0.0 0.0
 0.0 0.0
 0.0 0.0 1.0 0.0 0.0 0.0 0.0 0.0 0.0 0.0 0.0 0.0
 0.0 0.0
 0.0 0.0 0.0 1.0 0.0 0.0 0.0 0.0 0.0 0.0 0.0 0.0
 0.0 0.0
 0.0 0.0 0.0 0.0 1.0 0.0 0.0 0.0 0.0 0.0 0.0 0.0
 0.0 0.0
 0.0 0.0 0.0 0.0 0.0 1.0 0.0 0.0 0.0 0.0 0.0 0.0

```

0.0 0.0
-1.0 0.0 1.0 0.0 0.0 0.0 0.0 0.0 0.0 0.0 0.0 0.0
0.0 0.0
-1.0 0.0 0.0 1.0 0.0 0.0 0.0 0.0 0.0 0.0 0.0 0.0
0.0 0.0
1.0 0.0 1.0 0.0 1.0 0.0 0.0 0.0 0.0 0.0 0.0 0.0
0.0 0.0
1.0 0.0 0.0 1.0 1.0 0.0 0.0 0.0 0.0 0.0 0.0 0.0
0.0 0.0
-1.0 0.0 0.0 0.0 0.0 1.0 0.0 0.0 0.0 0.0 0.0 0.0
0.0 0.0
-1.0 0.0 0.0 0.0 0.0 0.0 0.0 0.0 0.0 0.0 0.0 0.0
0.0 0.0
1.0 0.0 0.0 0.0 1.0 0.0 0.0 0.0 0.0 0.0 0.0 0.0
0.0 0.0
2.0 0.0 0.0 0.0 1.0 0.0 0.0 0.0 0.0 0.0 0.0 0.0
0.0 0.0
0.0 0.0 1.0 0.0 1.0 0.0 0.0 0.0 0.0 0.0 0.0 0.0
0.0 0.0
0.0 0.0 0.0 1.0 1.0 0.0 0.0 0.0 0.0 0.0 0.0 0.0
0.0 0.0
0.0 0.0 0.0 0.0 0.0 1.0 0.0 0.0 0.0 0.0 0.0 0.0
0.0 0.0
0.0 0.0 0.0 0.0 0.0 0.0 0.0 1.0 0.0 0.0 0.0 0.0
0.0 0.0
0.0 0.0 0.0 0.0 0.0 0.0 0.0 0.0 1.0 0.0 0.0 0.0
0.0 0.0
0.0 0.0 0.0 0.0 0.0 0.0 0.0 0.0 0.0 1.0 0.0 0.0
0.0 0.0
0.0 0.0 0.0 0.0 0.0 0.0 0.0 0.0 0.0 0.0 1.0 0.0
0.0 0.0
1.0 0.0
0.0 0.0 0.0 0.0 0.0 0.0 0.0 0.0 0.0 0.0 0.0 0.0
0.0 1.0
0.0 0.0 1.0 0.0 1.0 0.0 0.0
0.0 0.0 0.0 1.0 1.0 0.0 0.0
-2.0 0.0 1.0 0.0 0.0 0.0 0.0
-2.0 0.0 0.0 1.0 0.0 0.0 0.0
1.0 1.0 2.0 2.0 -2.0 0.0 0.0 1.0 1.0 1.0 1.0 -1.0
-1.0 -1.0 0.0 0.0 0.0 0.0
1.0 1.0 2.0 2.0
0.100000000000E+01 0.100000000000E+01 0.100000000000E+01
0.100000000000E+01 0.100000000000E+01 0.100000000000E+01
0.100000000000E+01 0.166000000000E-12 0.363000000000E-11
0.272000000000E+12 0.249000000000E+12 0.1437485804298E-10
0.100000000000E-13 0.113000000000E+10 0.479000000000E+17
0.168000000000E+04 0.954000000000E+03 0.5555926728269E-02
0.793000000000E-05 0.520000000000E-05 0.270000000000E+02
0.0 2.0 -1.0 0.0 0.0 0.0 0.0 0.0 -2.0 1.0 0.0 0.0
0.0 0.0

```

```

0.0 2.0 0.0 -1.0 0.0 0.0 0.0 0.0 -2.0 0.0 1.0 0.0
0.0 0.0
-1.0 1.0 0.0 0.0 0.0 0.0 1.0 -1.0 0.0 0.0 0.0
0.0 0.0
-1.0 -1.0 0.0
0.3498599888209E-10
0.5410000000000E-05 0.7000000000000E-04 0.4731500000000E+23
0.5604500000000E+17
1.0 2.0 2.0
0.5000000000000E+00 0.9400000000000E+00
0.0 2.0 -1.0 0.0 0.0 0.0 0.0 0.0 0.0 0.0 -2.0
1.0 0.0
0.0 2.0 0.0 -1.0 0.0 0.0 0.0 0.0 0.0 0.0 -2.0
0.0 1.0
0.2965075279164E-03 0.3328535713677E-13 0.2111547492216E-19
0.3400000000000E+00 0.5934003764072E-03
0.2000000000000E-09
0.5951961764072E-03
0.3399999999000E+00
0.1100000000000E+03
0.1143405799714E-02
0.1524315047968E+00
0.7389968334491E-08 0.3397034923721E+00 0.2946972398001E-03
0.9944108441660E-10 0.1835782379119E-05 0.2688565942003E+00
0.5486499774234E+02
0.0000000000000E+00 0.0000000000000E+00 0.0000000000000E+00
0.0000000000000E+00
0.2054945710463E-16 0.3498597833263E-10 0.7085051310593E-28
0.1567699932467E-34
0.9995999680597E+00 0.9493511419008E+00
0.2587301587302E-08 0.3500000000000E+03
CC
CC*****
CC
CC PART5 : WELL DATA
CC
CC*****
CC
CC
CC FLAG FOR BOUNDARIES
*--- IBOUND IZONE
0 0
CC
CC TOTAL NUMBER OF WELLS, WELL RADIUS FLAG, FLAG FOR TIME OR COURANT NO.
*---- NWELL IRO ITSTEP NWREL
2 2 1 2
CC
CC WELL ID,LOCATIONS,AND FLAG FOR SPECIFYING WELL TYPE, WELL RADIUS, SKIN
*---IDW IW JW IFLAG RW SWELL IDIR IFIRST ILAST IPRF
1 1 1 1 .003 0. 3 1 1 0
CC
CC WELL NAME
*---- #1

```

```

INJECTOR
CC
CC MAX. AND MIN. ALLOWABLE BOTTOMHOLE PRESSURE AND RATE
*----ICHEK PWFMIN PWFMAX QTMIN QTMAX
  0  0.  20000.  0.  200.
CC
CC WELL ID,LOCATIONS,AND FLAG FOR SPECIFYING WELL TYPE, WELL RADIUS, SKIN
*----IDW IW  JW  IFLAG  RW  SWELL IDIR IFIRST ILAST IPRF
  2 100  1  2  .003  0.  3  1  1  0
CC
CC WELL NAME
*---- #2
PRODUCER
CC
CC MAX. AND MIN. ALLOWABLE BOTTOMHOLE PRESSURE AND RATE
*----ICHEK PWFMIN PWFMAX QTMIN QTMAX
  0  0.  20000.  0.  0.
CC
CC ID,INJ. RATE AND INJ. COMP. FOR RATE CONS. WELLS FOR EACH PHASE (L=1,3)
*----ID QI(M,L) C(M,KC,L)
  1  0.0019 0.99 0. 0.0 0.41 0.000001 0.000001 0.01 0. 0.000001 0.17 0.17 111. 0.000001
  1  0.  13*0.
  1  0.  13*0.
CC
CC ID, BOTTOM HOLE PRESSURE FOR PRESSURE CONSTRAINT WELL (IFLAG=4)
*----ID PWF
  2  14.47
CC
CC CUM. INJ. TIME , AND INTERVALS (PV OR DAY) FOR ERITING TO OUTPUT FILES
*----TINJ(PV) CUMPR1 CUMHI1 WRHPV WRPRF  RSTC
  0.25  0.05 0.05  0.05 0.05  5.
CC
CC FOR IMES=2, ITIME=1, INI. DT ,CONC. TOLERANCE, MAX.,MIN. COURANT NUMBERS
*----DT DCLIM(KC=1,16) CNMAX CNMIN
  0.000001 0.05 0.05 0.05 0.05 0.05 0.05 0.05 0.05 0.05 0.05 0.05 0.05 0.05 0.1 .0001
cc
cc
*--- ibmod
  0
CC
CC IRO, ITIME, NEW FLAGS FOR ALL THE WELLS
*---- IRO ITIME IFLAG(M),M=1,NWELL
  2  1  1  2
CC
CC NUMBER OF WELLS CHANGES IN LOCATION OR SKIN OR PWF
*----NWEL1
  0
CC
CC NUMBER OF WELLS WITH RATE CHANGES, ID
*----NWEL2 ID
  1  1
CC
CC ID,INJ. RATE AND INJ. COMP. FOR RATE CONS. WELLS FOR EACH PHASE (L=1,3)

```



```

*----ID QI(M,L) C(M,KC,L)
  1 0.0019 1. 0. 0.0 0.37 0.000001 0.000001 2*0. 0.0000001 0.097 0.097 111. 0.000001
  1 0. 13*0.
  1 0. 13*0.
CC
CC CUM. INJ. TIME , AND INTERVALS (PV OR DAY) FOR ERITING TO OUTPUT FILES
*----TINJ CUMPR1 CUMHI1 WRHPV WRPRF RSTC
  2.5 0.05 0.05 0.05 0.05 5
CC
CC FOR IMES=2, ITIME=1, INI. DT ,CONC. TOLERANCE, MAX.,MIN. COURANT NUMBERS
*----DT DCLIM(KC=1,16) CNMAX CNMIN
0.00001 0.05 0.05 0.05 0.05 0.05 0.5 0.05 0.05 0.05 0.05 0.05 0.05 0.05 0.2 .0001

```

```

CC*****
CC
CC BRIEF DESCRIPTION OF DATA SET : UTCHEM (VERSION 2011_1)
CC
CC*****
CC ALKALI-FLOOD Coreflood (ALK or ALK2.1)
CC
CC
CC PROCESS : 1D ALKALINE/SURFACTANT/POLYMER
CC
CC COORDINATES : CARTESIAN
CC
CC GRID BLOCKS : 100X1X1
CC DATE : 05/05/2014
CC
CC*****
CC
CC*****
CC PART1 : RESERVOIR DESCRIPTION
CC
CC*****
CC
CC
*---RUNNO
ALK-21
CC
CC
*---TITLE

CC
CC SIMULATION FLAGS
*--- IMODE IMES IDISPC ICWM ICAP IREACT IBIO ICOORD ITREAC ITC IGAS IENG
      1 4 0 0 0 3 0 1 0 0 0 0
CC
CC NUMBER OF GRID BLOCKS AND FLAG SPECIFIES CONSTANT OR VARIABLE GRID SIZE
*---NX NY NZ IDXYZ IUNIT
      100 1 1 0 0
CC
CC CONSTANT GRID BLOCK SIZE IN X-Y DIRECTIONS (FT)
*---DX DY DZ
      0.00953 0.1351 0.1351
CC
CC TOTAL NO. OF COMPONENTS, NO. OF TRACERS,NO. OF GEL COMPONENTS
*---N NO NTW NTA NGC NG NOTH
      13 0 0 0 5 0 0
CC
CC
*--- SPNAME(I),I=1,N
WATER

```

```

OIL
SURFACTANT
POLYMER
ANION
CALCIUM
ALC1
NONE
MG
CO3
Na
Hydr.
Acid
CC
CC FLAG INDICATING IF THE COMPONENT IS INCLUDED IN CALCULATIONS OR NOT
*----ICF(KC) FOR KC=1,N
  1 1 1 1 1 1 1 0 1 1 1 1
CC
CC*****
CC
CC PART2 : OUTPUT OPTIONS
CC
CC*****
CC
CC
CC FLAG FOR PV OR DAYS
*----ICUMTM ISTOP IOUTGMS
  1 1 0
CC
CC FLAG INDICATING IF THE PROFILE OF KCTH COMPONENT SHOULD BE WRITTEN
*----IPRFLG(KC),KC=1,N
  1 1 1 1 1 1 1 0 1 1 1 1
CC
CC FLAG FOR PRES,SAT.,TOTAL CONC.,TRACER CONC.,CAP.,GEL, ALKALINE PROFILES
*----IPPRES IPSAT IPCTOT IPTBIO IPCAP IPGEL IPALK IPTEMP IPOBs
  1 1 1 0 0 0 1 0 0
CC
CC FLAG FOR WRITING SEVERAL PROPERTIES
*----ICKL IVIS IPER ICNM ICSE IFOAM IHYST INONEQ
  1 1 1 1 1 0 0 0
CC
CC FLAG FOR WRITING SEVERAL PROPERTIES TO PROF
*----IADS IVEL IRKF IPHSE
  1 1 1 1
CC
CC*****
CC
CC PART3 : RESERVOIR PROPERTIES
CC
CC*****
CC
CC
CC MAX. SIMULATION TIME ( PV )
*---- TMAX

```

```

2.5
CC
CC ROCK COMPRESSIBILITY (1/PSI), STAND. PRESSURE(PSI)
*----COMPR    PSTAND
    0.    0.
CC
CC FLAGS INDICATION CONSTANT OR VARIABLE POROSITY, X,Y,AND Z PERMEABILITY
*----IPOR1 IPERMX IPERMY IPERMZ  IMOD ITRNZ  INTG
    0  0  3  3  0  0  0
CC
CC CONSTANT POROSITY
*----PORC1
    0.243
CC
CC CONSTANT X-PERMEABILITY (MILIDARCY)
*----PERMX(I)
    2666.0
CC
CC CONSTANT Y-PERMEABILITY MULTIPLIER
*----FACTY
    1.
CC
CC CONSTANT Z-PERMEABILITY MULTIPLIER
*----FACTZ
    1.
CC
CC FLAG FOR CONSTANT OR VARIABLE DEPTH, PRESSURE, WATER SATURATION
*----IDEPTH IPRESS ISWI  ICWI
    0  0  0  -1
CC
CC DEPTH OF THE FIRT GRID BLOCK
*----DEPTH(I)
    0.0
CC
CC INITIAL CORE PRESSURE
*----PRESS
    14.47
CC
CC INITIAL WATER SATURATION
*----SWI
    0.49
CC
CC CONSTANT CHLORIDE AND CALCIUM CONCENTRATIONS (MEQ/ML)
*----C50  C60
    0.23  1.E-006
CC
CC*****
CC
CC  PART4 : PHYSICAL PROPERTY DATA
CC
CC*****
CC
CC

```

```

CC OIL CONC. AT PLAIT POINT FOR TYPE II(+)AND TYPE II(-), CMC
*---- C2PLC C2PRC EPSME IHAND
    0.  1.  .0010510093751  0
CC
CC FLAG INDICATING TYPE OF PHASE BEHAVIOR PARAMETERS
*---- IFGHBN
    0
CC SLOPE AND INTERCEPT OF BINODAL CURVE AT ZERO, OPT., AND 2XOPT SALINITY
CC FOR ALCOHOL 1
*----HBNS70 HBNC70 HBNS71 HBNC71 HBNS72 HBNC72
    0.0 .062  0.036  0.034  0.0  0.15
CC SLOPE AND INTERCEPT OF BINODAL CURVE AT ZERO, OPT., AND 2XOPT SALINITY
CC FOR ALCOHOL 2
*----HBNS80 HBNC80 HBNS81 HBNC81 HBNS82 HBNC82
    0.  0.  0.  0.  0.  0.
CC
CC LOWER AND UPPER EFFECTIVE SALINITY FOR ALCOHOL 1 AND ALCOHOL 2
*----CSEL7 CSEU7 CSEL8 CSEU8
    0.28  0.6  0.  0.
CC
CC THE CSE SLOPE PARAMETER FOR CALCIUM AND ALCOHOL 1 AND ALCOHOL 2
*----BETA6 BETA7 BETA8
    0.0  0.  0.
CC
CC FLAG FOR ALCOHOL PART. MODEL AND PARTITION COEFFICIENTS
*----IALC OPSK7O OPSK7S OPSK8O OPSK8S
    0  0.  0.  0.  0.
CC
CC NO. OF ITERATIONS, AND TOLERANCE
*----NALMAX EPSALC
    20  0.0001
CC
CC ALCOHOL 1 PARTITIONING PARAMETERS IF IAIC=1
*----AKWC7 AKWS7 AKM7 AK7  PT7
    4.671  1.79  48.  35.31  0.222
CC
CC ALCOHOL 2 PARTITIONING PARAMETERS IF IALC=1
*----AKWC8 AKWS8 AKM8 AK8  PT8
    0.  0.  0.  0.  0.
CC
CC IFT MODEL FLAG
*----IFT
    1
CC
CC INTERFACIAL TENSION PARAMETERS
*---- CHUH  AHUH
    0.3  10.0
CC
CC LOG10 OF OIL/WATER INTERFACIAL TENSION
*----XIFTW
    1.3
CC
CC

```

```

*---IMASS icor
  0  0
cc
cc
*--- iwalt iwalf
  0  0
CC
CC CAPILLARY DESATURATION PARAMETERS FOR PHASE 1, 2, AND 3
*---ITRAP T11    T22    T33
  2  300.  1300.  300.
CC
CC RELATIVE PERM and pc model
*---IPERM  IRTYPE
  0  0
CC
CC FLAG FOR CONSTANT OR VARIABLE REL. PERM. PARAMETERS
*---ISRW IPRW IEW
  0  0  0
CC
CC CONSTANT RES. SATURATION OF PHASES 1,2,AND 3 AT LOW CAPILLARY NO.
*---S1RWC S2RWC S3RWC
  0.15 .51 0.15
CC
CC CONSTANT ENDPOINT REL. PERM. OF PHASES 1,2,AND 3 AT LOW CAPILLARY NO.
*---P1RW P2RW P3RW
  0.025 1.0 0.025
CC
CC CONSTANT REL. PERM. EXPONENT OF PHASES 1,2,AND 3 AT LOW CAPILLARY NO.
*---E1W E2W E3W
  2.  2.  2
CC
CC RES. SATURATION OF HPASES 1,2,AND 3 AT HIGH CAPILLARY NO.
*---S1RC S2RC S3RC
  0.  0.0  0.
CC
CC ENDPOINT REL. PERM. OF PHASES 1,2,AND 3 AT HIGH CAPILLARY NO.
*---P1RC P2RC P3RC
  1  1.0  1.
CC
CC REL. PERM. EXPONENT OF PHASES 1,2,AND 3 AT HIGH CAPILLARY NO.
*---E13CW E23C E31C
  1.  1.0  1.
CC
CC WATER AND OIL VISCOSITY , RESERVOIR TEMPERATURE
*---VIS1 VIS2 TEMPV
  1.  220.0  0.
CC Mu_p: the polymer viscosity in equation 5.4; delta_0: equation 5.5; c: equation 4.13
CC COMPOSITIONAL PHASE VISCOSITY PARAMETERS
*--- Nu    Nu_prime Mu_p delta_0 c
  1.8    3.9    50.    0.01  0.
CC
CC PARAMETERS TO CALCULATE POLYMER VISCOSITY AT ZERO SHEAR RATE
*---AP1 AP2 AP3

```

```

80.0 200.0 28000
CC
CC PARAMETER TO COMPUTE CSEP,MIN. CSEP, AND SLOPE OF LOG VIS. VS. LOG CSEP
*----BETAP CSE1 SSLOPE
1 0.01 -0.36
CC
CC PARAMETER FOR SHEAR RATE DEPENDENCE OF POLYMER VISCOSITY
*----GAMMAC GAMHF POWN IPMOD ishear rweff GAMHF2
4.0 3. 1.6 0 0 0.25 0
CC
CC FLAG FOR POLYMER PARTITIONING, PERM. REDUCTION PARAMETERS
*----IPOLYM EPHI3 EPHI4 BRK CRK RKCUT
1 1. 1. 1. 0.4 1.
CC
CC SPECIFIC WEIGHT FOR COMPONENTS 1,2,3,7,AND 8 , AND GRAVITY FLAG
*----DEN1 DEN2 DEN23 DEN3 DEN7 DEN8 IDEN
0.43353 0.33353 0.33353 0.35353 0.346 0 1
CC
CC FLAG FOR CHOICE OF UNITS ( 0:BOTTOMHOLE CONDITION , 1: STOCK TANK)
*----ISTB
0
CC
CC COMPRESSIBILITY FOR VOL. OCCUPYING COMPONENTS 1,2,3,7,AND 8
*----COMPC(1) COMPC(2) COMPC(3) COMPC(7) COMPC(8)
0.0 0.0 0. 0. 0.
CC
CC CAPILLARY PRESSURE PARAMETERS, WATER-WET OR OIL-WET PC CURVE FLAG
*----ICPC IEPC IOW
0 0 0
CC
CC
*----CPC
0.00
CC
CC
*----EPC
2.
CC
CC MOLECULAR DIFFUSIVITY OF KCTH COMPONENT IN PHASE 1 (D(KC),KC=1,N)
*----D(1) D(2) D(3) D(4) D(5) D(6) D(7) D(8) D(9) D(10) D(11)
13*0.
CC
CC MOLECULAR DIFFUSIVITY OF KCTH COMPONENT IN PHASE 2 (D(KC),KC=1,N)
*----D(1) D(2) D(3) D(4) D(5) D(6) D(7) D(8) D(9) D(10) D(11)
13*0.
CC
CC MOLECULAR DIFFUSIVITY OF KCTH COMPONENT IN PHASE 3 (D(KC),KC=1,N)
*----D(1) D(2) D(3) D(4) D(5) D(6) D(7) D(8) D(9) D(10) D(11)
13*0.
CC
CC LONGITUDINAL AND TRANSVERSE DISPERSIVITY OF PHASE 1 (FT)
*----ALPHAL(1) ALPHAT(1)
0.001 0.00

```

```

CC
CC LONGITUDINAL AND TRANSVERSE DISPERSIVITY OF PHASE 2 (FT)
*----ALPHAL(2)  ALPHAT(2)
    0.01    0.0
CC
CC LONGITUDINAL AND TRANSVERSE DISPERSIVITY OF PHASE 3 (FT)
*----ALPHAL(3)  ALPHAT(3)
    0.01    0.0
CC
CC FLAG TO SPECIFY ORGANIC ADSORPTION CALCULATION
*----IADSO
    0
CC
CC SURFACTANT AND POLYMER ADSORPTION PARAMETERS
*----AD31 AD32  B3D  AD41  AD42  B4D  IADK, IADS1, FADS  REFK
    1.0 2.0 1000. 2.0 0.2 100.0 0 0 0 0 1
2 1 300
7.0 11.0 11.0 0.25
.065 .103
1
0.025 0.01 0.03
7 18 4 4 3 1
7 1 4 12
5 4 1 2 3
0 0 0
6
CALCIUM                2.00
MAGNESIUM              2.00
CARBON (AS CARBOBATES) -2.00
SODIUM                 1.00
HYDROGEN (REACTIVE)    1.00
ACID (PETROLEUM)      -1.00
CHLORINE               -1.00
HYDROGEN ION
SODIUM ION
CALCIUM ION
MAGENSIUM ION
CARBONATE ION
PETROLEUM ACID IN OIL
WATER
CALCIUM MONOHYDROXIDE ION
MAGNESIUM MONOHYDROXIDE ION
CA (HC03) +
MG (HCO3) +
PETRLEUM ACID ANION
HYDROXIDE ION
BICARBONATE ION
DISSOLVED CARBON MONOHYDROXIDE
AQUEOUS CALCIUM CARBONATE
AQUEOUS MAGNESIUM CARBONATE
PETROLEUM ACID IN WATER
CALCIUM CARBONATE(SOLID)
MAGNESIUM CARBONATE (SOLID)

```


CALCIUM HYDROXIDE (SOLID)
 MAGNESIUM HYDROXIDE(SOLID) (*
 SORBED HYDROGEN ION
 SORBED SODIUM ION
 SORBED CALCIUM ION
 SORBED MAGNESIUM ION (*
 SURF. ASSOCIATED SODIUM ION
 SURF. ASSOCIATED CALCIUM ION
 SURF. ASSOCIATED MAGNESIUM ION

4
 0. 0. 1. 0. 0. 0. 0. 1. 0. 1. 0. 0. 0. 0. 0.
 1. 0. 0.
 0. 0. 0. 1. 0. 0. 0. 0. 1. 0. 1. 0. 0. 0. 0.
 0. 1. 0.
 0. 0. 0. 0. 1. 0. 0. 0. 0. 1. 1. 0. 0. 1. 1.
 1. 1. 0.
 0. 1. 0. 0. 0. 0. 0. 0. 0. 0. 0. 0. 0. 0. 0.
 0. 0. 0.
 1. 0. 0. 0. 0. 1. 2. 1. 1. 1. 1. 0. 1. 1. 2.
 0. 0. 1.
 0. 0. 0. 0. 0. 1. 0. 0. 0. 0. 0. 1. 0. 0. 0.
 0. 0. 1.
 1. 0. 1. 0.
 0. 1. 0. 1.
 1. 1. 0. 0.
 0. 0. 0. 0.
 0. 0. 2. 2.
 0. 0. 0. 0.
 0. 0. 1. 0.
 0. 0. 0. 1.
 0. 0. 0. 0.
 0. 1. 0. 0.
 1. 0. 0. 0.
 0. 0. 0. 0.
 0. 1. 0.
 0. 0. 1.
 0. 0. 0.
 1. 0. 0.
 0. 0. 0.
 0. 0. 0.
 1.0 0.0 0.0 0.0 0.0 0.0 0.0 0.0 0.0 0.0 0.0 0.0
 0.0 0.0
 0.0 1.0 0.0 0.0 0.0 0.0 0.0 0.0 0.0 0.0 0.0 0.0
 0.0 0.0
 0.0 0.0 1.0 0.0 0.0 0.0 0.0 0.0 0.0 0.0 0.0 0.0
 0.0 0.0
 0.0 0.0 0.0 1.0 0.0 0.0 0.0 0.0 0.0 0.0 0.0 0.0
 0.0 0.0
 0.0 0.0 0.0 0.0 1.0 0.0 0.0 0.0 0.0 0.0 0.0 0.0
 0.0 0.0
 0.0 0.0 0.0 0.0 0.0 1.0 0.0 0.0 0.0 0.0 0.0 0.0

```

0.0 0.0
-1.0 0.0 1.0 0.0 0.0 0.0 0.0 0.0 0.0 0.0 0.0 0.0
0.0 0.0
-1.0 0.0 0.0 1.0 0.0 0.0 0.0 0.0 0.0 0.0 0.0 0.0
0.0 0.0
1.0 0.0 1.0 0.0 1.0 0.0 0.0 0.0 0.0 0.0 0.0 0.0
0.0 0.0
1.0 0.0 0.0 1.0 1.0 0.0 0.0 0.0 0.0 0.0 0.0 0.0
0.0 0.0
-1.0 0.0 0.0 0.0 0.0 1.0 0.0 0.0 0.0 0.0 0.0 0.0
0.0 0.0
-1.0 0.0 0.0 0.0 0.0 0.0 0.0 0.0 0.0 0.0 0.0 0.0
0.0 0.0
1.0 0.0 0.0 0.0 1.0 0.0 0.0 0.0 0.0 0.0 0.0 0.0
0.0 0.0
2.0 0.0 0.0 0.0 1.0 0.0 0.0 0.0 0.0 0.0 0.0 0.0
0.0 0.0
0.0 0.0 1.0 0.0 1.0 0.0 0.0 0.0 0.0 0.0 0.0 0.0
0.0 0.0
0.0 0.0 0.0 1.0 1.0 0.0 0.0 0.0 0.0 0.0 0.0 0.0
0.0 0.0
0.0 0.0 0.0 0.0 0.0 1.0 0.0 0.0 0.0 0.0 0.0 0.0
0.0 0.0
0.0 0.0 0.0 0.0 0.0 0.0 0.0 1.0 0.0 0.0 0.0 0.0
0.0 0.0
0.0 0.0 0.0 0.0 0.0 0.0 0.0 0.0 1.0 0.0 0.0 0.0
0.0 0.0
0.0 0.0 0.0 0.0 0.0 0.0 0.0 0.0 0.0 1.0 0.0 0.0
0.0 0.0
0.0 0.0 0.0 0.0 0.0 0.0 0.0 0.0 0.0 0.0 1.0 0.0
0.0 0.0
1.0 0.0
0.0 0.0 0.0 0.0 0.0 0.0 0.0 0.0 0.0 0.0 0.0 0.0
0.0 1.0
0.0 0.0 1.0 0.0 1.0 0.0 0.0
0.0 0.0 0.0 1.0 1.0 0.0 0.0
-2.0 0.0 1.0 0.0 0.0 0.0 0.0
-2.0 0.0 0.0 1.0 0.0 0.0 0.0
1.0 1.0 2.0 2.0 -2.0 0.0 0.0 1.0 1.0 1.0 1.0 -1.0
-1.0 -1.0 0.0 0.0 0.0 0.0
1.0 1.0 2.0 2.0
0.100000000000E+01 0.100000000000E+01 0.100000000000E+01
0.100000000000E+01 0.100000000000E+01 0.100000000000E+01
0.100000000000E+01 0.166000000000E-12 0.363000000000E-11
0.237000000000E+12 0.224000000000E+12 0.7917078606491E-11
0.140000000000E-12 0.135000000000E+11 0.272000000000E+17
0.578000000000E+04 0.185000000000E+04 0.3059975166926E-02
0.793000000000E-05 0.520000000000E-05 0.270000000000E+02
0.0 2.0 -1.0 0.0 0.0 0.0 0.0 0.0 -2.0 1.0 0.0 0.0
0.0 0.0

```

```

0.0 2.0 0.0 -1.0 0.0 0.0 0.0 0.0 -2.0 0.0 1.0 0.0
0.0 0.0
-1.0 1.0 0.0 0.0 0.0 0.0 1.0 -1.0 0.0 0.0 0.0
0.0 0.0
-1.0 -1.0 0.0
0.4898549357910E-10
0.5410000000000E-05 0.7000000000000E-04 0.4731500000000E+23
0.5604500000000E+17
1.0 2.0 2.0
0.5000000000000E+00 0.9400000000000E+00
0.0 2.0 -1.0 0.0 0.0 0.0 0.0 0.0 0.0 0.0 -2.0
1.0 0.0
0.0 2.0 0.0 -1.0 0.0 0.0 0.0 0.0 0.0 0.0 -2.0
0.0 1.0
0.2187711689474E-03 0.2336276138245E-13 0.1848291102813E-19
0.2300000000000E+00 0.4794079529757E-03
0.2000000000000E-09
0.4795673529757E-03
0.2299999999000E+00
0.1100000000000E+03
0.8461059352980E-03
0.2050130252966E+00
0.7419187108109E-08 0.2297812287311E+00 0.2356204586802E-03
0.9915197107255E-10 0.2296065473390E-05 0.1991538940647E+00
0.5489998104509E+02
0.0000000000000E+00 0.0000000000000E+00 0.0000000000000E+00
0.0000000000000E+00
0.4270440255620E-16 0.4898545087470E-10 0.1733499898875E-27
0.4783462041004E-34
0.9997039505939E+00 0.9330494484385E+00
0.2587301587302E-08 0.3500000000000E+03
CC
CC*****
CC
CC PART5 : WELL DATA
CC
CC*****
CC
CC
CC FLAG FOR BOUNDARIES
*--- IBOUND IZONE
0 0
CC
CC TOTAL NUMBER OF WELLS, WELL RADIUS FLAG, FLAG FOR TIME OR COURANT NO.
*---- NWELL IRO ITSTEP NWREL
2 2 1 2
CC
CC WELL ID,LOCATIONS,AND FLAG FOR SPECIFYING WELL TYPE, WELL RADIUS, SKIN
*---IDW IW JW IFLAG RW SWELL IDIR IFIRST ILAST IPRF
1 1 1 1 .003 0. 3 1 1 0
CC
CC WELL NAME
*---- #1

```

```

INJECTOR
CC
CC MAX. AND MIN. ALLOWABLE BOTTOMHOLE PRESSURE AND RATE
*----ICHEK PWFMIN PWFMAX QTMIN QTMAX
  0 0. 20000. 0. 200.
CC
CC WELL ID,LOCATIONS,AND FLAG FOR SPECIFYING WELL TYPE, WELL RADIUS, SKIN
*----IDW IW JW IFLAG RW SWELL IDIR IFIRST ILAST IPRF
  2 100 1 2 .003 0. 3 1 1 0
CC
CC WELL NAME
*----#2
PRODUCER
CC
CC MAX. AND MIN. ALLOWABLE BOTTOMHOLE PRESSURE AND RATE
*----ICHEK PWFMIN PWFMAX QTMIN QTMAX
  0 0. 20000. 0. 0.
CC
CC ID,INJ. RATE AND INJ. COMP. FOR RATE CONS. WELLS FOR EACH PHASE (L=1,3)
*----ID QI(M,L) C(M,KC,L)
  1 0.004 1. 0. 0.0 0.0 0.006 0.000001 0.0 0.0 0.000001 0.077 0.077 111. 0.000001
  1 0. 13*0.
  1 0. 13*0.
CC
CC ID, BOTTOM HOLE PRESSURE FOR PRESSURE CONSTRAINT WELL (IFLAG=4)
*----ID PWF
  2 14.47
CC
CC CUM. INJ. TIME , AND INTERVALS (PV OR DAY) FOR ERITING TO OUTPUT FILES
*----TINJ(PV) CUMPR1 CUMHI1 WRHPV WRPRF RSTC
  0.25 0.05 0.05 0.05 0.05 5.
CC
CC FOR IMES=2, ITIME=1, INI. DT ,CONC. TOLERANCE, MAX.,MIN. COURANT NUMBERS
*----DT DCLIM(KC=1,16) CNMAX CNMIN
  0.000001 0.05 0.05 0.05 0.05 0.05 0.05 0.05 0.05 0.05 0.05 0.05 0.05 0.05 0.1 .0001
cc
cc
*--- ibmod
  0
CC
CC IRO, ITIME, NEW FLAGS FOR ALL THE WELLS
*---- IRO ITIME IFLAG(M),M=1,NWELL
  2 1 1 2
CC
CC NUMBER OF WELLS CHANGES IN LOCATION OR SKIN OR PWF
*----NWEL1
  0
CC
CC NUMBER OF WELLS WITH RATE CHANGES, ID
*----NWEL2 ID
  1 1
CC
CC ID,INJ. RATE AND INJ. COMP. FOR RATE CONS. WELLS FOR EACH PHASE (L=1,3)

```

```

*----ID QI(M,L) C(M,KC,L)
  1 0.004 1.  0. 0.0  0.0 0.000001 0.000001 2*0. 0.0000001 0.045 0.045 111. 0.000001
  1 0.  13*0.
  1 0.  13*0.
CC
CC CUM. INJ. TIME , AND INTERVALS (PV OR DAY) FOR ERITING TO OUTPUT FILES
*----TINJ  CUMPR1  CUMHI1  WRHPV  WRPRF  RSTC
  2.5  0.05  0.05  0.05  0.05  5
CC
CC FOR IMES=2, ITIME=1, INI. DT ,CONC. TOLERANCE, MAX.,MIN. COURANT NUMBERS
*----DT  DCLIM(KC=1,16)  CNMAX  CNMIN
0.00001 0.05 0.05 0.05 0.05 0.05 0.5 0.05 0.05 0.05 0.05 0.05 0.05 0.05 0.2 .0001

```

Bibliography

- Acosta, E. J., Yuan, J. S., and Bhakta, A. S. (2008). "The Characteristic Curvature of Ionic Surfactants." *Journal of Surfactants and Detergents*, 11(2), 145–158.
- Adkins, S., Liyanage, P., Pinnawala Arachchilage, G. W. P., Mudiyansele, T., Weerasooriya, U., and Pope, G. (2010). "A New Process for Manufacturing and Stabilizing High-Performance EOR Surfactants at Low Cost for High-Temperature, High-Salinity Oil Reservoirs." *SPE Improved Oil Recovery Symposium*.
- Anand, J., Somerton, W. H., and Gomaa, E. (1973). "Predicting Thermal Conductivities of Formations From Other Known Properties." *Society of Petroleum Engineers Journal*, 13(5).
- Andelman, D. (1995). "Electrostatic properties of membranes: the Poisson-Boltzmann theory." *Handbook of biological physics*, 1, 603–642.
- Andelman, D., Cates, M. E., Roux, D., and Safran, S. A. (1987). "Structure and phase equilibria of microemulsions." *The Journal of Chemical Physics*, 87(12), 7229.
- Andelman, D., Kawakatsu, T., and Kawasaki, K. (1992). "Equilibrium shape of two-component unilamellar membranes and vesicles." *EPL (Europhysics Letters)*, 19(1), 57.
- Anisimov, M., and St. Pierre, H. (2008). "Diverging curvature correction to the interfacial tension in polymer solutions." *Physical Review E*, 78(1).
- Appell, J., Porte, G., and Buhler, E. (2005). "Self-Diffusion and Collective Diffusion of Charged colloids Studied by Dynamic Light Scattering." *arXiv:cond-mat/0506656*.
- Ardali, M., Barrufet, M., Mamora, D., and Qiu, F. (2012). "A Critical Review of Hybrid Steam/Solvent Processes for the Recovery of Heavy Oil and Bitumen." *SPE Annual Technical Conference and Exhibition*.
- Arleth, L., and Pedersen, J. (2001). "Droplet polydispersity and shape fluctuations in AOT [bis(2-ethylhexyl)sulfosuccinate sodium salt] microemulsions studied by contrast variation small-angle neutron scattering." *Physical Review E*, 63(6).
- Audet, C., and Dennis, J. E. (2004). "A Pattern Search Filter Method for Nonlinear Programming without Derivatives." *SIAM Journal on Optimization*, 14(4), 980–1010.
- Bachu, S. (1993). "Basement heat flow in the Western Canada Sedimentary Basin." *Tectonophysics*, 222(1), 119–133.
- Al-Bahlani, A.-M., and Babadagli, T. (2009). "SAGD laboratory experimental and numerical simulation studies: A review of current status and future issues." *Journal of Petroleum Science and Engineering*, 68(3-4), 135–150.
- Ball, J. T., and Pitts, M. J. (1984). "Effect of Varying Polyacrylamide Molecular Weight on Tertiary Oil Recovery From Porous Media of Varying Permeability." Society of Petroleum Engineers.

- Barentin, C., Ybert, C., Di Meglio, J.-M., and Joanny, J.-F. (1999). "Surface shear viscosity of Gibbs and Langmuir monolayers." *Journal of Fluid Mechanics*, 397, 331–349.
- Batchelor, G. K. (1977). "The effect of Brownian motion on the bulk stress in a suspension of spherical particles." *Journal of Fluid Mechanics*, 83(01), 97–117.
- Benedouch, D., Chen, S. H., and Koehler, W. C. (1983). "Structure of ionic micelles from small angle neutron scattering." *The Journal of Physical Chemistry*, 87(1), 153–159.
- Berg, R. F., Moldover, M. R., and Huang, J. S. (1987). "Quantitative characterization of the viscosity of a microemulsion." *The Journal of Chemical Physics*, 87(6), 3687.
- Bergström, L. M. (2006). "Bending Elasticity of Charged Surfactant Layers: The Effect of Mixing." *Langmuir*, 22(16), 6796–6813.
- Bhuyan, D., Lake, L., and Pope, G. (1990). "Mathematical modeling of high-pH chemical flooding." *SPE Reservoir Engineering*, 5(2), 213–220.
- Binder, K., Block, B., Das, S. K., Virnau, P., and Winter, D. (2011). "Monte Carlo methods for estimating interfacial free energies and line tensions." *Journal of Statistical Physics*, 144(3), 690–729.
- Binks, B. P., Meunier, J., Abillon, O., and Langevin, D. (1989). "Measurement of film rigidity and interfacial tensions in several ionic surfactant-oil-water microemulsion systems." *Langmuir*, 5(2), 415–421.
- Block, B. J., Das, S. K., Oettel, M., Virnau, P., and Binder, K. (2010). "Curvature dependence of surface free energy of liquid drops and bubbles: A simulation study." *The Journal of chemical physics*, 133(154702), 154702.
- Blokhuis, E. M., and Kuipers, J. (2006). "Thermodynamic expressions for the Tolman length." *The Journal of Chemical Physics*, 124(7), 074701.
- Bodet, J. F., Bellare, J. R., Davis, H. T., Scriven, L. E., and Miller, W. G. (1988). "Fluid microstructure transition from globular to bicontinuous in mid-range microemulsion." *The Journal of Physical Chemistry*, 92(7), 1898–1902.
- Bogdanov, I., Torres, J., El Ganaoui, K., and Kamp, A. (2010). "The Influence of Salt Concentration in Injected Water on Low Frequency Electrical-Heating Assisted Bitumen Recovery." *SPE Improved Oil Recovery Symposium*.
- Bourrel, M., Salager, J. L., Schechter, R. S., and Wade, W. H. (1980). "A correlation for phase behavior of nonionic surfactants." *Journal of Colloid and Interface Science*, 75(2), 451–461.
- Brady, J. F. (1993). "The rheological behavior of concentrated colloidal dispersions." *Journal of Chemical Physics*, 99(1), 567–581.
- Burauer, S., Belkoura, L., Stubenrauch, C., and Strey, R. (2003). "Bicontinuous microemulsions revisited: a new approach to freeze fracture electron microscopy (FFEM)." *Colloids and Surfaces A: Physicochemical and Engineering Aspects*, 228(1-3), 159–170.
- Burrowes, A., Teare, M., Marsh, R., Gigantelli, P., Macgillivray, J., and Evans, C. (2011). "Alberta's Energy Reserves 2010 and Supply/Demand Outlook 2011–2020." *Energy Resources Conservation Board Publication*.

- Carrero, E., Queipo, N. V., Pintos, S., and Zerpa, L. E. (2007). "Global sensitivity analysis of Alkali-Surfactant-Polymer enhanced oil recovery processes." *Journal of Petroleum Science and Engineering*, 58(1-2), 30-42.
- Cash, L., Cayias, J. L., Fournier, G., Macallister, D., Schares, T., Schechter, R. S., and Wade, W. H. (1977). "The application of low interfacial tension scaling rules to binary hydrocarbon mixtures." *Journal of Colloid and Interface Science*, 59(1), 39-44.
- Cates, M. E., Andelman, D., Safran, S. A., and Roux, D. (1988). "Theory of microemulsions: comparison with experimental behavior." *Langmuir*, 4(4), 802-806.
- Cayias, J. L., Schechter, R. S., and Wade, W. H. (1976). "Modeling Crude Oils for Low Interfacial Tension." *Society of Petroleum Engineers Journal*, 16(6).
- Cazabat, A. M., and Langevin, D. (1981). "Diffusion of interacting particles: Light scattering study of microemulsions." *The Journal of Chemical Physics*, 74(6), 3148-3158.
- Cebula, D. J., Ottewill, R. H., Ralston, J., and Pusey, P. N. (1981). "Investigations of microemulsions by light scattering and neutron scattering." *J. Chem. Soc., Faraday Trans. 1*, 77(11), 2585-2612.
- Chang, H., Farouq Ali, S., and George, A. (1992). "Performance Of Horizontal-Vertical Combinations For Steamflooding Bottom Water Formations." *Journal of Canadian Petroleum Technology*, 31(5).
- Cheng, X., McCoy, J. H., Israelachvili, J. N., and Cohen, I. (2011). "Imaging the Microscopic Structure of Shear Thinning and Thickening Colloidal Suspensions." *Science*, 333(6047), 1276-1279.
- Cheng, Z., Zhu, J., Chaikin, P., Phan, S.-E., and Russel, W. (2002). "Nature of the divergence in low shear viscosity of colloidal hard-sphere dispersions." *Physical Review E*, 65(4).
- Chhetri, A. B., and Islam, M. R. (2008). "A Critical Review of Electromagnetic Heating for Enhanced Oil Recovery." *Petroleum Science and Technology*, 26(14), 1619-1631.
- Computer Modelling Group. (2011). "Computer Modelling Group (CMG) LTD, STARS User Manual, Version 2011.10."
- Cosgrove, T., White, S. J., Zarbakhsh, A., Heenan, R. K., and Howe, A. M. (1995). "Small-angle scattering studies of sodium dodecyl sulfate interactions with gelatin. 1." *Langmuir*, 11(3), 744-749.
- Cross, M. M. (1965). "Rheology of non-Newtonian fluids: A new flow equation for pseudoplastic systems." *Journal of Colloid Science*, 20(5), 417-437.
- Daicic, J., Fogden, A., Carlsson, I., Wennerström, H., and Jönsson, B. (1996). "Bending of ionic surfactant monolayers." *Physical Review E*, 54(4), 3984.
- Daicic, J., Olsson, U., and Wennerstroem, H. (1995). "Phase equilibria of balanced microemulsions." *Langmuir*, 11(7), 2451-2458.
- Dannhauser, W., and Cole, R. H. (1955). "Dielectric Properties of Liquid Butyl Alcohols." *The Journal of Chemical Physics*, 23(10), 1762.

- Das, S. (2008). "Electro-Magnetic Heating in Viscous Oil Reservoir." *SPE International Thermal Operations and Heavy Oil Symposium*.
- Davies, J. T. (1957). "A quantitative kinetic theory of emulsion type, I. Physical chemistry of the emulsifying agent." *Proceedings of the 2nd International Congress on Surface Activity*, 426.
- Davis, J. R. (1994). *Stainless Steels*. ASM International.
- Delshad, M., Han, C., Koyassan Veedu, F., and Pope, G. (2011). "A Simplified Model for Simulations of Alkaline-Surfactant-Polymer Floods." *SPE Reservoir Simulation Symposium*.
- Delshad, M., Pope, G. A., and Sepehrnoori, K. (1996). "A compositional simulator for modeling surfactant enhanced aquifer remediation, 1 formulation." *Journal of Contaminant Hydrology*, 23(4), 303–327.
- Delshad, M., Pope, G. A., and Sepehrnoori, K. (2000). "UTCHEM version 9.0 technical documentation." *Center for Petroleum and Geosystems Engineering, The University of Texas at Austin, Austin, Texas*, 78751.
- Dobrosavljević, A. S., and Maglić, K. D. (1992). "Measurements of specific heat and electrical resistivity of austenitic stainless steel (St. 1.4970) in the range 300–1500 K by pulse calorimetry." *International journal of thermophysics*, 13(1), 57–64.
- Dustin Walker. (2011). "Experimental investigation of the effect of increasing the temperature on ASP flooding." University of Texas at Austin.
- Espinosa, G., and Langevin, D. (2009). "Interfacial Shear Rheology of Mixed Polyelectrolyte–Surfactant Layers." *Langmuir*, 25(20), 12201–12207.
- Evilevitch, A., Lobaskin, V., Olsson, U., Linse, P., and Schurtenberger, P. (2001). "Structure and Transport Properties of a Charged Spherical Microemulsion System." *Langmuir*, 17(4), 1043–1053.
- Farago, B., Monkenbusch, M., Goecking, K. D., Richter, D., and Huang, J. S. (1995). "Dynamics of microemulsions as seen by neutron spin echo." *Physica B: Condensed Matter*, 213, 712–717.
- Feldman, Y., Kozlovich, N., Nir, I., and Garti, N. (1995). "Dielectric relaxation in sodium bis (2-ethylhexyl) sulfosuccinate–water–decane microemulsions near the percolation temperature threshold." *Physical Review E*, 51(1), 478.
- Feldman, Y., Kozlovich, N., Nir, I., Garti, N., Archipov, V., Idiyatullin, Z., Zuev, Y., and Fedotov, V. (1996). "Mechanism of transport of charge carriers in the sodium bis (2-ethylhexyl) sulfosuccinate-water-decane microemulsion near the percolation temperature threshold." *The Journal of Physical Chemistry*, 100(9), 3745–3748.
- Feller, S. E., and Pastor, R. W. (1999). "Constant surface tension simulations of lipid bilayers: the sensitivity of surface areas and compressibilities." *The Journal of chemical physics*, 111, 1281.
- Feng, J. J., Liu, C., Shen, J., and Yue, P. (2005). "An energetic variational formulation with phase field methods for interfacial dynamics of complex fluids: advantages and challenges." *Modeling of soft matter*, Springer, 1–26.
- Flaaten, A., Nguyen, Q., Pope, G., and Zhang, J. (2008). "A Systematic Laboratory Approach to Low-Cost, High-Performance Chemical Flooding." *SPE/DOE Improved Oil Recovery Symposium*.

- Fortenberry, R. (2013). "Experimental Demonstration and Improvement of Chemical EOR Techniques in Heavy Oils." University of Texas at Austin.
- Fortenberry, R., Kim, D. H., Nizamidin, N., Adkins, S., Pinnawala Arachchilage, G., Koh, H. S., Weerasooriya, U., and Pope, G. (2013). "Use of Co-Solvents to Improve Alkaline-Polymer Flooding." *SPE Annual Technical Conference and Exhibition*.
- Foss, D. R., and Brady, J. F. (2000). "Structure, diffusion and rheology of Brownian suspensions by Stokesian dynamics simulation." *Journal of Fluid Mechanics*, 407(1), 167–200.
- Frank, C., Frielinghaus, H., Allgaier, J., and Prast, H. (2007). "Nonionic Surfactants with Linear and Branched Hydrocarbon Tails: Compositional Analysis, Phase Behavior, and Film Properties in Bicontinuous Microemulsions." *Langmuir*, 23(12), 6526–6535.
- De Gennes, P. G., and Taupin, C. (1982). "Microemulsions and the flexibility of oil/water interfaces." *The Journal of Physical Chemistry*, 86(13), 2294–2304.
- Ghoufi, A., and Malfreyt, P. (2011). "Mesoscale modeling of the water liquid-vapor interface: A surface tension calculation." *Physical Review E*, 83(5).
- Gill, P., Murray, W., and Wright, M. (1981). *Practical optimization*. Academic Press.
- Glandt, C. A., and Chia-Fu, H. (1992). "Electric Preheating in Low-Injectivity Tar Sand Deposits." *SPE/DOE Enhanced Oil Recovery Symposium*.
- Golubović, L., and Lubensky, T. C. (1990). "Thermal fluctuations and phase equilibrium in microemulsions." *Physical Review A*, 41(8), 4343.
- Gózdź, W. T., and Hołyst, R. (1996). "Triply periodic surfaces and multiply continuous structures from the Landau model of microemulsions." *Physical Review E*, 54(5), 5012–5027.
- Gradzielski, M., and Hoffmann, H. (1999). "Rheological properties of microemulsions." *Handbook of microemulsion science and technology*, 357–386.
- Gradzielski, M., Langevin, D., and Farago, B. (1996). "Experimental investigation of the structure of nonionic microemulsions and their relation to the bending elasticity of the amphiphilic film." *Physical Review E*, 53(4), 3900.
- Griffin, W. C. (1949). "Classification of Surface-Active Agents by HLB." *Journal of the Society of Cosmetic Chemists*, 1, 311.
- Gross, S., and Reusken, A. (2013). "Numerical simulation of continuum models for fluid-fluid interface dynamics." *The European Physical Journal Special Topics*, 222(1), 211–239.
- Guering, P., and Lindman, B. (1985). "Droplet and bicontinuous structures in microemulsions from multicomponent self-diffusion measurements." *Langmuir*, 1(4), 464–468.
- Gurkov, T. D., and Kralchevsky, P. A. (1990). "Surface tension and surface energy of curved interfaces and membranes." *Colloids and Surfaces*, 47, 45–68.
- Hackett, J. L., and Miller, C. A. (1988). "Microemulsion to liquid-crystal transition in two anionic surfactant systems." *SPE reservoir engineering*, 3(3), 791–800.

- Harting, J., Giupponi, G., and Coveney, P. V. (2007). "Structural transitions and arrest of domain growth in sheared binary immiscible fluids and microemulsions." *Physical Review E*, 75(4), 041504.
- Hattori, Y., Ushiki, H., Courbin, L., and Panizza, P. (2007). "Slow relaxation mode in concentrated oil-in-water microemulsions consisting of repulsive droplets." *Physical Review E*, 75(2), 021504.
- Hayter, J. B. (1992). "A self-consistent theory of dressed micelles." *Langmuir*, 8(12), 2873–2876.
- Helfrich, W. (1973). "Elastic properties of lipid bilayers: theory and possible experiments." *Z. Naturforsch. c*, 28(11), 693–703.
- Hellweg, T., Gradzielski, M., Farago, B., and Langevin, D. (2001). "Shape fluctuations of microemulsion droplets: a neutron spin-echo study." *Colloids and Surfaces A: Physicochemical and Engineering Aspects*, 183, 159–169.
- Hellweg, T., and Langevin, D. (1998). "Bending elasticity of the surfactant monolayer in droplet microemulsions: Determination by a combination of dynamic light scattering and neutron spin-echo spectroscopy." *Physical Review E*, 57(6), 6825.
- Hennes, M., and Gompper, G. (1996). "Dynamical behavior of microemulsion and sponge phases in thermal equilibrium." *Physical Review E*, 54(4), 3811.
- Hiebert, A. D., Capjack, C. E., Chute, F. S., and Vermeulen, F. E. (1983). "A simulation code for investigating 2D heating of material bodies by low frequency electric fields." *Applied Mathematical Modelling*, 7(5), 366–371.
- Hirasaki, G., and Lawson, J. B. (1986). "An electrostatic approach to the association of sodium and calcium with surfactant micelles." *SPE Reservoir Engineering*, 1(2), 119–130.
- Hirose, Y., Komura, S., and Andelman, D. (2012). "Concentration fluctuations and phase transitions in coupled modulated bilayers." *Physical Review E*, 86(2), 021916.
- Hoffmann, H. (1994). "Viscoelastic Surfactant Solutions." *Structure and Flow in Surfactant Solutions*, C. A. Herb and R. K. Prud'homme, eds., American Chemical Society, Washington, DC, 2–31.
- Holmberg, K. (2003). *Surfactants and polymers in aqueous solution*. John Wiley & Sons, Chichester [etc.].
- Horai, K. (1971). "Thermal conductivity of rock-forming minerals." *Journal of Geophysical Research*, 76(5), 1278–1308.
- Huang, J. S., Milner, S. T., Farago, B., and Richter, D. (1987). "Study of dynamics of microemulsion droplets by neutron spin-echo spectroscopy." *Physical review letters*, 59(22), 2600–2603.
- Huh, C. (1983). "Equilibrium of a microemulsion that coexists with oil or brine." *Old SPE Journal*, 23(5), 829–847.
- Imhof, A., van Blaaderen, A., Maret, G., Mellema, J., and Dhont, J. K. G. (1994). "A comparison between the long-time self-diffusion and low shear viscosity of concentrated dispersions of charged colloidal silica spheres." *The Journal of Chemical Physics*, 100(3), 2170.
- Israelachvili, J. (1994). "The science and applications of emulsions — an overview." *Colloids and Surfaces A: Physicochemical and Engineering Aspects*, 91, 1–8.

- Israelachvili, J. N. (2011). *Intermolecular and surface forces: revised third edition*. Academic press.
- Israelachvili, J. N., Mitchell, D. J., and Ninham, B. W. (1976). "Theory of self-assembly of hydrocarbon amphiphiles into micelles and bilayers." *Journal of the Chemical Society, Faraday Transactions 2: Molecular and Chemical Physics*, 72, 1525–1568.
- Jackson, A. C. (2006). "Experimental Study of the Benefits of Sodium Carbonate on Surfactants for Enhanced Oil Recovery." University of Texas at Austin.
- Jahn, W., and Strey, R. (1988). "Microstructure of microemulsions by freeze fracture electron microscopy." *The Journal of Physical Chemistry*, 92(8), 2294–2301.
- Jia, Z.-P., Wang, R., Chen, Q.-Y., Xie, H., Ma, J., Liu, Y.-Y., and Wang, J. (2009). "CE of Small DNA Fragments Using Linear Polyacrylamide Matrices." *Chromatographia*, 70(7-8), 1127–1134.
- Jouffroy, J., Levinson, P., and de Gennes, P. G. (1982). "Phase equilibria involving microemulsions (Remarks on the Talmon-Prager model)." *Journal de Physique*, 43(8), 1241–1248.
- Kabalnov, A., Lindman, B., Olsson, U., Piculell, L., Thuresson, K., and Wennerström, H. (1996). "Microemulsions in amphiphilic and polymer-surfactant systems." *Colloid and Polymer Science*, 274(4), 297–308.
- Kahlweit, M., Strey, R., and Busse, G. (1991). "Effect of alcohols on the phase behavior of microemulsions." *The Journal of Physical Chemistry*, 95(13), 5344–5352.
- Kahlweit, M., Strey, R., and Haase, D. (1985). "Phase behavior of multicomponent systems water-oil-amphiphile-electrolyte. 3." *The Journal of Physical Chemistry*, 89(1), 163–171.
- Kawabata, Y., Nagao, M., Seto, H., Komura, S., Takeda, T., Schwahn, D., Yamada, N. L., and Nobutou, H. (2004). "Temperature and pressure effects on the bending modulus of monolayers in a ternary microemulsion." *Physical review letters*, 92(5), 56103.
- Kegel, W. K., Bodnar, I., and Lekkerkerker, H. N. (1995). "Bending elastic moduli of the surfactant film and properties of a Winsor II microemulsion system." *The Journal of Physical Chemistry*, 99(10), 3272–3281.
- Kellay, H., Meunier, J., and Binks, B. P. (1993). "Saddle-splay modulus of the AOT monolayer in the AOT-brine-oil system." *Physical review letters*, 70(10), 1485–1488.
- Kleinert, H. (1986). "Thermal softening of curvature elasticity in membranes." *Physics Letters A*, 114(5), 263–268.
- Koci, P., and Mohiddin, J. (2007a). "Realistic History Matching of Cyclic Steam Stimulation Performance of Several Groups of Multilateral Wells in the Peace River Field, Canada." *EUROPEC/EAGE Conference and Exhibition*.
- Koci, P., and Mohiddin, J. (2007b). "Peace River Carmon Creek Project—Optimization of Cyclic Steam Stimulation Through Experimental Design." *SPE Annual Technical Conference and Exhibition*.

- Koehler, R. D., Raghavan, S. R., and Kaler, E. W. (2000). "Microstructure and Dynamics of Wormlike Micellar Solutions Formed by Mixing Cationic and Anionic Surfactants." *The Journal of Physical Chemistry B*, 104(47), 11035–11044.
- Komura, S. (2007). "Mesoscale structures in microemulsions." *Journal of Physics: Condensed Matter*, 19(46), 463101.
- Kotlarchyk, M., Sheu, E. Y., and Capel, M. (1992). "Structural and dynamical transformations between neighboring dense microemulsion phases." *Physical Review A*, 46(2), 928.
- Kozlov, M. M., and Helfrich, W. (1992). "Effects of a cosurfactant on the stretching and bending elasticities of a surfactant monolayer." *Langmuir*, 8(11), 2792–2797.
- Kralchevsky, P. A., Eriksson, J. C., and Ljunggren, S. (1994). "Theory of curved interfaces and membranes: mechanical and thermodynamical approaches." *Advances in colloid and interface science*, 48, 19–59.
- Krieger, I. M., and Dougherty, T. J. (1959). "A mechanism for non-Newtonian flow in suspensions of rigid spheres." *Journal of Rheology*, 3, 137.
- Krishnamurthy, L., Weigert, E. C., Wagner, N. J., and Boris, D. C. (2004). "The shear viscosity of polyampholyte (gelatin) stabilized colloidal dispersions." *Journal of Colloid and Interface Science*, 280(1), 264–275.
- De Kruif, C. G., van Iersel, E. M. F., Vrij, A., and Russel, W. B. (1985). "Hard sphere colloidal dispersions: Viscosity as a function of shear rate and volume fraction." *The Journal of Chemical Physics*, 83(9), 4717.
- Langevin, D. (1988). "Microemulsions." *Accounts of Chemical Research*, 21(7), 255–260.
- Langevin, D. (1992). "Micelles and microemulsions." *Annual Review of Physical Chemistry*, 43(1), 341–369.
- Larter, S. R., Adams, J., Gates, I. D., Bennett, B., and Huang, H. (2008). "The origin, prediction and impact of oil viscosity heterogeneity on the production characteristics of tar sand and heavy oil reservoirs." *Journal of Canadian Petroleum Technology*, 47(1), 52.
- Leaver, M. S., and Olsson, U. (1994). "Viscosity of a nonionic microemulsion near emulsification failure." *Langmuir*, 10(10), 3449–3454.
- Lelanne-Cassou, C., Carmona, I., Fortney, L., Samii, A., Schechter, R. S., Wade, W. H., Weerasooriya, V., and Yiv, S. (1983). "Binary Surfactant Mixtures for Minimizing Alcohol Cosolvent Requirements." *SPE Annual Technical Conference and Exhibition*.
- Levitt, D., Bourrel, M., Bondino, I., Jouenne, S., and Gingras, J.-P. (2011). "The Interpretation of Polymer Coreflood Results for Heavy Oil." *SPE Heavy Oil Conference and Exhibition*.
- Levitt, D., Jackson, A., Heinson, C., Britton, L., Malik, T., Dwarakanath, V., and Pope, G. (2006). "Identification and Evaluation of High-Performance EOR Surfactants." *SPE/DOE Improved Oil Recovery Symposium*.
- Lisy, V., and Brutovsky, B. (2000). "Interpretation of static and dynamic neutron and light scattering from microemulsion droplets: Effects of shape fluctuations." *Physical Review E*, 61(4), 4045.

- Lu, J., Brown, J. S., Liotta, C. L., and Eckert, C. A. (2001). "Polarity and hydrogen-bonding of ambient to near-critical water: Kamlet-Taft solvent parameters." *Chemical Communications*, (7), 665–666.
- Lu, J., Pope, G., and Weerasooriya, U. (2013). "Stability Investigation in Low-Tension Surfactant Floods." *2013 SPE International Symposium on Oilfield Chemistry*.
- Luo, W., and Torabi, F. (2013). "Coupling of Solvent and Hot Water to Improve Heavy Oil Recovery: Experimental and Simulation Studies." *SPE Heavy Oil Conference Canada*.
- Mahjoub, H. F., Bourgaux, C., Sergot, P., and Kleman, M. (1998). "Evidence of a sponge-to-lamellar phase transition under shear by x-ray scattering experiments in a couette cell." *Physical review letters*, 81(10), 2076–2079.
- Mahjoub, H. F., McGrath, K. M., and Kleman, M. (1996). "Phase transition induced by shearing of a sponge phase." *Langmuir*, 12(13), 3131–3138.
- Majolino, D., Mallamace, F., Venuto, S., and Micali, N. (1990). "Viscosity measurements in dense microemulsions." *Physical Review A*, 42(12), 7330.
- Masih, S., Ma, K., Sanchez, J., Patino, F., and Boida, L. (2012). "The Effect of Bottom Water Coning and Its Monitoring for Optimization in SAGD." *SPE Heavy Oil Conference Canada*.
- McGee, B. (2008). "Electro-Thermal Pilot in the Athabasca Oil Sands: Theory Versus Performance." *Canadian International Petroleum Conference/SPE Gas Technology Symposium 2008 Joint Conference*.
- McGee, B. C., and Vermeulen, F. E. (1996). "Electrical Heating with Horizontal Wells The Heat Transfer Problem." *International Conference on Horizontal Well Technology*.
- McGee, B. C. W., and Vermeulen, F. E. (2007). "The Mechanisms of Electrical Heating for the Recovery of Bitumen From Oil Sands." *The Journal of Canadian Petroleum Technology*, 46(1-6).
- McGee, B. C. W., Vermeulen, F. E., and Yu, L. (1999). "Field test of electrical heating with horizontal and vertical wells." *Journal of Canadian Petroleum Technology*, 38(03).
- Medina-Noyola, M. (1988). "Long-time self-diffusion in concentrated colloidal dispersions." *Physical review letters*, 60(26), 2705.
- Di Meglio, J. M., Dvolaitzky, M., and Taupin, C. (1985). "Determination of the rigidity constant of the amphiphilic film in ' birefringent microemulsions'; the role of the cosurfactant." *The Journal of Physical Chemistry*, 89(5), 871–874.
- Meredith, W., Kelland, S.-J., and Jones, D. M. (2000). "Influence of biodegradation on crude oil acidity and carboxylic acid composition." *Organic Geochemistry*, 31(11), 1059–1073.
- Messina, R. (2009). "Electrostatics in soft matter." *Journal of Physics: Condensed Matter*, 21(11), 113102.
- Mewis, J., and Wagner, N. J. (2012). *Colloidal suspension rheology*. Cambridge University Press.
- Mihcakan, I. M., and C.W., V. (1986). "Blending Alkaline and Polymer Solutions Together Into a Single Slug Improves EOR." Society of Petroleum Engineers.

- Milner, S. T., Cates, M. E., and Roux, D. (1990). "Hydrodynamic modes and topology in microemulsions and L3 phases." *Journal de Physique*, 51(22), 2629–2639.
- Milner, S. T., and Safran, S. A. (1987). "Dynamical fluctuations of droplet microemulsions and vesicles." *Physical Review A*, 36(9), 4371.
- Mitchell, D. J., and Ninham, B. W. (1983). "Electrostatic curvature contributions to interfacial tension of micellar and microemulsion phases." *The Journal of Physical Chemistry*, 87(16), 2996–2998.
- Mohammadi, H., Delshad, M., and Pope, G. (2009). "Mechanistic Modeling of Alkaline/Surfactant/Polymer Floods." *SPE Reservoir Evaluation & Engineering*, 12(4).
- Moreira, A. G., and Netz, R. R. (2000). "Strong-coupling theory for counter-ion distributions." *EPL (Europhysics Letters)*, 52(6), 705.
- Morse, D. C. (1994). "Topological instabilities and phase behavior of fluid membranes." *Physical Review E*, 50(4), R2423.
- Morse, D. C. (1997). "Entropy and fluctuations of monolayers, membranes, and microemulsions." *Current opinion in colloid & interface science*, 2(4), 365–372.
- Moulik, S. P., and Paul, B. K. (1998). "Structure, dynamics and transport properties of microemulsions." *Advances in Colloid and Interface science*, 78(2), 99–195.
- Murray, B. S., Drummond, C. J., Grieser, F., and White, L. R. (1990). "Determination of electrostatic surface potentials of oil-in-water microemulsion droplets using a lipoidal acid-base spectroscopic probe." *Journal of physical chemistry*, 94(17), 6804–6812.
- Mutyala, S., Fairbridge, C., Paré, J. R. J., Bélanger, J. M. R., Ng, S., and Hawkins, R. (2010). "Microwave applications to oil sands and petroleum: A review." *Fuel Processing Technology*, 91(2), 127–135.
- Naji, A., Jungblut, S., Moreira, A. G., and Netz, R. R. (2005). "Electrostatic interactions in strongly coupled soft matter." *Physica A: Statistical Mechanics and its Applications*, 352(1), 131–170.
- Nelson, R. C., Lawson, J. B., Thigpen, D. R., and Stegemeier, G. L. (1984). "Cosurfactant-enhanced alkaline flooding." *SPE Enhanced Oil Recovery Symposium*.
- Nielsen, L. E. (1974). *Mechanical properties of polymers and composites*. Dekker New York.
- Niggemann, G., Kummrow, M., and Helfrich, W. (1995). "The bending rigidity of phosphatidylcholine bilayers: dependences on experimental method, sample cell sealing and temperature." *Journal de Physique II*, 5(3), 413–425.
- Oliveira, H., Barillas, J. L., da Mata, W., and Dutra, T. (2009). "Energetic Optimization to Heavy Oil Recovery by Electromagnetic Resistive Heating (ERH)." *Latin American and Caribbean Petroleum Engineering Conference*.
- Omari, A., Moan, M., and Chauveteau, G. (1989). "Wall effects in the flow of flexible polymer solutions through small pores." *Rheologica Acta*, 28(6), 520–526.
- Opawale, F. O., and Burgess, D. J. (1998). "Influence of interfacial properties of lipophilic surfactants on water-in-oil emulsion stability." *Journal of colloid and interface science*, 197(1), 142–150.

- Oskouei, S. J. P., Maini, B., Moore, R. G., and Mehta, S. A. (2012). "Effect of initial water saturation on the thermal efficiency of the steam-assisted gravity-drainage process." *Journal of Canadian Petroleum Technology*, 51(5), 351–361.
- Ottewill, R. H., and Williams, N. S. J. (1987). "Study of particle motion in concentrated dispersions by tracer diffusion." *Nature*, 325, 232–234.
- Pätzold, G., and Dawson, K. (1996). "Connection of microstructure to rheology in a microemulsion model." *Physical Review E*, 54(2), 1669.
- Perez-Casas, S., Castillo, R., and Costas, M. (1997). "Effect of alcohols in AOT reverse micelles. A heat capacity and light scattering study." *The Journal of Physical Chemistry B*, 101(36), 7043–7054.
- Perlmutter, J. D., and Sachs, J. N. (2011). "Interleaflet Interaction and Asymmetry in Phase Separated Lipid Bilayers: Molecular Dynamics Simulations." *Journal of the American Chemical Society*, 133(17), 6563–6577.
- Peter, U., Roux, D., and Sood, A. K. (2001). "Observation of a topological relaxation mode in microemulsions." *Physical review letters*, 86(15), 3340–3343.
- Peyrelasse, J., Moha-Ouchane, M., and Boned, C. (1988). "Viscosity and the phenomenon of percolation in microemulsions." *Physical Review A*, 38(8), 4155.
- Pincus, P., Joanny, J.-F., and Andelman, D. (1990). "Electrostatic interactions, curvature elasticity, and steric repulsion in multimembrane systems." *EPL (Europhysics Letters)*, 11(8), 763.
- Pizarro, J. O. S., and Trevisan, O. V. (1990). "Electrical heating of oil reservoirs: numerical simulation and field test results." *Journal of Petroleum Technology*, 42(10), 1,320–1,326.
- Pope, G., Tsaur, K., Schechter, R., and Wang, B. (1982). "The Effect of Several Polymers on the Phase Behavior of Micellar Fluids." *Society of Petroleum Engineers Journal*, 22(6).
- Porcar, L., Hamilton, W., Butler, P., and Warr, G. (2002). "Scaling of Shear-Induced Transformations in Membrane Phases." *Physical Review Letters*, 89(16).
- Porte, G., Appell, J., Bassereau, P., and Marignan, J. (1989). "L_α to L₃: a topology driven transition in phases of infinite fluid membranes." *Journal de Physique*, 50(11), 1335–1347.
- Rangel-German, E. R., Schembre, J., Sandberg, C., and Kovsky, A. R. (2004). "Electrical-heating-assisted recovery for heavy oil." *Journal of Petroleum Science and Engineering*, 45(3-4), 213–231.
- Reed, R. L., and Healy, R. N. (1977). "Some physicochemical aspects of microemulsion flooding: a review." *Improved Oil Recovery by Surfactant and Polymer Flooding*, 383–437.
- Reekmans, S., Luo, H., Van der Auweraer, M., and De Schryver, F. C. (1990). "Influence of alcohols and alkanes on the aggregation behavior of ionic surfactants in water." *Langmuir*, 6(3), 628–637.
- Rekvis, L., Hafskjold, B., and Smit, B. (2004). "Simulating the effect of surfactant structure on bending moduli of monolayers." *The Journal of chemical physics*, 120, 4897.

- Rice, S. A., Kok, A. L., and Neate, C. J. (1992). "A Test of the electric heating process as a means of stimulating the productivity of an oil well in the Schoonebeek Field." *Annual Technical Meeting*.
- Safinya, C. R., Sirota, E. B., Roux, D., and Smith, G. S. (1989). "Universality in interacting membranes: The effect of cosurfactants on the interfacial rigidity." *Physical review letters*, 62(10), 1134–1137.
- Safran, S. A. (1991). "Bicontinuous to lamellar transitions in L3 phases and microemulsions." *Langmuir*, 7(9), 1864–1866.
- Safran, S. A. (1999). "Curvature elasticity of thin films." *Advances in Physics*, 48(4), 395–448.
- Safran, S. A., Pincus, P. A., Andelman, D., and MacKintosh, F. C. (1991). "Stability and phase behavior of mixed surfactant vesicles." *Physical Review A*, 43(2), 1071.
- Safran, S. A., Roux, D., Cates, M. E., and Andelman, D. (1986). "Origin of middle-phase microemulsions." *Physical review letters*, 57(4), 491–494.
- Safran, S. A., Webman, I., and Grest, G. S. (1985). "Percolation in interacting colloids." *Physical Review A*, 32(1), 506.
- Sagi, A. R., Thomas, C., Bian, Y., Kwan, J., Salehi, M., Hirasaki, G., Puerto, M., and Miller, C. (2013). "Laboratory Studies for Surfactant Flood in Low-Temperature, Low-Salinity Fractured Carbonate Reservoir." *2013 SPE International Symposium on Oilfield Chemistry*.
- Sagis, L. M. C. (2011). "Dynamic properties of interfaces in soft matter: Experiments and theory." *Reviews of Modern Physics*, 83(4), 1367–1403.
- Sahni, A., Kumar, M., Knapp, R. B., and Livermore, L. (2000). "Electromagnetic heating methods for heavy oil reservoirs." *SPE/AAPG Western Regional Meeting*.
- Salager, J. L., Morgan, J. C., Schechter, R. S., Wade, W. H., and Vasquez, E. (1979). "Optimum Formulation of Surfactant/Water/Oil Systems for Minimum Interfacial Tension or Phase Behavior." *Society of Petroleum Engineers Journal*, 19(2).
- Salager, J.-L., and Antón, R. E. (1999). *Ionic microemulsions*. Marcel Dekker: New York.
- Salager, J.-L., Marquez, N., Graciaa, A., and Lachaise, J. (2000). "Partitioning of ethoxylated octylphenol surfactants in microemulsion-oil-water systems: influence of temperature and relation between partitioning coefficient and physicochemical formulation." *Langmuir*, 16(13), 5534–5539.
- Saskoil, S., and Butler, R. (1990). "The Production Of Conventional Heavy Oil Reservoirs With Bottom Water Using Steam-Assisted Gravity Drainage." *Journal of Canadian Petroleum Technology*.
- Scalettar, B. A., Abney, J. R., and Owicki, J. C. (1988). "Theoretical comparison of the self diffusion and mutual diffusion of interacting membrane proteins." *Proceedings of the National Academy of Sciences*, 85(18), 6726–6730.
- Schechter, R. S., and Bourrel, M. (1998). *Microemulsions and related systems*. New York: Marcel Dekker.
- Schick, M. (2012). "Membrane heterogeneity: Manifestation of a curvature-induced microemulsion." *Physical Review E*, 85(3), 031902.

- Seto, A. C., and Bharatha, S. (1991). "Thermal Conductivity Estimation From Temperature Logs." *SPE International Thermal Operations Symposium*.
- Shah, A., Fishwick, R., Wood, J., Leeke, G., Rigby, S., and Greaves, M. (2010). "A review of novel techniques for heavy oil and bitumen extraction and upgrading." *Energy & Environmental Science*, 3(6), 700.
- Shah, D. O., and Schechter, R. S. (1977). *Improved oil recovery by surfactant and polymer flooding*. Academic Pr.
- Shell Canada Limited. (2009). "Application for Approval of the Carmon Creek Project. Volume 1: Project Description."
- Sheu, E. Y., Chen, S.-H., Huang, J. S., and Sung, J. C. (1989). "Nonexponential relaxations in dense microemulsion near the glasslike transition." *Physical Review A*, 39(11), 5867.
- Shin, H., and Choe, J. (2009). "Shale Barrier Effects on the SAGD Performance." *SPE/EAGE Reservoir Characterization & Simulation Conference*.
- Shinoda, K., and Arai, H. (1964). "The Correlation between Phase Inversion Temperature In Emulsion and Cloud Point in Solution of Nonionic Emulsifier." *The Journal of Physical Chemistry*, 68(12), 3485–3490.
- Sierra, R., Tripathy, B., Bridges, J. E., and Ali, S. M. (2001). "Promising progress in field application of reservoir electrical heating methods." *SPE International Thermal Operations and Heavy Oil Symposium*.
- Sohrabi, B., Bazayari, A., and Hashemianzadeh, M. (2010). "Effect of ethylene glycol on micellization and surface properties of Gemini surfactant solutions." *Colloids and Surfaces A: Physicochemical and Engineering Aspects*, 364(1-3), 87–93.
- Solairaj, S., Britton, C., Lu, J., Kim, D. H., Weerasooriya, U., and Pope, G. (2012). "A New Correlation to Predict the Best Surfactant Structure for Chemical EOR." Society of Petroleum Engineers.
- Sorbie, K. S. (1991). *Polymer-improved oil recovery*. Blackie ; CRC Press, Glasgow; Boca Raton, Fla.
- Sorensen, J. A., and Glass, G. E. (1987). "Ion and temperature dependence of electrical conductance for natural waters." *Analytical Chemistry*, 59(13), 1594–1597.
- Sottmann, T., Strey, R., and Chen, S.-H. (1997). "A small-angle neutron scattering study of nonionic surfactant molecules at the water–oil interface: Area per molecule, microemulsion domain size, and rigidity." *The Journal of Chemical Physics*, 106(15), 6483.
- Strey, R. (1993). "On the Stability Range of Microemulsions: From the Tricritical Point to the Lamellar Phase in Water/Formamide-Octane-CiEj Systems." *Berichte der Bunsengesellschaft für physikalische Chemie*, 97(5), 742–750.
- Strey, R. (1994). "Microemulsion microstructure and interfacial curvature." *Colloid & Polymer Science*, 272(8), 1005–1019.
- Strey, R., and Jonströmer, M. (1992). "Role of medium-chain alcohols in interfacial films of nonionic microemulsions." *The Journal of Physical Chemistry*, 96(11), 4537–4542.

- Szleifer, I., Kramer, D., Ben-Shaul, A., Roux, D., and Gelbart, W. M. (1988). “Curvature elasticity of pure and mixed surfactant films.” *Physical review letters*, 60(19), 1966–1969.
- Taghavifar, M., Upamali, K. A. N., Sepehrnoori, K., and Pope, G. A. (n.d.). “Partitioning of Large Poly(Acrylamide)s in Polymer-Microemulsion Systems.”
- Talmon, Y., and Prager, S. (1978). “Statistical thermodynamics of phase equilibria in microemulsions.” *The Journal of Chemical Physics*, 69(7), 2984.
- Tanaka, H., Isobe, M., and Miyazawa, H. (2006). “Shear-induced discontinuous and continuous topological transitions in a hyperswollen membrane system.” *Physical Review E*, 73(2).
- Teraoka, I. (2002). *Polymer solutions an introduction to physical properties*. Wiley, New York.
- Teubner, M., and Strey, R. (1987). “Origin of the scattering peak in microemulsions.” *The Journal of Chemical Physics*, 87(5), 3195.
- The Mathworks Inc. (2010). *Genetic algorithm and pattern search toolbox, user guide, version 2*. The Mathworks Inc, Natick, MA. The Mathworks Inc.
- Tlusty, T., Safran, S. A., and Strey, R. (2000). “Topology, phase instabilities, and wetting of microemulsion networks.” *Physical review letters*, 84(6), 1244–1247.
- Veenstra, H., Verkooijen, P. C., van Lent, B. J., van Dam, J., de Boer, A. P., and Nijhof, A. P. H. (2000). “On the mechanical properties of co-continuous polymer blends: experimental and modelling.” *Polymer*, 41(5), 1817–1826.
- Vinson, P. K., Sheehan, J. G., Miller, W. G., Scriven, L. E., and Davis, H. T. (1991). “Viewing microemulsions with freeze-fracture transmission electron microscopy.” *The Journal of Physical Chemistry*, 95(6), 2546–2550.
- Wade, W. H., Morgan, J. C., Jacobson, J. K., and Schechter, R. S. (1977). “Low interfacial tensions involving mixtures of surfactants.” *Old SPE Journal*, 17(2), 122–128.
- Wagner, N. J., and Brady, J. F. (2009). “Shear thickening in colloidal dispersions.” *Physics Today*, 62(10), 27–32.
- Walker, D., Britton, C., Kim, D. H., Dufour, S., Weerasooriya, U., and Pope, G. (2012). “The Impact of Microemulsion Viscosity on Oil Recovery.” *SPE Improved Oil Recovery Symposium*.
- Wennerström, H., and Olsson, U. (2009). “Microemulsions as model systems.” *Comptes Rendus Chimie*, 12(1), 4–17.
- Van der Werff, J. C., and De Kruif, C. G. (1989). “Hard-sphere colloidal dispersions: The scaling of rheological properties with particle size, volume fraction, and shear rate.” *Journal of Rheology*, 33, 421.
- Widom, B. (1984). “A model microemulsion.” *The Journal of Chemical Physics*, 81(2), 1030.
- Willemse, R. C., Speijer, A., Langeraar, A. E., and Posthuma de Boer, A. (1999). “Tensile moduli of co-continuous polymer blends.” *Polymer*, 40(24), 6645–6650.
- Winsor, P. A. (1954). *Solvent properties of amphiphilic compounds*. Butterworths Scientific Publications.

- Winterhalter, M., and Helfrich, W. (1992). "Bending elasticity of electrically charged bilayers: coupled monolayers, neutral surfaces, and balancing stresses." *The Journal of Physical Chemistry*, 96(1), 327–330.
- Yang, G., and Butler, R. (1992). "Effects Of Reservoir Heterogeneities On Heavy Oil Recovery By Steam-Assisted Gravity Drainage." *Journal of Canadian Petroleum Technology*, 31(8).
- Yu, W., Zhou, W., and Zhou, C. (2010). "Linear viscoelasticity of polymer blends with co-continuous morphology." *Polymer*, 51(9), 2091–2098.
- Zhao, D., and Gates, I. (2013). "Stochastic Optimization of Hot Water Flooding Strategy in Thin Heavy Oil Reservoirs." *SPE Heavy Oil Conference Canada*.
- Zhao, P., Jackson, A., Britton, C., Kim, D., Britton, L., Levitt, D., and Pope, G. (2008). "Development of high-performance surfactants for difficult oils." *SPE/DOE Symposium on Improved Oil Recovery*.
- Zhong, L., Yu, D., Yang, H., Sun, Y., Wang, G., and Zheng, J. (2011). "Feasibility Study on Producing Heavy Oil by Gas and Electrical Heating Assisted Gravity Drainage." *The Offshore Technology Conference*.
- Zhu, Z., and Zeng, F. (2012). "Evaluation of the Hybrid Process of Electrical Resistive Heating and Solvent Injection Through Numerical Simulations." *SPE Heavy Oil Conference Canada*.